Numerical and plasma theoretical quantification of impurity effects on characteristic measurements in the nuclear fusion experiment Wendelstein 7-X

Inaugural-Dissertation

zur Erlangung des Doktorgrades
der Mathematisch-Naturwissenschaftlichen Fakultät
der Heinrich-Heine-Universität Düsseldorf

vorgelegt von

JÖRG COSFELD

aus Düsseldorf

DÜSSELDORF, SEP 2020

aus dem Institut für Energie- und Klimaforschung – Plasmaphysik
des Forschungszentrum Jülich.

Gedruckt mit der Genehmigung der
Mathematisch-Naturwissenschaftlichen Fakultät der
Heinrich-Heine-Universität Düsseldorf

Berichterstatter:
1. Prof. Dr. Yunfeng Liang
2. Prof. Dr. Reinhold Egger

Tag der mündlichen Prüfung: 09.09.2020

ABSTRACT

Nuclear fusion is the most promising candidate for solving modern mankind's lack of a renewable primary energy source. However, available magnetic concepts must be optimized in the plasma edge region where temperatures of several million degrees Celsius are reached. The core plasma interacts with system boundaries in the plasma edge region, which therefore has a significant role in confining fusion plasma.

Transport effects in such a plasma has to be studied in its details. The Wendelstein 7-X (W7-X) is one of the world's most modern nuclear fusion experiments. Its complex magnetic design allows a confined plasma without the need of an induced plasma current. Clean hydrogen plasmas are not considered as clean hydrogen plasmas. This is because impure particles are unintentionally introduced into the plasma through interactions with plasma-facing wall components.

This study was dedicated to acquiring further information about impurity effects within the complex plasma edge region of the W7-X. EMC3-EIRENE simulations were applied for this task. Furthermore, a numerical plasma edge tool that solves self-consistent three-dimensional fluid equations in a given magnetic configuration was used. Any numerical description of plasma showed a vast number of free system input parameters. These were constrained via the input of characteristic plasma edge measurements in the W7-X. Obtained numerical solutions were then compared with the experimental results of the diagnostics results. Langmuir probes were the main focus of this study because their recorded data are directly linked to a quantification of the impurity content in the considered plasma. Theory shows that measured electron densities n are only accessible via an effective charge state Z_{eff}, which is often assumed to be equal to one.

Assumptions about the impurity content were replaced with numerically assessed quantifications and used in iterative refinement processes for various Langmuir probe diagnostics. Furthermore, multi-species impurity simulations were considered in respect of impurity release rates into the plasma. Subsequently, assessed release rates were compared to frequently used empirical release rates, enabling a direct insight into the impurity species charge state distribution.

In addition, iterative processes were conducted for W7-X plasmas when consistency between the EMC3-EIRENE simulation and several diagnostics (including Langmuir probes) was given.The W7-X underwent updates including one for the heat exhaust concept, from operational phase OP1.1 to OP1.2. Both operational phases were studied regarding the impurity effects in the plasma edge region, and a comparison between the results of the applied iterative process for OP1.1 and OP1.2 were given.

KURZFASSUNG

Die Fusion zweier Kerne, mit anderen Worten die Kernfusion, ist der vielversprechendste Kandidat um die Lücke der modernen und erneuerbaren Energiequellen zu schließen. Jedoch sind dazu magnetisch optimierte Topologien von Nöten, welche den Rand des Fusionsplasma von der ersten Wand des Experimentes fernhalten. Hier kommt es zu Temperaturen von mehreren Millionen Grad Celsius. Die Randschicht des Plasmas und ihre Grenze zu dem Plasmakern spielt daher eine tragende Rolle.
Transporteffekte in solch einem Plasma müssen im Detail studiert werden, um die Dynamik des Plasmas bewerten zu können. Wendelstein 7-X (W7-X) ist eines der modernsten Kernfusion Experimente. Kein induzierter Plasma Strom ist für den Betrieb von W7-X von Nöten da eine komplexe Verdrillung der magnetischen Spulen das Plasma im Experiment einschließt. Diese Plasmen stehen bei magnetischen Feldfehlern oder Instabilitäten im direkten Kontakt zu der ersten Wand des Experiments. Dort gelangen Verunreinigungen in das Plasma. Ein angestrebtes reines Wasserstoffplasma nimmt Verunreinigungen auf und darf nicht weiter als Wasserstoffplasma theoretisch beschrieben werden. Die vorliegende Arbeit dient der Erforschung detaillierter Einsichten und Informationen über den Einfluss von Verunreinigungen und deren Effekte auf den Rand eines W7-X Fusionplasmas. Dazu werden EMC3-EIRENE Simulationen ausgeführt, welche dann als numerische Diagnostik für den Plasmarand dienen. EMC3-EIRENE löst selbstkonsistent dreidimensionale Fluidgleichungen in einer beliebigen magnetischen Konfiguration. Jegliche dreidimensionale Plasmabeschreibung, auch EMC3-EIRENE, hat eine Vielfalt von verschiedenen freien Systemparametern welche über die Hinzunahme von charakteristischen Plasmarand Diagnostiken eingeschränkt worden sind. Simulationsergebnisse werden dann wiederum zum Vergleich mit den angewendeten Diagnostiken herangezogen. Langmuir Proben und EMC3-EIRENE Simulationen, bilden den Kern dieser Vergleiche, da die Datenverarbeitung der Langmuir Proben direkt mit der Verunreinigungsmenge des Plasmas korreliert. Hier zeigt sich, dass gemessene Elektronendichten nur über eine effektive Ladungszahl, welche ungleich eins ist, reproduziert werden. Diese Ladungszahl ist oft gleich eins angenommen worden.
Annahmen über die effektive Ladungszahl des Plasmas und damit Annahmen über die Menge an Verunreinigungen im Plasma werden durch numerisch erschlossene Quantisierungen der effektiven Ladungszahl ersetzt. Dazu dient ein neu definierter iterativer Prozess zwischen experimentellen und numerischen Befunden. Weiter, sind Simulationen ausgeführt worden, welche nicht nur Kohlenstoff als Verunreinigung zulassen sondern auch Sauerstoff als sekundäre Verunreinigung. Hiervon lassen sich im direkten Vergleich, nur sehr schwer messbare, Befunde ableiten und Vorhersagen für zukünftige Plasmen in Wendelstein 7-X treffen. Abschließend werden alle Befunde für die erste und zweite Operationsphase von Wendelstein 7-X gegenüber gestellt, um einen direkten Vergleich zwischen Plasmaparametern zu ermöglichen. Hier zeigen sich deutliche Unterschiede da große Umbauten an W7-X , zwischen den Operationsphasen stattgefunden haben.

TABLE OF CONTENTS

List of Figures

CHAPTER 1

INTRODUCTION

The controlled fusion of two different atomic nuclei is one of the most promising options for future power sources. In particular, the inexhaustible access to the required fuel as well as carbon dioxide (CO_2)-free emission energy gain have motivated worldwide research. The energy gained results from the binding energy difference between two atomic nuclei, which must be lighter than iron. The hydrogen isotopes deuterium D and tritium T fuse to a single helium core with one neutron as a side product; 17.6 *MeV is released in this process,*

$$D + T \rightarrow \mathrm{He}\ (3.5\mathrm{MeV}) + n\ (14.1\mathrm{MeV}) \quad . \tag{1.0.0.1}$$

Process (1.0.0.1) *shows the most feasible fusion process. However, strong plasma confinement is required because Coulomb collisions and their particle interactions have a larger scattering cross-section than does process* (1.0.0.1).
Earthly fusion processes cannot be conducted through gravitational forces such as stellar nuclear fusion. Thus, manmade nuclear fusion depend on earthly created forces from magnetic fields, which are formed in a symmetric torus. Plasma particles, which are fully ionized atoms and electrons, follow magnetic field lines because of the acting Lorentz force. One difference exists between the tokamak and stellarator concepts; although both rely on a toroidal-shaped magnetic field, the way this field is created differs. Tokamaks use a less complex field structure than stellarators do. Symmetric poloidal coils are placed along a toroidal experiment chamber equidistant from each other. These are superconducting and used for the creation of the toridal magnetic field. A plasma current is induced as a supplementary poloidal field. Plasma particles obey the superposition of the toroidal and poloidal field and orbit within the torus. By contrast, stellarators do not require a poloidal-induced plasma current. Rather, the superposition field is obtained from twisted superconducting coils, which give the stellarator its complex design.

The triple product quantifies the quality of the created magnetic field with respect to particle confinement. It is defined as the product of the plasma density n, plasma temperature T, and the energy confinement time τ_E, $n \cdot T \cdot \tau_E$. Until now, confinement times reached by modern tokamaks reach $\tau_E \approx 1$s, whereas those of modern stellarators reach $\tau_E \approx 0.2$s. The reason for this is the tokamaks' simplicity in coil design compared with that of stellarators. Thus, research on tokamaks is more advanced than that on stellarators [1, 2].

One of the main problems in fusion research is plasma particles not following the magnetic field configuration because of instabilities and interactions. Those that carry high energies, in the form of heat, are able to reach installations or first-wall elements and damage them. Therefore, particle exhaust is a crucial design point for tokamaks and stellarators.

The construction phase of the most modern fusion experiment Wendelstein 7-X (W7-X) was completed in 2015 after 22 years.W7-X features five identical modules expanding over 72° of the torus, containing the magnetic coils and first-wall elements. These installations have the same toroidal and poloidal position for each module. A limiter was installed in each module for the first operational phase (OP1.1), lasting until March 2016. Limiters are, in their basic concept, target plates that act as a heat exhaust to prevent first-wall elements from damage. They are constructed from high heat resistant materials to withstand high energy loads. Closed magnetic field lines are intersected by the limiter tip. One separates the region between closed and open magnetic field lines at the limiter tip's position and defines the position of the last closed flux surface (LCFS). The second operational phase (OP1.2) began in September 2017 and lasts until now. In contrast to the limiter, a divertor was installed in each module for the second operational phase. Divertor plates do not suffer from direct contact with the plasma edge. Closed magnetic field lines that are disjointed from the main magnetic field configuration are called magnetic islands. Instead, the magnetic configuration is tweaked to favor magnetic islands that are in front of divertor plates. Thus, these island structures are used to divert heat from fusion plasma and protect first-wall elements. However, plasma instabilities often cause the plasma reaching the divertor and limiter installations or even first-wall elements. When this happens, sufficiently high plasma temperatures hold enough energy to vaporize and melt surface structures. The plasma absorbs these material structures as impurities and ionizes them; furthermore, it loses energy because the released impurities increase radiative losses. This directly correlates to the triple product and confinement time τ_E, which is reduced.

The three-dimensional (3D) complex geometry of the W7-X needs set of diagnostics throughout the machine to quantify the aforementioned effects. W7-X is equipped with numerous diagnostic ports to assure such quantification. One of the simplest yet meaningful diagnostics is the Langmuir probe; a Langmuir probe is set to a bias voltage and plunges into the plasma edge over a split second. Interpretations of the measured voltages caused by the bombardment of charged plasma particles demand knowledge about the exact plasma composition, including impurities. Therefore, interpretations of Langmuir probe measurements depend strongly on the number and weight of impurities in the plasma.

W7-X's complex geometry cannot be simplified using established two-dimensional models because these depend on a tokamak-like geometry; a full 3D description of the system is required. Well-established code packages (including their theory), such as B2-EIRENE [3], EDGE2D [4], and SOLPS-ITER [5], are not applicable for this kind of geometry. However, the code package EMC3-EIRENE, especially through the versatility in its applicability to all types of experiment geometries, provides a solution to this problem. This has already been proven via the successful application of EMC3-EIRENE to the W7-X's predecessor, W7-AS [6], as well as the Large Helical Device (LHD) [7]. EMC3 solves a set of fluid equations based on Braginskii equations [8], whereas EIRENE solves a kinetic transport equation in phase space for neutral particles. Both their algorithms follow a Monte Carlo scheme, and furthermore, EMC3 has the valuable option of treating any impurities in a given geometry.

1.1 Nuclear fusion

A fusion plasma can only be maintained if direct contact with the experimental wall elements is prevented, because otherwise the plasma would quickly cool. Thus, one confines the plasma with magnetic fields, which takes advantage of the fact that it is a fully ionized gas.
Free charged particles are confined through the Lorentz force of an applied magnetic field. Here, the Lorentz force acts perpendicular to the magnetic field and the particles' motion. The particles' motion is directly affected by it, but it accelerates them in a perpendicular direction, resulting in a guiding center motion. Thus, confined particles will circle around a magnetic field line, with a gyro-radius that is anti-proportional to the strength of the applied magnetic field.
In Section 1.2, an introduction is provided to the tokamak and stellarator, including their magnetic topology. Subsequently, Section 2.2 presents an introduction to three-dimensional boundary plasma physics.

1.2 Magnetically confined fusion plasma experiments

A stationary proton, or a proton moving along a magnetic field line, feels no acting force. However, this changes if the proton moves across field lines. Then, the magnetic field will push it in a perpendicular direction. Hydrogen ions and electrons have the same charge but of opposite signs, which results in the Lorentz force acting upon them in opposite directions. Field lines are like invisible railroad tracks that guide the motion of these charged particles [9]. This means that field lines that have a dead end on a boundary surface cannot prevent direct plasma wall contact. However, charged particles cannot cross field lines because of the acting magnetic force. Nuclear fusion scientists' solution to this problem is to generate a magnetic field with field lines that close on themselves and not on wall elements. The simplest magnetic topology that features closed magnetic field lines is a torus. Ions and electrons cannot find a way out by moving along a field line. The torus is filled with field lines that can be split in groups of toroidal and poloidal field lines. The first runs in a toroidal direction

along the torus, whereas the latter runs around the torus in a poloidal direction. Combining these will result in a helix that is bent into a circle. The magnetic field line density is higher on the inside of the torus than on the outside because an inner toroidal field line travels a shorter distance within the torus than an outer one; see Figure 1.1. Furthermore, charged particles will no longer gyrate in a

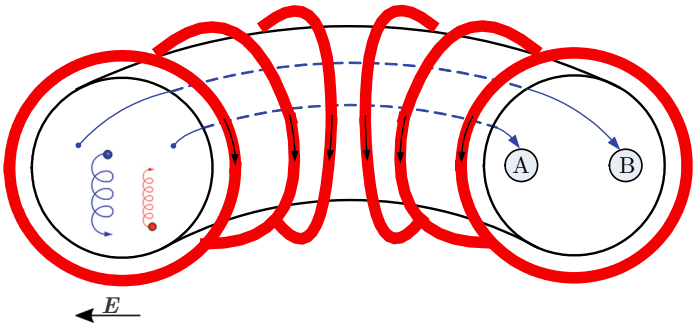

Figure 1.1: Coils that generate a toroidal magnetic field. Field line A travels a shorter distance than field line B. Electron (red) and ion (blue) upward and downward drifts are depicted in the left cross section of the torus. Figure adapted from [9].

perfect toroidal circle. The acting Lorentz force is stronger on the right-hand side of the orbit, and thus a charged particle will turn more tightly on the inside. The charged particles' guiding center drifts either downward (ions) or upward (electrons). An electric field is the consequence of that which acts against the particle confinement (see the black arrow in Figure 1.1). Ions are accelerated outward on the outward pointing part of their gyro motion and decelerated on their inward pointing part. This is also the case for electrons but they are pushed to the right instead of the left. However, the drift from the electric field component also points downward. The result is an $\boldsymbol{E} \times \boldsymbol{B}$ drift that acts perpendicular to the magnetic and electric field.
A solution to this problem was proposed by Spitzer [10], which was to twist the torus into the shape of a pretzel [9]. The described gradient of the field line density would be asymmetric at the two outermost points of the pretzel. Thus, upward and downward drifts would be compensated for because the stronger magnetic field would change its side. Spitzer [10] named this kind of magnetic configuration a stellarator (in a figure-of-eight). Stellarators are difficult to make, especially because the coils must be accurate enough to keep the field lines from wandering out to the walls [9].
A different idea is the combination of toroidal and poloidal magnetic field lines results in a helical field line, which compensates the up- and downward drifts of the charged particles and is used by a tokamak.

1.2.1 Tokamak

The word tokamak comes from the Russian words *toroidalnaya kamera magnitnaya katushka*, meaning "toroidal chamber magnetic coils." The toroidal field is simply created by the magnetic

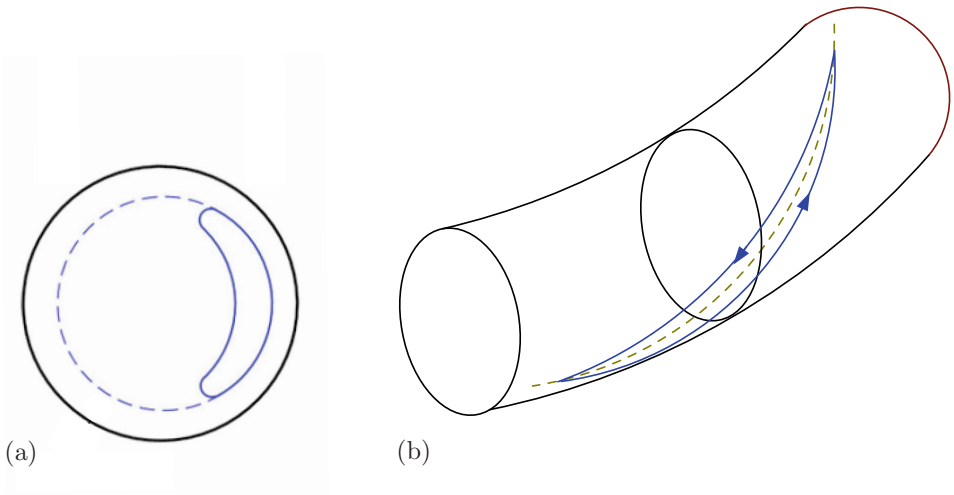

Figure 1.2: Sketch of a banana orbit of a single ion in (a) a poloidal cross section and (b) a torus segment. Dashed ion trajectories represent ions that are not reflected (high momentum component parallel to the magnetic field) and solid trajectories represent reflected ions in a banana orbit. Figure taken from [9].

coils, as shown in Figure 1.1, and brought into superposition with a poloidal magnetic field created by a driven plasma current (the driven current flows in the toroidal direction). In this way, not only is the necessary twist in the magnetic field achieved but also the plasma undergoes ohmic heating. However, there is a limit to how much current can pass through the plasma, similar to the limit on a generic ohmic resistor. So called kinks can be evoked if the plasma current is to high. A kink in an otherwise straight (along the toroidal coordinate) current path is a so-called kink instability. It pushes the plasma-driven current outward and limits the maximal plasma current to the Kruskal–Shafranov limit [11]. Thus, the plasma is pushed off the torus poloidal center, which is not desirable. Figure 1.1 shows that the magnetic field line density is higher on the inside of the torus than on the outside. Thus, a tokamak has no uniformly distributed magnetic field, and particles traveling on a field gradient might be reflected. Ions that do not have enough momentum parallel to the magnetic field will be reflected and return on a slightly different path; see Figure 1.2. The dashed line is the path of a passing ion—one that has sufficient high momentum parallel to the magnetic field and is not reflected. Solid lines represent the paths of ions that are reflected. Mapping these to a single poloidal cross-section introduces so-called banana orbits (see Figure 1.2(a)). Collisions between ions caught on these bananas permit them to jump from one banana orbit to the next, which is called neoclassical diffusion and is much faster than normal diffusion processes [1]. The confinement time of a plasma is reduced from minutes to seconds. Impurities which a high cross field transport play a key role here. However, the equilibrium of a tokamak consists of nested magnetic flux surfaces in the form of differently sized tori. These different tori are formed by the helical field line. As mentioned in Chapter 1.2, a field line can end on first wall elements or close itself after a finite number of revolutions around

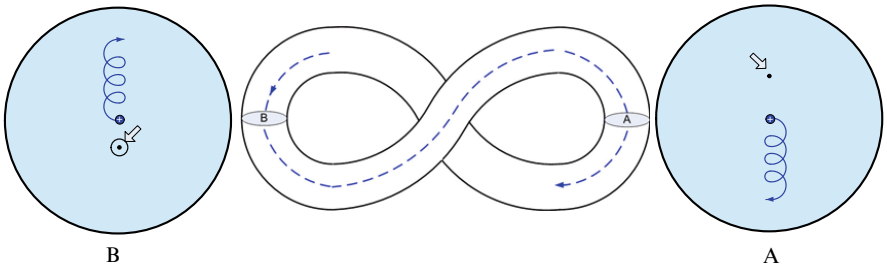

Figure 1.3: A twisted version of the torus topology shown in Figure 1.1. Point A and B are the outermost positions of the pretzel, and detailed cross-sections of position A and B are shown to the left and right. Figure taken from [9].

the torus.

1.2.2 Stellarator

The main difference between a stellarator and a tokamak is the way the poloidal field component of the stellarator's magnetic topology is generated. Subsection 1.2.1 introduces the tokamak's plasma-driven current for generating the helical twist of the magnetic field lines. For stellarators, the idea presented in Figure 1.3 is continued. Either the experimental vessel can be twisted or external coils can be twisted to achieve a helical twist of the magnetic field lines. In both cases, the construction phase of all components poses a challenging task to modern fusion research. Examples of these concepts include the Large Helical Device (LHD) and the aforementioned Wendelstein 7-X (W7-X; see the detailed introduction in Chapter 2). Stellarator operations are not limited by effects such as the previously mentioned kink instability because no plasma-driven current exists. Thus, stellarators are more suitable for steady-state and continuous operation, which is one of the highest demands of fusion research [1]. Tokamak plasmas are symmetric at any arbitrary poloidal cross-section taken from Figure 1.1, but stellarators do not have this kind of symmetry.

1.3 The problem of three-dimensional edge impurity transport

Impurities are unavoidable in plasma, such as that shown in 1.0.0.1 [1]. Helium atoms might pollute an experimental plasma as ash from a previous plasma remains in the experiment after the fusion plasma is terminated. However, plasma surface interactions are also unavoidable, resulting in impurity atoms and molecules being released into the plasma edge through evaporation and sputtering. These impurities all too frequently have harmful consequences for the plasma because they cool the main plasma. Early nuclear fusion experiments were constructed from medium Z (charge number; here steel or higher Z materials) materials that had direct contact with the plasma and limited the access of the today's fusion experiment's temperatures. Additionally, imperfect magnetic field

geometries resulted in impurity radiation accounting for almost all the energy loss from the central region of the main plasma into the plasma edge [1].
However, modern experiment setups reduce the significance of impurity radiation by a considerable amount because the overall vessel conditions are improved. Low Z materials are used and upgrades to the vacuum limit and magnetic confinement have been achieved.
The power that is lost over different impurity elements varies quite significantly, as Figure 1.4 shows. Modern stellarators and tokamaks reach temperatures that can easily strip all orbital electrons from

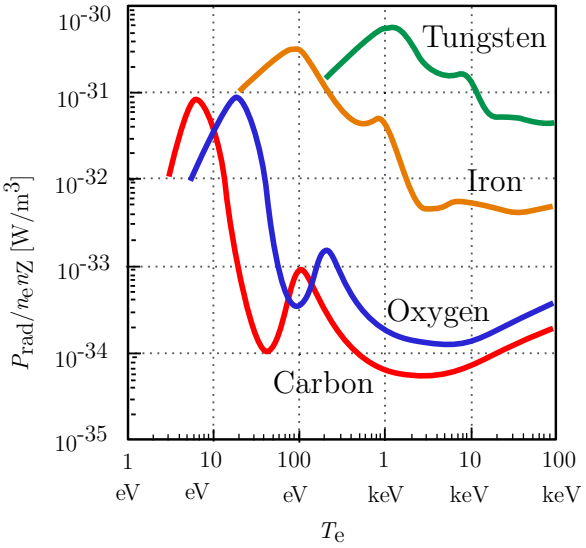

Figure 1.4: Overview of the power that is lost P_{rad} over carbon, oxygen, iron, and tungsten impurities normed to the electron density of the main plasma n_{e} and the combined impurity charge density n_{Z}, plotted against the corresponding electron temperature T_{e}. Figure adapted from [1].

the impurity molecules. These impurities radiate near the SOL where the electron temperature profile is still low enough. This can lead to a spontaneous disruption of the plasma through excessive edge cooling [12].
The most simple source and sink for impurities are the installations in the experiment vessel, often constructed from carbon. Neutral carbon atoms (or different atoms to the installation's material) are released into the plasma through sputtering and evaporation. These neutral atoms are then ionized on their way deeper into the plasma. A considerable number of them return directly to the installation's surface (particle sink), but some reach inner sections or even the core region. The lifetime of an impurity particle consists of three major parts, namely the source, edge transport, and transport in the main plasma; Figure 1.5 presents sketches of these three areas. The plasma only has direct contact with heat diverting installations of the experiment such as a limiter or divertor. However, charge exchange neutrals do not follow magnetic confinement and can bombard first-wall elements, a consequence of which is chemical sputtering. However, this impurity source is neglected in the scope of Figure 1.5. The parallel impurity transport within the plasma edge is much faster than

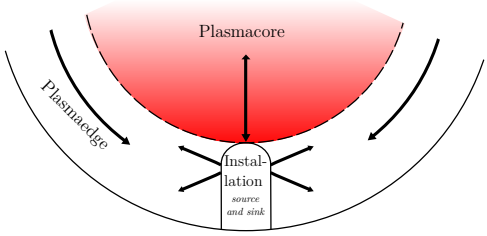

Figure 1.5: Schematic of the lifetime of an impurity atom released from an installation's surface into plasma. It can travel over the LCFS (dashed line) into the core region of the plasma, along a field line in the SOL. Figure adapted from [1].

the transport across field lines, and impurities will uniformly distribute at the plasma edge before they even partially enter the main plasma. Thus, physics in the plasma edge in direct contact with the experiment's installations are of great interest to this thesis.

1.4 This thesis

The most practical way of confronting detailed experimental measurements of edge impurities in such a way as to extract the underlying physics—i.e. to perform interpretative studies—is by the use of impurity source/transport codes.

Peter C. Stangeby [1]

Stangeby postulated in his book *The Plasma Boundary of Magnetic Fusion Devices* that the comprehension of impurity effects on plasma edge diagnostics is only assessable in direct comparison to numerical impurity source/transport codes. Hence, the motivation behind this thesis was to take Stangeby's hypothesis and expand it to a theoretical and numerical quantification – using the code package EMC3-EIRENE – of impurity effects in the fusion experimental stellarator W7-X. A detailed introduction to EMC3-EIRENE is provided in Chapter 3. These quantifications are confronted with characteristic fusion plasma measurements. Different magnetic configurations of the first and second operational phase of W7-X – a limiter configuration followed by a divertor configuration – as well as their heat exhaust concepts play crucial roles because they affect key plasma parameters. The result is a variation in the magnitude of impurity effects on these parameters.
Information from several diagnostics is required to limit the number of remaining free EMC3-EIRENE simulation parameters. Through considering these diagnostics for simulation parameters, EMC3-EIRENE can be used as a numerical tool. Evaluations of additional measurements that are not used

to construct the compared simulation, as well as predictions of immeasurable plasma parameters, are made available. From this, an interactive connection point between diagnostics and the EMC3-EIRENE simulation emerges because the used Langmuir probe measurement interpretations depend on the exact plasma particle composition, including impurities. Hence, this thesis focuses on assessing a quantification for this composition, which is the effective charge state Z_{eff}. This quantification has great importance because Z_{eff} is applied at the connection between the simulation and measurement to iteratively refine measurement and simulation interpretations. This thesis addresses the following key questions, which are sorted by the chapter structure of the thesis for readability:

Chapter 2

- What are characteristic plasma edge measurements in respect of the magnetic topology of W7-X? How can they profit from the impurity studies of this thesis?
- What input can plasma edge diagnostics provide to impurity studies?
- Why is the impurity transport and its quantification a key problem for long-pulse steady state plasma operation in W7-X?

Chapter 3

- How are fluid model equations of the EMC3 model derived and solved with a kinetic Monte Carlo solving scheme?
- What is the direct interface between EMC3 and the EIRENE code?
- Which are the important model parameters in respect of interpretative impurity studies?

Chapter 4

- What are the quantifications of assessed impurity effects and what roles do they play in respect of characteristic plasma edge measurements of W7-X in a limiter configuration?
- What are the results of a direct comparison of plasma edge modeling and measurement?
- Can predictions for future W7-X plasmas be made (based on the applied interpretive study)?

Chapter 5
The same questions are answered here as in Chapter 4; however, Chapter 5 focuses on the study of the questions answered in Chapter 4 concerning to W7-X in divertor configuration. Nevertheless,

- What are the limits to the applied interpretative studies, and hence the limits of the impurity transport code?
- Can any predictions for future fusion plasmas been made?

- What can one learn from a direct comparison between limiter and divertor plasmas?

To answer the research questions stated above, the remainder of this thesis is organized as follows:

- Chapter 2 provides a general introduction to the magnetic configuration of a stellarator and the particle confinement principle. These concepts are exported to W7-X, followed by a discussion of all utilized diagnostics. In particular, diagnostics that depend on the knowledge of Z_{eff}, as there are Langmuir probes, are focused on in this chapter.

- Chapter 3 discusses the main structure of the code package EMC3-EIRENE with a focus on the impurity transport model. EMC3 can be segmented into different modules, which are applied to calculate the three main plasma parameters: the plasma density, plasma temperature, and momentum of the plasma particles. The computational domain is discussed, including boundary conditions, in particular the implementation of limiter and divertor installations. Boundary conditions between the plasma edge and installations become critical because these installations are constructed from carbon and iron. Thus, they are sources of plasma impurities. Furthermore, the exact ECM3-EIRENE simulation scheme is presented in all its detail.

- Chapter 4 is one of two essential chapters of this thesis (the other being Chapter 5). A direct comparison between simulation and measurement results from OP1.1 is conducted. Limiter installed Langmuir probes are used as first constraints to free simulation parameters. Simulation results are then compared with the results of other Langmuir probes and additional diagnostics. Numerically assessed Z_{eff} results are then used to refine Langmuir probe interpretations and further reused in an iterative manner to constrain the simulation results and Langmuir probe measurements. Additionally, simulations of an oxygen leak within the experiment configuration are conducted to gain detailed information, about which impurities are the fusion plasma's main component.

- Chapter 5 follows the same structure as Chapter 4, except only divertor plasmas from OP1.2 are considered. However, some key features differ from Chapter 4. Separation effects of key plasma parameters are observable within magnetic islands in front of the divertor target plates. If the coordinates of the considered Langmuir probes lie within a separated area, such as the plasma temperature, a direct comparison is restricted. Thus, free parameters of first divertor plasma simulations use Thomson scattering measurements rather than Langmuir probe measurements to constrain them. Only here is a direct comparison with measured Z_{eff} values possible through postprocessing the utilized Thomson scattering measurements. This limitation exists because of the diagnostics' lack of availability in OP1.1 as well as partly in OP1.2. Similar to Chapter 4, an oxygen leak is simulated within the experimental configuration.

- Chapter 6 connects Chapters 4 and 5, and thus OP1.1 and OP1.2, through a direct comparison of the Z_{eff}, u, and exact plasma particle composition. A summary of this thesis' core results is given, as well as conclusions and recommendations for further research topics.

1.5 Publications

In the following the contributions to journals, conferences and work shops are indicated. Oral contributions are underlined. Resulting publications in journals are in a bold font.

- **J. Cosfeld**, M. Rack, D. Reiter, P. Drews, Y. Feng, and D. Zhang, "Impact of impurities on the effective charge state distribution in the limiter plasmas of Wendelstein 7-X", *Nuclear Materials and Energy*, vol. 18, pp. 307–311, 2019.
- **J. Cosfeld**, P. Drews, B. Blackwell, M. Jakubowski, H. Niemann, D. Zhang, Y. Feng, "Numerical estimate of multi-species ion sound speed of Langmuir probe interpretations in edge plasmas of Wendelstein 7-X", Accepted for publication in *Plasma Science and Technology*, 2020.
- P. Drews, C. Killer, J. Cosfeld, A. Knieps, S. Brezinsek, M. Jakubowski, C. Brandt, S. Bozhenkov, A. Dinklage, J. Cai, and others, "Edge plasma measurements on the OP 1.2 a divertor plasmas at W7-X using the combined probe", *Nuclear Materials and Energy*, vol. 19, pp. 179–183, 2019.
- A. Krämer-Flecken, X. Han, T. Windisch, J. Cosfeld, P. Drews, G. Fuchert, Geiger, O. Grulke, C. Killer, A. Knieps, and others, "Investigation of turbulence rotation and radial electric field in the island divertor and plasma edge at W7-X", *Plasma Physics and Controlled Fusion*, vol. 61, no. 5, pp. 054003, 2019.
- J. Cosfeld, M. Rack, D. Reiter, P. Drews, B. Blackwell, D. Zhang, and Y. Feng, "3D resolved effective charge state reconstruction with EMC3-EIRENE", *International Conference on Plasma Surface Interactions in Controlled Fusion Devices*, 2018.
- J. Cosfeld, M. Rack, D. Reiter, Y. Feng, and the Wendelstein 7-X Team, "The impact of carbon and oxygen impurities on the effective charge state distribution in Wendelstein 7-X", *DPG Spring Meeting*, 2018.
- P. Drews, H. Niemann, J. Cosfeld, Y. Gao, J. Geiger, O. Grulke, M. Henkel,D. Höschen, K. Hollfeld, C. Killer, and others, "Magnetic configuration effects on the edge heat flux in the limiter plasma on W7-X measured using the infrared camera and the combined probe", *Plasma Science and Technology*, vol. 20, no. 5 pp. 054003, 2018.
- SC. Liu, Y. Liang, P. Drews, A. Krämer-Flecken, X. Han, D. Nicolai, G. Satheeswaran, NC. Wang, JQ. Cai, A. and Charl, J. Cosfeld, and others, "Observations of the effects of magnetic topology on the SOL characteristics of an electromagnetic coherent mode in the first experimental campaign of W7-X", *Nuclear Fusion*, vol. 58, no. 4, pp. 046002, 2018.

- S. Xu, M. Rack, Y. Liang, J. Huang, M. Jia, Y. Feng, J. Cosfeld, H. Zhang, S. Liu, Y. Gao, and others, "First three-dimensional edge plasma transport simulations with magnetic perturbations induced by lower hybrid waves on EAST", *Nuclear Fusion*, vol. 58, no. 10, pp. 106008, 2018.
- J. Cosfeld, M. Rack, D. Reiter, Y. Feng, P. Drews, B. Blackwell, D. Zhang, and the Wendelstein 7-X Team, "EMC3-EIRENE as complementary "numerical diagnostic" on Wendelstein 7-X", *643rd Wilhelm and Else Heraeus Seminar – Impact of 3D magnetic fields on hot plasmas*, 2017.
- J. Cosfeld, M. Rack, D. Reiter, Y. Feng, and the Wendelstein 7-X Team, "Analytic solutions of the simplified EMC3 model", *DPG Spring Meeting*, 2016.
- M. Rack, D. Reiter, F. Hasenbeck, Y. Feng, P. Börner, A-C. Weger, J. Cosfeld, "A fluid-kinetic approach for 3D plasma edge transport in He plasma", *Nuclear Fusion*, vol. 57, no. 5, pp. 056011, 2017.

CHAPTER 2

THE WENDELSTEIN 7-X STELLARATOR

This chapter focuses on an introduction to the experimental stellarator Wendelstein 7-X (W7-X). Questions already mentioned in Section 1.4 are answered in this chapter to provide a better understanding of the connection between plasma edge measurements and the applied impurity studies. These questions are as follows:

- *What are the characteristic plasma edge measurements in respect to the magnetic topology of W7-X? – and in which way can they profit from the impurity studies of this thesis?*
- *What input can plasma edge diagnostics provide to impurity studies?*
- *Why is the impurity transport and its quantification a key problem for long-pulse steady state plasma operation in W7-X?*

The first question is crucial because numerical impurity studies have a strong dependence on free parameter constraints from characteristic plasma edge measurements. However, it is shown that this dependence is bi-directional because Langmuir probe measurements rely on estimates of the plasma's impurity content, which is only accessible via interpretative impurity studies. The exact input of plasma edge diagnostics are the answer to the second key questions of this chapter. Thus, bi-directional coupling of diagnostic and numerical results gains increasing importance throughout the entire thesis, as Chapters 4 and 5 couple these results in a iterative manner. However, an answer to the main motivation of the conducted impurity studies, and thus to the third key question of this chapter, is given. First, limiter plasma does not exhibit marginal impurity content, which is consistent with the first calculations of the numerical impurity studies. These impurities can affect the overall plasma confinement and performance, which needs to be studied. An introduction and motivation to the impact of impurities on the plasma performance is provided in Section 2.4 of this chapter.

For current experiments such as the W7-X, only safety limits on heat loads on the first wall limit the discharge duration. Mostly injected neutral beams or electromagnetic waves are used to heat and ignite the plasma. The main difference with the tokamak's design is the modified shape of the toroidal stellarator coils. The W7-X is optimized to mitigate both neoclassical and anomalous transport. Neoclassical transport occurs because of their non-axisymmetry along the toroidal direction, and describes the influence of the toroidal magnetic field configuration, collisional transport effects, and stability of the plasma, onto the plasma's transport. However, if one assumes stationary plasma, any time derivations of these dynamics are neglected, yet fusion plasmas are often not stationary. Gradients in plasma pressure often cause plasma turbulence. Transport effects evoked by this are referred to as anomalous transport.
W7-X started its first operational phase (OP1.1) in late 2015 with a limiter configuration to test the magnetic configuration's quality. In 2017, the second operational phase (OP1.2) with a divertor configuration began. For both cases, EMC3 EIRENE modeling was used for the quantification of plasma dynamics near first-wall elements. Thus, computational simulations are critical for interpreting and understanding the W7-X [13]. The stellarator W7-X is set up with five-fold symmetry and does not share the simple design of a tokamak. Asymmetric field errors can be caused by magnetic islands which are not desirable. Furthermore, these errors can be estimated and covered with corrections in the magnetic configuration through error coils. For the standard configuration of the W7-X, the strong effect of its error field (not covered by error coils) in the edge island remnant region, which partially breaks the aforementioned symmetry, modeling is still useful for the comparison of diagnostics to assess the effect of the error field. The W7-X has a plethora of plasma diagnostics, and among those used for the analysis in this thesis are Langmuir probes, Thomson scattering, bolometers, and infrared cameras. These diagnostics are intended to supply relevant plasma parameters in the various cross-sections of the W7-X to better understand transport along the field lines from the main plasma onto the plasma-facing components as well as from module to module. One measurement that is only really available for the core plasma is the effective charge state of the plasma, which depends strongly on the impurity content, and therefore on the quality and character of the plasma wall interaction. The efficient operation of any fusion device, existing or planned, is strongly influenced by the impurity content of the plasma and its management (or rather mitigation), power losses due to radiation limit the maximum energy contained in the core plasma.
The well-established Monte-Carlo-code EMC3-EIRENE [14, 15] is applied to simulate transport effects near the first-wall elements of the W7-X with two different heat exhausting concepts: the limiter operational phase OP1.1 and the divertor operational phase OP1.2. The limiter configuration was selected for the first operational phase, because the limiter is the simplest heat exhaust concept for a fusion experiment. Single limiter tiles intersect with the scrape-off layer (SOL) and conduct heat away from the plasma in the form of particles. Any target plate that is hit by an incident particle recycles as neutral particle back into the plasma, unless the neutral particle is pumped out of the experiment chamber or a baffle structure prevents this. W7-X limiter tiles remain rather small (compared with

divertor target plates) and are placed at five equidistant poloidal cross-sections with no significant toroidal expansion. Orbiting particles on magnetic flux surfaces are able to hit these tiles, and generally parallel heat transport along the toroidal magnetic field is limited in this manner. Divertor targets expand further in the toroidal direction of the machine because of the chosen magnetic configuration of OP1.2, where magnetic islands with toroidal expansions are used to modify the radial distance between the last closed flux surface (LCFS) and target plates. Magnetic islands act as a baffle structure to prevent neutral particles from reentering the plasma. Figuratively speaking, rather than a parallel heat-transport "roadblock" by limiter tiles, the W7-X's island divertors mainly utilize perpendicular heat transport to lead heat away from the plasma. Both concepts define the boundaries at the plasma edge, and thus must be considered when interpreting and understanding the progress of the first W7-X plasmas. OP1.1 and OP1.2 are key elements and are of particular interest to this thesis.

2.1 Wendelstein 7-X

The first plasmas of the superconducting fusion experimental stellarator W7-X were ignited at the beginning of December 2015 after a construction phase of 15 years [16]. The W7-X was designed to establish the magnetic confinement concept of a stellarator with significantly enhanced plasma performance in terms of particle confinement [16] compared with previous experimental stellarators. The control of neoclassical transport plays a key role here; 50 modular and 20 planar superconducting coils are used as key components to achieve a variety of magnetic configurations. They are twisted to eliminate $\nabla \cdot \boldsymbol{B}$ and curvature drifts. An overview of these drifts can be found in [17]. However, in regions where the magnitude of the magnetic field weakens, particles are trapped by the magnetic mirror effect. They no longer orbit around the torus, and rather become trapped in so-called banana-shaped orbits. Collisions between a trapped and free particle allow the trapped one to change its position, and thus to another banana orbit. A neoclassical diffusion is introduced in addition to a classical one. In the last decade, stellarators were optimized to remove their specific deficiencies; the W7-X is optimized to have low neoclassical transport.
The magnetic topology of the experiment is a result of its five-fold symmetry. The W7-X has five identical modules with up–down symmetry between two halves of each module (see one module in Figure 2.1) [16]. Aside from the magnetic components, 299 ports of different sizes and shapes allow access for diagnostics, heating systems, and pumping systems from outside the experimental stellarator. During the first operational phase (OP1.1), the plasma was limited to the LCFS by a limiter to a machine-averaged radius of $a = 0.49$ m. Limiter targets were installed in each module, for a total of five limiters used. The targets were graphite plates without active cooling mechanisms.
In OP1.2, the heat exhaust concept was changed from the limiter concept to a divertor concept. Again, graphite was used to construct the target plates, which were not actively cooled. Table (a) and (b) provide overviews of OP1.1 and OP1.2's key parameters, respectively. The major difference,

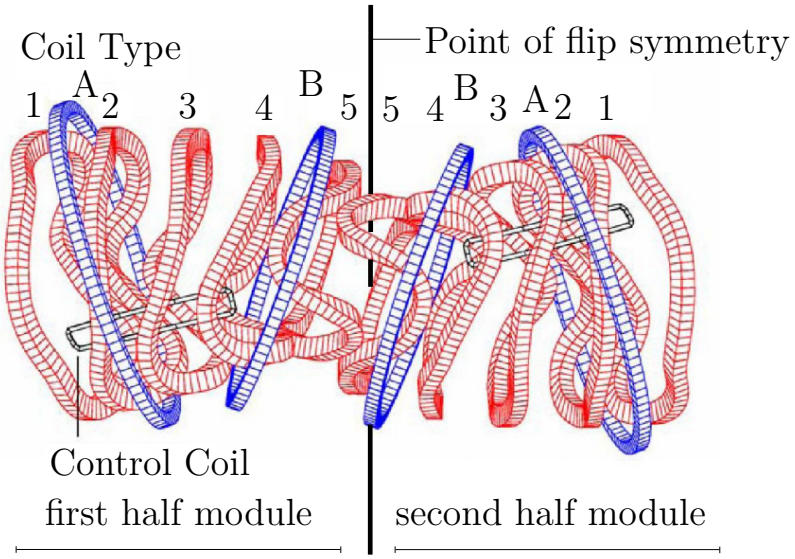

Figure 2.1: Schematic of one magnetic module of the W7-X, comprised of two flip-symmetric half-modules, each containing five nonplanar coils (red) and two planar coils (blue). Taken from [18].

Table (a) Major parameters of OP1.1 plasmas

Quantity Q	$\min(Q)$	$\max(Q)$
Plasma volume	-	30 m^2
Major radius	-	5.5 m
Minor radius	-	0.49 m
ECRH	0.6 MW	4.3MW
Confined energy	0.05 MJ	4MJ
Plasma duration	0.05 s	6 s

Table (b) Major parameters of OP1.2 plasmas

Quantity Q	$\min(Q)$	$\max(Q)$
Plasma volume	-	30 m^2
Major radius	-	5.5 m
Minor radius	-	0.53 m
ECRH	0.5 MW	10MW
Confined energy	0.05 MJ	10MJ
Plasma duration	0.05 s	100 s

Figure 2.2: Machine parameters in (a) OP1.1 and (b) OP1.2. Parameters taken from [2, 16, 18–20].

aside from the magnetic configuration, between the two operational phases is the amount of applied heating power, and thus the duration of the electron cyclotron resonance heating system (ECRH). The main mechanism uses the gyrotron millimeter wave source, which was invented in the mid-1970s. For the W7-X, an ECRH system capable of 10 MW heating distributed over a continuous operation of 30 min at 140 GHz was demanded [16]. Ten Gyrotron tubes supply this power with an effective frequency output of 100 – 200 GHz. For a standard electron wave, a dispersion relation of [21],

$$\boldsymbol{k} = \frac{\omega}{c_\mathrm{s}}\sqrt{1 - \frac{\omega_\mathrm{pe}^2}{\omega(\omega \pm \omega_\mathrm{ce})}} \quad , \tag{2.1.0.1}$$

is given, where ω is the electromagnetic wave frequency, ω_pe is the plasma frequency of the electrons, ω_ce is the cyclotron frequency of the electrons, and c_s denotes the vacuum speed of sound. Electromagnetic waves can either rotate clockwise or counter-clockwise, which are treated with the term $\omega \pm \omega_\mathrm{ce}$ in equation (2.1.0.1). As the electron density in the plasma is increased, the phase velocity of the electrons increases while the group velocity decreases until $\omega = \omega_\mathrm{pe}$ is reached. In case of $\omega = \omega_\mathrm{ce}$, the electromagnetic wave is absorbed by the plasma. Then, the phase vector $\boldsymbol{k}$ of the magnetic field lies in phase with the electrons' gyration frequency, resulting in the electrons being heated. The effective frequency output must be tuned carefully in respect of the given plasma density.

2.1.1 Limiter configuration

Early tokamak experiments utilized a "bar-like" limiter design that featured an installation protruding from the first wall into the chamber. Plasma particles that follow along the field lines around the experiment were transported radially outward until they reached a field line, which passed within a gyroradius of the limiter-bar, at which point they impacted onto the limiter [22]. These particles recycled as neutral atoms and molecules from the limiter's surface back to the plasma. A gap between the LCFS of the plasma and limiter bar-end is filled with neutral gas. Hard limitations on the lifetime of a limiter are set as the total amount of particles that impact the limiter. Expected sputtering rates of the limiter's surface structure of 5 – 50cm/year are realistic [23].
Plasma limiting surfaces, used in OP1.1, featured an allowed maximum heat energy of $\int P\mathrm{d}t = 2$ MJ (with the discharge duration of Table (a), see Figure 2.2). The ECRH system was used to heat the plasma at a maximum of 5 MW [24]. The solid surfaces of the limiter define the outer edge of the plasma. Various limiter shape concepts exist, including a radial, poloidal, and toroidal form (see Figure 2.3). The limiter serves the purpose of protecting the plasma-facing wall components from heat disturbances, which cause plasma instabilities such as $\boldsymbol{E} \times \boldsymbol{B}$-, $\nabla \boldsymbol{B}$ and curvature-drifts.
A modern design of fusion experiments demands limiters capable of heat loads that exceed the heat-flux limitations of design (a) in Figure 2.3. The limiter surface is then extended in the toroidal direction to distribute the heat more uniformly over the limiter, as shown in Figure 2.3 (c). A simple expansion of the limiter in the poloidal direction allows the limiter tip to intersect a rather large portion of several magnetic flux surfaces. Such an intersection provides a dead end to the trajectory of a particle. The distance along the magnetic field within the SOL between two contacts points – one

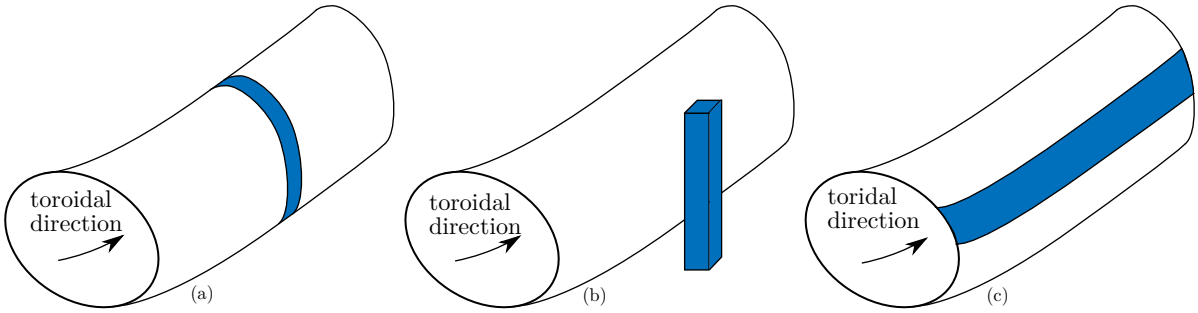

Figure 2.3: Schematic overview of different limiter concepts: (a) poloidal, (b) radial, and (c) toroidal concepts. Figure style adapted from Figure 6.8 of [22].

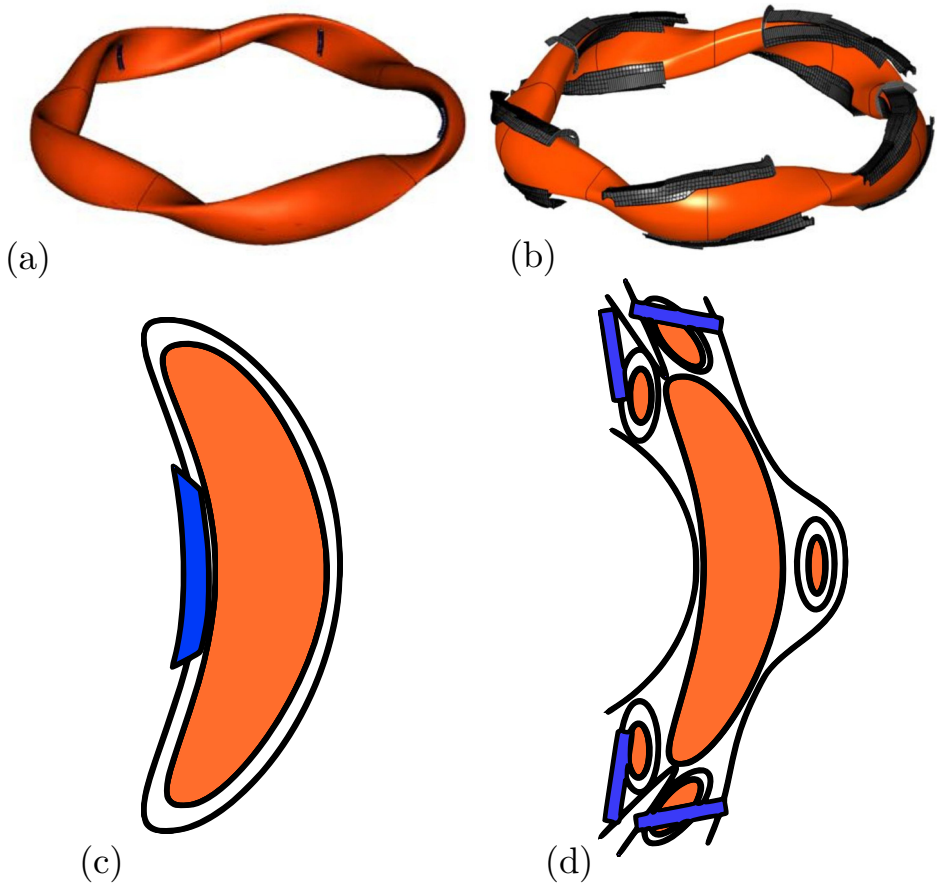

Figure 2.4: Sketches of the heat exhausting concepts of OP1.1 (a) and OP1.2 (b) shown in the top row. Plasma cross sections (orange) of limiter concept (c) and the island divertor concept (d) are shown in the bottom row. Limiter and divertor tiles are shown in blue. Figure (a) and (b) taken from [19], (c) and (d) are taken from [25].

being the limiter and one being the starting point – with solid surfaces, is called the connection length L_c. Effectively, more particles are caught by the limiters with a poloidal expansion, which can grant more control over the plasma. The design of such a poloidal limiter expansion is slightly modified by a periodic repetition of these limiters in the toroidal direction. Hence, a toroidal expansion of a single limiter is obsolete. The final concept of W7-X's limiter design is shown in Figure 2.4 (a) and (c).

2.1.2 Divertor configuration

In a basic tokamak, a poloidal divertor configuration can be achieved using a second plasma current – parallel to the one that creates the poloidal magnetic field (see Figure 1.1) – within the plasma. This is induced using external conductors. Figure 2.5 presents an overview of a poloidal divertor. In the

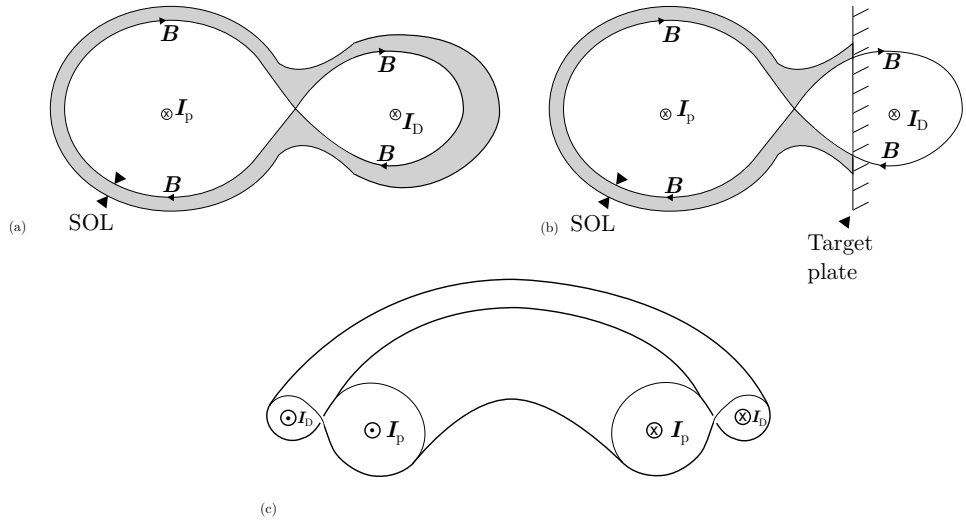

Figure 2.5: Sketches of the poloidal divertor concept of an arbitrary tokamak experiment. The plasma current $\boldsymbol{I}_\mathrm{p}$ and second plasma current $\boldsymbol{I}_\mathrm{D}$ from external conductors form a figure-of-eight poloidal cross-section in (a) and for an arbitrary section of the tokamak torus in (c). This cross-section is intersected by a target plate in subfigure (b). Figure adapted from [1].

poloidal plane, the magnetic topology makes a figure-of-eight shape that is then intersected by a target plate (see Figure 2.5(a) and (b)). The center point is called the magnetic X-point and features a poloidal magnetic field strength of zero. No SOL exists at this point. A sink action is introduced by the intersection of a solid target plate that cuts through the flux surfaces surrounding the magnetic field side built up by $\boldsymbol{I}_\mathrm{D}$. Thus, particles that have a cross-field transport component will diffuse across the LCFS and leave the SOL to the so-called divertor targets.

However, W7-X is a stellarator that features a strongly varying cross-section, it changes – as one proceeds in the toroidal direction – in a periodic order. The simple schematic shown in Figure 2.5 is not directly applicable to the W7-X. The LCFS of the W7-X's confinement area is defined either by the inner boundary of the core and SOL region of a natural island chain that is intersected by target plates or by an ergodized outer layer with remnants of X points of related islands [26]. Following the X point

along the toroidal direction gives a line of X points, the so-called X-line. These are, unlike the tokamak X-line shown in Figure 2.5, of a helical shape and depend on the rotational transform (introduced in the Section 2.2). In the case of extended islands, the positioning of the divertor elements along the helical edge areas with the strongest poloidal curvature of the magnetic surfaces allows the separation of the confined plasma from a less confined region at the boundary and the concentration of the plasma flow on target plates [26]. Hence, the LCFS is only defined by the magnetic field and island topology, which are intersected by different divertor target plates. The magnetic topology is chosen in such a manner that impurity influxes from plasma-facing vessel components into the plasma are reduced. Divertor plates with toroidal and radial expansions (in each single module) were installed. Figure 2.4 (b) shows the W7-X divertor concept of OP1.2, and subfigure (d) of Figure 2.4 shows the corresponding plasma cross-section. A divertor does not follow a complete orbit of the machine, but is rather split into segments for each module. It includes one pair of island divertor segments installed at the point of a bean-shaped cross-section for each module (see Figure 2.4(b)). In addition, for the final divertor design, a toroidal expansion of the divertor target plates is utilized. The target surface of the divertor is split into a vertical part mounted at the inner side of the vessel (near the limiter origin) and a horizontal part mounted at the outer side (see Figure 2.9 (b) and (d)). In combination, both divertor parts cover nearly 50% of the complete experiment vessel. Magnetic island structures are then intersected by divertor plates to ensure a particle flow from the plasma edge to the first wall. Hence, plasma wall interactions are decoupled from the confined region.
No infinite values exist for the connection length because of the cross-field transport in the SOL, neither for limiter nor divertor plasma. However, a limiter that is small in the poloidal toroidal direction will grant the plasma larger connection-length values. Figure 2.6 presents an overview of the different connection length cross-sections, at a toroidal angle of 200.4°, of the limiter and divertor configuration of W7-X. This cross-section is of special interest because a key diagnostic for this thesis is installed in it. The connection length is an important parameter for the power deposition onto the

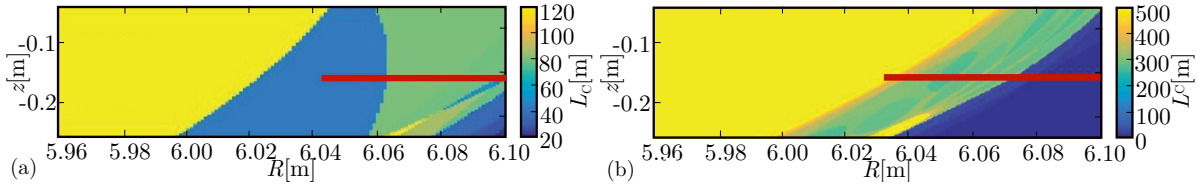

Figure 2.6: Cross-sections of (a) limiter plasma and (b) divertor plasma. The plunge path later used and compared with the Langmuir probe system is indicated in red. Figure taken from [27].

target plates. Larger connection lengths potentially lead to a wider striking pattern onto the target plates. A striking pattern is considered as the distribution of the magnetic field line ends mapped onto a target plate. This is a major difference to tokamaks (using a divertor concept) and the limiter configuration of W7-X because connection lengths are lower, even by a factor of 10 for the former. A wider striking pattern corresponds to a more homogeneous distribution of heat over the target plate,

which is favorable because target plates take less damage in this case. For the particular cross-section shown in Figure 2.6, the limiter case features connection lengths up to 100 m while the divertor features lengths up to 400 m. The inner region – colored in yellow in Figure 2.6 – corresponds to the core region and must be excluded from this comparison, because infinite connection lengths are not of interest. They simply do not affect the striking pattern on a limiter or divertor. A disadvantage of the island divertor, however, is its sensitivity to toroidal plasma currents and magnetic field errors [19]. Notably, a toroidal plasma current in a stellarator is not the plasma-driven current of a tokamak. However, early studies on the magnetic field configuration of W7-X found that measured deviations are smaller than one part in 100,000 [28]. Thus, a sensitivity study of the divertor shape is neglected in the scope of this thesis. The advantage of higher connection lengths – and thus of the divertor configuration of W7-X – is that particles in the SOL can diffuse at a longer distance to the magnetic field. However, the magnetic topology of the divertor configuration is more complex than the limiter configuration because the particles, in simple terms, travel longer distances. One advantage of the limiter is its simple design and the resulting advantageous time scale regarding its construction phase versus that of a divertor. Hence, the first plasmas in W7-X were limiter plasmas, followed by divertor plasmas.

2.2 The scrape-off layer of W7-X

The total magnetic field $\boldsymbol{B}$ in a stellarator is a superposition of the magnetic field in the toroidal B_φ and poloidal B_θ directions. A suitable coordinate system to describe the plasma dynamics in a toroidal symmetric geometry are spherical coordinates [29]. The same coordinate system can be used to describe more complex magnetic configurations , such as those of the W7-X. Hereinafter the toroidal angle φ, poloidal angle θ and radial coordinate r are used to describe the geometry of the W7-X. Here, R is the major radius of the machine. The center of an arbitrary poloidal cross section is named R_0. Furthermore, the height of this mid-coordinate is given by Z_0. This position stays untouched for an axisymmetric tokamak. However, R_0 and Z_0 undergo significant changes along the toroidal direction in the W7-X Thus, only an averaged (over the toroidal angle φ) center point is given to characterize the overall geometry of the W7-X. The minor radius a is measured from the mid-coordinate (R_0, Z_0) to the first wall. These radii are then grouped into a single averaged minor radius a. Figure 2.8 shows the coordinate system of a plasma confined in a torus.
The transport properties of plasma are separable along the magnetic field and perpendicular to this magnetic field line. The particles' mobility parallel to $\boldsymbol{B}$ is high in comparison to that perpendicular to $\boldsymbol{B}$, which is strongly reduced. A magnetic configuration is essential for isolating a fusion plasma from first-wall elements. In a toroidal closed magnetic field, the particle loss rate onto the first wall is then defined by the perpendicular transport. The W7-X's basic toroidal magnetic field is created by poloidal coils, which are placed along the vessel. These coils are twisted, as shown in Figure 2.1, to create a poloidal magnetic field component. Thus, the perpendicular transport is limited from

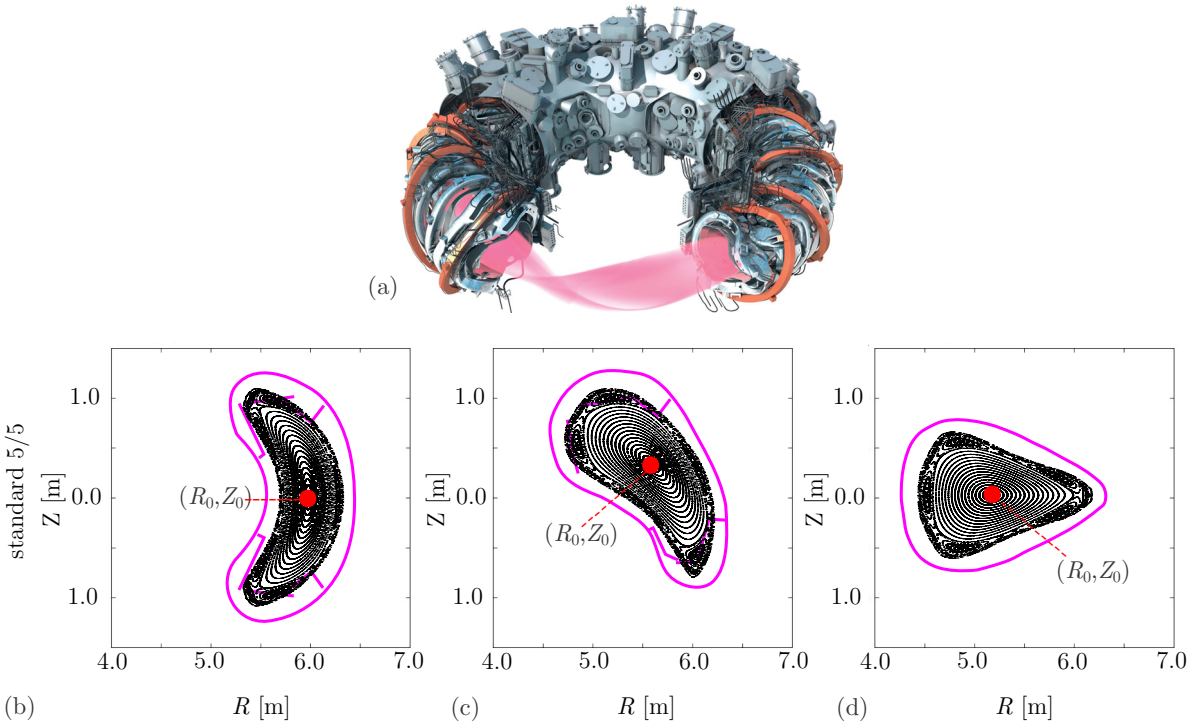

Figure 2.7: (a) The stellarator W7-X; (b)–(d) three different poloidal cross sections of OP1.2. The center point (R_0, Z_0) is indicated by the red dot. Figure concept taken from [30]; subfigure (a) taken from [2].

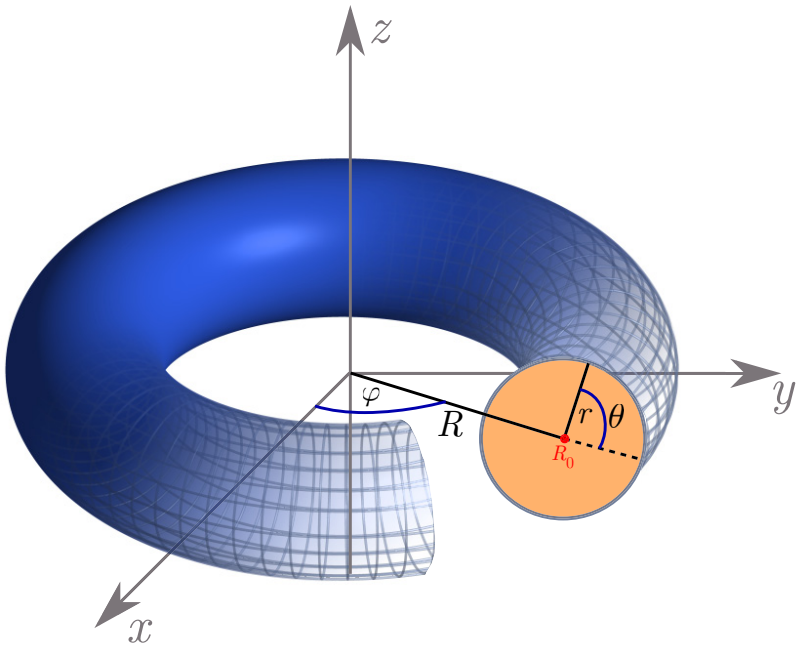

Figure 2.8: Geometry of plasma confined in a torus.

first-wall elements. Therefore, the total magnetic field is a superposition of a toroidal and poloidal field component and results in a helical shape. If the plasma is in equilibrium, the magnetic field lines form a nested structure of magnetic flux surfaces in the form of tori. Then, helical field lines can close themselves in a finite number of orbits or are intersected. Flux surfaces that are not intersected by any wall components are called closed, whereas intersected ones are called open flux surfaces. The LCFS defines the transition from the confined region (closed flux surfaces) to the SOL (open flux surfaces). Figure 2.9 provides an overview of the above mentioned definitions. The helical pitch of $\boldsymbol{B}$

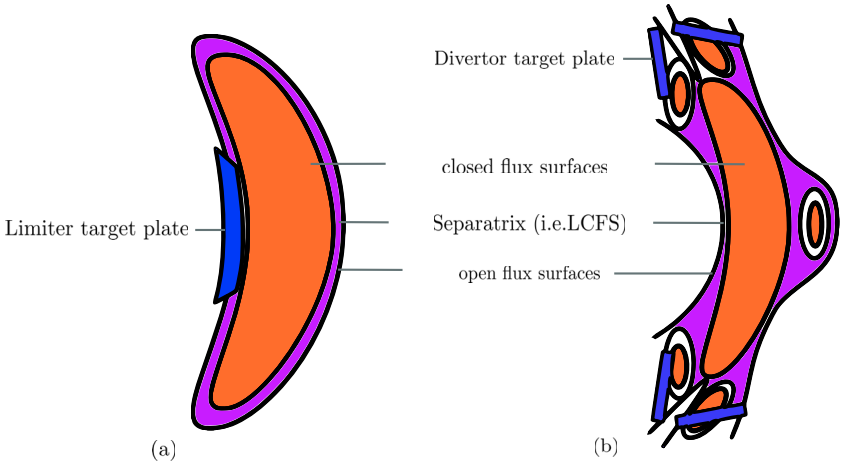

Figure 2.9: Sketch of (a) a limiter plasma and (b) a divertor plasma. Closed magnetic flux surfaces regions are indicated in orange while open flux surfaces are held magenta. Plasma limiting surfaces are blue.

is the reason for a field line to make from no poloidal transits (no pitch angle) to several (high pitch angle) per single toroidal orbit in the machine. Then, $d\theta/d\varphi$ gives the number of poloidal transits on a closed flux surface for one toroidal transit. The rotational transform is then calculated using the following equation,

$$\frac{d\theta}{d\varphi} = \frac{\iota}{2\pi} \quad , \tag{2.2.0.1}$$

where ι is the poloidal displacement after one toroidal transition; n is to quantify the periodicity of the magnetic field line structure in the poloidal direction, and m is used for the toroidal direction. Figure 2.10 presents an overview of m, n, and ι. The presented magnetic configuration has a poloidal periodicity of $m = 2$ for $\iota = \pi$. The magnetic configurations of the W7-X are categorized by the quotient n/m; every W7-X configuration shares the same n because a symmetry of five modules exists along the toroidal axis of the machine. The standard configuration is shown, with $n/m = 5/5$. However, the difference in the magnetic configuration is recognizable within the core region of the plasma. Whereas magnetic islands lie outside of the LCFS for OP1.2, magnetic islands lie within the core region for OP1.1. Details of the limiter and divertor concept are discussed in the following section.

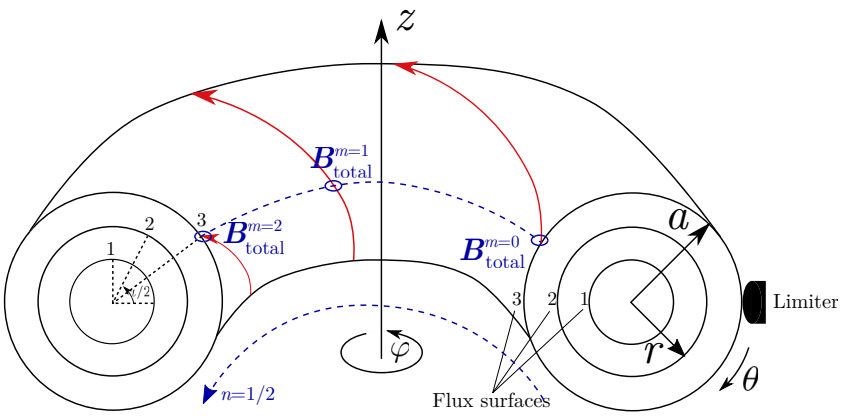

Figure 2.10: Sketch of an intersected toroidal fusion experiment. Closed magnetic flux surfaces are numbered 1, 2, and 3, from the innermost magnetic flux surface to the outermost. Magnetic configurations of OP1.1 and OP1.2 have far more magnetic flux surfaces than this exemplary sketch. The magnetic field B completes two poloidal orbits for half a toroidal orbit. Thus, one finds $m = 4$ for $n = 1$.

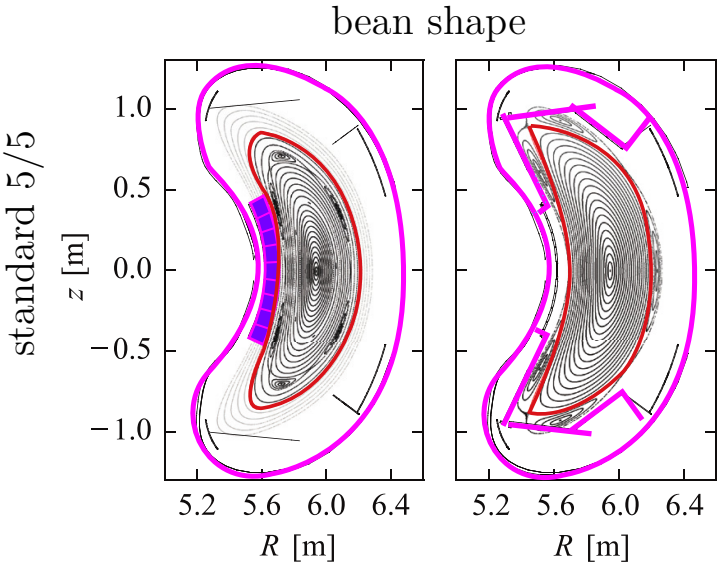

Figure 2.11: Overview of possible magnetic configurations for $\iota = 5/5$. The top row shows the standard configuration used in OP1.1, and the bottom row refers to OP1.2. Three prominent shapes of the magnetic configurations in the machine are shown: (a) bean-shaped, (b) teardrop, and (c) triangular cross-section. Figure concepts are taken from [30]. Plasma limiting surfaces are shown in bright magenta. Closed magnetic field lines are shown in red, whereas open ones are shown in blue and separated by the LCFS in dark blue. Isolated magnetic islands are shown in green.

2.3 Edge transport relevant diagnostics

Different W7-X diagnostics and instruments provide vital insights into the plasma scenarios of OP1.1 and OP1.2. Plasma must be heated to high temperatures to reach full ionization. Plasma features and dynamics can then be studied with a variety of diagnostics. An overview is provided in this section.

2.3.1 Langmuir probes

Langmuir probes are among the first diagnostics developed in the field of plasma science [31], and because of their simplicity they remain one of the most valuable tools for studying the edge plasma. The basic concept is to expose an electrically conductive rod or pin in the plasma while measuring the currents and voltages under various biases. Furthermore, Langmuir probes can be employed to obtain the n_e, electron temperature T_e, and plasma potential Φ using the current–voltage characteristic. Some drawbacks remain because the probe head is in direct plasma contact and must withstand high heat fluxes over a given plunge time interval. These sum to multiple tenths of eV [27] of the electron temperature. Moreover, the amount of collected particles must be sufficient to gain adequate statistics. Generally, an effective collector design has a well-defined collection area even after many exposures to plasma [32].

A Langmuir probe that is not connected to any plasma structures is electrically isolated from the

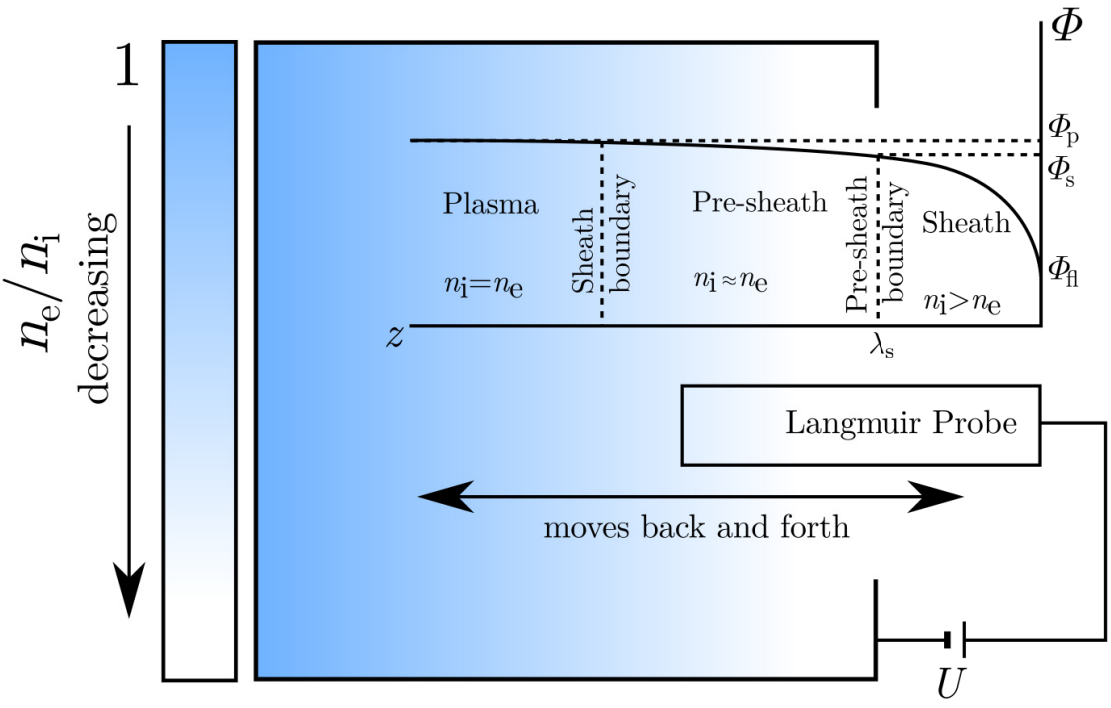

Figure 2.12: Sketch of a Langmuir probe recording the n_e and T_e of plasma (blue-shaded region). The color bar represents the plasma density. Figure adapted from Figures 9.8 and 9.9 of [17].

plasma. Then, electrons and ions (charged particles) stream onto a probe head and are absorbed. The thermal velocity of the electrons ($u_{\mathrm{e,th}} = \sqrt{\frac{2kT_\mathrm{e}}{m_\mathrm{e}}}$) exceeds that of the ions because of their mass difference (assuming $T_\mathrm{e} = T_\mathrm{i}$ for now). Thus, the probe head will be negatively charged. An electrostatic potential develops between the plasma and probe head, which shields electrons (Debye shielding) from the probe head. More ions are attracted, and as a consequence, a floating potential is reached with a spatial decay of λ_s. The electrostatic potential sheath Φ_s is only a couple of Debye lengths λ_D wide (see Figure 2.12). Slow electrons are not able to overcome this sheath potential, whereas ions are attracted by the sheath potential and further accelerated onto the probe head. This biasing causes a current to flow through the Langmuir pins.
The situation is changed if the probe is biased to a voltage U to allow an electrical current I to flow from the probe to the plasma. The distribution function of electrons that stream from the probe head area (size S) into the plasma is found [17] using,

$$f(u) = \left(\frac{m_\mathrm{e}}{2\pi T_\mathrm{e}}\right)^{3/2} \mathrm{e}^{-\frac{m_\mathrm{e}u_x^2}{2T_\mathrm{e}}} \mathrm{e}^{-\frac{m_\mathrm{e}u_y^2}{2T_\mathrm{e}}} \mathrm{e}^{-\frac{m_\mathrm{e}u_z^2 - 2e(\Phi-U)}{2T_\mathrm{e}}} \quad . \tag{2.3.1.1}$$

where velocity u of the streaming electrons to the plasma surface has the components $u_{\{x,y,z\}}$. Additionally, m_e gives the electron mass, T_e the electron temperature, Φ the electrostatic potential and U the probe voltage. Particles flowing into the sheath along z enter the plasma perpendicular to the probe head surface S. The current I_e is then calculated using [17],

$$I_\mathrm{e} = -eSn_\mathrm{e} \int \mathrm{d}u_x \int \mathrm{d}u_y \int \mathrm{d}u_z u_z f(u) \quad , \tag{2.3.1.2}$$

and ends at the integral solutions of,

$$I_\mathrm{e} = I_\mathrm{e,sat} \mathrm{e}^{\frac{e(\Phi-U)}{T_\mathrm{e}}} \quad \text{if} \quad U \leq \Phi \quad , \tag{2.3.1.3}$$

$$I_\mathrm{e} = I_\mathrm{e,sat} \quad \text{if} \quad U \geq \Phi \quad . \tag{2.3.1.4}$$

The electron saturation current reads as [17],

$$I_\mathrm{e,sat} = -enS\sqrt{\frac{T_\mathrm{e}}{2\pi m_\mathrm{e}}} \quad . \tag{2.3.1.5}$$

Calculating the electron density from $I_\mathrm{e,sat}$ is only possible at a low plasma pressure, where the mean free path is of the particles very long. Otherwise, the current collected by the probe is so large that it drains the plasma and changes its equilibrium properties. However, this ideal situation is rarely found in practical devices. Effects such as collisions and magnetic fields will lower the magnitude of $I_\mathrm{e,sat}$ and round off the knee, making U difficult to determine [9]. Expressions for the ions are obtained following the same scheme,

$$I_\mathrm{i,sat} = enS\sqrt{\frac{T_\mathrm{i}}{2\pi m_\mathrm{i}}} \quad . \tag{2.3.1.6}$$

Ions are then accelerated to the probe head while the ion source of the sheath (in front of the probe) does not supply enough charged particles to compensate a negative probe potential $-\Phi$. Hence, an

additional weak electric field is created. This second electric field is referred to as pre-sheath. Ions beyond the collection area of the single probe sheath are then attracted by the pre-sheath. Additional attracted ions have a flow velocity at the pre-sheath of $u_\mathrm{i} = c_\mathrm{s,i}$. For a positive probe head voltage $U > \Phi$, the kinetic ion energy reads [17] as follows,

$$e(\Phi - \Phi_\mathrm{s}) = \frac{1}{2} m_\mathrm{i} c_\mathrm{s,i}^2 \quad . \tag{2.3.1.7}$$

From now on, Φ_s is the sheath potential. Subsequently, the plasma is assumed to have a single ion species. No impurities are considered and the plasma is assumed to contain only pure hydrogen ions. With the simple definition of the ion speed of sound [1],

$$c_\mathrm{s} = \sqrt{\frac{T_\mathrm{i} + T_\mathrm{e}}{m_\mathrm{i}}} \quad , \tag{2.3.1.8}$$

equation (2.3.1.7) is then reduced to,

$$e(\Phi - \Phi_\mathrm{s}) = \frac{1}{2} (T_\mathrm{i} + T_\mathrm{e}) \quad . \tag{2.3.1.9}$$

The plasma can be treated as quasi-neutral until the sheath boundary is reached by the plasma ions because of Debye shielding effects. Using equations (2.3.1.1) and (2.3.1.9), the density n_s at the sheath boundary is obtained.

$$n_\mathrm{s} = n_\mathrm{e} \mathrm{e}^{-\frac{e(\Phi - \Phi_s)}{T_\mathrm{e}}} \approx 0.61 \cdot n_\mathrm{e} \quad . \tag{2.3.1.10}$$

Hence, the electron density decreases in the pre-sheath toward the sheath boundary. Ion fluxes onto the probe head then read as follows,

$$\Gamma_\mathrm{i} = 0.61 \cdot n_\mathrm{e} c_\mathrm{s} \quad . \tag{2.3.1.11}$$

All ions are absorbed by the probe, if the probe head has a negative voltage $U < \Phi$. Thus, the ion saturation current is given by,

$$I_\mathrm{i,sat} = 0.61 \cdot n_\mathrm{e} e S \sqrt{\frac{T_\mathrm{i} + T_\mathrm{e}}{m_\mathrm{i}}} \tag{2.3.1.12}$$

The electron density measured by a Langmuir probe head $n_\mathrm{e,LP}$ is then calculated from equation (2.3.1.12) [1],

$$n_\mathrm{e,LP} = \frac{I_\mathrm{i,sat} e}{0.61 \cdot S c_\mathrm{s}} \quad . \tag{2.3.1.13}$$

where m_i denotes the ion mass. Stangeby assumed the plasma flow to be iso-thermal [1]. The adiabatic index $\gamma = 1$ was already applied for equation (2.3.1.13). Plasma temperatures are given in eV, Boltzmann´s constant k is not introduced in equation (2.3.1.13). Equation (2.3.1.13) is often used to describe plasma scenarios that have carbon or oxygen as second plasma species in addition to hydrogen. However, necessary assumptions (up to this point) about plasma temperatures and

impurity contamination remain unexplored.

A multi-purpose manipulator (MPM) is a flexible tool for integrating several different diagnostic probe heads, mainly Langmuir, magnetic coil, and material probes [27, 33, 34] mounted on a combined probe [35]. Installed probes are then transported to the inner vacuum vessel edge, where they can be moved over an interval of an additional 350 mm with fast movement to measure plasma profiles. The system is then used to radially insert these probes into the plasma edge at a toroidal angle of 200°. Chosen toroidal and poloidal positions remain fixed during measurements (and both considered operational phases). Only the radial position of the MPM is variable. The original design included a set of several Langmuir probes and floating potential pins. Pin1 and Pin4 are used to measure the

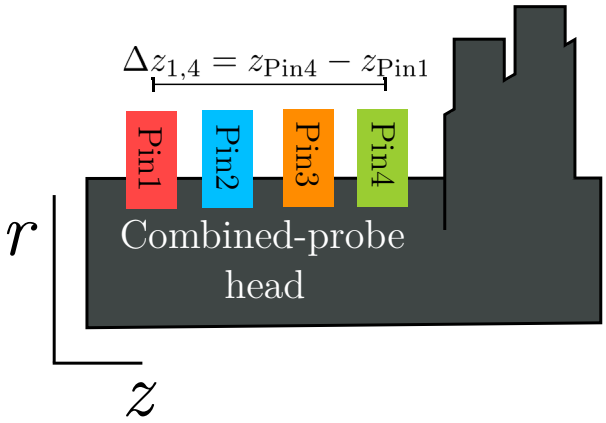

Figure 2.13: Side view of the MPM probe head, with Pins 1 to 4. Each pin corresponds to a single Langmuir probe. Different pins are used for n_e and T_e measurements.

floating potential Φ_{fl}. The electron temperature T_e is measured using Pin2 and calculated including Φ_{fl}, e.g. Pin1, Pin2 and Pin4 are used. Pin3 measures the saturation current $I_{i,sat}$. Applying equation (2.3.1.13) to Pin3 leads to n_e.
Figure 2.13 shows Pin1 to Pin4 and their different locations on the combined probe. The pins are separated in z direction by $\Delta z_{1,4} = 1.5$ cm. This is of particular importance for the presented study. In general, a mean coordinate $\langle z \rangle$ is defined for all measured profiles, neglecting $\Delta z_{1,4} = 1.5$ cm. In view of poloidal variations of the modeled quantities, it is advantageous to average the z-coordinate over all used pins. One can consider two exemplary cases in which, on the one hand, Pins 1, 2, 3, 4 are used, and on the other hand, Pins 1, 2, and 4 are used. Subsequently, the difference of averaged coordinates of used pins is given by $\langle z \rangle_{\mathrm{Pin}\{1,2,4\}} - \langle z \rangle_{\mathrm{Pin}\{1,2,3,4\}} = 0.375$ cm. This is of great importance because the coordinates of the four pins do not only cover a “small line” on their way in and out of the plasma, but rather an area of 1.5 cm $\cdot L_{\mathrm{plunge}}$. A comparison of numerical and experimental datasets results in an overlay of the data along the combined probe’s plunge path. The experimental coordinates are averaged and introduce spatial uncertainty to this direct comparison, but must be transferred to the computational domain. However, the exact coordinates might not be covered in the computational domain’s coordinates, which rather lie next to the combined probe’s coordinates

with a small offset. Subsequently, a second spatial uncertainty appears in the direct comparison. The combination of both play a crucial role later in this study.

2.3.2 Bolometer

The total radiation emitted by fusion plasma is a crucial insight into the energy balance. Because of particle interactions, a power loss of the plasma through radiation is possible. A bolometer measurement is sensitive to these power losses in the form of thermal heat load from photons [36]. In the W7-X, a single bolometer camera measures an integral of the line-of-sight from the signal [37]. Multiple cameras are installed at different ports to provide a complete view of the plasma cross-section (see Figure 2.14). The view angles of all cameras are integrated (over all camera channels) to obtain

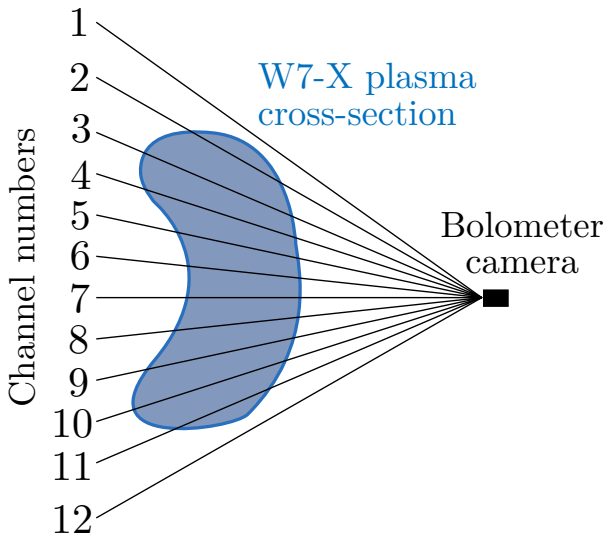

Figure 2.14: Sketch of a bolometer camera set-up for the W7-X.

the total radiated power in the considered cross-section. For W7-X a metal resistive detector was selected as the main signal detector [36] because metal resistive detectors cover almost the complete spectra of plasma's radiation pattern. A high spatial resolution along a sufficient amount of diagnostic channels is preferable. The colamination point of camera channels is critical for the design because the distance from this point to the detectors (passing several aperture elements) determines the viewing angle of the bolometer and width of the line of sight. The system has a spatial resolution of 5 cm and a viewing angle of 53° (respective to the magnetic axis). A spatial resolution greater than five cm introduces an uncertainty of ±2.5 to the exact position of the LCFS, which is a critical parameter for plasma edge simulations. Additionally, the number of lines that cover particular areas of interest in the machine differs. Thus, the coverage of areas of interest might lack a good resolution and the bolometric power must be considered inaccurate.

2.4 Importance of impurity transport to long-pulse steady-state operation

The physical mechanism causing the fusion plasma to collapse at high densities, mentioned in Section 1.3, is associated with a radiation collapse near low-temperature plasma edge regions. A radiation collapse is caused by the presence of impurities from the experiment vessel's first wall or installations. The plasma SOL density is increased – at a fixed heating power applied to the plasma – which causes the SOL temperature to drop. The same amount of heating power is simply distributed over more particles in the SOL. However, the plasma pressure remains approximately constant. The consequence is a huge increase in radiation power, lost over impurities in the SOL. At some point, the radiation losses become dominant rather than the thermal conductivity of the plasma. The plasma core radius becomes increasingly smaller, leading to instabilities and disruption of the plasma. This must be prevented because the main goal of fusion research is to achieve long-pulse plasmas in a steady-state. However, impurities and their disadvantageous effects make this a rocky road. The dynamics of impurities within a fusion plasma can be categorized into three main categories, which correspond to the already introduced main areas of the impurity transport, shown in Figure 1.5.

- The direct connection of the plasma edge to the surface of plasma facing wall components. This is an impurity source for the plasma through sputtering processes.
- Impurity influxes into the SOL over the inner and outer boundary.
- The confinement of the core plasmas and how they evolve under certain plasma conditions in respect of impurities.

Each of these impurity dynamic categories has its own complexity and relevance on the global impurity behavior. They can only be studied individually and the results subsequently fitted together. For a given core transport, the "effective" impurity source into the core plasma – determined by the impurity source strength and the SOL transport – is directly related to the core impurity concentration and, consequently, to the total radiation level in the equilibrium state [38]. The consequences of these unfavorable impurity confinement at high density manifest themselves in radiation losses that steadily rise throughout the pulse duration by accumulating impurity ions [39]. Plasmas that feature a radiation fraction of up to 50% – in respect to the applied heating power – have a high potential to degrade and end in the described radiation collapse. Thus, the plasma confinement time is a function of the electron density and applied heating power. The control of impurity confinement and impurity dynamics in the SOL plays a key role in long-pulse operation. Besides questions of impurity influxes and dynamics, a crucial question regarding the long-pulse operation phase of W7-X is the control heat flux reaching the divertor. The installed divertor for OP1.2 was uncooled and only a maximum total energy of 80 MJ was allowed to degrade along the divertor. Thus, first divertor plasmas were limited to a duration of 10–15 sec.

The accumulation of impurity particles can also occur through ripple effects in the magnetic topology of W7-X. As shown in Section 2.2 and Figure 2.7, the magnetic configurations underwent a significant change along the toroidal coordinate. This change was also notable for slightly modified magnetic configurations, namely the high and low mirror configurations. Currents in the control coils (see Figure 2.1) were altered to generate a magnetic field ripple as well as to operate the experiment in the low or high mirror configuration. This ripple is defined as the difference between the maximum and minimum magnetic field strength. A particle's motion will not be affected if its momentum is exactly along the parallel magnetic field; however, particles that travel with a parallel and perpendicular momentum component (to the magnetic field) may be reflected at the generated ripple's maximums and minimums; these maximums and minimums can act as potentials, as with the end of a magnetic bottle [17]. Thus, prohibited areas for particles are found in which particles have a greater potential difference from their starting point than their kinetic energy at the starting point—such particles are trapped. A figurative representation is an airplane forced to stay at a given height in a valley between different mountain summits [17]; wind could push the airplane further outward, which is a metaphor for a particle's drift (i.e., its perpendicular momentum component). The exact key parameters for the high and low mirror configurations can be found in [40].
The rotational transform from equation (2.2.0.1) is changed by a margin. Figure 2.15 shows the variation in the W7-X's magnetic configuration in a poloidal cross-section, taken at $\varphi = 0$. Changes

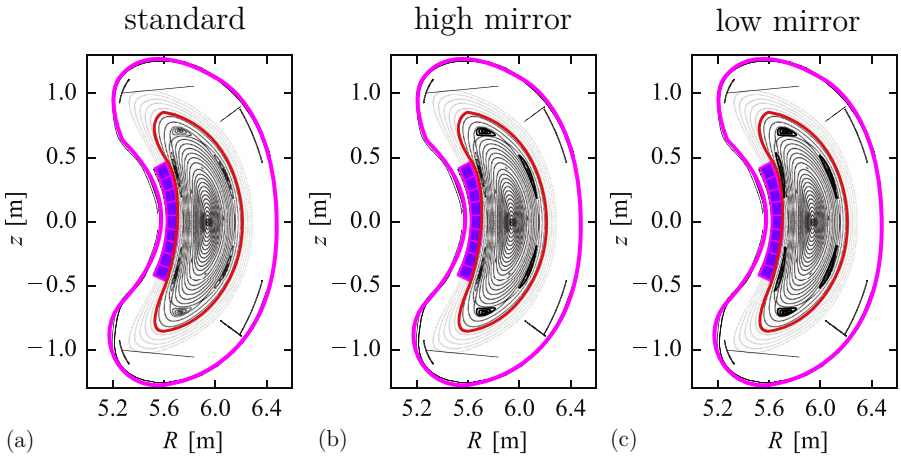

Figure 2.15: (a)–(c) show the poloidal cross-section of vacuum fields (at $\varphi = 0$) of the standard, low, and high mirror configurations of a limiter-operated W7-X. Figure concept taken from [41].

to the poloidal cross-section as well as to the rotational transform are neglected at this point. This might be an odd assumption at first glance, but it serves only as a first rule-of-thumb estimate of the impurity content of the plasmas shown in Figure 2.16. Dinklage *et al.* [42] found that the effective charge state Z_{eff}-profile could be estimated with values of 3.5, 2.5, or 1.5, as shown in Figure 2.17. Considered discharges were recorded using a Thomson scattering system and Limiter Langmuir probes, and the experiment was operated in the high and low mirror configurations. The discharges

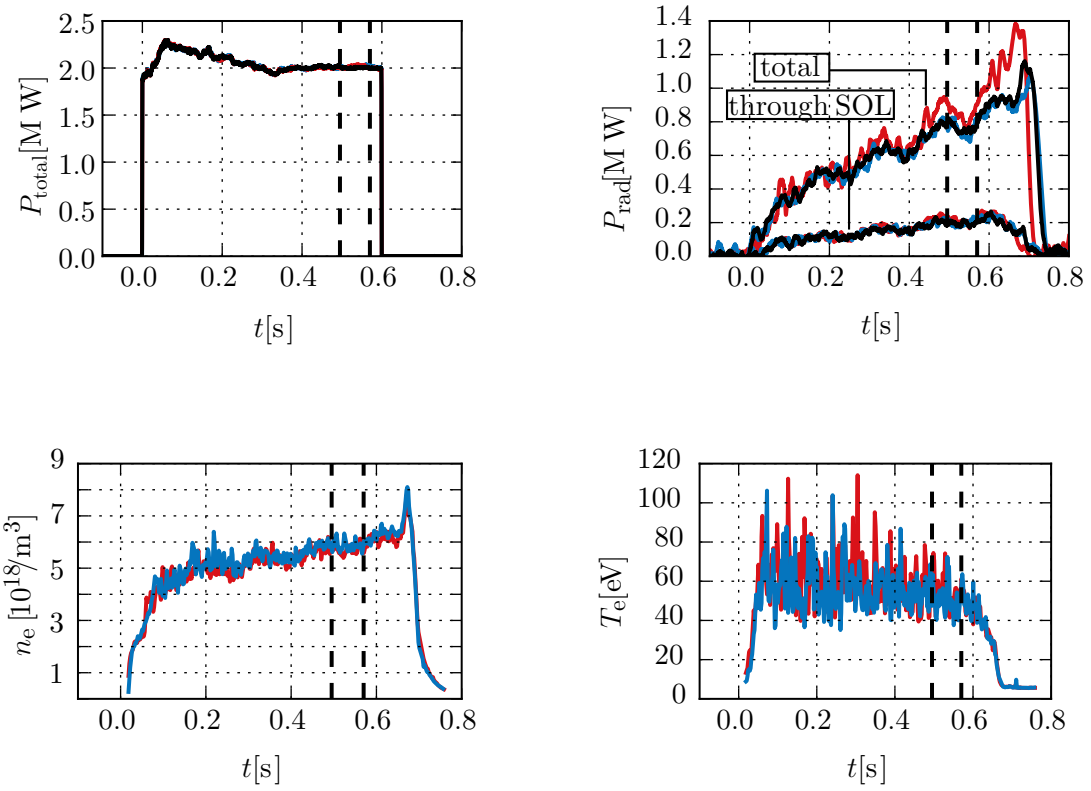

Figure 2.16: Overview of characteristic measurements of heating power (a), radiated power (b), and downstream n_e (c), T_e (d). Measurements (a) to (d) were conducted using bolometer and Langmuir probe measurements of a repetitive set of W7-X discharges. The color code refers to different discharges. Black: discharge 20160308.22, red: discharge 20160308.23, and blue: discharge 20160308.24. Upstream Langmuir probe measurements were performed at a specific time interval ($\Delta t = 0.05$ s), indicated by the vertical dashed lines.

were heated with an overall heating power (from the ECRH-heating system) of 1 MW and reached a radiation of 0.2 MW (see Figure 2.17(a)). Therefore, the radiated power from the plasma considered by Dinklage *et al.* shown in Figure 2.17 is lower than that of the plasma shown in Figure 2.16; differences between the magnetic configurations are neglected to enable a first rule-of-thumb comparison.
The Langmuir probe profiles in Figure 2.17 were already post-processed using the aforementioned effective charge state $Z_{\text{eff}} \in \{1.5, 2.5, 3.5\}$ and account for the electron densities of the impurities within the plasma. The effective charge state and corresponding effective mass of the impurity species can be calculated using the following equations,

$$Z_{\text{eff}} = \sum_i n_i Z_i^2 / \sum_i n_i Z_i \quad , \tag{2.4.0.1}$$

$$m_{\text{eff}} = \sum_i n_i m_i / \sum_i n_i \quad , \tag{2.4.0.2}$$

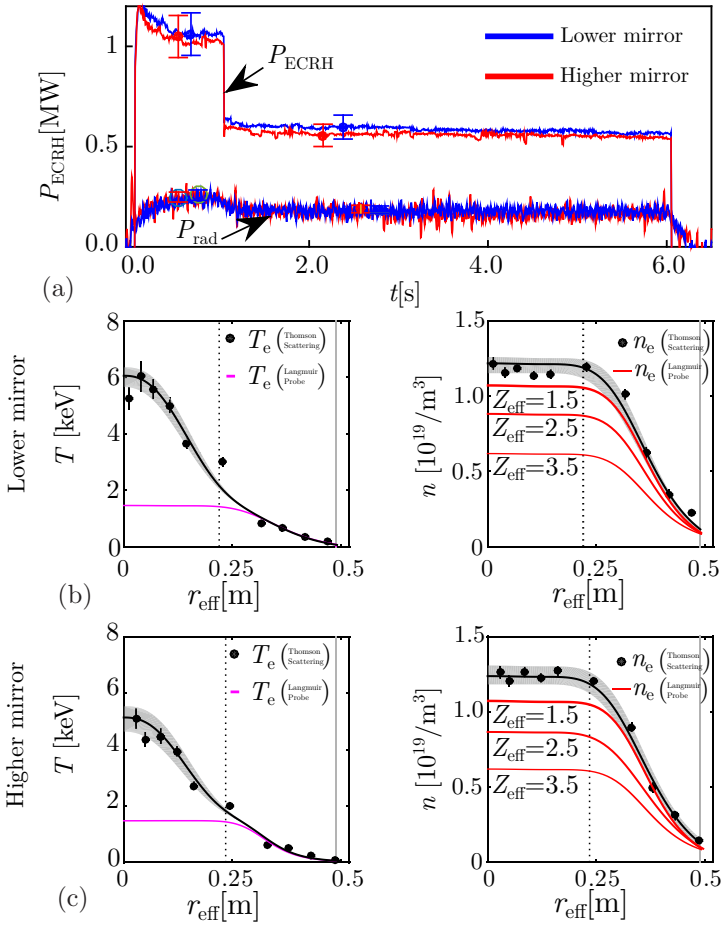

Figure 2.17: (a)–(c) are poloidal cross-sections (at $\varphi = 0$) of the low and high mirror configurations of OP1.2. Figure concept taken from [42].

where i represents the impurity's charge. However, only a first estimate was given in [42], which did not access the exact charge state distributions. Greater charge state densities, as well as access to higher charge state levels, are caused by higher radiation powers (see Figures 2.16 and 2.17(a), 0.8MW versus 0.2MW), assuming the radiated power is lost over the same impurities. The effective charge state density and mass change significantly.

The code package EMC3-EIRENE provides densities for the main plasma and every charge state of the considered plasma impurity (under the aforementioned assumptions). The effective charge state and effective mass can easily be deduced because every single charge state of the considered plasma species is a code output. An a posteriori approach was used to consider the effects of impurities on the electron density, thereby compensating for the limitations of the EMC3 impurity model. The results for Z_{eff} and m_{eff} are shown in Figure 2.18 (a) and (c), respectively, for simulation one of the key EMC3-EIRENE simulations (see Chapter 4). Because the Z_{eff} and m_{eff} profiles were not directly measurable during the limiter campaign [16, 19], an assumption of Z_{eff} and m_{eff} along the Langmuir

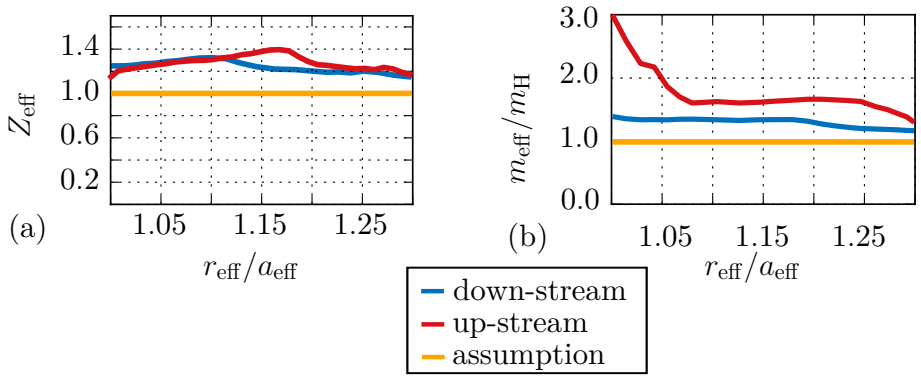

Figure 2.18: Comparison of the simulated Z_{eff} (top row) and m_{eff} (bottom row) at the down- (blue) and upstream (red) measurement locations with the previously made assumption $Z_{\mathrm{eff}} = 1$ and $m_{\mathrm{eff}} = 1$ (yellow). All results are plotted against the effective radius r_{eff} normalized to a_{eff}. Subplots (a) and (b) show the results of one of the key EMC3-EIRENE simulations, as discussed in Chapter 4.

probe measurement location had to be made. $Z_{\mathrm{eff}} = 1$ and $m_{\mathrm{eff}} = 1$ were initially assumed (i.e., a pure hydrogen plasma) at both the MPM and limiter Langmuir probe measurement locations (see Figures 4.2 and 4.4). These assumptions were revised because the Z_{eff} and m_{eff} peaks were above 1. Moreover, the electron density calculation based on the saturation current I_{sat} (used in the data interpretation process in [27]), measured by the Langmuir probes, was affected by a change in these effective values and presented subsection 2.3.1. Therefore, the discussion of measured Langmuir probe densities had to be extended to a multi-species plasma.

CHAPTER 3

EMC3-EIRENE

The EMC3 model equations are derived in this chapter to introduce the connection between a fluid and a kinetic plasma description. Thus , the first key question of this chapter is as follows,

- *How are fluid model equations of the EMC3 model derived and solved with a kinetic Monte Carlo solving scheme?*

The key to kinetically solving the EMC3 model equations is to bring the model equations in a Fokker-Plank like form. Furthermore, this chapter discusses the implementation of impurities in the EMC3 model and code package in respect of the motivating questions in Chapter 2. However, physical and chemical sputtering effects, and neutral particle sources are supplied to the EMC3 code via a direct coupling (via an interface) between EMC3 and EIRENE. Thus, the following question is answered in this chapter,

- *What is the direct interface between EMC3 and the EIRENE code?*

The impurity model of the EMC3 code is discussed in subsection 3.2.1 to meet the demands of an interpretative impurity study. However, some model inaccuracies remain, which are discussed as well. Coupled to this are the model's input parameters. Particle influxes from the system's inner and outer boundaries are essential for the code to run accurately. Thus, the third key question of this chapter is as follows,

- *Which are the important model parameters in respect of interpretative impurity studies?*

The exact implementation of the particle influxes, across the system boundaries, and thus the influx of impurities into the system, is discussed to answer this question. Furthermore, an overview of the system's boundaries on the EMC3 and EIRENE computational grid is given.

One of the fundamental singular elements of any nuclear fusion experiment, and thus for a stellarator, is a LCFS which delimits the SOL from the core region. Particle traces along flux tubes in the SOL are intersected by the limiter or divertor. Plasma particles travel from their arbitrary origin (after the plasma startup or sputtering process) along the magnetic flux surfaces in a guiding center motion. The length of the guiding center's trajectory is referred to by the connection length L_c. If the flux surface is closed, and hence belongs to the core region of the plasma, no distinct endpoint can be found. A rather sudden collapse of the plasma—and connected to that a termination of the magnetic field and flux surface—provides a "hard" endpoint to the confined particles' trajectory. If the flux surface is open, intersected by limiter target plates or a Langmuir probe, an end point is well defined. A finite L_c is found for open magnetic flux surfaces. A longer L_c, up to several hundred meters, provides more weight to the cross field transport in a perpendicular direction to the magnetic field [43]. Simple transport models such as the two-point model or onion skin model [1], based on the toroidal tokamak symmetry, do not apply for the W7-X's complex stellarator geometry (see Figure 2.4). An assessment of transport effects, both parallel and perpendicular to the magnetic field, with a full 3D resolution is demanded. Additionally, the complex geometry of the W7-X introduces a 3D plasma boundary. The present study applies the EMC3-EIRENE [14, 15] code package to meet the requirement of a 3D resolution of transport effects in the SOL.

3.1 From a kinetic to a fluid plasma description

In this section, a velocity distribution function $f_\alpha(\boldsymbol{v}, \boldsymbol{r}, t)$ is considered for each species of plasma (see Figure 3.1). The plasma is treated kinetically because the $\boldsymbol{v}$ gives an arbitrary particle its kinetic energy magnitude (assuming $m_\alpha << \boldsymbol{v}$). In fluid theory, the plasma parameters are functions of $\boldsymbol{r}$ and t , which is possible because the velocity distribution is assumed to be Maxwellian and can be specified by only one number of the temperature T (assuming $T = T_e = T_i$). Then, n_α (density of the plasma species α) is a function of $\boldsymbol{r}$ and t for the fluid description in a given volume V. In the kinetic description, $f_\alpha(\boldsymbol{v}, \boldsymbol{r}, t)$ is integrated over the velocity of the particles to obtain the density in the same given volume V,

$$n_\alpha = \int_V f_\alpha(\boldsymbol{r}, t) d\boldsymbol{v} \quad . \tag{3.1.0.1}$$

An exemplary distribution is shown in Figure 3.1. The Boltzmann equation is the equation that $f_\alpha(\boldsymbol{v}, \boldsymbol{r}, t)$ must fulfill,

$$\frac{\partial f_\alpha}{\partial t} + \boldsymbol{v} \cdot \nabla f_\alpha + \frac{\boldsymbol{F}}{m} \cdot \frac{\partial f_\alpha}{\partial \boldsymbol{v}} = \left(\frac{\partial f_\alpha}{\partial t}\right)_c \quad , \tag{3.1.0.2}$$

where $\boldsymbol{F}$ is the acting force and $\left(\partial f_\alpha / \partial t\right)_c$ is the time rate of change of $f(\boldsymbol{v}, \boldsymbol{r}, t)$ caused by collisions. In equation (3.1.0.2), $f(\boldsymbol{v}, \boldsymbol{r}, t)$ is simply written as f_α. This is followed throughout this section. Then, $\frac{\partial f_\alpha}{\partial t}$ is the explicit dependence of f_α on the system's time. If a described plasma holds enough temperature

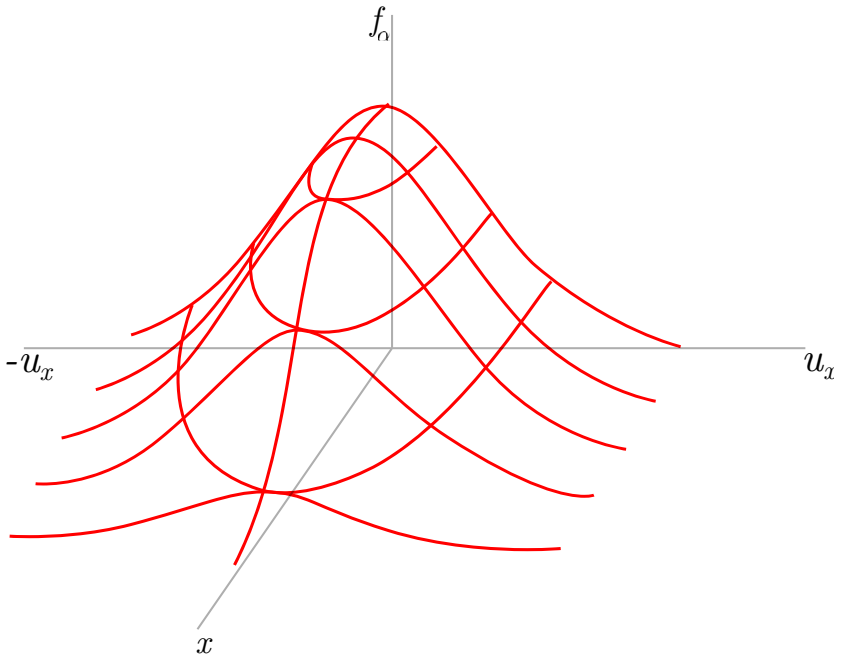

Figure 3.1: Spatially varying one-dimensional distribution function $f_\alpha(v_x, x)$, time invariant.

to allow collisions to be neglected, equation (3.1.0.2) can be rewritten as,

$$\frac{\partial f_\alpha}{\partial t} + \boldsymbol{v}\cdot\nabla f_\alpha + \frac{q}{m}(\boldsymbol{E}+\boldsymbol{v}\times\boldsymbol{B})\cdot\frac{\partial f_\alpha}{\partial \boldsymbol{v}} = 0 \quad . \tag{3.1.0.3}$$

Equation (3.1.0.3) is called the Vlasov equation. However, if the described plasma is not collision less one can approximate the right hand side of equation (3.1.0.3) with $\left(\frac{\partial f_\alpha}{\partial t}\right)_c = \frac{f_n - f_\alpha}{\tau}$, with f_n being the distribution function of neutral atoms and τ referring to a constant collision time between f_α and f_n particles. Alternatively the Krook collision term [9] can be used, which is a kinetic generalization of the right hand side $\left(\frac{\partial f_\alpha}{\partial t}\right)_c$, when Coulomb collisions are dominant in the plasma. Then, equation (3.1.0.2) can be written as the Fokker-Planck equation,

$$\frac{\partial f_\alpha}{\partial t} + \boldsymbol{v}\cdot\nabla f_\alpha + \frac{q}{m}(\boldsymbol{E}+\boldsymbol{v}\times\boldsymbol{B})\cdot\frac{\partial f_\alpha}{\partial \boldsymbol{v}} = -\frac{\partial}{\partial \boldsymbol{v}}\cdot(f_\alpha\langle\Delta\boldsymbol{v}\rangle)\frac{1}{2}\frac{\partial^2}{\partial\boldsymbol{v}\partial\boldsymbol{v}}\frac{1}{(f_\alpha\langle\Delta\boldsymbol{v}\Delta\boldsymbol{v}\rangle)} \quad , \tag{3.1.0.4}$$

where $\Delta\boldsymbol{v}$ is the change in velocity caused by a collision. A fluid description can be derived from the Boltzmann equation (3.1.0.3) using different statistical moments of $f_\alpha(\boldsymbol{v},\boldsymbol{r},t)$. The nth moment is defined as,

$$\langle f_\alpha(\boldsymbol{v},\boldsymbol{r},t)\rangle^n = \int \boldsymbol{v}^n f_\alpha(\boldsymbol{v},\boldsymbol{r},t)d\boldsymbol{v} \quad . \tag{3.1.0.5}$$

The plasma is then described as a fluid rather than by a velocity distribution of each plasma species. Through the application of equation (3.1.0.5), one finds that,

particle density (0. moment): $n_\alpha(\boldsymbol{r},t) = \int f_\alpha(\boldsymbol{v},\boldsymbol{r},t)d\boldsymbol{v}$, (3.1.0.6)

plasma momentum (1. moment): $\boldsymbol{u}_\alpha(\boldsymbol{r},t) = \frac{1}{n_\alpha(\boldsymbol{r},t)} \int \boldsymbol{v} f_\alpha(\boldsymbol{v},\boldsymbol{r},t) d\boldsymbol{v}$,

(3.1.0.7)

particle temperature (2. moment): $T_\alpha(\boldsymbol{r},t) = \frac{m_\alpha}{3 n_\alpha(\boldsymbol{r},t)} \int (\boldsymbol{v}-\boldsymbol{u}_\alpha)^2 f_\alpha(\boldsymbol{v},\boldsymbol{r},t) d\boldsymbol{v}$.

(3.1.0.8)

The term $\boldsymbol{v}-\boldsymbol{u}_\alpha$ is the thermal velocity of the particles. The lowest moment is then applied to the Vlasov equation ((3.1.0.3); including the collisional right-hand side) because an electric and magnetic field are present in a fusion experiment such as the W7-X,

$$\int \frac{\partial f_\alpha}{\partial t} d\boldsymbol{v} + \int \boldsymbol{v} \cdot \nabla f_\alpha d\boldsymbol{v} + \int \frac{q_\alpha}{m_\alpha} (\boldsymbol{E} + \boldsymbol{v} \times \boldsymbol{B}) \cdot \frac{\partial f_\alpha}{\partial \boldsymbol{v}} d\boldsymbol{v} = \int \left(\frac{\partial f_\alpha}{\partial t} \right)_c d\boldsymbol{v} \quad . \tag{3.1.0.9}$$

The first term gives,

$$\int \frac{\partial f_\alpha}{\partial t} d\boldsymbol{v} = \frac{\partial}{\partial t} \int f_\alpha d\boldsymbol{v} = \frac{\partial n_\alpha}{\partial t} \quad . \tag{3.1.0.10}$$

While $\boldsymbol{v}$ does not depend on time, the second term of equation (3.1.0.9) yields,

$$\int \boldsymbol{v} \nabla \cdot f_\alpha d\boldsymbol{v} = \nabla \cdot \int \boldsymbol{v} f_\alpha d\boldsymbol{v} = \nabla \cdot (n_\alpha \boldsymbol{u}_\alpha) \quad , \tag{3.1.0.11}$$

and the second moment was used in the last step of equation 3.1.0.11. The third term of equation (3.1.0.3) can be separated into integrals,

$$\int \frac{q_\alpha}{m_\alpha} (\boldsymbol{E} + \boldsymbol{v} \times \boldsymbol{B}) \cdot \frac{\partial f_\alpha}{\partial \boldsymbol{v}} d\boldsymbol{v} = \frac{q_\alpha}{m_\alpha} \int \boldsymbol{E} \cdot \frac{\partial f_\alpha}{\partial \boldsymbol{v}} d\boldsymbol{v} + \frac{q_\alpha}{m_\alpha} \int (\boldsymbol{v} \times \boldsymbol{B}) \cdot \frac{\partial f_\alpha}{\partial \boldsymbol{v}} d\boldsymbol{v} \quad . \tag{3.1.0.12}$$

The electric field cancels out the third term of equation 3.1.0.3, because one finds,

$$\frac{q_\alpha}{m_\alpha} \int \boldsymbol{E} \cdot \frac{\partial f_\alpha}{\partial \boldsymbol{v}} d\boldsymbol{v} = \frac{q_\alpha}{m_\alpha} \int \frac{\partial}{\partial \boldsymbol{v}} (f_\alpha \boldsymbol{E}) d\boldsymbol{v} = \int_{S\infty} f_\alpha \boldsymbol{E} dS \quad , \tag{3.1.0.13}$$

with the divergence integrated to give an value to $f\boldsymbol{E}$ on the surface S at a velocity of $v = \infty$. If f_α converges faster to 0 than $1/v^2$ with v diverging to ∞, $\int_{S\infty} f_\alpha \boldsymbol{E} dS$ vanishes to 0. Then, the $\boldsymbol{v} \times \boldsymbol{B}$ contribution to equation (3.1.0.12) is,

$$\int (\boldsymbol{v} \times \boldsymbol{B}) \frac{\partial f_\alpha}{\partial \boldsymbol{v}} d\boldsymbol{v} = \int \frac{\partial}{\partial \boldsymbol{v}} (f \boldsymbol{v} \times \boldsymbol{B}) d\boldsymbol{v} - \int \frac{\partial}{\partial \boldsymbol{v}} \times (f_\alpha \boldsymbol{v} \times \boldsymbol{B}) d\boldsymbol{v} \quad . \tag{3.1.0.14}$$

The first term $\int \frac{\partial}{\partial \boldsymbol{v}} (f_\alpha \boldsymbol{v} \times \boldsymbol{B}) d\boldsymbol{v}$ can again be understood as a surface integral. Assuming a Maxwellian distribution for f_α, f_α falls faster than any power of v as v diverges to ∞. Hence, the integral vanishes to 0. This is also true for the second integral, because the the magnetic field $\boldsymbol{v} \times \boldsymbol{B}$ is perpendicular to $\frac{\partial}{\partial \boldsymbol{v}}$. Thus, equations (3.1.0.13) and (3.1.0.14) do not have any contribution to a collisional Vlasov equation (see equation (3.1.0.9)). The overall number of particles within the plasma is conserved. In combination equations (3.1.0.9), (3.1.0.13), and (3.1.0.14) yield the continuity following equation,

$$\frac{\partial n_\alpha}{\partial t} + \nabla \cdot (n_\alpha \boldsymbol{u}_\alpha) = \int \left(\frac{\partial f_\alpha}{\partial t} \right)_c d\boldsymbol{v} \quad . \tag{3.1.0.15}$$

The right-hand side can be rewritten as,

$$\frac{\partial n_\alpha}{\partial t} + \nabla \cdot (n_\alpha \boldsymbol{u}_\alpha) = \int C_\mathrm{i} d\boldsymbol{v} + S_\mathrm{i} \quad , \tag{3.1.0.16}$$

where S_i is the ion source caused by collisions between electrons and neutrals. Furthermore, C_i is the collision term between ions and other particles. However, the ionization amount of ions is small compared with that of electrons. Thus, C_i is neglected and equation (3.1.0.16) reduces to,

$$\frac{\partial n_\alpha}{\partial t} + \nabla \cdot (n_\alpha \boldsymbol{u}_\alpha) = S_\mathrm{i} \quad . \tag{3.1.0.17}$$

The neutral particle source S_i is calculated using the EIRENE code. Equation 3.1.0.17 is the continuity equation of the plasma density. The equation connects the timewise change of n_α with the spatial change in flux $n_\alpha \boldsymbol{u}_\alpha$.
The first moment is now applied to the collisional Vlasov equation (3.1.0.9). Multiplying equation (3.1.0.9) with $m_\alpha \boldsymbol{v}$ followed by an integration over $d\boldsymbol{v}$ yields,

$$m_\alpha \int \boldsymbol{v} \frac{\partial f_\alpha}{\partial t} d\boldsymbol{v} + m_\alpha \int \boldsymbol{v}(\boldsymbol{v} \cdot \nabla) f_\alpha d\boldsymbol{v} + q_\alpha m_\alpha \int \boldsymbol{v}(\boldsymbol{E} + \boldsymbol{v} \times \boldsymbol{B}) \frac{\partial f_\alpha}{\partial \boldsymbol{v}} d\boldsymbol{v} = m_\alpha \int \boldsymbol{v} \left(\frac{\partial f_\alpha}{\partial t} \right)_c d\boldsymbol{v} \quad . \tag{3.1.0.18}$$

Again, equation (3.1.0.18) is discussed term by term, starting with the fist,

$$m_\alpha \int \boldsymbol{v} \frac{\partial f_\alpha}{\partial t} d\boldsymbol{v} = m_\alpha \frac{\partial}{\partial t} \int \boldsymbol{v} f_\alpha d\boldsymbol{v} = m_\alpha \frac{\partial f_\alpha}{\partial t} (n_\alpha \boldsymbol{u}) \quad . \tag{3.1.0.19}$$

Now, collisions change the momentum of the particles, introducing 3D stress into the fluid, which is covered by a stress tensor $\boldsymbol{P}$. The components are specified $\boldsymbol{P}_{\alpha\beta} = m_\alpha n_\alpha \langle v_k v_l \rangle$. The plasma component α moves in the k direction with v_k and the plasma component β moves in the l direction with v_l. Notably, $m_\alpha n_\alpha$ gives the magnitude for $\langle v_k v_l \rangle$, and one simply writes $\boldsymbol{P}_\alpha$. If f_α is assumed to be an isotropic Maxwellian, then $\boldsymbol{P}_\alpha$ can be written as (with $k = l$),

$$\boldsymbol{P}_\alpha = \begin{bmatrix} \boldsymbol{p}_\alpha & 0 & 0 \\ 0 & \boldsymbol{p}_\alpha & 0 \\ 0 & 0 & \boldsymbol{p}_\alpha \end{bmatrix} \quad . \tag{3.1.0.20}$$

where $\boldsymbol{p}_\alpha$ is the plasma pressure. The terms of $\boldsymbol{P}_\alpha$ can be split into an isotropic part $\boldsymbol{p}_\alpha$ and anisotropic viscosity tensor $\boldsymbol{\pi}_{\alpha,kl}$, which read

$$\boldsymbol{P}_\alpha = \boldsymbol{p}_\alpha \delta_{kl} + \boldsymbol{\pi}_{\alpha,kl} \tag{3.1.0.21}$$

Such collisions do not contribute to a diffusion, and thus gradients of the viscosity are neglected (neglecting $\nabla \cdot \boldsymbol{\pi}_{\alpha,kl}$). Furthermore, the friction between electrons and ions in plasma must obey,

$$\boldsymbol{P}_{\alpha=\mathrm{e}} = \boldsymbol{P}_\mathrm{ei} = -\boldsymbol{P}_\mathrm{ie} = \boldsymbol{P}_{\alpha=\mathrm{i}} \quad , \tag{3.1.0.22}$$

because the momentum of the particles must be conserved. One finds for the Tensor $\boldsymbol{P}_{\alpha\beta} = m_\alpha n_\alpha \langle v_k v_l \rangle$ that,

$$\boldsymbol{P}_\mathrm{ei} = m_\mathrm{e} n_\mathrm{e} (\boldsymbol{v}_\mathrm{e} - \boldsymbol{v}_\mathrm{i}) \nu_\mathrm{ei} \quad . \tag{3.1.0.23}$$

The collision frequency is given by ν_{ei}, and $\boldsymbol{P}_{ie}$ is found in the same manner. Collisions in a plasma are dominated by Coulomb collisions which are given by the Coulomb force. Therefore, $\boldsymbol{P}_{ei}$ must be proportional to e^2 (assuming a hydrogen plasma with electrons and single charged ions, $n_e = n_i = n$). Then, equation (3.1.0.23) can be rewritten as,

$$\boldsymbol{P}_{ei} = \eta e^2 n^2 (\boldsymbol{v}_e - \boldsymbol{v}_i) \quad , \quad \nu_{ei} = \frac{ne^2}{m}\eta \quad . \tag{3.1.0.24}$$

The third term of equation (3.1.0.18) can be rewritten as,

$$q_\alpha \int \boldsymbol{v}(\boldsymbol{E} + \boldsymbol{v} \times \boldsymbol{B}) \cdot \frac{\partial f_\alpha}{\partial \boldsymbol{v}} d\boldsymbol{v}$$

$$= q_\alpha \int \frac{\partial}{\partial \boldsymbol{v}} \cdot \left[f_\alpha \boldsymbol{v}(\boldsymbol{E} + \boldsymbol{v} \times \boldsymbol{B}) \right] d\boldsymbol{v} - q_\alpha \int f_\alpha \boldsymbol{v} \frac{\partial}{\partial \boldsymbol{v}} \cdot (\boldsymbol{E} + \boldsymbol{v} \times \boldsymbol{B}) d\boldsymbol{v} - q_\alpha \int f_\alpha (\boldsymbol{E} + \boldsymbol{v} \times \boldsymbol{B} \cdot \frac{\partial}{\partial \boldsymbol{v}} \boldsymbol{v}) d\boldsymbol{v} \tag{3.1.0.25}$$

The first two integrals of equation (3.1.0.25) cancel each other out, as in equations (3.1.0.13) and (3.1.0.14),

$$q_\alpha \int \boldsymbol{v}(\boldsymbol{E} + \boldsymbol{v} \times \boldsymbol{B}) \cdot \frac{\partial f_\alpha}{\partial \boldsymbol{v}} d\boldsymbol{v}$$

$$= \cancelto{0}{q_\alpha \int \frac{\partial}{\partial \boldsymbol{v}} \cdot \left[f_\alpha \boldsymbol{v}(\boldsymbol{E} + \boldsymbol{v} \times \boldsymbol{B}) \right] d\boldsymbol{v}} - \cancelto{0}{q_\alpha \int f_\alpha \boldsymbol{v} \frac{\partial}{\partial \boldsymbol{v}} \cdot (\boldsymbol{E} + \boldsymbol{v} \times \boldsymbol{B}) d\boldsymbol{v}}$$

$$- q_\alpha \int f_\alpha (\boldsymbol{E} + \boldsymbol{v} \times \boldsymbol{B} \cdot \cancelto{1}{\frac{\partial}{\partial \boldsymbol{v}} \boldsymbol{v}}) d\boldsymbol{v} \quad . \tag{3.1.0.26}$$

In the end the following is obtained through using the 1. moment in the final step,

$$q_\alpha \int \boldsymbol{v}(\boldsymbol{E} + \boldsymbol{v} \times \boldsymbol{B}) \cdot \frac{\partial f_\alpha}{\partial \boldsymbol{v}} d\boldsymbol{v} = -q_\alpha \int f_\alpha (\boldsymbol{E} + \boldsymbol{v} \times \boldsymbol{B}) d\boldsymbol{v} = -q_\alpha n_\alpha (\boldsymbol{E} + \boldsymbol{u} \times \boldsymbol{B}) \quad , \tag{3.1.0.27}$$

The remaining term, which has not been evaluated until now, is the second integral of equation (3.1.0.18) and can be rewritten as,

$$m_\alpha \int \boldsymbol{v}(\boldsymbol{v} \cdot \nabla) f_\alpha d\boldsymbol{v} = m_\alpha \int \nabla \cdot (f_\alpha \boldsymbol{v}\boldsymbol{v}) d\boldsymbol{v} = m_\alpha \nabla \cdot \int f_\alpha \boldsymbol{v}\boldsymbol{v} d\boldsymbol{v} \quad . \tag{3.1.0.28}$$

Here, reapplying the 1. moment leads to,

$$m_\alpha \nabla \cdot \int f_\alpha \boldsymbol{v}\boldsymbol{v} d\boldsymbol{v} = m_\alpha \nabla \cdot (n_\alpha \langle \boldsymbol{v}\boldsymbol{v} \rangle) \quad . \tag{3.1.0.29}$$

The thermal velocity $\boldsymbol{v} = \boldsymbol{u}_\alpha + \boldsymbol{w}$ from the 2. moment (see equation (3.1.0.8)), inserted into (3.1.0.29) yields,

$$m_\alpha \nabla \cdot (n_\alpha \langle \boldsymbol{v}\boldsymbol{v} \rangle) = m_\alpha \nabla \cdot (n_\alpha \boldsymbol{u}_\alpha \boldsymbol{u}_\alpha) + m_\alpha \nabla \cdot (n_\alpha \langle \boldsymbol{w}\boldsymbol{w} \rangle) + m_\alpha 2 \nabla \cdot (n_\alpha \boldsymbol{u}_\alpha \cancelto{0}{\langle \boldsymbol{w} \rangle}) \tag{3.1.0.30}$$

$$m_\alpha \nabla \cdot (n_\alpha \langle \boldsymbol{v}\boldsymbol{v} \rangle) = m_\alpha \nabla \cdot (n_\alpha \boldsymbol{u}_\alpha \boldsymbol{u}_\alpha) + \nabla \cdot \boldsymbol{P}_\alpha \quad , \tag{3.1.0.31}$$

where the averaged thermal velocity cancels to zero. The total stress tensor $\boldsymbol{P} = mn\langle \boldsymbol{w}\boldsymbol{w}\rangle$ can be found in term two of equation (3.1.0.31), but has no further meaning for this part of the derivation because it cancels out. An application of the product rule on (3.1.0.31) then yields,

$$\nabla\cdot(n_\alpha\langle \boldsymbol{v}\boldsymbol{v}\rangle) = \boldsymbol{u}_\alpha\nabla\cdot(n_\alpha\boldsymbol{u}_\alpha) + n_\alpha(\boldsymbol{u}_\alpha\cdot\nabla)\boldsymbol{u}_\alpha \tag{3.1.0.32}$$

Combining all results from equations (3.1.0.19), (3.1.0.24), and (3.1.0.27), one obtains

$$\begin{aligned} m_\alpha\frac{\partial}{\partial t}(n_\alpha\boldsymbol{u}_\alpha) + m_\alpha\boldsymbol{u}_\alpha\nabla\cdot(n_\alpha\boldsymbol{u}_\alpha) + m_\alpha n_\alpha(\boldsymbol{u}_\alpha\cdot\nabla)\boldsymbol{u}_\alpha + \nabla\cdot\boldsymbol{P}_\alpha - q_\alpha n_\alpha(\boldsymbol{E}+\boldsymbol{u}_\alpha\times\boldsymbol{B}) \\ = m_\alpha\int \boldsymbol{v}\left(\frac{\partial f_\alpha}{\partial t}\right)_c d\boldsymbol{v} \quad . \end{aligned} \tag{3.1.0.33}$$

Applying the continuity equation (3.1.0.15) to the first two terms of equation (3.1.0.33) yields the fluid equation of motion,

$$m_\alpha n_\alpha\left(\frac{\partial \boldsymbol{u}_\alpha}{\partial t} + (\boldsymbol{u}_\alpha\cdot\nabla)\boldsymbol{u}_\alpha\right) = q_\alpha n_\alpha(\boldsymbol{E}+\boldsymbol{u}_\alpha\times\boldsymbol{B}) - \nabla\cdot\boldsymbol{P}_\alpha + m_\alpha\int \boldsymbol{v}\left(\frac{\partial f_\alpha}{\partial t}\right)_c d\boldsymbol{v} \quad . \tag{3.1.0.34}$$

This equation describes the flow of the particles' momentum in the plasma. Here, the total stress tensor $\boldsymbol{P}_\alpha$ has the elements $P_\alpha = p_\alpha\delta_{kl} + \pi_{_\alpha,kl}$ with $\pi_{_\alpha,kl} = n_\alpha m_\alpha\langle w_k w_l - \frac{v_\alpha^2}{3}\delta_{kl}\rangle$ the viscosity tensor and it's entries. Inserting $\boldsymbol{P}_\alpha$ into equation (3.1.0.34) leads to,

$$m_\alpha n_\alpha\frac{\partial \boldsymbol{u}_\alpha}{\partial t} + m_\alpha n_\alpha\nabla\cdot(\boldsymbol{u}_\alpha\boldsymbol{u}_\alpha + \boldsymbol{\pi}_\alpha) = q_\alpha n_\alpha(\boldsymbol{E}+\boldsymbol{u}_\alpha\times\boldsymbol{B}) - \nabla\cdot\boldsymbol{p}_\alpha + \boldsymbol{R}_{\mathrm{ei}} + \boldsymbol{S}_{\mathrm{m}} \quad . \tag{3.1.0.35}$$

where $R_{\mathrm{ei}} = -R_{\mathrm{ie}}$ is the friction between the electrons and ions, and $\boldsymbol{S}_{\mathrm{m}}$ gives the momentum source caused by collisions on neutral particles.

The next magnetic moment, the 2. moment, is applied to equation (3.1.0.9) to derive the equation for the particles' energy flow. Thus, $m\boldsymbol{v}^2/2$ is multiplied to equation (3.1.0.9) and an integration over $d\boldsymbol{v}$ is performed.

$$\begin{aligned} \frac{m_\alpha}{2}\int \boldsymbol{v}^2\frac{\partial f_\alpha}{\partial t}d\boldsymbol{v} + \frac{m_\alpha}{2}\int \boldsymbol{v}^2(\boldsymbol{v}\cdot\nabla)f_\alpha d\boldsymbol{v} + \frac{q_\alpha m_\alpha}{2}\int \boldsymbol{v}^2(\boldsymbol{E}+\boldsymbol{v}\times\boldsymbol{B})\frac{\partial f_\alpha}{\partial t}d\boldsymbol{v} \\ = \frac{m_\alpha}{2}\int \boldsymbol{v}^2\left(\frac{\partial f}{\partial t}\right)_c d\boldsymbol{v} \quad . \end{aligned} \tag{3.1.0.36}$$

The Lorentz force acts perpendicular on the velocity $\boldsymbol{v}$; thus, no energy can be transferred to the particles in this manner. Because $\boldsymbol{v}\cdot(\boldsymbol{v}\times\boldsymbol{B})$ is again zero, one finds that,

$$\frac{m_\alpha}{2}\int \boldsymbol{v}^2\frac{\partial f_\alpha}{\partial t}d\boldsymbol{v} + \frac{m_\alpha}{2}\int \boldsymbol{v}^2(\boldsymbol{v}\cdot\nabla)f_\alpha d\boldsymbol{v} + q_\alpha n_\alpha\boldsymbol{u}_\alpha\cdot\boldsymbol{E} = \frac{m_\alpha}{2}\int \boldsymbol{v}^2\left(\frac{\partial f_\alpha}{\partial t}\right)_c d\boldsymbol{v} \quad . \tag{3.1.0.37}$$

Applying the 1. moment to the first and second terms while using (3.1.0.11) gives,

$$\frac{m_\alpha}{2}\int \boldsymbol{v}^2\frac{\partial f_\alpha}{\partial t}d\boldsymbol{v} + \frac{m_\alpha}{2}\int \boldsymbol{v}^2(\boldsymbol{v}\cdot\nabla)f_\alpha d\boldsymbol{v} = \frac{m_\alpha n_\alpha}{2}\frac{\partial}{\partial t}\langle \boldsymbol{v}^2\rangle + \frac{m_\alpha n_\alpha}{2}\nabla\langle \boldsymbol{v}^2\boldsymbol{v}\rangle \quad , \tag{3.1.0.38}$$

which further yields,

$$\frac{m_\alpha n_\alpha}{2}\frac{\partial}{\partial t}\langle \boldsymbol{v}^2\rangle + \frac{m_\alpha n_\alpha}{2}\nabla\langle \boldsymbol{v}^2\boldsymbol{v}\rangle + q_\alpha n_\alpha\boldsymbol{u}_\alpha\boldsymbol{E} = \frac{m_\alpha}{2}\int \boldsymbol{v}^2\left(\frac{\partial f_\alpha}{\partial t}\right)_c d\boldsymbol{v} \quad . \tag{3.1.0.39}$$

Separating term one of equation 3.1.0.38 into the mean particle velocity $\boldsymbol{u}_\alpha$ and a stochastic part can be used to obtain the following,

(3.1.0.40)
$$\frac{m_\alpha n_\alpha}{2}\frac{\partial}{\partial t}\langle \boldsymbol{v}^2\rangle = \frac{m_\alpha n_\alpha}{2}\frac{\partial}{\partial t}\langle(\boldsymbol{u}_\alpha+\boldsymbol{w})^2\rangle = \frac{m_\alpha n_\alpha}{2}\frac{\partial}{\partial t}\boldsymbol{u}_\alpha^2 + \frac{m_\alpha n_\alpha}{2}\frac{\partial}{\partial t}\boldsymbol{w}^2 = \frac{m_\alpha n_\alpha}{2}\frac{\partial}{\partial t}\boldsymbol{u}_\alpha^2 + \frac{3}{2}\frac{\partial}{\partial t}n_\alpha T_\alpha \quad .$$

Inserting expression (3.1.0.40) in equation (3.1.0.37) yields the following expression,

(3.1.0.41)
$$\frac{\partial}{\partial t}\left(\frac{m_\alpha n_\alpha}{2}\boldsymbol{u}_\alpha^2 + \frac{3}{2}n_\alpha T_\alpha\right) + \frac{m_\alpha n_\alpha}{2}\nabla\langle \boldsymbol{v}^2\boldsymbol{v}\rangle - q_\alpha n_\alpha \boldsymbol{u}_\alpha \boldsymbol{E} = \frac{m_\alpha}{2}\int \boldsymbol{v}^2\left(\frac{\partial f}{\partial t}\right)_c d\boldsymbol{v} \quad .$$

The right-hand side can be written as,

(3.1.0.42)
$$\frac{m_\alpha}{2}\int \boldsymbol{v}^2\left(\frac{\partial f}{\partial t}\right)_c d\boldsymbol{v} = Q_{\mathrm{ie}} + \boldsymbol{u}_\alpha\cdot\boldsymbol{R}_{\mathrm{ie}} + S_{\mathrm{e},\alpha} \quad ,$$

where $S_{\mathrm{e},\alpha}$ is the energy loss caused by collisions on neutrals, and $\boldsymbol{R}_{\mathrm{e,i}}$ is the friction. Furthermore, Q_{ie} gives a quantity for the amount of heat transferred from electrons to ions via collisions. This simply reads as,

(3.1.0.43)
$$Q_{\mathrm{ie}} = \frac{3m_{\mathrm{e}}n_{\mathrm{e}}}{m_{\mathrm{i}}\tau_e}(T_{\mathrm{e}} - T_{\mathrm{e}}) \quad .$$

Assuming the plasma to be free of fluxes gives $Q_{\mathrm{ie}} = -Q_{\mathrm{ie}}$. An equation system is formulated by inserting Q_{ie} and Q_{ie} into (3.1.0.42). Thus, the right-hand side of energy balance equation (3.1.0.41) has an expression for the electrons and the ions. A separate electron and ion energy balance equation is the result of the following:

(3.1.0.44)
$$\frac{\partial}{\partial t}\left(\frac{m_{\mathrm{e}}n_{\mathrm{e}}}{2}\boldsymbol{u}_{\mathrm{e}}^2 + \frac{3}{2}n_{\mathrm{e}}T_{\mathrm{e}}\right) + \frac{m_{\mathrm{e}}n_{\mathrm{e}}}{2}\nabla\langle \boldsymbol{v}^2\boldsymbol{v}\rangle - en_{\mathrm{e}}\boldsymbol{u}_{\mathrm{e}}\boldsymbol{E} = Q_{\mathrm{ie}} + \boldsymbol{u}_{\mathrm{e}}\cdot\boldsymbol{R}_{\mathrm{ie}} + \boldsymbol{S}_{\mathrm{e,e}}$$

(3.1.0.45)
$$\frac{\partial}{\partial t}\left(\frac{m_{\mathrm{i}}n_{\mathrm{i}}}{2}\boldsymbol{u}_{\mathrm{i}}^2 + \frac{3}{2}n_{\mathrm{i}}T_{\mathrm{i}}\right) + \frac{m_{\mathrm{i}}n_{\mathrm{i}}}{2}\nabla\langle \boldsymbol{v}^2\boldsymbol{v}\rangle - Zen_{\mathrm{i}}\boldsymbol{u}_{\mathrm{i}}\boldsymbol{E} = Q_{\mathrm{ei}} + \boldsymbol{u}_{\mathrm{i}}\cdot\boldsymbol{R}_{\mathrm{ie}} + \boldsymbol{S}_{\mathrm{e,i}} \quad .$$

A combined energy balance equation for the electrons and ions reads

(3.1.0.46)
$$\frac{\partial}{\partial t}\left(\frac{m_\alpha n_\alpha}{2}\boldsymbol{u}_\alpha^2 + \frac{3}{2}n_\alpha T_\alpha\right) + \frac{m_\alpha n_\alpha}{2}\nabla\langle \boldsymbol{v}^2\boldsymbol{v}\rangle - q_\alpha n_\alpha \boldsymbol{u}_\alpha \boldsymbol{E} = Q_{\alpha\beta} + \boldsymbol{u}_\alpha\cdot\boldsymbol{R}_{\mathrm{ie}} + \boldsymbol{S}_{\mathrm{in}}$$

The full set of fluid equations consists of the continuity equation, the equation of motion, and the energy balance equation:

(3.1.0.47)
$$\boxed{\frac{\partial n_\alpha}{\partial t} + \nabla\cdot(n_\alpha \boldsymbol{u}_\alpha) = S_{\mathrm{i}}}$$

(3.1.0.48)
$$\boxed{m_\alpha n_\alpha \frac{\partial \boldsymbol{u}_\alpha}{\partial t} + m_\alpha n_\alpha \nabla\cdot(\boldsymbol{u}_\alpha\boldsymbol{u}_\alpha + \boldsymbol{\pi}_\alpha) = q_\alpha n_\alpha(\boldsymbol{E} + \boldsymbol{u}_\alpha\times\boldsymbol{B}) - \nabla\cdot\boldsymbol{p}_\alpha + \boldsymbol{R}_{\mathrm{ei}} + \boldsymbol{S}_{\mathrm{m}}}$$

(3.1.0.49)
$$\boxed{\frac{\partial}{\partial t}\left(\frac{m_\alpha n_\alpha}{2}\boldsymbol{u}_\alpha^2 + \frac{3}{2}n_\alpha T_\alpha\right) + \frac{m_\alpha n_\alpha}{2}\nabla\langle \boldsymbol{v}^2\boldsymbol{v}\rangle - q_\alpha n_\alpha \boldsymbol{u}_\alpha \boldsymbol{E} = Q_{\alpha\beta} + \boldsymbol{u}_\alpha\cdot\boldsymbol{R}_{\mathrm{ie}} + \boldsymbol{S}_{\mathrm{in}}}$$

3.2 Derivation of the full EMC3-EIRENE model

The previous section presented the full derivation of a set of fluid equations from the Vlasov equation. With these, a plasma is described in terms of its density n, momentum $m\boldsymbol{u}$, and temperature T. A set of differential equations is formed that can only be solved through approximating higher-order moments (viscosity tensor π and heat flux $\boldsymbol{q}$) using gradients of lower ones.
For EMC3, the plasma is assumed to be in a stationary state. Time derivatives drop out of the set of fluid equations. Additionally, the plasma is assumed to be quasi-neutral $n_\mathrm{e} = n_\mathrm{i}$ and free of fluxes.

(3.2.0.1) time independent (stationary): $\dfrac{\partial}{\partial t} = 0$

(3.2.0.2) quasi-neutral: $n_\mathrm{e} = n_\mathrm{i}$

(3.2.0.3) flow-free plasma: $\boldsymbol{j} \equiv 0,\ \boldsymbol{u}_\mathrm{e} = \boldsymbol{u}_\mathrm{i} = \boldsymbol{u}$.

These assumptions are exemplary applied to the continuity equation (3.1.0.16) to quantify the importance regarding the EMC3 model. The transport is separated into the parallel (to $\boldsymbol{B}$, along $\hat{\mathbf{e}}_\parallel$) and perpendicular (to $\boldsymbol{B}$, along $\hat{\mathbf{e}}_\perp$) direction, because the magnetic field $\boldsymbol{B}$ is a superposition from the toroidal and poloidal magnetic field. The relation,

(3.2.0.4) $$\hat{\mathbf{e}}_\perp \hat{\mathbf{e}}_\perp = \boldsymbol{I} - \hat{\mathbf{e}}_\parallel \hat{\mathbf{e}}_\parallel \quad ,$$

is found, where $\boldsymbol{I}$ is the unity tensor. Using these assumptions on the continuity equation (3.1.0.16) yields,

$$\begin{aligned}
\cancelto{0}{\frac{\partial n}{\partial t}} + \nabla\cdot(n\boldsymbol{u}) &= S_\mathrm{i} \\
\nabla\cdot(\boldsymbol{I}\cdot n\boldsymbol{u}) &= S_\mathrm{i} \\
\nabla\cdot\left(\hat{\mathbf{e}}_\parallel\hat{\mathbf{e}}_\parallel\cdot n\boldsymbol{u} + \hat{\mathbf{e}}_\perp\hat{\mathbf{e}}_\perp\right) &= S_\mathrm{i} \\
\nabla\cdot\left(\hat{\mathbf{e}}_\parallel n u_\parallel - D\hat{\mathbf{e}}_\perp\hat{\mathbf{e}}_\perp\cdot\nabla n\right) &= S_\mathrm{i} \\
\nabla\cdot\left[n u_\parallel\hat{\mathbf{e}}_\parallel - D_\perp\nabla_\perp n\right] &= S_\mathrm{i} \quad ,
\end{aligned} \tag{3.2.0.5}$$

the first Braginskii equation. Here, transport effects are approximated with transport coefficients such as the perpendicular diffusion $D_\perp$.
Coming from the equation of motion (3.1.0.35), one finds the stationary momentum balance equation ($\boldsymbol{j} = 0$ is assumed, see (3.2.0.3)),

(3.2.0.6) $$m_\alpha n\nabla\cdot(\boldsymbol{u}\boldsymbol{u} + \boldsymbol{\pi}_\alpha) = q_\alpha n(\boldsymbol{E} + \boldsymbol{u}\times\boldsymbol{B}) - \nabla\cdot\boldsymbol{p}_\alpha + \boldsymbol{R}_\mathrm{ei} + \boldsymbol{S}_\mathrm{m} \quad .$$

Separating the electrons and ions' momentum balance equation gives an equation system, which must then be solved. Therefore, the momentum transfer to the velocity $u_\parallel$, $\boldsymbol{\pi}_\alpha$ is approximated. Here, $\boldsymbol{\pi}_\alpha$ is split into diffusive parallel $\eta_\parallel$ and diffuse perpendicular $\eta_\perp$ components,

(3.2.0.7) $$\pi_\parallel = -\eta_\parallel\frac{\partial u_\parallel}{\partial r_\parallel} \quad , \quad \pi_\perp = -\eta_\perp\frac{\partial u_\parallel}{\partial r_\perp}$$

A plasma with approximately the same electron and ion temperatures has a viscosity dominated by ions, the index α for the viscosity tensor π drops out. Furthermore, the electron mass is neglected because the $m_e << m_i$. The friction forces between electrons and ions can be neglected as well. Since the plasma is assumed to be flux free $\boldsymbol{j} = 0$, the electric field cancels out $\boldsymbol{E} = \eta_R \boldsymbol{j} = 0$. One finally obtains the second Braginskii equation,

$$\nabla \cdot \left[m_i n u_\parallel u_\parallel \hat{\mathbf{e}}_\parallel - \eta_\parallel \nabla_\parallel u_\parallel - D_\perp \nabla_\perp \left(m_i n u_\parallel \right) \right] = -\hat{\mathbf{e}}_\parallel \cdot \nabla p + S_m \quad . \tag{3.2.0.8}$$

The unity vectors $\hat{\mathbf{e}}_\parallel$ and $\hat{\mathbf{e}}_\perp$ are used for the continuity equation, as previously demonstrated, to separate the transport into parallel and perpendicular components (see equation (3.2.0.6)). The third Braginskii equation is found again by separating the parallel from the perpendicular component. However, first an expression for $\langle \boldsymbol{v}^2 \boldsymbol{v} \rangle$ must be found; $\langle \boldsymbol{v}^2 \boldsymbol{v} \rangle$ of (3.1.0.46) can be rewritten as follows,

$$\langle \boldsymbol{v}^2 \boldsymbol{v} \rangle = \langle (\boldsymbol{u} + \boldsymbol{w}^2)(\boldsymbol{u} + \boldsymbol{w}) \rangle \tag{3.2.0.9}$$

$$= \langle (\boldsymbol{u}^2 + \boldsymbol{w}^2)\boldsymbol{u} \rangle + 2\langle (\boldsymbol{u} \cdot \boldsymbol{w})\boldsymbol{u} \rangle + \langle (2\boldsymbol{u} \cdot \boldsymbol{w} + \boldsymbol{w}^2)\boldsymbol{w} \rangle + \langle \boldsymbol{u}^2 \boldsymbol{w} \rangle \tag{3.2.0.10}$$

Terms with a mean thermal velocity $\langle \boldsymbol{w} \rangle$ simply cancel out (see equation (3.1.0.30)). This yields,

$$\langle (\boldsymbol{u}^2 + \boldsymbol{w}^2)\boldsymbol{u} \rangle + \langle (2\boldsymbol{u} \cdot \boldsymbol{w} + \boldsymbol{w}^2)\boldsymbol{w} \rangle = \boldsymbol{u}^2 \boldsymbol{u} + \boldsymbol{u}\langle \boldsymbol{w}^2 \rangle + 2\boldsymbol{u}\langle \boldsymbol{w}\boldsymbol{w} \rangle + \langle \boldsymbol{w}^2 \boldsymbol{w} \rangle \quad . \tag{3.2.0.11}$$

where $\langle \boldsymbol{w}^2 \rangle$ is the plasma pressure $\frac{3p_\alpha}{nm_i}$ and $\langle \boldsymbol{w}\boldsymbol{w} \rangle$ is the stress tensor $\frac{\boldsymbol{P}_\alpha}{nm\alpha} = \boldsymbol{u}\frac{p_\alpha}{nm_\alpha} + \boldsymbol{u}\frac{\boldsymbol{\pi}_\alpha}{nm_\alpha}$. The assumptions about quasi neutral plasma and $\boldsymbol{j} = 0$ are already applied. Thus, one finds,

$$\boldsymbol{u}^2 \boldsymbol{u} + \boldsymbol{u}\langle \boldsymbol{w}^2 \rangle + 2\boldsymbol{u}\langle \boldsymbol{w}\boldsymbol{w} \rangle + \langle \boldsymbol{w}^2 \boldsymbol{w} \rangle = \boldsymbol{u}\left(\boldsymbol{u}^2 + 5\frac{p_\alpha}{nm_\alpha} \right) + 2\frac{\boldsymbol{u}\boldsymbol{\pi}_\alpha}{nm_\alpha} + \frac{\boldsymbol{q}_\alpha}{nm_\alpha} \quad . \tag{3.2.0.12}$$

Here, $\langle \boldsymbol{w}^2 \boldsymbol{w} \rangle = \frac{\boldsymbol{q}_\alpha}{nm_\alpha}$ is used, including the definition of the heat flux density,

$$\boldsymbol{q}_\alpha = -\kappa_{\alpha,\parallel} \hat{\mathbf{e}}_\parallel \hat{\mathbf{e}}_\parallel \cdot \nabla T_\alpha - \chi_{\alpha,\perp} n \hat{\mathbf{e}}_\perp \hat{\mathbf{e}}_\perp \cdot \nabla T_\alpha \tag{3.2.0.13}$$

$$= -\kappa_{\alpha,\parallel} \nabla_\parallel T_\alpha - \chi_{\alpha,\perp} n \nabla_\perp T_\alpha \tag{3.2.0.14}$$

The parallel heat diffusion coefficient $\kappa_{\alpha,\parallel}$ is assumed to be classical, whereas the perpendicular heat diffusion coefficient $\chi_{\alpha,\perp}$ is assumed to be anomal. With the assumption of stationary plasma, equation (3.1.0.46) then reads as follows,

$$\nabla \cdot \left(\frac{5}{2} n T_\alpha \boldsymbol{u} + \boldsymbol{q}_\alpha \right) + \nabla \cdot \left(\frac{1}{2} n m_\alpha \boldsymbol{u}^2 \boldsymbol{u} + \boldsymbol{u}\boldsymbol{\pi}_\alpha \right) - q_\alpha n_\alpha \boldsymbol{u}_\alpha \boldsymbol{E} = Q_{\alpha\beta} + \boldsymbol{u}_\alpha \cdot \boldsymbol{R}_{ie} + \boldsymbol{S}_{in} \tag{3.2.0.15}$$

Friction forces can again be neglected; hence, $\boldsymbol{u}_\alpha \cdot \boldsymbol{R}_{ie}$ simply cancels out. The electric field cancels out again because $\boldsymbol{E} = \eta_R \boldsymbol{j} = 0$. Finally, the first and second terms on the left-hand hand side of equation (3.2.0.15) can be compared regarding their order of magnitude. The adiabatic cooling $m_\alpha n/2 \boldsymbol{u}^2 \boldsymbol{u}$ is negligible with respect to $5/2 n T_\alpha \boldsymbol{u}$. Plasma particles are only able to reach velocities below the speed of sound $u_\alpha \leq c_{s,i}$ because of the choice of boundary conditions, which are discussed in the next section. Inserting equations (3.1.0.43) and (3.2.0.12) into (3.2.0.15) yields,

$$\nabla \cdot \left(\frac{5}{2} n T_\alpha \boldsymbol{u} + \boldsymbol{q}_\alpha \right) = \xi \frac{3 m_e n_e}{m_i \tau_{ee}} (T_e - T_i) + S_{e,\alpha} \begin{cases} +1 \text{ , for } \alpha = i \\ -1 \text{ , for } \alpha = e \end{cases} , \tag{3.2.0.16}$$

The scheme shown in equation (3.2.0.6) is used to split the parallel and perpendicular component of $\boldsymbol{u}$, obtaining

$$\nabla\cdot\left[\frac{5}{2}nT_\alpha u_\parallel\hat{\mathbf{e}}_\parallel-\kappa_{\alpha\parallel}\nabla_\parallel T_\alpha-\frac{5}{2}T_\alpha D_\perp\nabla_\perp n-\chi_{\alpha\perp}n\nabla_\perp T_\alpha\right] \tag{3.2.0.17}$$
$$=\xi\frac{3m_\mathrm{e}n_\mathrm{e}}{m_\mathrm{i}\tau_\mathrm{ee}}(T_\mathrm{e}-T_\mathrm{i})+S_{\mathrm{e},\alpha}-\delta_{\alpha\mathrm{e}}S_{\mathrm{e,cool}}\quad,\quad\xi=\begin{cases}+1\text{ , for }\alpha=\mathrm{i}\\-1\text{ , for }\alpha=\mathrm{e}\end{cases},$$

The full set of EMC3 model equations, derived from a set of fluid equations, reads,

$$\boxed{\nabla\cdot\left[nu_\parallel\hat{\mathbf{e}}_\parallel-D_\perp\nabla_\perp n\right]=S_\mathrm{i}}\quad, \tag{3.2.0.18}$$

$$\boxed{\nabla\cdot\left[m_\mathrm{i}nu_\parallel u_\parallel\hat{\mathbf{e}}_\parallel-\eta_\parallel\nabla_\parallel u_\parallel-D_\perp\nabla_\perp\left(m_\mathrm{i}nu_\parallel\right)\right]=-\hat{\mathbf{e}}_\parallel\cdot\nabla p+S_\mathrm{m}}\quad, \tag{3.2.0.19}$$

$$\boxed{\nabla\cdot\left[\frac{5}{2}nT_\alpha u_\parallel\hat{\mathbf{e}}_\parallel-\kappa_{\alpha\parallel}\nabla_\parallel T_\alpha-\frac{5}{2}T_\alpha D_\perp\nabla_\perp n-\chi_{\alpha\perp}n\nabla_\perp T_\alpha\right]=\xi\frac{3m_\mathrm{e}n_\mathrm{e}}{m_\mathrm{i}\tau_\mathrm{ee}}(T_\mathrm{e}-T_\mathrm{i})+S_{\mathrm{e},\alpha}-\delta_{\alpha\mathrm{e}}S_{\mathrm{e,cool}}}\quad,$$

$$\xi=\begin{cases}+1\text{ , for }\alpha=\mathrm{i}\\-1\text{ , for }\alpha=\mathrm{e}\end{cases}\quad. \tag{3.2.0.20}$$

3.2.1 EMC3 impurity model

Interactions between neutrals, plasma electrons, and ions are treated by the source terms S_i, S_m, and $S_{\mathrm{e},\alpha}$, which are obtained from the EIRENE code. Impurities released from plasma-facing wall components cool the electrons through energy sinks $S_{\mathrm{e,cool}}$ appearing only in the electron energy balance. The attenuation effects on n_e caused by impurity ions are neglected (i.e., $n_\mathrm{e}=n_\mathrm{i}$), with the main ions i only. Reprocessing measurement results often depends on this information because effective charge states of plasma are often assumed to be equal to one. Thus, the present study applied a newly introduced postprocessing step to account for impurity effects within the plasma. Implemented standard impurity models use only a strong reduced parallel force balance model, rather than a full transport equation in the form of 3.2.0.8 supplemented by electrical, frictional, and thermal forces (which were canceled out between electrons and main plasma ions in (equation 3.2.0.8)) [14]. The parallel impurity force balance (species/charge state α) in EMC3 reads ($\hat{\mathbf{e}}_\parallel\cdot\nabla=\nabla_\parallel$, $p_\alpha=n_\alpha T_\alpha$)

$$0=-\hat{\mathbf{e}}_\parallel\cdot\nabla p_\alpha+Z_\alpha n_\alpha eE_\parallel+\frac{\mu_{\alpha i}}{\tau_{\alpha i}}n_\alpha(u_{i\parallel}-u_{\alpha\parallel})+\alpha_{\alpha e}n_\alpha\nabla_\parallel T_e+\beta_{\alpha i}n_\alpha\nabla_\parallel T_i+S_{\mathrm{m}\alpha}\quad, \tag{3.2.1.1}$$

with the pressure gradient force, electric force, frictional force, and electron and ion thermal force, respectively. The momentum source $S_{\mathrm{m}\alpha}$, which is caused by ionization and recombination with neighboring charge states as well as interactions of impurity ions α with any of the kinetically treated species in EIRENE, is neglected: $S_{\mathrm{m}\alpha}=0$. μ is the reduced mass, and the collision times

$\tau_{\alpha i}$ and electron-ion thermal force coefficients $\alpha_{\alpha e} = 0.71 Z_\alpha^2$ are again taken from Braginskii [8]. A low impurity concentration limit ($n_\alpha \ll n_i$) expression for the ion-ion thermal force coefficient $\beta_{\alpha i}$ is used, which was originally derived by S. Chapman [44], and later frequently employed as an approximation in tokamak and stellarator edge transport models [45],

$$\beta_{\alpha i} = -3\,\frac{1-\tilde{\mu}-5\sqrt{2}\,(Z_\alpha/Z_i)^2\,(1.1\tilde{\mu}^{5/2}-0.35\tilde{\mu}^{3/2})}{2.6-2\tilde{\mu}+5.4\tilde{\mu}^2}, \quad \tilde{\mu} = \frac{m_\alpha}{m_\alpha + m_\mathrm{i}} \quad . \tag{3.2.1.2}$$

Instead of the Poisson equation, a "plasma approximation" is applied to express the parallel electric field in (equation 3.2.1.1) through the (here strongly reduced) electron momentum balance (neglecting all terms containing the electron mass),

$$eE_\parallel = -\frac{1}{n_e}\nabla_\parallel p_e - \alpha_{ie}\nabla_\parallel T_e \quad . \tag{3.2.1.3}$$

Inserting this into (3.2.1.1) provides the explicit expression for the parallel impurity ion flow velocity $u_{\alpha\parallel}$ [14],

$$\begin{aligned} u_{\alpha\parallel} = u_{i\parallel} \quad &+ \quad \frac{\tau_{\alpha i}}{\mu_{\alpha i}}\left[(\beta_{\alpha i}-1)\nabla_\parallel T_i - \frac{Z_\alpha}{n_e}\nabla_\parallel p_e + (\alpha_{\alpha e} - Z_\alpha \alpha_{ie})\nabla_\parallel T_e\right] \\ &+ \quad \frac{\tau_{\alpha i}}{\mu_{\alpha i} n_\alpha} T_i \nabla_\parallel n_\alpha \quad . \end{aligned} \tag{3.2.1.4}$$

The first part on the right-hand side is denoted by $U_{\alpha\parallel}$ and the (binary) diffusion coefficient is introduced because of friction between the main ions and impurity ions $D^f_{\alpha\parallel} = \tau_{\alpha i} T_i/\mu_{\alpha i}$ a diffusion–advection expression for the parallel impurity ion flux Γ_α results in,

$$\Gamma_{\alpha\parallel} = n_\alpha u_{\alpha\parallel} = n_\alpha U_{\alpha\parallel} - D^f_{\alpha\parallel}\nabla_\parallel n_\alpha \quad . \tag{3.2.1.5}$$

Inserting (3.2.1.5) into (3.1.0.15) leads to an impurity continuity equation,

$$\nabla\cdot\left[n_\alpha U_{\alpha\parallel}\hat{\mathbf{e}}_\parallel - D^f_{\alpha\parallel}\nabla_\parallel n_\alpha - D_\perp \nabla_\perp n_\alpha\right] = S_\alpha \quad . \tag{3.2.1.6}$$

In addition, $T_\alpha = T_\mathrm{i}$ is assumed for all impurity species α, and each charge state is treated as a separate fluid. The (particle) source term S_α provides coupling between neighboring charge states due to ionization and recombination, and, for the single-charged impurity ion, the ionization rate from neutral impurity atoms. The latter are launched monoenergetically from target surfaces with a given release fraction, and then simply exponentially decay due to ionization into the plasma. An identity-preserving Lagrangian scheme is utilized for the transfer from neutral to ionized impurities (rather than resampling from volumetric neutral impurity sources), distinct from the current resampling coupling procedure for neutrals and molecules treated fully kinetically by EIRENE. In principle, no limitation exists on the number of impurity species (within the trace impurity transport model), as long as the concentration of impurities is limited by the assumption $n_\alpha \ll n_\mathrm{e}$ and inter-impurity effects (other than those in the source terms) can be neglected. Equation (3.2.1.6) for n_α is then coupled to the electron energy balance equation (3.2.0.17) of the main plasma though the cooling term $S_{\mathrm{e,cool}}$. A detailed discussion of impurity radiation and the resulting cooling effect on the energy balance equation (3.2.0.17) is given in [46].

3.2.2 Fokker-Planck form of the EMC3 model

The derived model equations for the EMC3 model (see equations (3.2.0.18), (3.2.0.19), and (3.2.0.20)) are of a type similar to the FPE. However, analytic solutions for the FPE are only found under special assumptions in a reduction in system complexity. This is clearly not possible for the problem at hand. A numerical treatment for the complexity of the W7-X and its 3D geometry is demanded. If one inserts the assumption concerning the parallel velocity $u_\parallel = u_{\parallel,\mathrm{c}} + \nabla D_\parallel$ into the continuity equation (3.2.0.18), one finds that,

$$\begin{aligned}\nabla\cdot\left[nu_\parallel\hat{\mathbf{e}}_\parallel - D_\perp\nabla_\perp n\right] &= \nabla\cdot\left[nu_\parallel u_{\parallel,\mathrm{c}}\hat{\mathbf{e}}_\parallel + nu_\parallel\nabla D_\parallel\hat{\mathbf{e}}_\parallel - D_\perp\nabla_\perp n\right]\\ &= \nabla\cdot\left[nu_\parallel - \nabla(\boldsymbol{D}n)\right]\\ &= \nabla\cdot\left[nu_{\parallel,\mathrm{c}} - \boldsymbol{D}\nabla n\right] = S_\mathrm{i}\quad . \end{aligned}\tag{3.2.2.1}$$

From here, a time derivative can be set to zero at the front of the equation, because the plasma is assumed to be in a stationary state. However, this brings the continuity rather close to an FPE-like equation,

$$\frac{\partial n}{\partial t} + \nabla\cdot\left[nu_{\parallel,\mathrm{c}} - \boldsymbol{D}\nabla n\right] = S_\mathrm{i}\quad ,\tag{3.2.2.2}$$

$$\Leftrightarrow \frac{\partial\mathscr{F}}{\partial t} + \nabla\cdot[\mathscr{F}\mathscr{U} - \boldsymbol{D}\nabla\mathscr{F}] = S\quad ,\tag{3.2.2.3}$$

where $\mathscr{U}$ is the convection and $\boldsymbol{D}$ is the diffusion tensor. Now, $\mathscr{F}$ represents the different plasma parameter because there are n, $u_\parallel$, T_e and T_i. Table 3.2 provides an overview. The FPE is originally used

Table (a) — Fokker-Planck equation

$\mathscr{F}$	$\mathscr{U}$	D	S
n	$\begin{pmatrix}0\\0\\u_\parallel\end{pmatrix}$	$\begin{pmatrix}D_\perp & 0 & 0\\ 0 & D_\perp & 0\\ 0 & 0 & D_\perp\end{pmatrix}$	S_i
$u_\parallel$	$\begin{pmatrix}-mD_\perp\hat{\boldsymbol{e}}_\perp\boldsymbol{\nabla}n\\ -mD_\perp\hat{\boldsymbol{e}}_\perp\boldsymbol{\nabla}n\\ mnu_\parallel\end{pmatrix}$	$\begin{pmatrix}mnD_\perp & 0 & 0\\ 0 & mnD_\perp & 0\\ 0 & 0 & \eta_\parallel\end{pmatrix}$	$-\hat{\boldsymbol{e}}_\perp\cdot\boldsymbol{\nabla}p + S_m$
T_α	$\begin{pmatrix}-5/2D_\perp\hat{\boldsymbol{e}}_\perp\\ -5/2D_\perp\hat{\boldsymbol{e}}_\perp\\ 5/2nu_\parallel\end{pmatrix}$	$\begin{pmatrix}n\chi_{\alpha\perp} & 0 & 0\\ 0 & n\chi_{\alpha\perp} & 0\\ 0 & 0 & \kappa_{\alpha\perp}\end{pmatrix}$	$\xi\dfrac{3m_\mathrm{i}n_\mathrm{e}}{m_\mathrm{e}\tau_\mathrm{ee}}(T_\mathrm{e}-T_\mathrm{i})$

Figure 3.2: Overview of the transport coefficients $\mathscr{U}$,$\mathscr{D}$, and plasma quantity $\mathscr{F}$ used in the FPE.

to describe the Brown motion of particles. A Markov process is used to connect the FPE (macroscopic description) to a microscopic system. Here, plasma quantities are a function of the time t and the spatial coordinate $\boldsymbol{\rho}$, which results in $\mathscr{F}(\boldsymbol{\rho},t)$. The probability of changing from state $(\boldsymbol{\rho},t)$ to $(\boldsymbol{\rho}^*,t+\tau)$

is then given by the probability of change $\mathscr{T}(\boldsymbol{\rho}, t|\boldsymbol{\rho}^*, t+\tau)$. A spatial displacement lies between $\boldsymbol{\rho}$ and $\boldsymbol{\rho}^*$, $\boldsymbol{\rho} = \boldsymbol{\rho}^* + \Delta\boldsymbol{\rho}$. State $\mathscr{F}(\boldsymbol{\rho}^*, t+\tau)$ is then given by,

$$\mathscr{F}(\boldsymbol{\rho}^*, t+\tau) = \int \mathscr{T}(\boldsymbol{\rho}, t|\boldsymbol{\rho}^*, t+\tau)\mathscr{F}(\boldsymbol{\rho}, t+\tau)d\boldsymbol{\rho} \tag{3.2.2.4}$$

Next, a Taylor expansion around $\Delta\boldsymbol{\rho}$ and τ yields,

$$\frac{\partial \mathscr{F}}{\partial t} + \nabla\cdot\left[\mathscr{F}\frac{1}{\tau}\int \Delta\rho\mathscr{T}(\boldsymbol{\rho}, t|\boldsymbol{\rho}^*, t+\tau)d\Delta\rho - \nabla\cdot\left(\mathscr{F}\frac{1}{2\tau}\int \Delta\rho\Delta\rho\mathscr{T}(\boldsymbol{\rho}, t|\boldsymbol{\rho}^*, t+\tau)d\Delta\rho\right)\right] + \frac{\mathscr{O}(\tau^2)}{\tau} = 0 \tag{3.2.2.5}$$

Equation (3.2.2.5) has the same FPE-like form as equation (3.2.2.3). A coefficient comparison between these gives,

$$\mathscr{U} = \nabla\cdot\frac{1}{\tau}\int \Delta\rho\mathscr{T}(\boldsymbol{\rho}, t|\boldsymbol{\rho}^*, t+\tau)d\Delta\rho \tag{3.2.2.6}$$

$$\boldsymbol{D} = \frac{1}{2\tau}\int \Delta\rho\Delta\rho\mathscr{T}(\boldsymbol{\rho}, t|\boldsymbol{\rho}^*, t+\tau)d\Delta\rho \tag{3.2.2.7}$$

The error term $\frac{\mathscr{O}(\tau^2)}{\tau}$ of the Taylor expansion was neglected. Equation (3.2.2.4) then gives a linear approximation around τ for the FPE (3.2.2.3). Hence, the Markov process connects macroscopic transport coefficients such as $\mathscr{U}$ and D to the microscopic process. Macroscopic quantities $\mathscr{F}$, $\mathscr{U}$, D, and $\mathscr{T}$ depend on the microscopic quantities $\boldsymbol{\rho}$ and $\Delta\boldsymbol{\rho}$. Two distinct coordinate systems, macroscopic and microscopic, are applied to these quantities. Following equation (3.2.2.3), $\nabla\cdot\boldsymbol{D}$ must be considered. Using the definition of the unity tensor $\boldsymbol{I}$ from equation (3.2.0.4) yields,

$$\nabla\cdot\boldsymbol{D} = \nabla\cdot\left[D\hat{\mathbf{e}}_\parallel\hat{\mathbf{e}}_\parallel + D_\perp\left(\boldsymbol{I} - \hat{\mathbf{e}}_\parallel\hat{\mathbf{e}}_\parallel\right)\right] \tag{3.2.2.8}$$

$$= \nabla D_\perp + \hat{\mathbf{e}}_\parallel\hat{\mathbf{e}}_\parallel\cdot\nabla(D_\parallel - D_\perp) + \hat{\mathbf{e}}_\parallel(D_\parallel - D_\perp)\nabla\cdot\hat{\mathbf{e}}_\parallel + (D_\parallel - D_\perp)(\hat{\mathbf{e}}_\parallel\cdot\nabla)\hat{\mathbf{e}}_\parallel \quad . \tag{3.2.2.9}$$

The first perpendicular vector is selected as $\hat{\mathbf{e}}^1_\perp = -\frac{(\hat{\mathbf{e}}_\parallel\cdot\nabla)\hat{\mathbf{e}}_\parallel}{|(\hat{\mathbf{e}}_\parallel\cdot\nabla)\hat{\mathbf{e}}_\parallel|}$, based on the last term of equation (3.2.2.9). The second perpendicular direction follows from the cross product between $\hat{\mathbf{e}}_\parallel$ and $\hat{\mathbf{e}}^1_\perp$, $\hat{\mathbf{e}}^2_\perp = \hat{\mathbf{e}}_\parallel\times\hat{\mathbf{e}}^1_\perp$, while $\hat{\mathbf{e}}_\parallel$ remains unchanged. An overview of the unity vectors is presented in Figure 3.3. Transport coefficients $\boldsymbol{D}$ and $\mathscr{U}$ change because of the change in the coordinate system,

$$\boldsymbol{D} = \begin{pmatrix} D_\perp & 0 & 0 \\ 0 & D_\perp & 0 \\ 0 & 0 & D_\parallel \end{pmatrix} \quad , \quad \mathscr{U}^* = \mathscr{U} + \nabla\boldsymbol{D} \quad , \tag{3.2.2.10}$$

$$\mathscr{U}^* = \begin{pmatrix} \hat{\mathbf{e}}^1_\perp\cdot(\mathscr{U} + \nabla D_\perp) - (D_\parallel - D_\perp)\left|(\hat{\mathbf{e}}_\parallel\cdot\nabla)\hat{\mathbf{e}}_\parallel\right| \\ \hat{\mathbf{e}}^2_\perp\cdot(\mathscr{U} + \nabla D_\perp) \\ \hat{\mathbf{e}}_\parallel(\mathscr{U} + \nabla D_\parallel) + (D_\parallel - D_\perp)\nabla\cdot\hat{\mathbf{e}}_\parallel \end{pmatrix} \quad . \tag{3.2.2.11}$$

Then, equation (3.2.2.4) can be solved using the Ansatz equation,

$$\mathscr{T}(\boldsymbol{\rho}, \tau) = \frac{1}{8}\sum_{m,n,l=1}^{2}\delta(\rho_\parallel - \rho^*_{\parallel,m}(\tau))\delta(\rho^1_\perp - \rho^{*1}_{\perp,n}(\tau))\delta(\rho^2_\perp - \rho^{*2}_{\perp,l}(\tau)) \quad . \tag{3.2.2.12}$$

This Ansatz equation contains a spatial displacement δ along $\hat{\mathbf{e}}_\parallel, \hat{\mathbf{e}}^1_\perp$, and $\hat{\mathbf{e}}^2_\perp$. Thus, $\rho^*_{\parallel,m}$ is the particle's location after a time τ and the spatial displacement $\delta(\rho_\parallel - \rho^*_{\parallel,m}(\tau))$ in the direction of $\hat{\mathbf{e}}_\parallel$. All off-diagonal elements cancel out in their orthogonal coordinates [47]. The coordinates $\rho^{\{1,2\}}_{\{\parallel,\perp\}}$ are defined to obey the coordinate system constructed from the vectors $\hat{\mathbf{e}}_\parallel, \hat{\mathbf{e}}^1_\perp$, and $\hat{\mathbf{e}}^2_\perp$. Figure 3.3 presents an overview of a single Monte Carlo step with the spatial range of $\Delta\boldsymbol{\rho}$. The simplest case occurs for

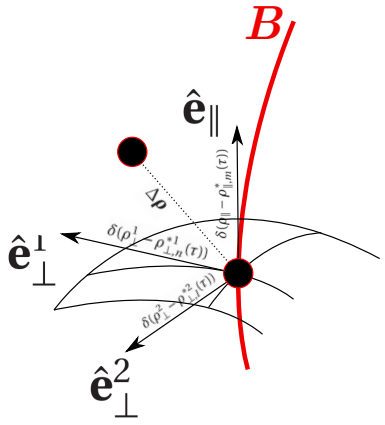

Figure 3.3: A single Monte Carlo step with a spatial range of $\Delta\boldsymbol{\rho}$ in the coordinate system constructed by $\hat{\mathbf{e}}_\parallel, \hat{\mathbf{e}}^1_\perp$, and $\hat{\mathbf{e}}^2_\perp$.

$m, n, n = 2$,

$$\begin{aligned}
\rho_\parallel &= \mathscr{U}^*_{\rho_\parallel}\tau \pm \sqrt{2D_\parallel\tau} \\
\rho^1_\perp &= \mathscr{U}^*_{\rho^1_\perp}\tau \pm \sqrt{2D_\perp\tau} \\
\rho^2_\perp &= \mathscr{U}^*_{\rho^2_\perp}\tau \pm \sqrt{2D_\perp\tau}
\end{aligned} \tag{3.2.2.13}$$

Thus, the simplest Monte Carlo step is given by the sum of $\rho_\parallel, \rho^1_\perp$ and $\rho^2_\perp$ from equation 3.2.2.13,

$$\Delta\boldsymbol{\rho} = \rho_\parallel + \rho^1_\perp + \rho^2_\perp \tag{3.2.2.14}$$

$$= \mathscr{U}^*_{\rho_\parallel}\tau \pm \sqrt{2D_\parallel\tau} + \mathscr{U}^*_{\rho^1_\perp}\tau \pm \sqrt{2D_\perp\tau} + \mathscr{U}^*_{\rho^2_\perp}\tau \pm \sqrt{2D_\perp\tau} \quad . \tag{3.2.2.15}$$

Combining equations (3.2.2.11) and (3.2.2.15) yields,

$$\begin{aligned}
\Delta\boldsymbol{\rho} = &\left[\mathscr{U} + \nabla D_\perp + \hat{\mathbf{e}}_\parallel\hat{\mathbf{e}}_\parallel\cdot\nabla(D_\parallel - D_\perp) + \hat{\mathbf{e}}_\parallel(D_\parallel - D_\perp)\nabla\cdot\hat{\mathbf{e}}_\parallel + (D_\parallel - D_\perp)(\hat{\mathbf{e}}_\parallel\cdot\nabla)\hat{\mathbf{e}}_\parallel\right]\tau \\
&+ \xi_{\rho_\parallel}\sqrt{2D_\parallel\tau} + \xi_{\rho^1_\perp}\sqrt{2D_\perp\tau} + \xi_{\rho^2_\perp}\sqrt{2D_\perp\tau} \quad .
\end{aligned} \tag{3.2.2.16}$$

Independent randomly generated variables $\xi_{\rho_\parallel}$, $\xi_{\rho^1_\perp}$, and $\xi_{\rho^2_\perp}$ are introduced, each having only two discrete values: –1 and +1. Thus the followed fluid parcels undergo a stochastic random walk. Sample fluid parcels with an assigned weight w_j (given by the source volume) are represented by the described stochastic process and its single trajectories (see Figure 3.3).These sample fluids are often referred to as Monte Carlo particles. These particles are then traced until their trajectory ends

at target plates of the first wall. The sampling of many trajectories provides an approximation of the distribution function $\mathscr{F}$. A track length estimator is used to obtain a measurement for the length l_{ji} a Monte Carlo particle j travels in a cell i . The distribution function $\mathscr{F}_i$ for cell i is then calculated using,

$$\mathscr{F}_i = \frac{1}{V_i} \sum_{j=1}^{N_{\mathrm{MC}} \text{ in each cell } i} w_j \frac{l_{ji}}{v_{ji}} = \frac{1}{V_i} \sum_{j=1}^{N_{\mathrm{MC}} \text{ in each cell } i} w_j \tau_{ji} \quad , \tag{3.2.2.17}$$

with the cell volume V_i, the statistical weight of the jth Monte Carlo particle, the particle's velocity v_{ji}, and the time spent by the particle in cell i τ_{ji}. The sum is taken over all particles that pass through cell i. Thus, the total number of Monte Carlo particles within cell i is given by $N_{\mathrm{MC}}(i)$. However, an average of each $\mathscr{F}_i$ leads to the overall quantity $\mathscr{F}$.

The grid on which the Monte Carlo particles are summed to $\mathscr{F}_i$ differs from that used to discretize the magnetic field $\boldsymbol{B}$. Monte Carlo particles are summed on the so-called "physical grid" because this grid is used to assess physical plasma values. The construction of the magnetic grid is discussed in the section 3.4.

To quantify the quality of the approximation of $\mathscr{F}_i$, a relaxation factor F_{relax} is defined. This connects step k with step $k-1$ in a stochastic process of k steps, yielding,

$$\mathscr{F}_i = F_{\mathrm{relax}} \mathscr{F}_i^{k-1} + F_{\mathrm{relax}} \mathscr{F}_i^{k} \quad . \tag{3.2.2.18}$$

Thus, a requirement for the EMC3 code to converge is a slight change in $\mathscr{F}_i$, which is defined as,

$$\text{relative change} = \frac{\sum_i \left| \mathscr{F}_i^{k-1} - \mathscr{F}_i \right| V_i}{\sum_i \left(\mathscr{F}_i^{k-1} - \mathscr{F}_i \right) V_i} * 100\% \tag{3.2.2.19}$$

If the relative change drops close to 1%, this simulation can be considered to have converged.

3.3 EMC3-EIRENE interface

For the numerical solution of the discussed EMC3-EIRENE model equations (3.2.0.5), (3.2.0.8), and (3.2.0.17) information is required about the source terms S_{i}, S_{m}, and $S_{\mathrm{e},\alpha}$ (stated on the right hand side). As previously mentioned, these source terms are supplied by the Monte Carlo neutral particle code EIRENE [15]. However, a primary distribution of neutral particle sources is required to trace neutral particles and calculate various collision processes with the background plasma. The background plasma is supplied by EMC3 on a computational domain that differs from the EIRENE computational domain. EIRENE operates on a grid wider and deeper than the EMC3 grid.

The source terms and strength of the neutral particles are determined by the recycling process of ions in plasma-facing wall components; neutral particles are then traced using EIRENE. A proportion of recycled neutral particles are fully ionized in the SOL because of sufficient high temperatures and must be treated as impurity ions in the background plasma. Thus, a cooling term $S_{\mathrm{e},\alpha}$, obtained for EMC3 from EIRENE, quantifies the energy loss caused by radiation on impurity particles. Volumetric

sources from equations (3.2.0.5), (3.2.0.8), and (3.2.0.17) are determined using EIRENE and input to the EMC3 model/code. EMC3 and EIRENE cover the complete SOL with their own computational grid. However, the computational domain of EIRENE is further extended into the core region (behind the SOL of the plasma). All neutral particles that are ionized in this small overlap (between the EIRENE grid and core region) tend to contribute to a particle influx into the SOL region of the EMC3 computational domain. EMC3 does not supply model equations to describe dynamics in the core plasma. Hence, the LCFS is the inner interface between the EMC3 and EIRENE computational domain. The flux of particles leaving the SOL is set as equal to the flux of particles entering it at this inner boundary (a detailed discussion can be found in section 3.4). In other words, the plasma parameters at the inner boundary are chosen such that all neutral particles will ionize at the position of the SOL.
The EMC3 code is separated into several modules that calculate the plasma parameters of the EMC3 model equations discussed in section 3.2. Modules are executed in an iterative mode until convergence for calculated plasma parameters is obtained in the eye of the user. Experience with the code plays a key role here.

3.4 Aspects of full 3D EMC3-EIRENE simulations

The EMC3 code consists of three modules for the calculation of individual plasma parameters, such as the electron and ion temperatures $T_{\mathrm{e,i}}$, electron density n_{e}, and plasma particle velocity $u_{\mathrm{i},\parallel}$ parallel to the magnetic field $\boldsymbol{B}$ [46]. Plasma parameters are evaluated on a computational grid, which is based on a reconstruction of magnetic field lines.
Subsection 2.1.1 introduced different operational phases of the W7-X that differ in their key parameters because of different heat exhausting concepts. The major difference is the magnetic configuration of OP1.1 and OP1.2 (see Figure 2.4). Thus, OP1.1 and OP1.2 demand different computational grids because their magnetic configurations differ significantly. In this section, the machine setup for OP1.1 is used as an example for a discussion of the system boundaries. Limiting surfaces defining the LCFS are approximated in the computational grid by "cutting out" all cells that lie within the geometry of these targets. This is indicated by the red shaded region in Figure 3.4, which shows the limiter's implementation within the computational grid. Because the five-fold and up-down symmetry of the W7-X, this computational grid covers a toroidal spread of $\Delta\varphi = \frac{1}{2} \cdot \frac{360^\circ}{5} = 36^\circ$, which is sufficient for EMC3-EIRENE simulations to assess the W7-X's plasma parameters. Boundary conditions are necessary for solving any differential equation on a computational grid, which extends to EMC3 model equations. The EMC3 model is capable of treating several types of boundary conditions (see Figure 3.5). These are **inner-**, **outer-**, and **target boundary conditions**.

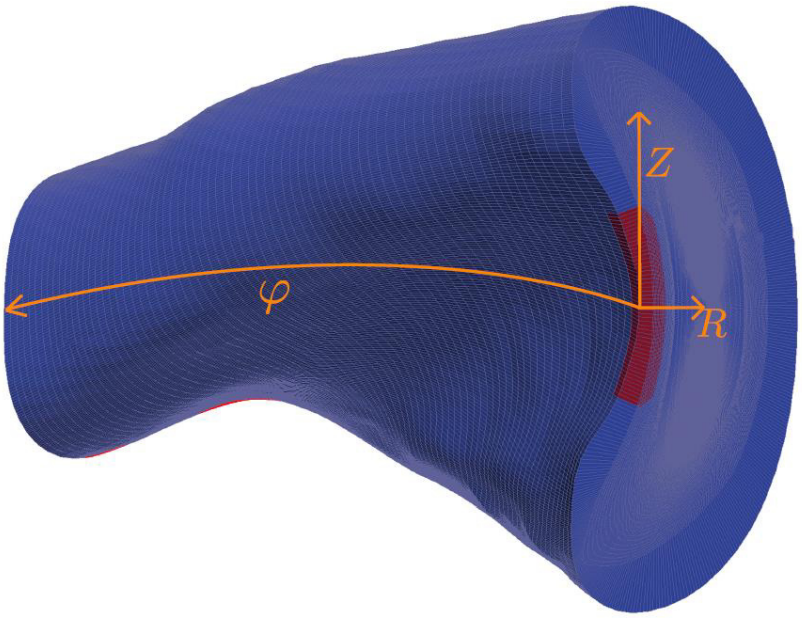

Figure 3.4: Schematic of the computational grid (blue-shaded region) with the implementation of the limiting surface of the limiter (red-shaded region). The coordinate system is denoted by R, φ, and Z (orange).

Inner boundary conditions:
At the inner boundary, a particle influx from the core plasma is prescribed. This influx can be separated and characterized in different flux types. The neutral particle influx from the main plasma is obtained from EIRENE because the computational grid of EIRENE is extended further into the core plasma.

- $\Gamma^{p}_{\text{in}} \equiv$ *Particle* influx from main plasma
- $\Gamma^{m}_{\text{in},\parallel} \equiv$ Parallel *momentum* influx
- $\Gamma^{e}_{\text{in}} \equiv$ influx of the *energy* from electrons and ions
- $\Gamma^{\text{imp},a}_{\text{in}} \equiv$ influx for an impurity species a .

The total particle influx Γ^{p}_{in} from the core plasma is obtained by the overlap of the computational grid of EMC3 and EIRENE (see Figure 3.11). All neutral particles that are ionized within this overlap are counted as a contribution to Γ^{p}_{in}. No cross-field transport of parallel momentum is assumed at the inner boundary; $\Gamma^{m}_{\text{in},\parallel} = 0$ follows from that. The energy influx Γ^{e}_{in} into the SOL is set to the effective heating power $P^{\text{SOL}}_{\text{heat}} = P_{\text{heating}} - P_{\text{rad}}$ taken from experimental measurements. P_{total} is the total heating power and $P^{\text{SOL}}_{\text{rad}}$ the overall lost power caused by radiation effects in the SOL. The effective heating power $P^{\text{SOL}}_{\text{heat}}$ is uniformly distributed over electrons and ions (the distribution can be chosen). Therefore, electron influxes $\Gamma_{\text{in,e}}$ equal ion influxes $\Gamma_{\text{in,i}}$. Mass accumulation is suppressed

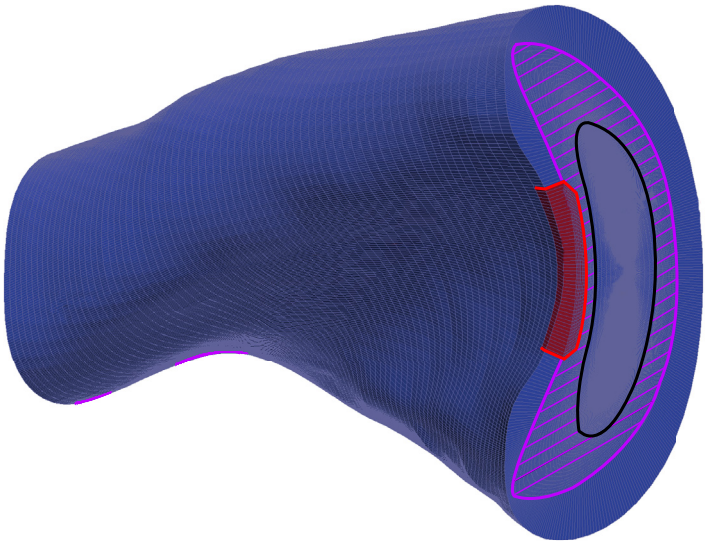

Figure 3.5: The same Figure as 3.4, but instead of the coordinate system, code-specific boundary surfaces are highlighted. Boundaries are depicted as follows: inner (black), outer (magenta), and target boundary (red).

for the impurities within the core plasma because the mass-balance is assumed to be in a steady state,

$$\sum_{a=0}^{Z} \Gamma_{\text{in}}^{\text{imp},a} = 0 \quad . \tag{3.4.0.1}$$

The computational grid overlap is depicted in Figure 3.5. Areas of the computational domain are shown by the magenta-striped region, which does not extend to the first system boundary. Energy influxes are set to the effective heating power, which is taken from experimental measurements and equally distributed over the electrons and ions as a first guess.

Outer boundary conditions:

For the diffusive perpendicular transport processes, an exponential decay length $\lambda_{n,T}$ is assumed. This decay is related to absorption processes at the outer system boundary.Hence, outer simulation boundaries of EIRENE are further extended outside of where the EMC3 computational grid reaches; thus, the complete limiter configuration is included. A crucial aspect here is that neutral plasma particles that are not traveling on closed field lines can propagate freely near the vessel wall.

Target boundary conditions:
At the limiter surfaces, a full recombination of plasma particles into neutral particles is assumed, for the shown setup. Plasma particles approach the limiter or divertor surface at the speed of sound c_s [1]. Their thermal distribution is represented by Maxwellians. Ions and electrons then undergo elastic or inelastic scattering events with the surface atoms. Incident ions and electrons may be reflected with a great fraction of their incident energy and only undergo few collisions. Alternatively, they may lose a great portion of their incident energy because of many collisions and enter equilibrium with the surface atoms. Furthermore, they diffuse within the surface structure and are re-emitted into the plasma with the surface thermal energy. The reflected particles are primarily neutrals; however, not all particles are reflected in realistic scenarios because incident particles reside in interstitial sites or defects. This particle flux is called the recycling flux; particles that advect back into the plasma provide the neutral particle source. Subsequently, neutral particles are ionized on their way back into the plasma and are implemented in EMC3 as sources. The Bmohm criterion provides the boundary condition for the parallel momentum $u_{i,\parallel} = c_s$. Atoms being removed from plasma-facing wall elements as a consequence of the impact of incident plasma particles is known as sputtering. It is the binding energy of surface atoms overcome by the energy transfer of incident plasma particles, which is known as physical sputtering. A sputtering coefficient S, defined as the number of atoms liberated per incident ion or electron, can be measured. EMC3 allows an impurity influx $\Gamma_{in}^{imp,a}$ from the target plates into the plasma. The plasma loses a portion of its energy to each impurity particle until P_{rad}^{SOL} (as an input parameter in the sum) is reached. Results of the heat flux onto target plates from a completed EMC3-EIRENE can be used to calculate the overall impurity release rate $R^{H\rightarrow X}$. Only hydrogen atoms contribute to the heat flux onto the target plate; this is because hydrogen is the main plasma component and an impurity contribution that is not yet implemented in the EMC3 impurity model [48]. Thus, one must pay attention to neglecting other plasma species when conducting a comparison between the numerical value $R^{H\rightarrow X}$ to an experimental sputtering coefficient S.
EMC3 boundary conditions are accompanied by the following free simulation parameters: ion density n_i, anomalous diffusion coefficient $D_\perp$, thermal diffusion coefficients for electrons and ions $\chi_{e,i\perp}$, and the previously discussed overall heating power P_{heat}^{SOL} plus the power P_{rad}^{SOL} lost through radiation effects within the SOL. Constraints for these free input parameters must be found by experimental measurements to characterize the plasma transport problem. Next, this section discusses the EMC3-EIRENE module sequence, because dependencies between the EMC3 model equations demand a designated order of modules.

- **STREAMING**: calculates the plasma density and momentum (see equations (3.2.0.5) and (3.2.0.8)).

- **ENERGY**: calculates the plasma temperatures for the electrons and the ions (see equation (3.2.0.17)).

- **NEUTRAL**: calculates and updates the source terms via EIRENE.

- **POSTPROCESSING**: calculates the heat flux on limiter or divertor tiles.

- **IMPURITY**: calculates influence of impurity particles on the main plasma from equation (3.2.1.6).

The set of EMC3 model equations is split into modules. Module **STREAMING** calculates the density and momentum of plasmas through solving equations (3.2.0.5) and (3.2.0.8). Equation (3.2.0.17) is solved for the electrons and ions through the module **ENERGY**. In the first part of a coupled EMC3-EIRENE simulation, **ENERGY** and **STREAMING** are conducted. All fluxes across the inner and outer boundaries of the EMC3 computational are set to zero; additionally, no volumetric sources are allowed. Hence, S_i and S_m equal zero. First approximations of plasma densities and momenta independent on these sources are obtained. Inner boundary conditions are then set to $\Gamma_\mathrm{in} = \Gamma_\mathrm{out}$, and the decay length $\lambda_{n,T}$ is set to 4 cm. **ENERGY** and **STREAMING** are coupled and rerun four times to improve the first approximations of $T_\mathrm{e,i}$, n_e, and M . The iterative reapplication of these two modules must not be intersected by a third module until now. Percentage changes of these plasma values are observed (after each module) via equation (3.2.2.19), to check for a convergence in $T_\mathrm{e,i}$, n_e, and M. First approximations are still not accurate, although the percentage change of the plasma parameters is reduced because volumetric particle sources have not yet been calculated.
Next, the module **NEUTRAL** is conducted, generating particle fluxes over the inner boundary Γ_in as well as volumetric particle sources. These sources are then used in the module **STREAMING**. A coupling of **STREAMING**, **ENERGY**, and **NEUTRAL** is then iterated to refine the convergence and percentage change of $T_\mathrm{e,i}$, n_e, and M . If the percentage change drops below 1%, this simulation is considered to have converged (the relative change is given by equation (3.2.2.19)).
At this point, an EMC3-EIRENE simulation of a nonimpurity plasma (pure hydrogen plasma) is converged and can be evaluated and analyzed in **POSTPROCESSING**. However, the SOL of a fusion plasma is not as clean as that of a pure hydrogen plasma, and thus impurities must be considered with the **IMPURITY** module. The same boundary conditions are applied for this module as for the previously used modules. **IMPURITY** makes every single ionization state of the considered impurity species assessable. Thus, a complete rerun of **NEUTRAL**, **STREAMING**, and **ENERGY** is executed to update $T_\mathrm{e,i}$, n_e, and M after the **IMPURITY** module is run. Figure 3.6 depicts the complete EMC3-EIRENE sequence. The generation of a computational domain starts by tracing field lines from a two-dimensional grid structure, which is placed at a toroidal element of $\varphi = 0°$. The generation of an EMC3 computational domain underlies a field-line tracing code that calculates the toroidal magnetic field line configuration of the considered plasma scenario in a customizable manner. Here, a standard field-line integration procedure for individual particles traced by EMC3 is computationally

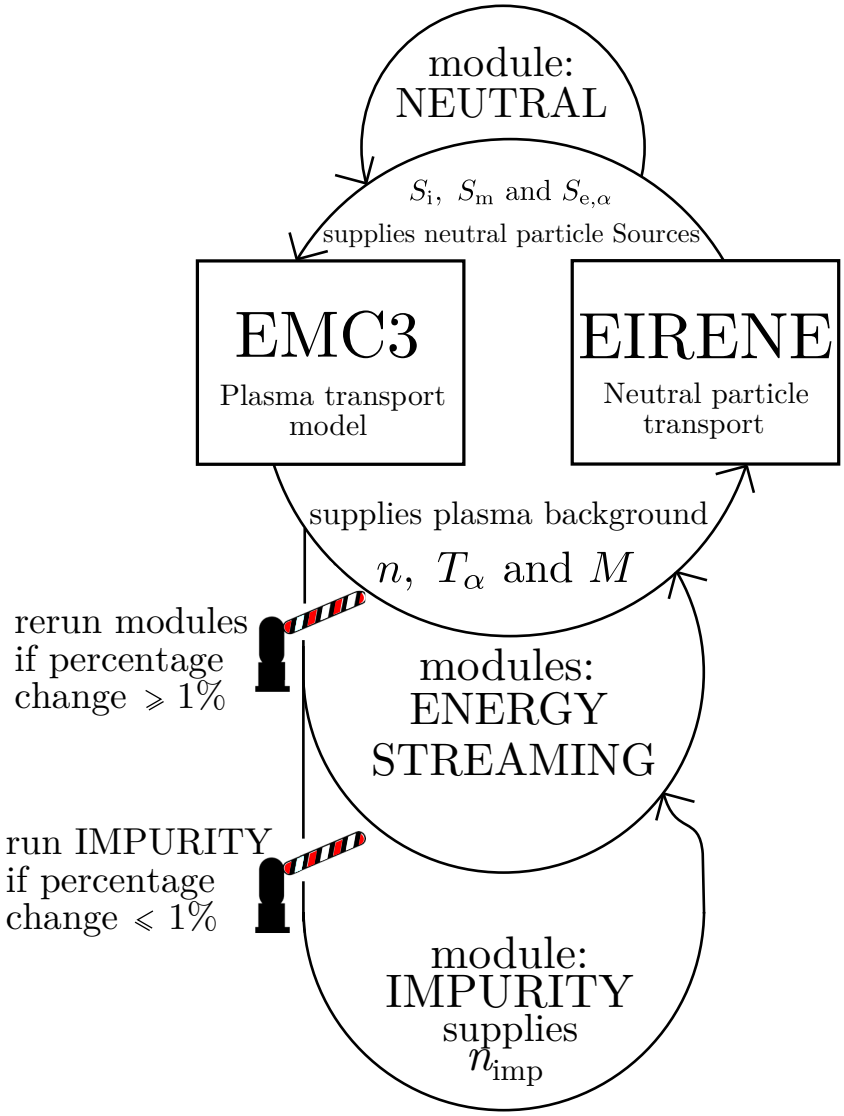

Figure 3.6: Schematic overview of the operation procedure of EMC3-EIRENE modules.

expensive, and therefore unrealistic. However, the code relies instead on an field reconstruction from a precalculated computational domain at discrete points through interpolation. If the magnetic boundary can be represented by nested, closed magnetic surfaces, as in ideal axisymmetric tokamaks, field lines can be accurately traced using the standard magnetic Boozer coordinates, r, θ, and φ of the magnetic field [48]. These coordinates are stored on a three-dimensional mesh through the linear relation $\theta = \theta_0 + \iota(r) \cdot (\varphi - \varphi_0)$. Here, r is the magnetic surface's coordinate, ι is the rotational transform (see equation (2.2.0.1)) of this magnetic surface, and θ_0 and φ_0 are toroidal and poloidal reference angles of the field line on the surface.

The starting point of all cell mapping techniques for magnetic confined plasmas is a subdivision of the plasma's toroidal expansion into m subdomains. One refers to these subdomains often as zones. Then, an arbitrary two-dimensional poloidal cross-section φ_0^m of the given experiment plasma is

selected. Grid contours (e.g., flux surfaces) have to be nested and closed. Furthermore, they extend radially inward inside the LCFS to match the confined region of the plasma. Now, magnetic field lines are numerically integrated in the $\pm\varphi$ direction to both zones' ends of the φ_-^m ($-\varphi$ direction) and φ_+^m ($+\varphi$ direction). Within these the coordinates φ_k are stored for each intermediate toroidal cut k (see Figure3.7). A set of 3D flux tubes in zone m, in r,θ,φ, is the result. One continues to construct the

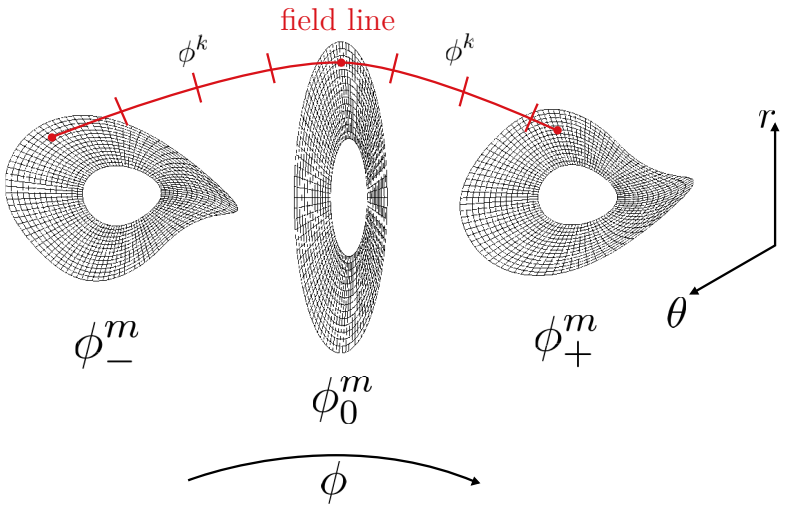

Figure 3.7: Arbitrary grid structure defined on a poloidal cross-section at the position φ_0^m and mapped over two zones, with three intermediate $k = 3$ toroidal cuts, to form a set finite flux tubes. Figure adapted from [49].

same 3D structure for zone $m+1$. This scheme is followed until a full toroidal period is completed. One finds that

$$\boldsymbol{B}(R,z,\varphi^*) = \boldsymbol{B}(R,-z,-\varphi^*) \tag{3.4.0.2}$$

because of the W7-X's flip side geometry (see Figure 2.4). Here, $\varphi^* = \varphi - \varphi_s$ holds, where φ_s is the flip-side poloidal cross section. Thus, restricting the field line integration to half a toroidal period is sufficient because of equation (3.4.0.2). A limitation to the presented method remains because the toroidal deformation of the nested flux tubes must not be too strong [49]. However, a relevant study proved that for the W7-X, a single zone was sufficient for satisfying the convexity constraint for all cells of the mesh [49]. Figure 3.5 illustrates flux tubes that are toroidally deformed because of the magnetic shear. Field lines within each zone (m and $m+1$ for Figure 3.5) are referred to as r and θ. The values of r and θ lie between 0 and 1 for the bottom, top, left, and right sides of the flux tube boundaries (see Figure 3.9). Then, the coordinates of any toroidal cut φ_k (see Figure 3.7) is calculated by a bilinear interpolation from the stored values on the corner points $\{x_{i,j,k}\} = x_{i,j,k}, x_{i+1,j,k}, x_{i,j+1,k}, x_{i+1,j+1,k}$, shown in Figure 3.9:

$$\begin{aligned} x(r,\theta,\varphi_k) = x_{i,j,k} &+ r(x_{i+1,j,k} - x_{i,j,k}) + \theta(x_{i,j+1,k} - x_{i,j,k}) \\ &+ r\theta(x_{i+1,j+1,k} - x_{i,j+1,k} - x_{i+1,j,k} + x_{i,j,k}) \quad . \end{aligned} \tag{3.4.0.3}$$

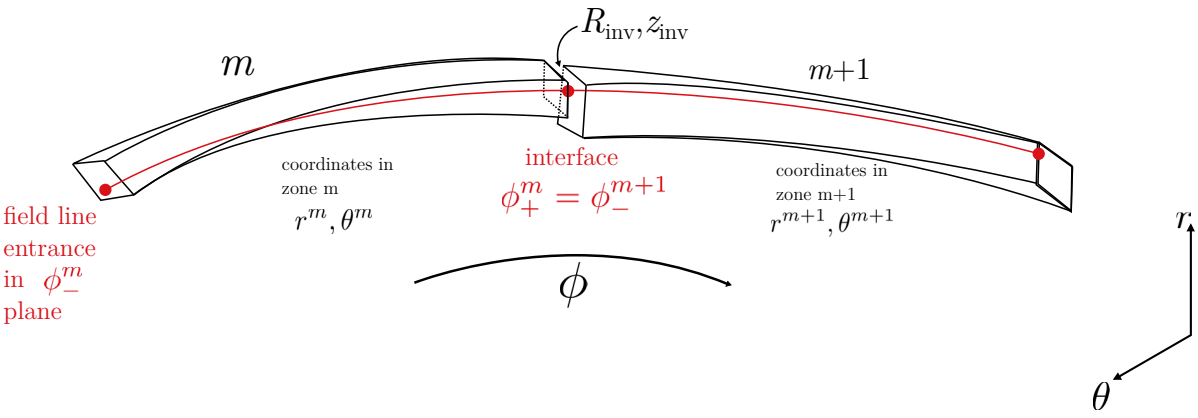

Figure 3.8: Sketch of two flux tube ends adjacent to one another that do not fit in terms of size or form; both tubes share a common intersection (at $\varphi_+^m = \varphi_-^{m+1}$) and field line. Figure adapted from [49].

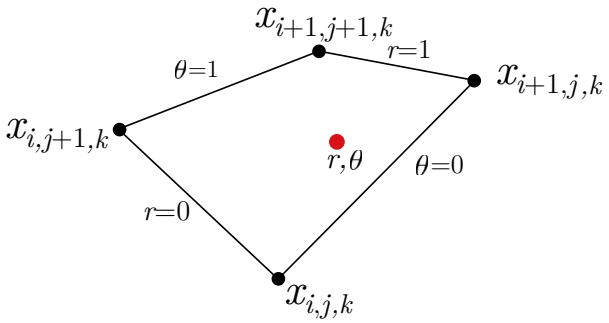

Figure 3.9: A rectangular flux tube cross-section k within zone m; corner points of the cross-section are indexed by $x_{i,j}$. Figure adapted from [49].

Equation 3.4.0.4 can be written as,

$$x = f(\xi, \{x_{i,j,k}\}) \quad , \tag{3.4.0.4}$$

where ξ is the Boozer coordinates r, θ of the shown flux tube cross-section k. The Cartesian coordinates are transformed into Boozer coordinates; then, the Boozer coordinates ξ^m give the position of the flux tube in zone m. At the interface between zone m and $m+1$, the coordinate transformation for zone m has the form of,

$$x_{\{m=m+1\}} = f(\xi^m, \{x^m_{i,j,+}\}) \quad . \tag{3.4.0.5}$$

By inverting the transformation (3.4.0.5), the Cartesian flux tube coordinates for zone $m+1$ read as,

$$x_{m=m+1} = f(\xi^{m+1}, \{x^{m+1}_{i,j,-}\}) \quad . \tag{3.4.0.6}$$

Combining equations (3.4.0.5) and (3.4.0.6) to,

$$f(\xi^m, \{x^m_{i,j,+}\}) = x_{m=m+1} = f(\xi^{m+1}, \{x^{m+1}_{i,j,-}\}) \quad , \tag{3.4.0.7}$$

showing that the applied integration of field lines can be treated as a conventional coordinate transformation, which uses $x_{m=m+1}$ as an intermediate parameter [49]. The real space coordinate $x_{m=m+1}$ is not changed by the transition from zone m to $m+1$. Once a field line is chosen in a given zone, it extends continuously into the adjoining zone and its field line are uniquely determined in all zones [49]. However, the utilized computational domain shown in Figures 3.4 and 3.5 (with boundary conditions) was created using only a single zone. This was possible because of the W7-X's five-fold and flip-side symmetry (see equation (3.4.0.2)). Thus, a single zone covers a toroidal spread of 36°. Additional features, such as extra target plates, can be considered in the magnetic topology. Hence, the starting points of the magnetic flux surfaces can be chosen and traced in the poloidal cross-section. Limiter and divertor target plates must be implemented within the computational domain. The described scheme for creating a computational domain is followed, and then target plates are "cut out" from each poloidal cross φ_k section of the computational domain (see Figure 3.10). A greater toroidal expansion occurs for divertor target plates than for limiter ones, and thus, $\varphi_k^{\text{cutout,lim}} < \varphi_k^{\text{cutout,div}}$. The toroidal cell boundaries between a plasma cell and a cut-out target plate cell are used to define the boundary conditions for the plasma, such as the Bohm criterion for this thesis. Recorded fluxes (numerical results) are used to calculate the start distribution of neutral particles, which stream back into the plasma. A vital aspect for a successful EMC3-EIRENE simulation, aside

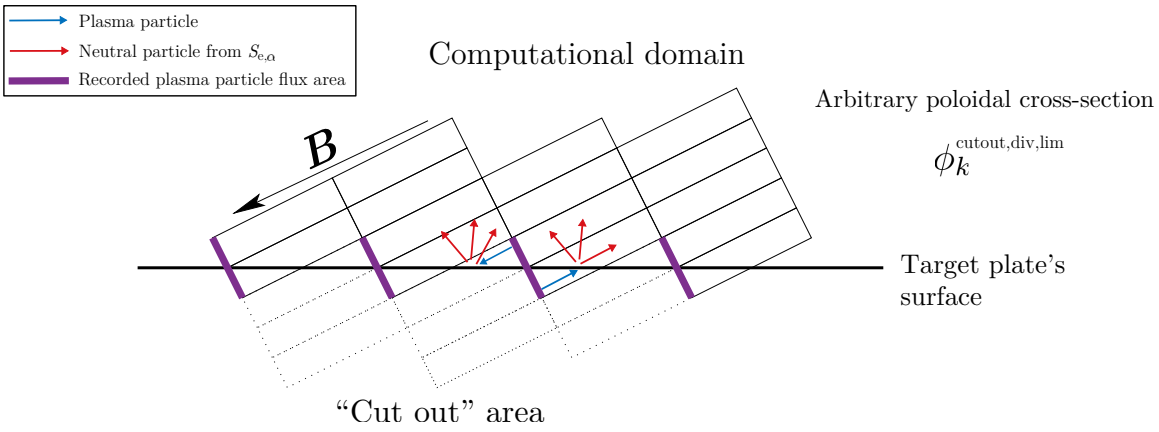

Figure 3.10: Target plates (black) are "cut out" of an arbitrary poloidal cross section $\varphi_k^{\text{cutout,div,lim}}$. Plasma fluxes onto the target plates are denoted by the magenta areas, where boundary conditions are set. The start distribution of the neutral particles (red) are determined by these fluxes.

from correctly choosing the boundary conditions and constrained input parameters, is an accurate computational domain. EMC3-EIRENE is a plasma edge code, which evaluates plasma parameters in the computational domain by summing over all computational fluid parcels within it. Fluid parcels are defined in this computational domain, which is not necessarily the same grid used for field line tracing because the sum of tracked field lines is independent from the magnetic field structure. For limiting surfaces, all cells of the EMC3 computational domain are cut out where the cell center lies or within the limiting installation. Mapping on the surface of the EIRENE computational domain is done.

During operational phase 1.1, the W7-X is in a limiter configuration; hence, plasma-limiting target plates must be included in the computational domain. However, they remain "cut out" for plasma particles because they do not exist beyond target surfaces and boundaries. Figure 3.11 shows the complete cross-section (at $\varphi = 0°$) of the EMC3-EIRENE computational domain. Limiter tiles are included in the first toroidal segment of the shown computational domain and do not expand into other segments. Including a single limiter in the computational domain accounts for a plasma

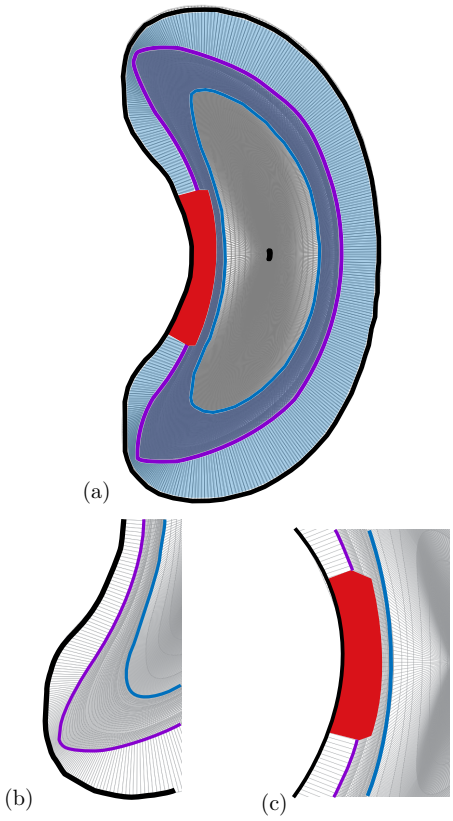

Figure 3.11: EMC3-EIRENE computational domain for the limiter configuration of W7-X. Outer and inner system boundaries are black, the outer EMC3 boundary is shown in magenta, the inner EMC3 boundary is shown in light blue, and the limiter is the red-shaded region. Furthermore, the EMC3-grid is shown by the darker blue-shaded region and the EIRENE grid is shown in the light blue-shaded region; (a) is a complete poloidal cross-section of the computational domain; and (b) and (c) show a lower part and mid-plane section of (a).

scenario of five limiters because the simulation effort for the considered plasma scenario can be reduced to 1/10 using the module periodicity of W7-X.

At the inner boundary of the EMC3 domain (the magenta line in Figure 3.11), the particle influx Γ_{in} is defined. For the outer boundary (light blue in Figure 3.11) of the EMC3 domain, decay lengths for the temperature $T_{\text{e,i}}$ and density n_{e} of the main plasma are chosen. If particles reach limiting surfaces (red-shaded region in Figure 3.11), a full recombination of these particles into neutrals is assumed.

Hence, neutral carbon impurities (for example) can advect back into the plasma and ionize on the way. These boundary conditions were discussed in detail in section 3.4. A second option for including impurities in an EMC3-EIRENE simulation is to add additional point sources into the computational domain. Outgassing released from first wall components is considered in this manner. A uniformly distributed release from the first wall is assumed. For 36 toroidal segments, 15 poloidally distributed point sources are defined. In total, 540 additional impurity point sources are distributed along the first wall (see Figure 3.12). The computational domain used in the present study covers a toroidal

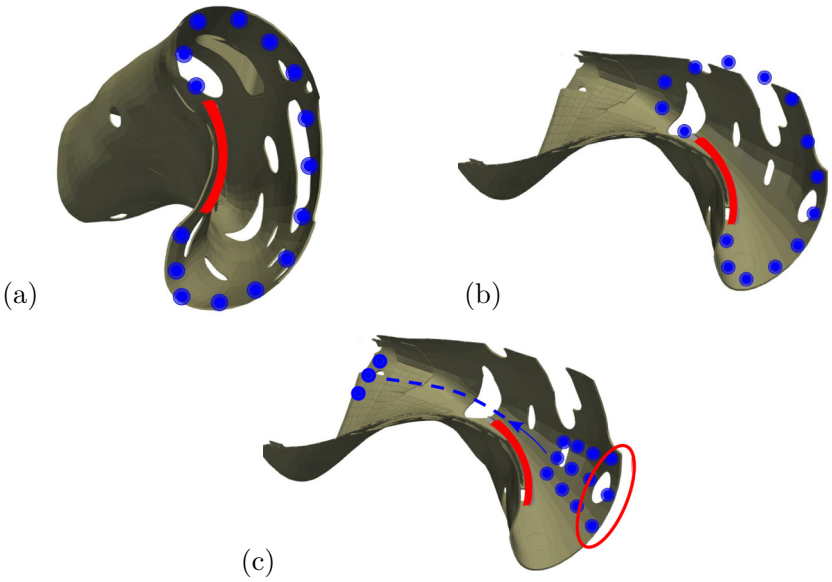

Figure 3.12: Schematic (1/10) of the W7-X covered by the computational domain; (a) shows the first toroidal sector element with additional impurity point sources uniformly distributed poloidally; (b) shows the same sector from a different viewing angle; and (c) shows the distribution of three exemplary oxygen point sources (marked red) along each toroidal sector. In all three schematic plots, the impurity source for the main impurities (coming from the limiter tiles) are indicated by the red tiles.

segment of $\Delta\varphi_{\mathrm{tor}} = 36^\circ = 72 \cdot \delta\varphi_{\mathrm{tor}}$ (with $\delta\varphi_{\mathrm{tor}}$ denoting the toroidal discretization) with a resolution of $\Delta R = 0.44$ cm in the radial direction and a poloidal grid for each of the 72 poloidal cross-sections (with a poloidal discretization of $\delta\theta_{\mathrm{pol}} = 0.7^\circ$). An island divertor was introduced for operational phase 1.2 (OP1.2.). This concept consists of five distinct divertor modules (each module has an upper and lower divertor part), which must be implemented in the EMC3 computational domain as limiting surfaces. A toroidal expansion of the divertor tiles is part of the divertor concept (presented in subsection 2.1.2, see Figure 2.4). Divertor target plates are then implemented in a sequence of toroidal segments. Figure 2.4 shows that the beginnings and ends of the upper and lower divertor tiles do not share the same toroidal segment; however, they do share the same toroidal segments in which an up–down symmetry of the magnetic field configuration is given. The first toroidal segment $\varphi = 0^\circ$ of the EMC3 grid is set to this symmetric point. Figure 3.13 shows the upper and lower divertor tiles

(red lines). The same boundary conditions are applied for this computational domain, as discussed in subsection 2.1.1.

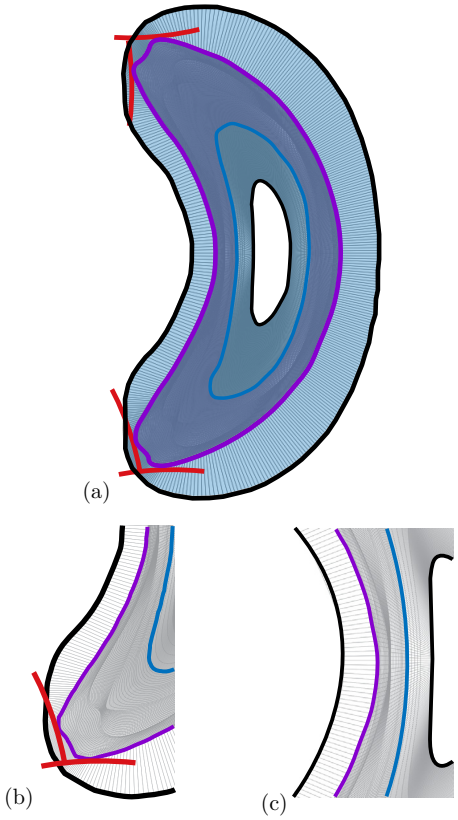

Figure 3.13: The same as Figure 3.11, but the W7-X is shown in its divertor configuration.

CHAPTER 4

PLASMA EDGE MODELING FOR THE LIMITER CONFIGURATION OF W7-X

In this chapter, previously introduced simulation sequences are used to compare numerical results with characteristic diagnostic findings. A direct comparison between modeling and measurements is conducted for electron densities, electron temperatures, and the deposited heat flux onto limiter tiles. Any code input parameters must be initially guessed or estimated if they are not constrained to exact values. Characteristic measurements for the main input parameters, such as the applied plasma heating power, the power that is lost in the SOL, initial plasma densities, and temperatures, are used to constrain EMC3-EIRENE input parameters to the considered W7-X discharge plasma. Here the answers to the first key question of this chapter are found, which is as follows,

- *What are the quantifications of the assessed impurity effects and what role do they play in respect of characteristic plasma edge measurements of W7-X in limiter configuration?*

At best, several recorded datasets of different diagnostics are available for a single discharge. A vast knowledge of input parameter constraints is required because the amount of free parameters must be reduced. This is done with each constrained input parameter. The remaining free parameters must be guessed on the basis of experience and often-utilized values. As a first step, the consistency between different Langmuir probe measurements (taken from a single discharge) and the corresponding EMC3-EIRENE simulation are checked. Only after consistency is achieved between diagnostic and numerical findings can the results be used to perform interpretative impurity studies and find the answer to the second key question of this chapter,

- *What are the results for a direct comparison of plasma edge modeling and measurement?*

Converged impurity studies have the plasma's exact impurity content as a result. Based on this, predictions of future plasma scenarios can be made. Hence, the final key question is as follows,

- *Can predictions for future W7-X plasmas be made?*

Figure 4.1 provides an overview about which measured properties are used to constrain EMC3-EIRENE input parameters. Initial EMC3-EIRENE reference simulations are constrained with limiter

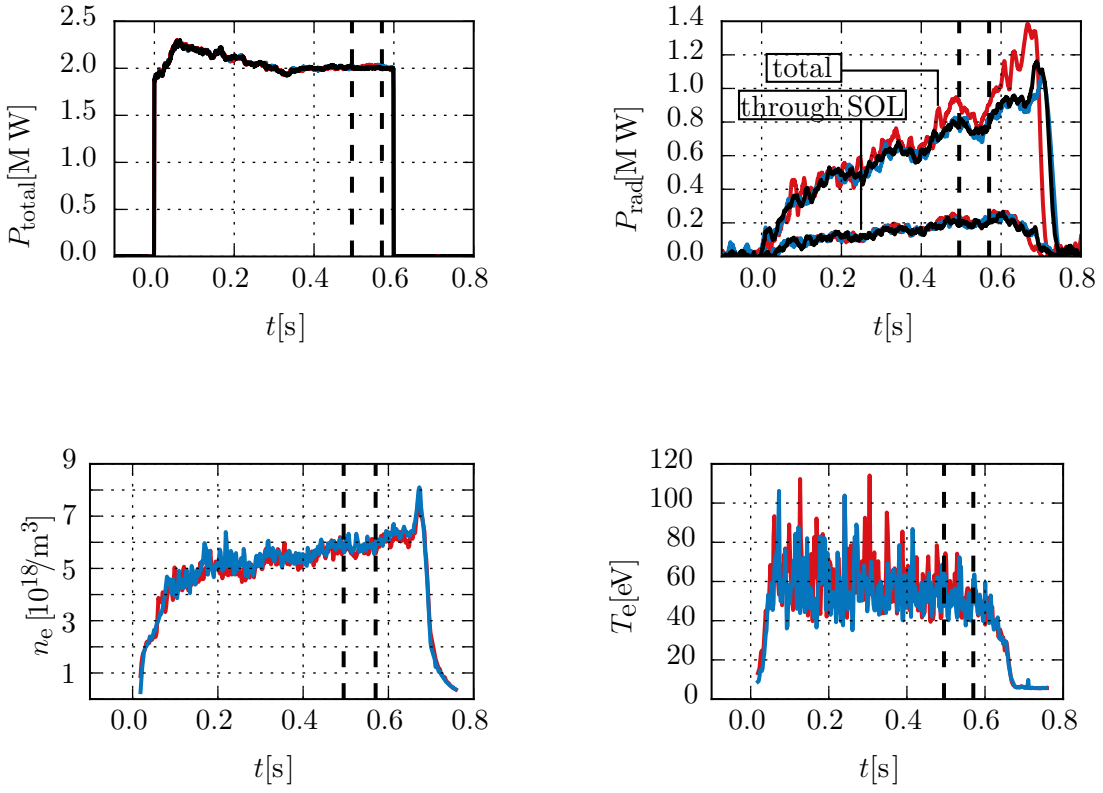

Figure 4.1: Overview of characteristic measurements of heating power (a), radiated power (b), and down-stream n_e (c), T_e (d). Measurements (a) to (d) were conducted using bolometer and Langmuir probe measurements of a repetitive set of W7-X discharges. The color code refers to different discharges. Black: discharge 20160308.22, red: discharge 20160308.23, and blue: discharge 20160308.24. Upstream Langmuir probe measurements were performed at a specific time interval ($\Delta t = 0.05$ s), indicated by the vertical dashed lines.

Langmuir probe measurements [50] (constraining n_e and T_e), the applied ECRH heating power, and lastly the lost power measured by the bolometer. The electron density and temperature are set at the LCFS, which is the inner system boundary (see Figure 3.11). Subsequently, the remaining free input parameters of the EMC3 code are the transport coefficients $D_\perp = 3\chi_{e,\perp} = 3\chi_{i,\perp}$. Figure 4.1 illustrates a reference plasma scenario that must be matched by these free input parameters. A bolometric power measurement (discussed in subsection 2.3.2) is used as a measure for the total and SOL power loss ($P_{\text{rad}}^{\text{total}}$ and $P_{\text{rad}}^{\text{SOL}}$). EMC3-EIRENE requires $P_{\text{rad}}^{\text{SOL}}$ as an input parameter, and thus, the simulated plasma is not pure hydrogen plasma. The radiated power $P_{\text{rad}}^{\text{SOL}}$ is lost over carbon impurities for now (entering the plasma from the target boundary condition). These plasmas were selected because of the availability of sufficient spatially resolved MPM and limiter Langmuir probe measurements

for the discharges. However, the post processing of the diagnostic's findings assumes a hydrogen plasma which is not realistic. A small time interval Δt is indicated in Figure 4.1, which refers to the plunge time of the MPM into the plasma (see subsection 2.3.1). The saturation current of the ions is recorded (see subsection 2.3.1) with probe heads placed on the limiter and the MPM. Measured plasma parameters which are within Δt are considered as constraining input parameters for EMC3-EIRENE. The code demands the electron density and temperature measured at the LCFS surface as input parameter. However, the probe head of the MPM does not reach this position, although limiter Langmuir probes record n_e^{LCFS} and T_e^{LCFS} at the LCFS because the position of the LCFS is defined by the limiter. A limiter Langmuir probe is placed at the limiter tip to measure plasma parameters at the LCFS's position. Averaging n_e^{LCFS} and T_e^{LCFS} over Δt provides the constraining input parameters $n_e^{LCFS} = 6 \times 10^{18}$ m^{-3} and $T_e^{LCFS} = 50$ eV, respectively. A power of $P_{heat}^{SOL} = 1.32$ MW is recorded with the bolometer (see section 2.14) and taken as another input parameter. Hereafter, this simulation setup is on referred to by Λ. A comparison between simulated and limiter Langmuir probe measurements

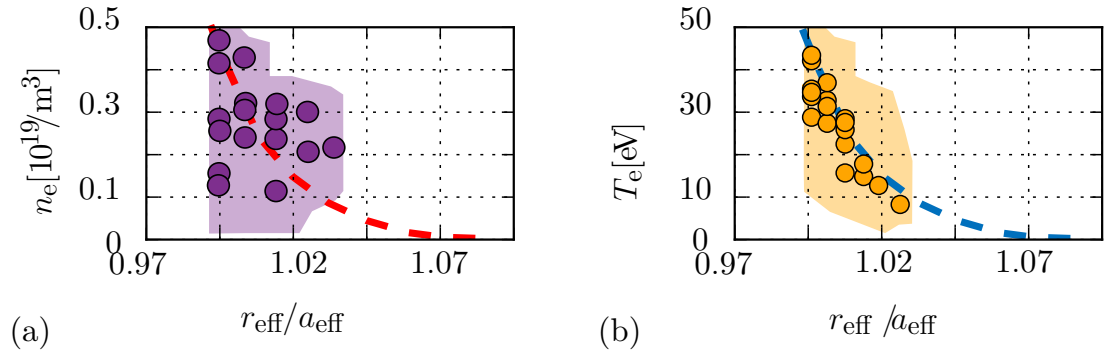

Figure 4.2: Limiter Langmuir probe comparison of density n_e (a) and temperature T_e (b) of the EMC3-EIRENE simulation (dashed) and limiter Langmuir probe measurements (dots, uncertainties of the measurements lie within the shaded regions) plotted against the effective radius r_{eff}. The effective radius r_{eff} is calculated using the averaged radius of the complete experiment, with a_{eff} characterizing the position of the LCFS. Simulation parameters: $P_{heat}^{SOL} = 1.32$ MW, $P_{rad}^{SOL} = 120$ kW, $n_e^{LCFS} = 6 \times 10^{18}$ m^{-3}, $T_e^{LCFS} = 50$ eV, $D_\perp = 0.5$ m^2/s, and $\chi_{e,i\perp} = 3D_\perp$.This simulation setup is referred to as Λ.

shows consistency at first (see Figure 4.2). However, limiter Langmuir probe measurements were performed with eroded probe heads and must be treated with caution. Hence, only the trend of these measurements is comparable to the simulation results of Λ, although these measurements were used as initial input parameter constraints. The large error bars shown in Figure 4.2 are not meaningful for the comparison process regarding simulation Λ. A quasi-consistency is enforced because n_e^{LCFS} and T_e^{LCFS} reference measurements are taken as input parameters. The next logical step is to include a second reference point in the comparison between measurements and simulations to further

strengthen the consistency. However, first attempts at a comparison between simulations and MPM Langmuir probe measurements do not show this consistency. Electron density and temperature profiles mismatch over three quarters of the measurement region of the MPM. These mismatches are shown in Figure 4.3 and are distinctly observable close to the LCFS. An applied radial shift of 4 cm (as a first guess) brings the measurement results reasonably close to the modeling results. This

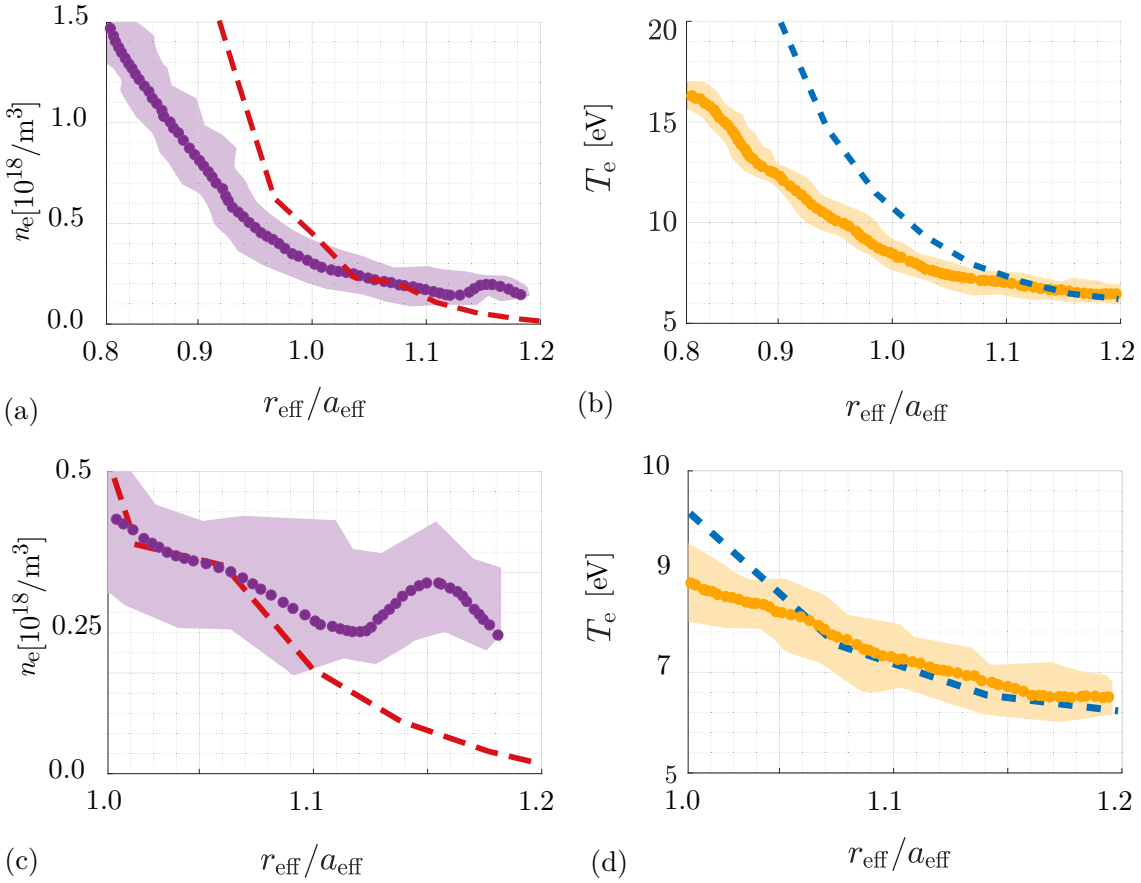

Figure 4.3: First up-stream comparison of the density n_e (a) and temperature T_e (b) of EMC3-EIRENE simulation (dashed) and manipulator Langmuir probe measurements (dots, uncertainties of the measurements shown in the shaded region) plotted against the effective radius r_{eff}. Simulation parameters from Λ. (c) and (d) are magnifications of (a) and (b) close to the LCFS.

guess was then confirmed through a necessary hardware readjustment of 6 cm. Measurement results shown in Figure 4.4 (a) and (b) are spatially readjusted, leading to both MPM and limiter Langmuir probe measurements being consistent with simulation Λ. A small offset between up-stream MPM measurements and EMC3-EIRENE simulations remains regarding the radial outermost positions of the MPM (see Figure 4.4). This offset is negligible because the error is dominated by the overall agreement of the measurement and simulation.

A third reference point to further constrain the input parameters of Λ is given by heat flux measure-

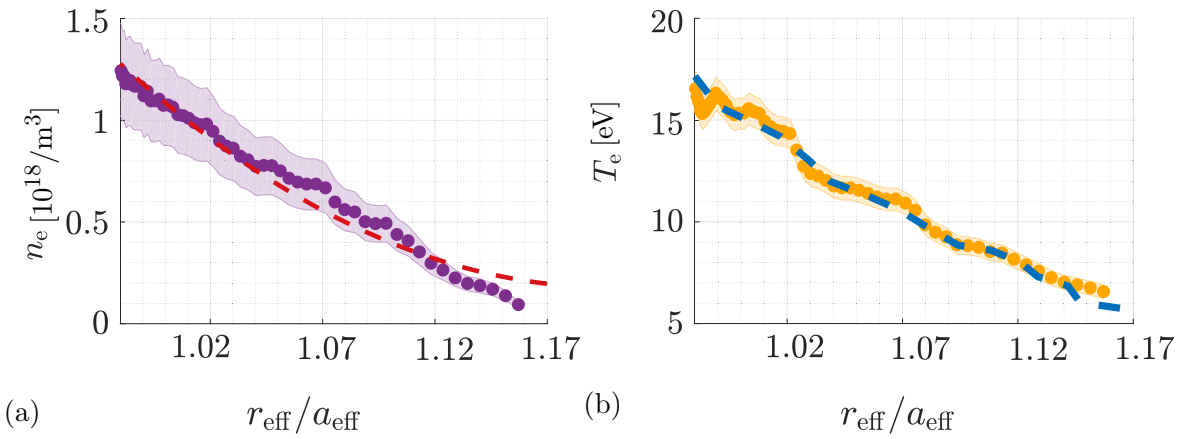

Figure 4.4: Upstream comparison of the density n_e (a) and temperature T_e (b) of EMC3-EIRENE simulation (dashed) and manipulator Langmuir probe measurements (dots, uncertainties of the measurements shown in the shaded region) plotted against the effective radius r_{eff}. Simulation parameters from Λ.

ments with infrared camera systems [51]. Radial heat flux profiles onto the limiter surface at a height of $Z = \pm 20$ cm are shown in Figure 4.5. The surface coordinate s is given by the limiter extended in

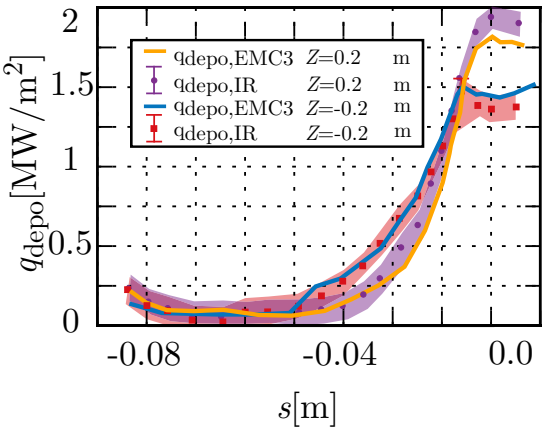

Figure 4.5: Comparison between EMC3-EIRENE simulation (solid) and heat flux measurements (dots) and their uncertainties (shaded region) plotted against the surface coordinate s of the limiter. Simulation parameters from Λ.

the plasma, with $s = 0$ marking the limiter tip (reference plots in [51]). Both selected heat-flux profiles show consistency with simulation Λ.

4.0.1 A shortcut to a multi species sound speed

Simulation Λ is now the fundament for studying further plasma properties, such as the effective charge state Z_{eff} and effective mass m_{eff} of the considered discharges. As previously mentioned, these discharges are contaminated with impurities such as carbon and oxygen, which enter from in-vessel components. Thus, a basic comparison process was applied as an interpretative synthetic tool to assess missing information on the impurity contamination in these discharges, which is only difficult to assess using any diagnostic.
An expression for the overall speed of sound c_{s} for a multi-species plasma was formulated by Tokar [52],

$$c_{\mathrm{s}}^{\mathrm{multi}} = \sqrt{\frac{\sum_{i=0}^{\kappa} \Gamma_i (T_i + Z_i T_{\mathrm{e}})}{\sum_{i=0}^{\kappa} \Gamma_i m_i}} \quad , \quad \Gamma_i = n_i u_i \quad . \tag{4.0.1.1}$$

The adiabatic index is set to $\gamma = 1$ and k drops out because of the previously selected units for the plasma temperatures. Furthermore, u_i represents the velocity of one plasma species out of κ plasma species. Hence, u_i is a contribution to the specific plasma species flow Γ_i.
A calculation of $c_{\mathrm{s}}^{\mathrm{multi}}$ for a plasma containing partially ionized carbon impurities results in quite sophisticated algebra. Hence, other studies on the transition from a single-species to multi-species plasma scenario introduce the idea of using the effective charge state distribution Z_{eff} as a "shortcut" on a single-species description [53, 54]. The calculation of an individual ion speed of sound for each plasma species is avoided. Thus, Z_{eff} becomes an approximation of the sum over all charge states i in the multi-species plasma and converts the scenario to a contaminated single-species plasma; the same goes for m_{eff}. Here, the main plasma is assumed to be contaminated by a single impurity species such as carbon or oxygen. Carbon is chosen as the main impurity for plasma scenario Λ to account for graphite limiter tiles. This study substitutes Z for Z_{eff} and m_{i} for m_{eff} in equation (2.3.1.13) following the introduced transition,

$$c_{\mathrm{s}}^{\mathrm{single}} = \sqrt{\frac{T_{\mathrm{i}} + Z T_{\mathrm{e}}}{m_{\mathrm{i}}}} \xrightarrow[m \to m_{\mathrm{eff}}]{Z \to Z_{\mathrm{eff}}} c_{\mathrm{s}}^{\mathrm{single}^*} = \sqrt{\frac{T_{\mathrm{i}} + Z_{\mathrm{eff}} T_{\mathrm{e}}}{m_{\mathrm{eff}}}} \quad . \tag{4.0.1.2}$$

The effective charge and mass over all plasma species is calculated using,

$$Z_{\mathrm{eff}} = \frac{\sum_{i=0}^{\kappa} n_i Z_i^2}{\sum_{i=0}^{\kappa} n_i Z_i} \quad , \quad m_{\mathrm{eff}} = \frac{\sum_{i=0}^{\kappa} n_i m_i}{\sum_{i=0}^{\kappa} n_i} \quad . \tag{4.0.1.3}$$

This study continues to insert Z_{eff} and m_{eff} in equation (4.0.1.2) ,

$$\left(c_{\mathrm{s}}^{\mathrm{single}^*}\right)^2 = \left(T_{\mathrm{i}} + \frac{\sum_{i=0}^{\kappa} n_i Z_i^2}{\sum_{i=0}^{\kappa} n_i Z_i} T_{\mathrm{e}}\right) \cdot \left(\frac{\sum_{i=0}^{\kappa} n_i}{\sum_{i=0}^{\kappa} n_i m_i}\right) \quad . \tag{4.0.1.4}$$

Multiplying both factors and identifying a common denominator leads to,

$$\left(c_{\mathrm{s}}^{\mathrm{single}^*}\right)^2 = \frac{\sum_{i=0}^{\kappa} n_i \sum_{i=0}^{\kappa} n_i Z_i T_{\mathrm{i}} + \overbrace{\sum_{i=0}^{\kappa} n_i Z_i^2 \sum_{i=0}^{\kappa} n_i}^{\approx \left(\sum_{i=0}^{\kappa} n_i Z_i\right)^2} T_{\mathrm{e}}}{\sum_{i=0}^{\kappa} n_i m_i \sum_{i=0}^{\kappa} n_i Z_i} \quad . \tag{4.0.1.5}$$

Subsequently, a quite radical assumption $\sum_{i=0}^{\kappa} n_i Z_i^2 \sum_{i=0}^{\kappa} n_i \approx \left(\sum_{i=0}^{\kappa} n_i Z_i\right)^2$ is made. The range of validity of this assumption is discussed later in this section. After simple algebraic steps, one finds,

$$\approx \frac{\sum_{i=0}^{\kappa} n_i \sum_{i=0}^{\kappa} n_i Z_i T_\mathrm{i} + \left(\sum_{i=0}^{\kappa} n_i Z_i\right)^2 T_\mathrm{e}}{\sum_{i=0}^{\kappa} n_i m_i \sum_{i=0}^{\kappa} n_i Z_i} \quad . \tag{4.0.1.6}$$

This study assumes for the last step, that all plasma species' velocities u_i have the same velocity u, and that the ion temperature T_i is equal for every plasma species' ion temperature,

$$\left(c_\mathrm{s}^{\mathrm{single}^*}\right)^2 = \frac{\sum_{i=0}^{\kappa} n_i T_\mathrm{i} + \sum_{i=0}^{\kappa} n_i Z_i T_\mathrm{e}}{\sum_{i=0}^{\kappa} n_i m_i} \underset{T_\mathrm{i}=T_i \ \forall \ i}{\overset{u_i=u \ \forall \ i}{=}} \frac{\sum_{i=0}^{\kappa} u n_i T_i + \sum_{i=0}^{\kappa} u n_i Z_i T_\mathrm{e}}{\sum_{i=0}^{\kappa} u n_i m_i} \tag{4.0.1.7}$$

$$\overset{\Gamma_i = u n_i}{=} \frac{\sum_{i=0}^{\kappa} \Gamma_i (T_i + Z_i T_\mathrm{e})}{\sum_{i=0}^{\kappa} \Gamma_i m_i} = \left(c_\mathrm{s}^{\mathrm{multi}}\right)^2 \quad . \tag{4.0.1.8}$$

In equation (4.0.1.5), an odd assumption, lets call it Ω,

$$\sum_{i=0}^{\kappa} n_i Z_i^2 \sum_{i=0}^{\kappa} n_i \approx \left(\sum_{i=0}^{\kappa} n_i Z_i\right)^2 \quad , \tag{4.0.1.9}$$

was used to make the transition from $c_\mathrm{s}^{\mathrm{single}}$ over $c_\mathrm{s}^{\mathrm{single}^*}$ to $c_\mathrm{s}^{\mathrm{multi}}$ possible. Hence, the introduction of Z_eff and m_eff to equation (2.3.1.13) can only be applied if Ω is true. To quantify the extent of the uncertainty generated by introducing Ω, this study calculates the difference $\Omega_{12} \equiv \Omega_1 - \Omega_2$ between $\Omega_1 \equiv \sum_{i=0}^{\kappa} n_i Z_i^2 \sum_{i=0}^{\kappa} n_i$ and $\Omega_2 \equiv \left(\sum_{i=0}^{\kappa} n_i Z_i\right)^2$ and rewrites the series to obtain two double series expressions of Ω_1 and Ω_2,

$$\Omega_1 = \sum_{j=0}^{\kappa} \sum_{i=0}^{\kappa} n_j Z_j^2 n_i \quad , \quad \Omega_2 = \sum_{j=0}^{\kappa} \sum_{i=0}^{\kappa} n_j Z_j n_i Z_i \quad . \tag{4.0.1.10}$$

The series indices j and i again represent $\kappa + 1$ plasma species. Now, the difference Ω_{12} reads as follows,

$$\Omega_{12} = \sum_{j=0}^{\kappa} \sum_{i=0}^{\kappa} n_j Z_j^2 n_i - \sum_{j=0}^{\kappa} \sum_{i=0}^{\kappa} n_j Z_j n_i Z_i \tag{4.0.1.11}$$

$$= \sum_{j=0}^{\kappa} \sum_{i=0}^{\kappa} \left(n_j Z_j^2 n_i - n_j Z_j n_i Z_i\right) \quad . \tag{4.0.1.12}$$

Terms with $i = j$ cancel out in equation (4.0.1.12) through the use of the Kronecker delta. Now, Ω_{12} equals zero if $i = j$. The assumption that the plasma only holds a second plasma species (impurity) for the main hydrogen plasma ($Z_0 = 1$) is valid because of the extraction of the main plasma component ($i = 0$ and $j = 0$) from Ω_{12},

$$\Omega_{12} = \sum_{i=1}^{\kappa} n_0 n_i (1 - Z_i) + \sum_{j=1}^{\kappa} n_0 Z_j n_j (Z_j - 1) + \sum_{j=1}^{\kappa} \sum_{i=1}^{\kappa} \left(n_j Z_j n_i (Z_j - Z_i)\right) \quad . \tag{4.0.1.13}$$

Each series starts from $j = 1$ and $i = 1$ and describes the charge states from the second impurity plasma species. Hence, $Z_i = i$ and $Z_j = j$ can be used to further simplify equation (4.0.1.13),

$$\Omega_{12} = \sum_{i=1}^{\kappa} n_0 n_i (1-i) + \sum_{j=1}^{\kappa} n_0 j n_j (j-1) + \sum_{j=1}^{\kappa} \sum_{i=1}^{\kappa} n_j j n_i (j-i) \quad . \tag{4.0.1.14}$$

The uncertainty Ω_{12} can then be calculated using equation (4.0.1.14). This study proceeds with the same algebra for Ω_2 to find,

$$\Omega_2 = \sum_{i=1}^{\kappa} n_0 n_i i + \sum_{j=1}^{\kappa} n_0 n_j j + \sum_{j=1}^{\kappa} \sum_{j=1}^{\kappa} n_j j n_i i \quad . \tag{4.0.1.15}$$

Equations (4.0.1.14) and (4.0.1.15) are then used to obtain the uncertainty Ω_{12} i a percentage,

$$\delta_{\Omega_{12}} = \frac{\Omega_{12}}{\Omega_2} \quad . \tag{4.0.1.16}$$

An exemplary hydrogen plasma scenario $\Lambda^{\text{exemplary}}$ (main plasma density n_{H}) and equation (4.0.1.16) can be used to give a first simple error estimation. This example scenario contains carbon impurities, and each carbon impurity's charge state has a density of $n_{\text{C}^i} = 0.1 n_{\text{H}}$. One obtains an uncertainty using assumption Ω for $\Lambda^{\text{exemplary}}$ of of $\delta_{\Omega_{12}} = 61.7\%$. However, $\Lambda^{\text{exemplary}}$ is an overestimation of the impurity densities for the charge states $Z = \{1, 4, 5, 6\}$. All individual density values n_i and the main plasma density $n_H = n_{i=0} = n_{j=0}$ in Figure 4.6 (b) are used to calculate a more precise uncertainty $\delta_{\Omega_{12}}$. Then, assumption Ω leads to a maximum uncertainty of 21.7% for the considered plasma scenario Λ. Furthermore, values of chart (b) shown in Figure 4.6 can then also be used to calculate the overall uncertainty $\delta_{c_{\text{s}}^{\text{multi}}}$ for equation (4.0.1.2), which is introduced via assumption Ω. T_{e} and T_{i} from the EMC3-EIRENE simulation (peak values) of plasma scenario Λ are then used to find $\delta_{c_{\text{s}}^{\text{multi}}}$ to be at a maximum of 8%. Thus, the shown simplification of a multi-species description of the plasma $c_{\text{s}}^{\text{multi}}$ to a single-species description, including the effective charge state and mass, $c_{\text{s}}^{\text{single}^*}$ has a peak uncertainty of 22%. Next, equation (4.0.1.2) is used to describe a multi species plasma, because a maximum uncertainty $\delta_{\Omega_{12}} = 22\%$ leading to $\delta_{c_{\text{s}}^{\text{multi}}} = 8\%$ for plasma scenario Λ is acceptable at the MPM measurement location. Assessed sound speed profiles differ by 8% (see Figure 4.7). A recalibration of the MPM and limiter Langmuir probe datasets is necessary, in which the assessed more trustworthy profiles of Z_{eff} and m_{eff} and thus more trustworthy profiles of $c_{\text{s}}^{\text{single}^*}$ are applied. Effects of Z_{eff} and m_{eff} are grouped by $c_{\text{s}}^{\text{single}^*}$. However, particular effects of the effective charge state and mass are discussed partly for each simulation.

4.0.2 Iteratively refining Langmuir probe measurements

An iterative process $\Xi_{c_{\text{s}}^{\text{single}*}}$ based on $c_{\text{s}}^{\text{single}^*}$ (including Z_{eff} and m_{eff}) is discussed in this section, , followed by a discussion of an iterative process (named $\Xi_{c_{\text{s}}^{\text{multi}}}$) based on $c_{\text{s}}^{\text{multi}}$ (no effective values used) and a comparison of them.

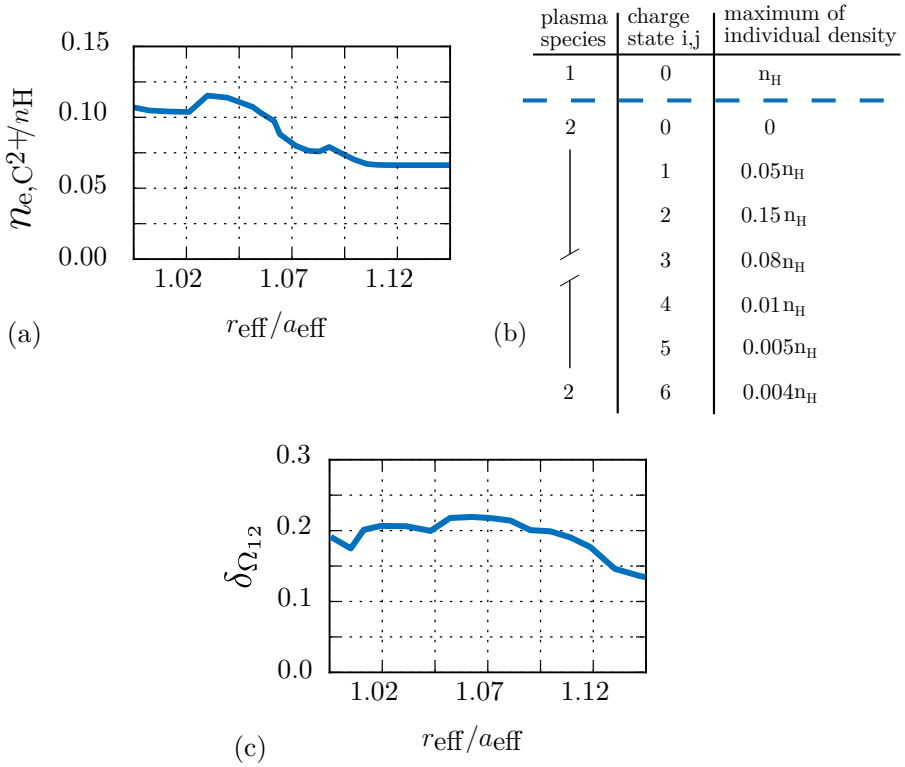

Figure 4.6: (a) Maximum density $n_{e,C^{2+}}$ of the impurity plasma species (carbon for the considered plasma scenario) plotted against r_{eff}; (b) chart of each maximum individual charge state density of hydrogen and carbon; and (c) $\delta_{\Omega_{12}}$ profile calculated via profiles shown in chart (b). Simulation results are taken from simulation $\Lambda^{l_{end}}$.

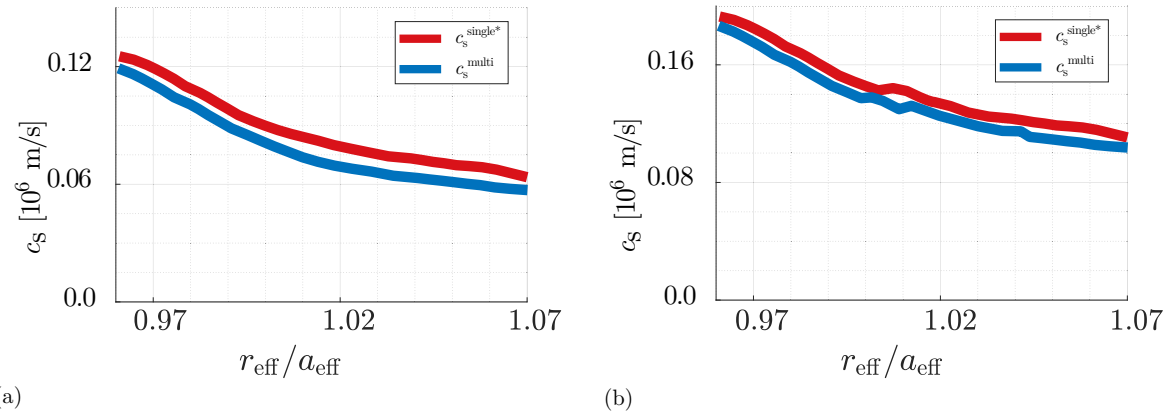

Figure 4.7: (a) Comparison of the effective speed of sound $c_s^{single^*}$ with the multi-species speed of sound c_s^{multi} at the MPM measurement location; (b) the same comparison plot as (a) but taken at the limiter LP position.

The first iterative step starts at the simulation setup Λ. In Figure 2.18(a) and (b), the effective charge state and mass are grouped to $c_s^{\text{single}^*}$ and applied to recalculate equation (2.3.1.13) (see 4.7(a)). A reprocessed measured electron density $n_{e,\text{MPM}}$ is obtained. First, iterative substeps are taken. The

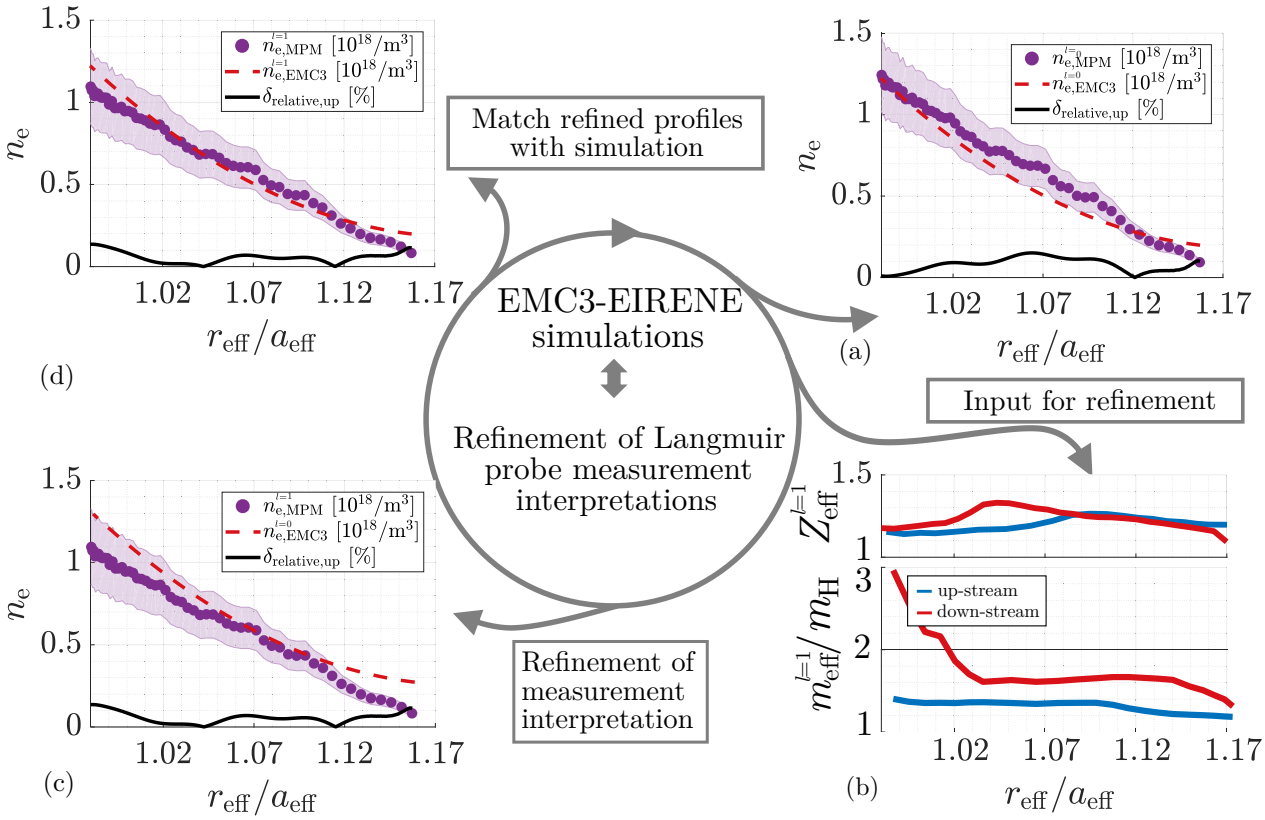

Figure 4.8: Schematic overview of the first step $l = 1$ of the iterative process for up-stream measurements. The electron density from Λ (a), $Z_{\text{eff}} = 1$ and $m_{\text{eff}} = 1$ were assumed for $n_{e,\text{MPM}}$. Deduced Z^l_{eff} and m^l_{eff} profiles (b). Relative deviation $\delta^l_{\text{relative,up}}$ (see equation (4.0.2.1)) plotted in the comparison plot of the numeric and measured density datasets (c) and (d). A reworking of plot 4.4 is shown in (d).

previously discussed comparison of measurement and simulation must be redone to match numerical results to the reprocessed measurement using simulation constraints. A detailed discussion of this iterative process can be found in [55]. An offset is established between $n_{e,\text{EMC3}}$ and $n_{e,\text{MPM}}$ (see Figure 4.8). The first iterative step is taken if the chosen simulation constraints lead again to consistency between $n_{e,\text{EMC3}}$ and $n_{e,\text{MPM}}$. Each iterative step l corresponds to the redone simulation. The simulation setup $\Lambda = \Lambda^{l=1}$ marks the first iterative step and $\Lambda^{l_{\text{end}}}$ the last. Profiles for Z_{eff} and m_{eff} are deduced in each iterative step and used to recalibrate the Langmuir probe measurements. Figure 4.8 provides an overview of step $l = 1$ in single substeps. First, MPM measurements (see Figure 4.4) of n_e are used as a reference in Figure 4.8. The iterative step begins with the assessment of $Z^{l=1}_{\text{eff}}$ and $m^{l=1}_{\text{eff}}$ in subplots (a) and (b) of Figure Figure 4.8. Substep (c) uses an update of $n^{\Lambda^{l=1}}_{e,\text{MPM}}$ by including $Z^{l=1}_{\text{eff}}$ and $m^{l=1}_{\text{eff}}$ using equations (4.0.1.2) and (2.3.1.13). Notably, a displacement regarding $n^{l=1}_{e,\text{MPM}}$ between substeps (a) and (c) is observed. The introduced displacement must be matched

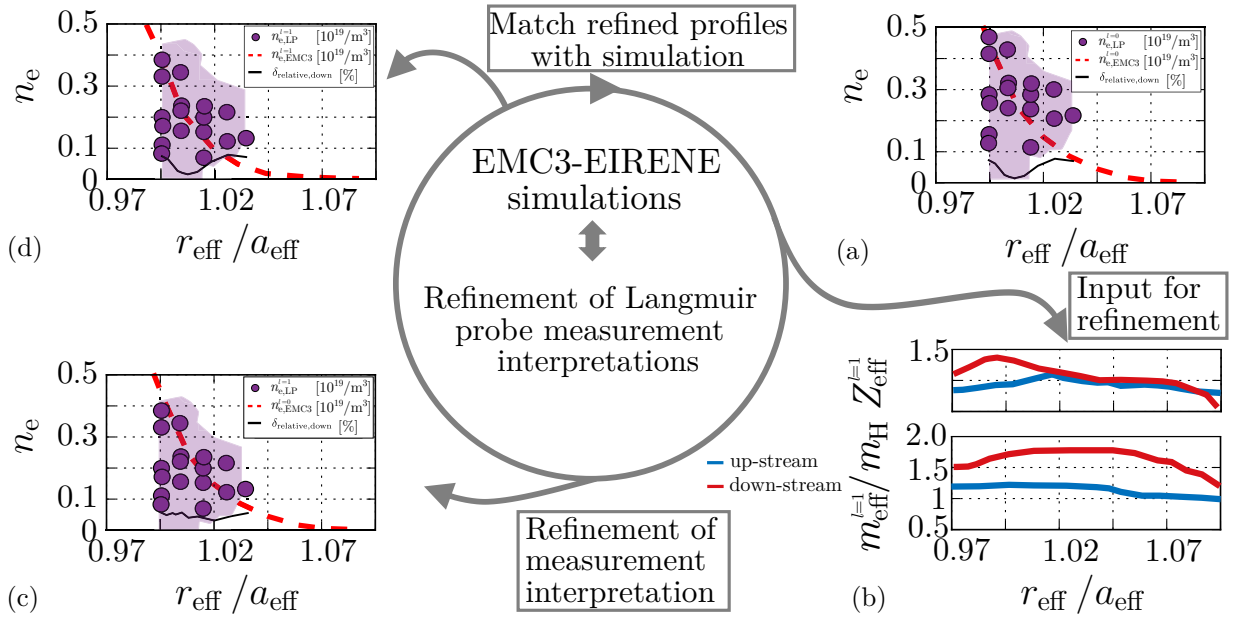

Figure 4.9: The same Figure as 4.9, but applied for limiter Langmuir probes.

with the input parameters of EMC3-EIRENE; mainly input density n_{e}. This density is decreased from $n_{\mathrm{e}} = 3 \times 10^{18}$ m^{-3} to 2.853×10^{18} m^{-3} and the shown profiles match again; thus, the first iterative step $l = 1$ is completed. This study applies the same scheme for limiter Langmuir probe measurements and obtains consistency between EMC3-EIRENE simulation and limiter Langmuir probe measurements after the first iterative step $l = 1$, as shown in Figure 4.9. The same assessed input density $n_{\mathrm{e}} = 2.853 \times 10^{18}$ m^{-3} is reapplied. The relative deviation for the first and each subsequent iterative step (for the comparison of MPM and limiter Langmuir probe measurements) is calculated using,

$$\delta^{l=1}_{\mathrm{relative}} = \mathrm{mean}\left(\frac{n^{l=1}_{\mathrm{e,EMC3}} - n^{l=1}_{\mathrm{e,LP}}}{n^{l=1}_{\mathrm{e,EMC3}}}\right) \quad . \tag{4.0.2.1}$$

Then, a quantification is obtained for the convergence of refined density profiles to each other. The next iterative steps are performed following the same substeps for each iterative step l . An appropriate factor ε^l for the next step $l+1$ is then calculated using equation (2.3.1.13) and the right-hand side of (4.0.1.2),

$$\varepsilon^l(r) = \frac{n^l_{\mathrm{e,MPM}}(r)}{n^{l-1}_{\mathrm{e,MPM}}(r)} = \sqrt{\frac{T_{\mathrm{i}}^{l-1}(r) + Z_{\mathrm{eff}}^{l-1}(r)\,T_{\mathrm{e}}^{l-1}(r)}{m_{\mathrm{eff}}^{l-1}(r)} \cdot \frac{m^l_{\mathrm{eff}}(r)}{T_{\mathrm{i}}^{l}(r) + Z_{\mathrm{eff}}^{l}(r)\,T_{\mathrm{e}}^{l}(r)}} \quad . \tag{4.0.2.2}$$

The presented Langmuir probe measurements (MPM and limiter) are updated with the Z_{eff} and m_{eff} profiles from simulation $\Lambda^{l=2}$. Executing the iterative process $\Xi_{c_{\mathrm{s}}^{\mathrm{single*}}}$ until ε^l shows a convergence to a consistent assessment of Z_{eff} and m_{eff} from the EMC3-EIRENE simulation. The considered Langmuir probe measurements cannot separate the recorded electron temperature T_{e} from the ion temperature T_{i}. Thus, T_{e} and T_{i} profiles are taken from simulation Λ^l in each step l.

Consistency is achieved between the EMC3-EIRENE simulation $\Lambda^{l_{\text{end}}}$ for each considered Langmuir probe measurement, as shown in 4.10. The relative change of ε^l is plotted against each iterative

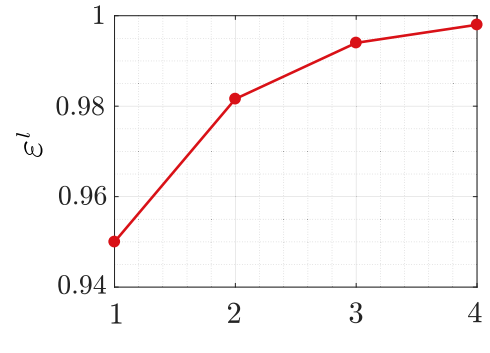

(a) iterative step l

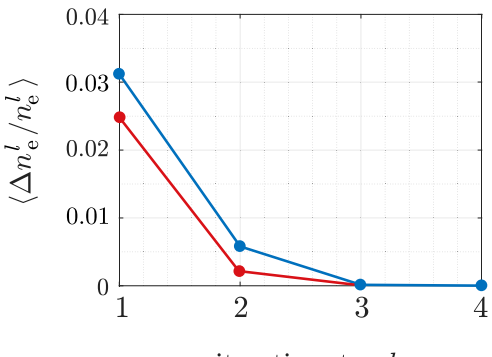

(b) iterative step l

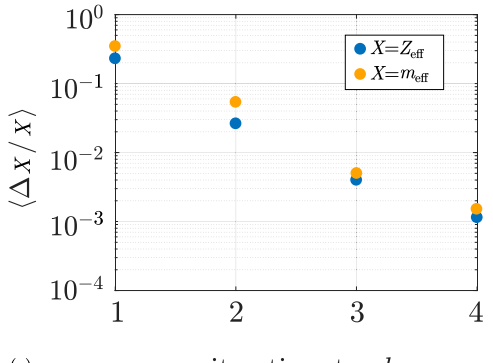

(c) iterative step l

(d)

step l	input density [m^3/10^{18}]	ε^l	$\langle \Delta Z_{\text{eff}} / Z_{\text{eff}} \rangle$	$\langle \Delta m_{\text{eff}} / m_{\text{eff}} \rangle$	$\langle \Delta n_{\text{e,MPM}}^l / n_{\text{e,MPM}}^l \rangle$
1	3	0.951	0.23	0.25	0.31
2	2.853	0.982	0.026	0.036	0.005
3	2.801	0.992	0.009	0.014	0.003
4	2.793	0.997	0.003	0.005	0.001

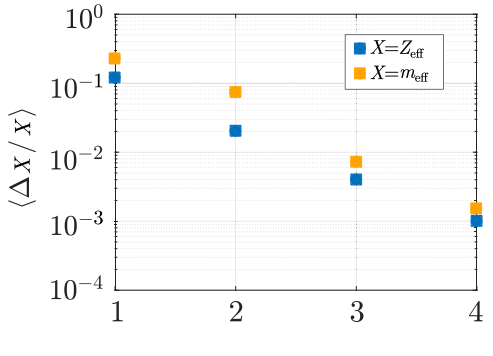

(e) iterative step l

(f)

step l	input den [m^3/10^{18}]	ε^l	$\langle \Delta Z_{\text{eff}} / Z_{\text{eff}} \rangle$	$\langle \Delta m_{\text{eff}} / m_{\text{eff}} \rangle$	$\langle \Delta n_{\text{e,MPM}}^l / n_{\text{e,MPM}}^l \rangle$
1	3	0.951	0.3883	0.2551	0.323
2	2.853	0.982	0.1173	0.0703	0.0073
3	2.801	0.992	0.0054	0.0061	0.0024
4	2.793	0.997	0.0004	0.002	0.0012

Figure 4.10: Factor ε^l plotted against each iterative step in (a). The relative change of the refined Langmuir probe measurement of (MPM position: blue, limiter position: red) plotted against each iteration step in (b). The relative change in the Z_{eff} and m_{eff} profiles at the MPM location is plotted against each iterative step in (c) for the limiter measurement location in (e). Simulation parameters are taken from plasma scenario Λ, but n_e is iterated from 3×10^{18} m^{-3} down to 2.8432×10^{18} m^{-3}. Chart (d) shows the exact values of each iterative step for the MPM and limiter measurement locations in (f).

step in Figure 4.10 (a). Figure 4.10 (b) shows the relative change of n_e (MPM and limiter Langmuir

probes) plotted against iterative steps l. Changes of Z_{eff} and m_{eff} over the iterative step l (both shown in (c) of Figure 4.10) reach values below 1% for an input density of 2.793×10^{18} m^{-3} of plasma scenario $\Lambda^{l_{\text{end}}}$. Final assessed Z_{eff} and m_{profiles} corresponding to plasma scenario $\Lambda^{l_{\text{end}}}$ are shown in Figure 2.18. These profiles are then used to assess the final refined MPM and limiter Langmuir probe measurements, since Z_{eff} and m_{eff} converge to values below 1%. An overall consistency is obtained and shown in Figure 4.11. Figure 4.10 (b) shows the relative change of n_{e} (MPM and limiter Langmuir probes) plotted against iterative steps l. Changes of Z_{eff} and m_{eff} over the iterative step l (both shown in (c) of Figure 4.10) reach values below 1% for an input density of 2.793×10^{18} m^{-3} of plasma scenario $\Lambda^{l_{\text{end}}}$. Figure 2.18 shows the final assessed Z_{eff} and m_{eff} profiles corresponding to plasma scenario $\Lambda^{l_{\text{end}}}$. These profiles are then used to assess the final refined MPM and limiter Langmuir probe measurements, because Z_{eff} and m_{eff} converge to values below 1%. An overall consistency is obtained and shown in Figure 4.11. Up-stream MPM measurements are refined by 12% to more

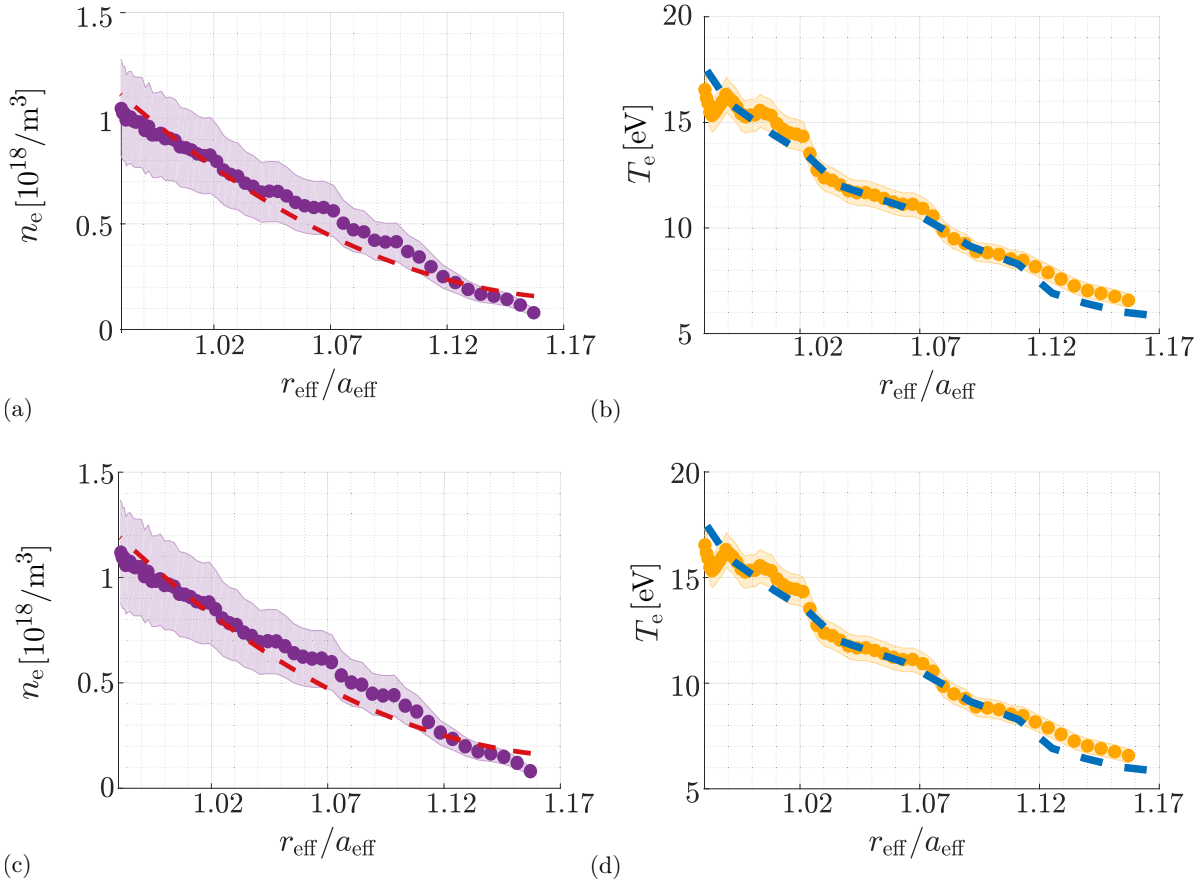

Figure 4.11: Final comparison between EMC3-EIRENE simulation (dashed) and $Z_{\text{eff}}^{l_{\text{end}}}$ adjusted manipulator Langmuir probe measurements (dots). Plot (a) shows n_{e}, and (b) shows T_{e}. Simulation parameters used from plasma scenario $\Lambda^{l_{\text{end}}}$ of iterative process $\Xi_{c_{\text{s}}^{\text{single}*}}$. Subfigures (c) and (d) are the same plots as (a) and (b) but for process $\Xi_{c_{\text{s}}^{\text{multi}}}$.

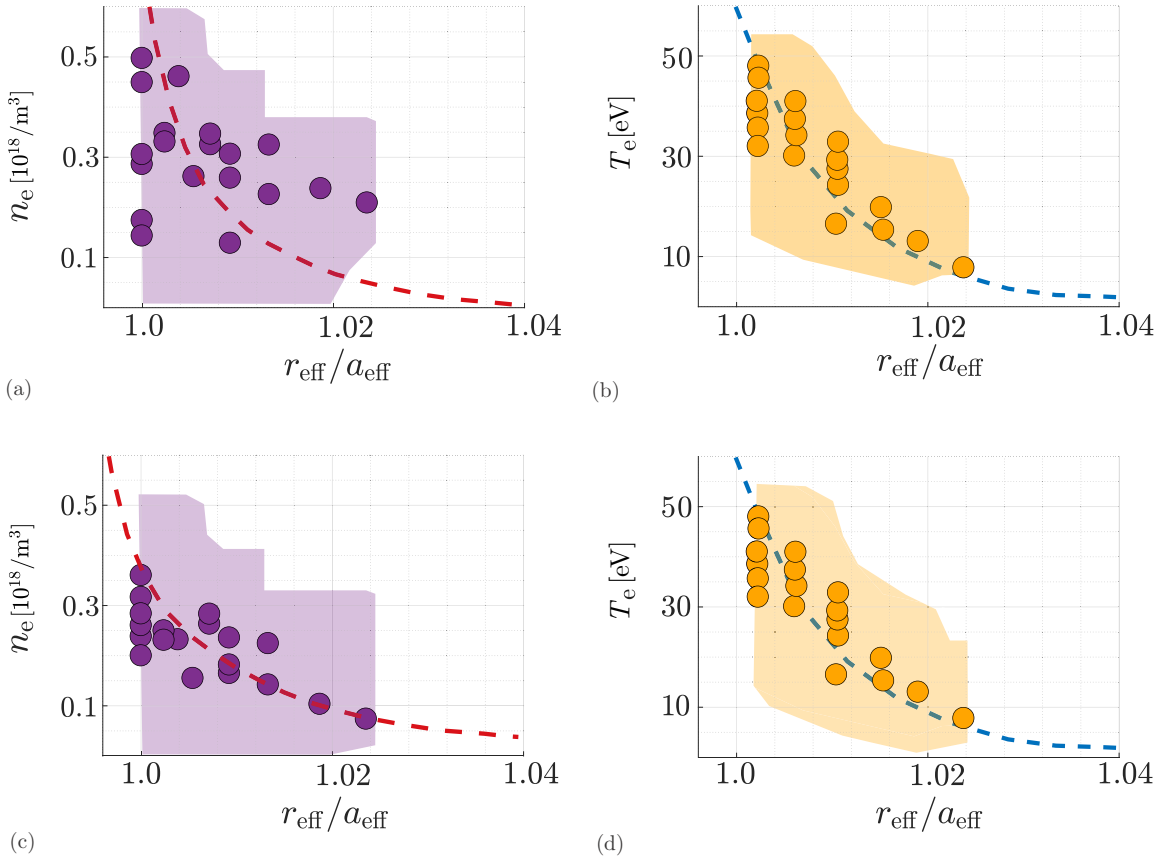

Figure 4.12: Final comparison between EMC3-EIRENE simulation (dashed) and $Z_{eff}^{l_{end}}$ adjusted Limiter Langmuir probe measurements (dots). Plot (a) shows n_e, and (b) shows T_e. Simulation parameters used are from plasma scenario $\Lambda^{l_{end}}$ of iterative process $\Xi_{c_s^{single*}}$. Subfigures (c) and (d) are the same plots as (a) and (b) but for process $\Xi_{c_s^{multi}}$.

correct and consistently assessed profiles. EMC3-EIRENE simulations provide overall consistent profiles between MPM and limiter Langmuir probe measurements and more reasonable estimations of Z_{eff} and m_{eff}. Resulting final profiles of plasma scenario $\Lambda^{l_{end}}$ and reinterpreted MPM and limiter Langmuir probe measurements are shown in Figure 4.11 (MPM, (c) and (d)) and Figure 4.12 (limiter Langmuir probes, (c) and (d)). Profiles assessed in each iterative step l are shown in the appendix A. Refined measurement datasets lie at the bottom end of the error bars (a negative deviation between profiles) for the unrefined $n_{e,MPM}$ profiles in Figure 4.4. Hence, a refinement of Langmuir probe measurement results seems unnecessary at first sight. A simple explanation can be found in the amount of impurity contamination in simulation Λ. Effective charge states peaking for each iterative steps l around 1.4 show relatively clean plasma for OP1.1 limiter plasmas. This might be caused by the choice of target boundary condition. Impurities stream into the plasma until the constrained portion of radiated power is lost over them. The fraction of $P_{heat}^{SOL}/P_{rad}^{SOL}$ raises to a critical parameter. If a plasma would lose all its heating power over radiation, $P_{heat}^{SOL}/P_{rad}^{SOL}$ equals 1. The complete heating

power is lost over radiation on impurities and would be immediately terminated. However, Figure 4.1 shows a fraction $P_{\text{heat}}^{\text{SOL}}/P_{\text{rad}}^{\text{SOL}} = 2.5$, and thus a plasma scenario with a decreased potential for impurity heat rad contamination.

A repetition of the discussed $\Xi_{c_s^{\text{single}*}}$ iterative process with c_s^{multi} follows the same route to converged plasma profiles. The iterative process based on c_s^{multi} is referred to by $\Xi_{c_s^{\text{multi}}}$. Iterative steps concluded with c_s^{multi} are hereafter referred to using m. Therefore, the first simulation setup $\Lambda = \Lambda^{l=1} = \Lambda^{m=1}$ is identical for iterative processes $\Xi_{c_s^{\text{single}*}}$ and $\Xi_{c_s^{\text{multi}}}$. The profiles in Figure 4.4 are again applied as initial references, and then c_s^{multi}, Z_{eff}, and m_{eff} profiles are deduced and used to rework $n_{\text{e,MPM}}$ and $n_{\text{e,LP}}$. Figure 4.13 presents a direct comparison with Figure 4.8. The difference for a direct comparison

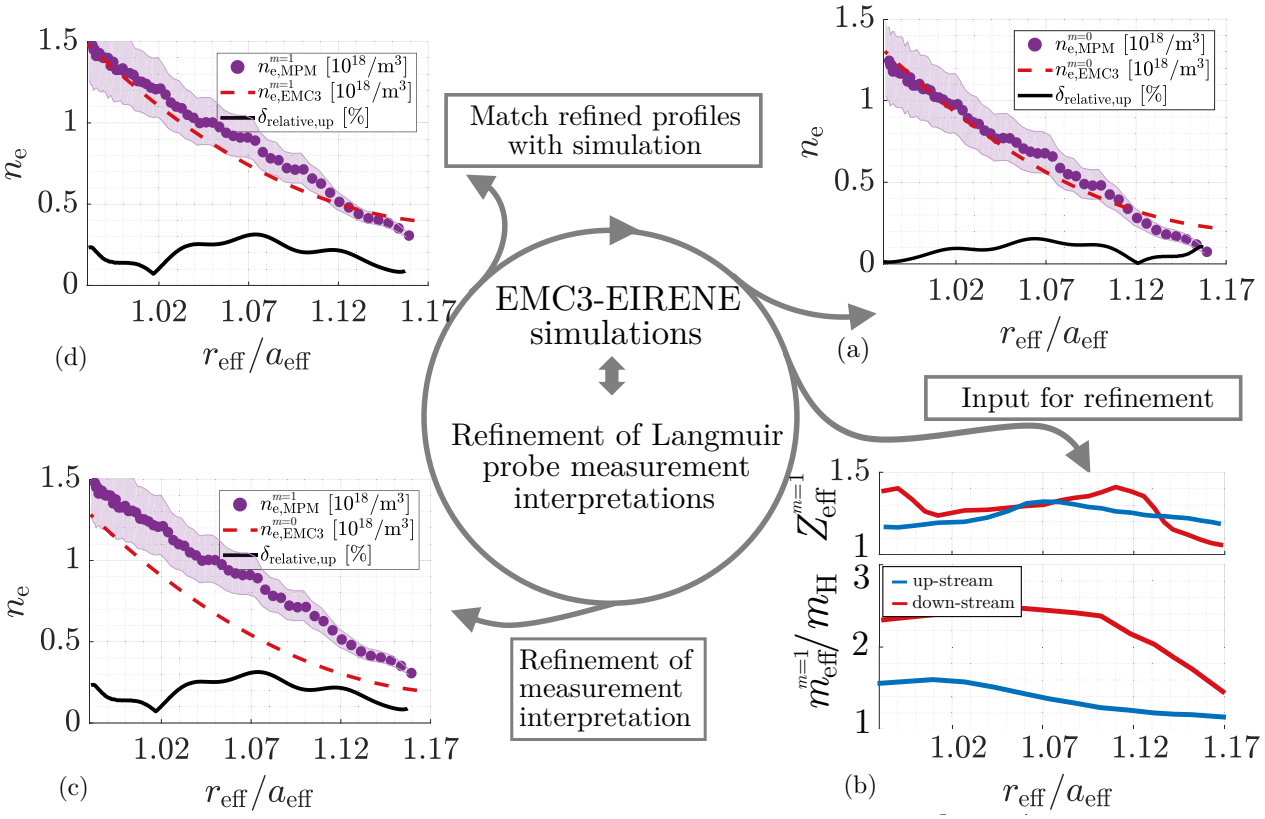

Figure 4.13: The same Figure as 4.9, but for the iterative process $\Xi_{c_s^{\text{multi}}}$.

between iterative processes $\Xi_{c_s^{\text{single}*}}$ and $\Xi_{c_s^{\text{multi}}}$ remains quite marginal (see Figure 4.8 vs. Figure 4.13 and Figure 4.9 vs. Figure 4.14). However, $n_{\text{e,MPM}}$ profiles are shifted to higher density values for $m = 1$ rather than lower density values for $l = 1$. Reworked measured electron density profiles show roughly the same percentile change in the first iterative steps $l = m = 1$, a first indication of a similar convergence as for process $\Xi_{c_s^{\text{multi}}}$ compared with $\Xi_{c_s^{\text{single}*}}$. Hence, the quantified error $\delta_{\Omega_{12}}$ between $c_s^{\text{single}*}$ and c_s^{multi} is not expected to affect the convergence of the $\Xi_{c_s^{\text{single}*}}$ and $\Xi_{c_s^{\text{multi}}}$.

A direct comparison between Figures 4.10 and 4.15 shows a first indication of the $\Xi_{c_s^{\text{multi}}}$ convergence trend, which is confirmed. The relative change for Z_{eff}, m_{eff}, and n_e^m converge to values below 5% for

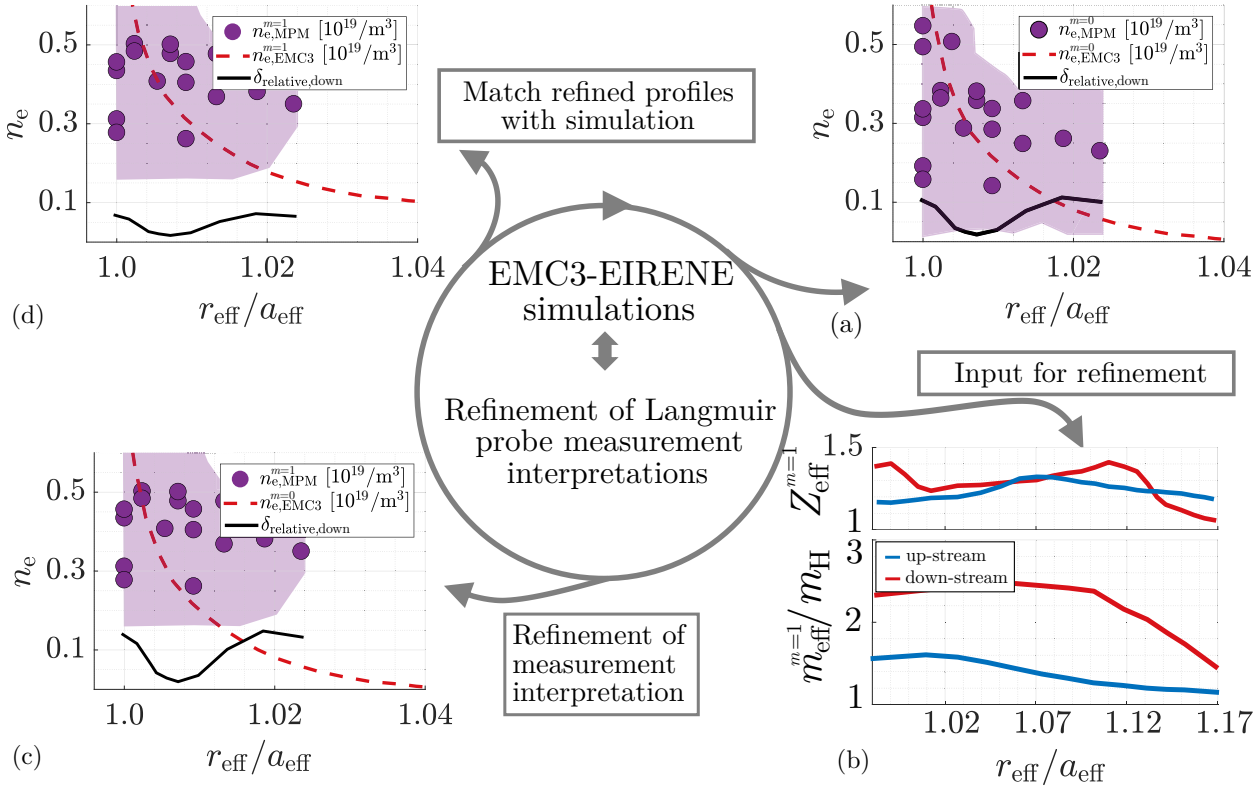

Figure 4.14: The same Figure as 4.9 but for iterative process $\Xi_{c_s^{\text{multi}}}$ applied on limiter Langmuir probes

both Langmuir probe measurement locations. A considerable difference between processes $\Xi_{c_s^{\text{single*}}}$ and $\Xi_{c_s^{\text{multi}}}$ is the magnitude of ϵ^m versus ϵ^l . Since $\epsilon^{m=1} > 1$ is given for $m = 1$, $n_{\text{e,MPM}}$, and $n_{\text{e,LP}}$ profiles are shifted to higher values. Z_{eff} and m_{eff} profiles peak at higher values for process $\Xi_{c_s^{\text{multi}}}$ than for $\Xi_{c_s^{\text{single*}}}$ (see Figure 4.8(b) versus Figure 4.13(b)), which results in a different and more drastic change in $n_{\text{e,MPM}}$. However, the overall convergence trend of process $\Xi_{c_s^{\text{single*}}}$ is re-established with the use of Z_{eff} and m_{eff} for the next iterative steps.

Figure 4.13 shows refined limiter measurement datasets compared with the EMC3-EIRENE plasma scenario $\Lambda^{l_{\text{end}}}$ for iterative processes $\Xi_{c_s^{\text{single*}}}$ and $\Xi_{c_s^{\text{multi}}}$. The electron density was refined by 8% (see Figure 4.11) compared with a refinement of 12% applied to up-stream profiles for process $\Xi_{c_s^{\text{single*}}}$; 7.6% and 19% are the MPM and limiter Langmuir probe refinement values for process $\Xi_{c_s^{\text{multi}}}$, respectively. In summary, initial assumptions that Z_{eff} and m_{eff} equal 1 are proven plausible. At first glance, reinterpreting Langmuir probe measurements appears to be irrelevant and incorrect. This incorrectness corresponds to the limiter measurement location that is contaminated with heavier and higher charged impurities than the MPM measurement location (see Figure 4.6). At first, one would expect a stronger refinement for the limiter measurement profiles than for the MPM profiles, because limiter taken Z_{eff} and m_{eff} profiles exceed those from the MPM. However, the proportionality of $Z_{\text{eff}}/m_{\text{eff}}$ must be studied because the speed of sound (4.0.1.2) is affected by Z_{eff} in the nominator and

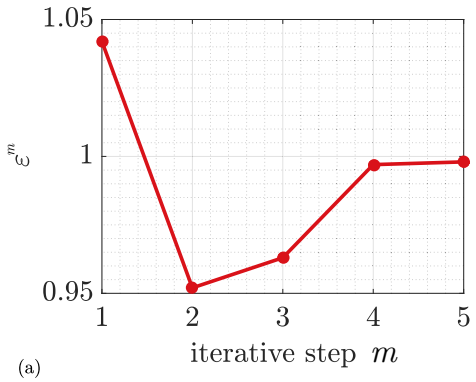

(a)

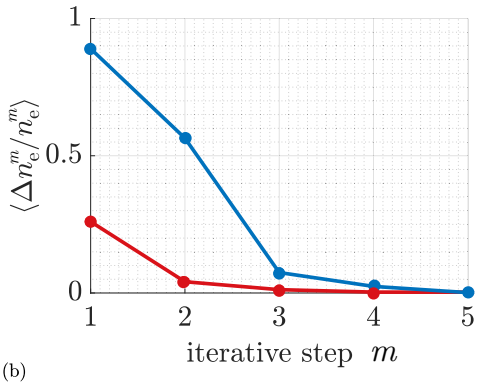

(b)

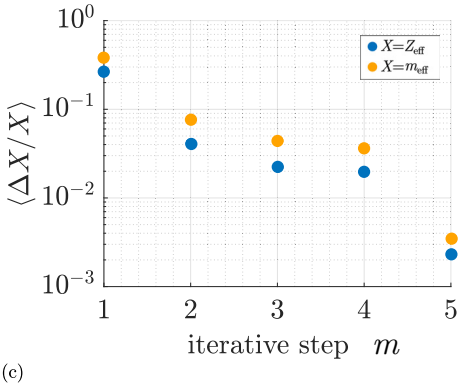

(c)

step l	input density [m^3/10^{18}]	ε^m	$\langle \Delta Z_{\rm eff}/Z_{\rm eff} \rangle$	$\langle \Delta m_{\rm eff}/m_{\rm eff} \rangle$	$\langle \Delta n_{\rm e,MPM}^l / n_{\rm e,MPM}^l \rangle$
1	3	1.042	0.2302	0.3849	0.26
2	3.126	0.952	0.0413	0.0762	0.0413
3	2.9786	0.963	0.0221	0.0439	0.0121
4	2.87	0.997	0.0199	0.0357	0.0032
5	2.8432	0.998	0.0023	0.0035	0.003

(d)

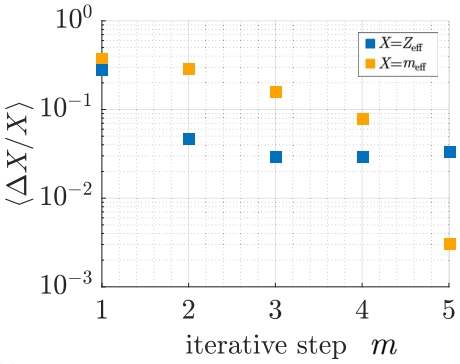

(e)

step l	input den [m^3/10^{18}]	ε^m	$\langle \Delta Z_{\rm eff}/Z_{\rm eff} \rangle$	$\langle \Delta m_{\rm eff}/m_{\rm eff} \rangle$	$\langle \Delta n_{\rm e,MPM}^l / n_{\rm e,MPM}^l \rangle$
1	3	1.042	0.2952	0.369	1.12
2	3.126	0.952	0.0474	0.2853	0.564
3	2.9786	0.963	0.0292	0.1574	0.0745
4	2.87	0.997	0.0289	0.0783	0.024
5	2.8432	0.998	0.0336	0.003	0.0014

(f)

Figure 4.15: The same Figure as 4.10 but for ϵ^m.

m_{eff} in the denominator. Proportionality $c_s \propto Z_{\mathrm{eff}}/m_{\mathrm{eff}}$ does not vary much between the up – stream

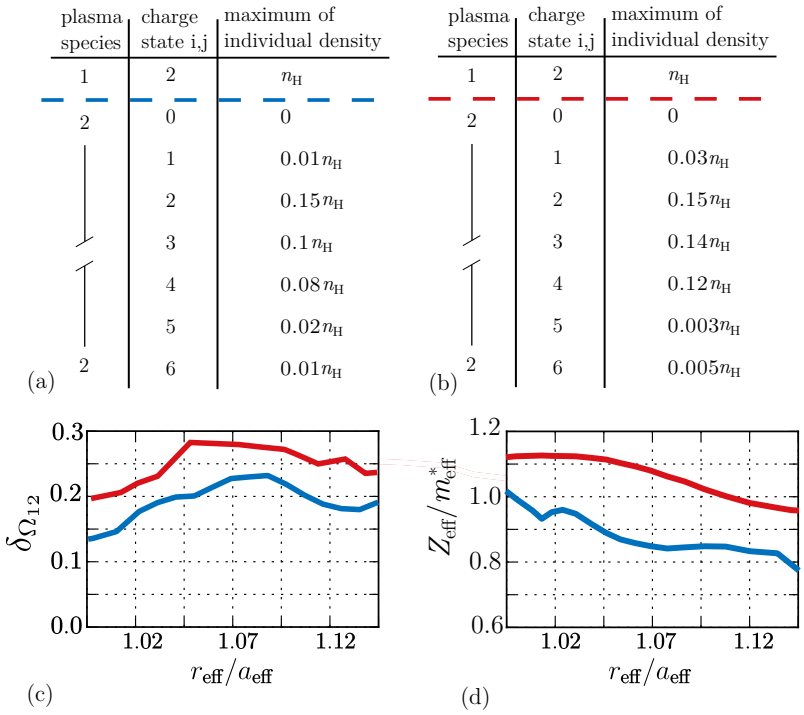

Figure 4.16: Overview of the errors caused by the assumption Ω for δ_{Omega} for the EMC3-EIRENE simulation $\Lambda^{l_{\mathrm{end}}}$ at the limiter (red) and MPM (blue) Langmuir probe positions in (c). The error estimations are calculated with values shown in chart (a) for up-stream and (b) down-stream. The proportionality $c_s \propto Z_{\mathrm{eff}}/m^*_{\mathrm{eff}}$ plotted in (d) of process $\Xi_{c_s^{\mathrm{single}*}}$. The effective mass is normed to the hydrogen mass $m^*_{\mathrm{eff}} = m_{\mathrm{eff}}/m_{\mathrm{H}}$.

and limiter Langmuir probe's position in Figure 4.16. Hence, the effects of a highly effective charge state are suppressed because this comes with a higher effective mass. Plasma scenarios with Z_{eff} values exceeding $m_{\mathrm{eff}}/m_{\mathrm{H}}$ do not follow this suppression. One can infer that a plasma scenario with higher heating powers would provide such a case.

Each simulation is accompanied by a scan over the initially guessed or experimentally (not fully) specified free input parameters (with possible large spatial uncertainties of the bolometric power measurement, see subsection 2.3.2), such as the diffusion coefficient $D_\perp$ and radiated power in the $P^{\mathrm{SOL}}_{\mathrm{rad}}$. This scan results in a sensitivity study to cover the influence of these free input parameters. The diffusion coefficient $D_\perp$ is chosen in $D_\perp \in [0.4,\ 0.5,\ 0.6]$ m^2/s and $P^{\mathrm{SOL}}_{\mathrm{rad}}$ is chosen in $P^{\mathrm{SOL}}_{\mathrm{rad}} = [60,\ 120,\ 180]$ kW for each iterative step l . The variation of $D_\perp$ and $P^{\mathrm{SOL}}_{\mathrm{rad}}$ resulted in profiles, which again show consistency between $n_{\mathrm{e,EMC3}}$ and $n_{\mathrm{e,MPM}}$ (for each iterative step l). The resulting change of $n_{\mathrm{e,EMC3}}$ is observable in the enclosed area of $n^{D}_{\mathrm{e,EMC3}}$ and $n^{P_{\mathrm{rad}}}_{\mathrm{e,EMC3}}$ of Figure 4.17. The overlap of $n_{\mathrm{e,EMC3}}$ and measured $n_{\mathrm{e,MPM}}$ (with error bars) remains high; thus, the consistency between $n_{\mathrm{e,EMC3}}$ and measured $n_{\mathrm{e,MPM}}$ is preserved concerning the variations in $D_\perp$ and $P^{\mathrm{SOL}}_{\mathrm{rad}}$. However, the variations

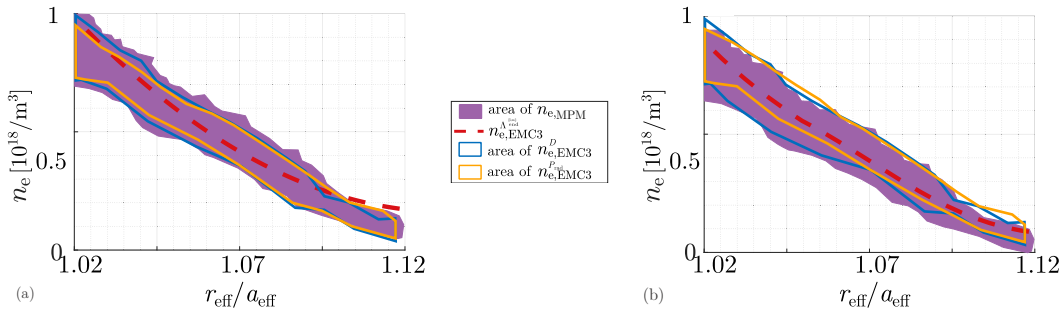

Figure 4.17: Overview of the influence of a variation over D and $P_{\mathrm{rad}}^{\mathrm{SOL}}$ on $n_{\mathrm{e,EMC3}}$, plotted in translucent areas that entail the simulation results for $n_{\mathrm{e,EMC3}}^{D}$ and $n_{\mathrm{e,EMC3}}^{P_{\mathrm{rad}}^{\mathrm{SOL}}}$ (plotted in comparison to the magenta shaded area of $n_{\mathrm{e,MPM}}$ and $n_{\mathrm{e,EMC3}}^{\Lambda^{l}_{\mathrm{end}}}$ as a guide for the eye). Results of process $\Xi_{c_s^{\mathrm{single}*}}$ in (a), process $\Xi_{c_s^{\mathrm{multi}}}$ in (b).

in $D_{\perp}$ and $P_{\mathrm{rad}}^{\mathrm{SOL}}$ result in quite large spans for $n_{\mathrm{e,EMC3}}^{D}$ and $n_{\mathrm{e,EMC3}}^{P_{\mathrm{rad}}}$. This is acceptable because the compared Langmuir probe measurements exhibit larger uncertainties than does the variation span.

4.0.3 Influence of main impurities and their quantification on limiter plasmas

Adding oxygen to the considered plasma scenario allows for an opportunity to study the effect of plasmas with a higher number of impurity species. The lost power in the SOL is now radiated over carbon plus additional oxygen impurities. An additional free simulation parameter is introduced to whichever fraction of $P_{\mathrm{rad}}^{\mathrm{SOL}}$ is lost over carbon ($P_{\mathrm{rad}}^{\mathrm{C}}$) and to whichever over oxygen ($P_{\mathrm{rad}}^{\mathrm{O}}$). Thus, an initial guess $P_{\mathrm{rad}}^{\mathrm{C}}/P_{\mathrm{rad}}^{\mathrm{O}}$ is required. Target elements exposed as limiter consist of carbon, thereby defining a natural location for a carbon source. By contrast, oxygen could reach the main plasma via several ways. A release by outgassing from first-wall elements must be considered, and thus, an oxygen source model is applied to treat this outgassing. 15 polodially distributed oxygen point sources are implemented for 36 toroidal planes; hence, 540 oxygen point sources are uniformly distributed along the wall (see Figure 4.18). With a fixed total radiation power $P_{\mathrm{rad}}^{\mathrm{SOL}}$, the total carbon and oxygen release rates are adjusted, respectively, to meet the required radiation fraction $P_{\mathrm{rad}}^{\mathrm{C}}/P_{\mathrm{rad}}^{\mathrm{O}}$ in such a manner that the overall impurity source rates provide the requested $P_{\mathrm{rad}}^{\mathrm{C}}$ and $P_{\mathrm{rad}}^{\mathrm{O}}$ radiation losses. From this and the EMC3-EIRENE model's output, the required carbon and oxygen release rates are interfered.

A new iteration between experimental datasets and simulations is started for each chosen ratio $P_{\mathrm{rad}}^{\mathrm{C}}/P_{\mathrm{rad}}^{\mathrm{O}}$. This iteration follows the scheme of the aforementioned iterative process. The input parameter of the radiated power in the SOL $P_{\mathrm{rad}}^{\mathrm{total}} = (P_{\mathrm{rad}}^{\mathrm{C}} + P_{\mathrm{rad}}^{\mathrm{O}})$ is still constrained by the bolometric power measurement (see subsection 2.3.2). Furthermore, a scan over the range from $P_{\mathrm{rad}}^{\mathrm{O}} = 0.1$ to 0.9 is conducted. Subsequently, the fraction of 0.1 corresponds to predominantly carbon-polluted plasma, such as plasma scenario Λ. A carbon-polluted plasma scenario Λ^{C} and an oxygen-polluted

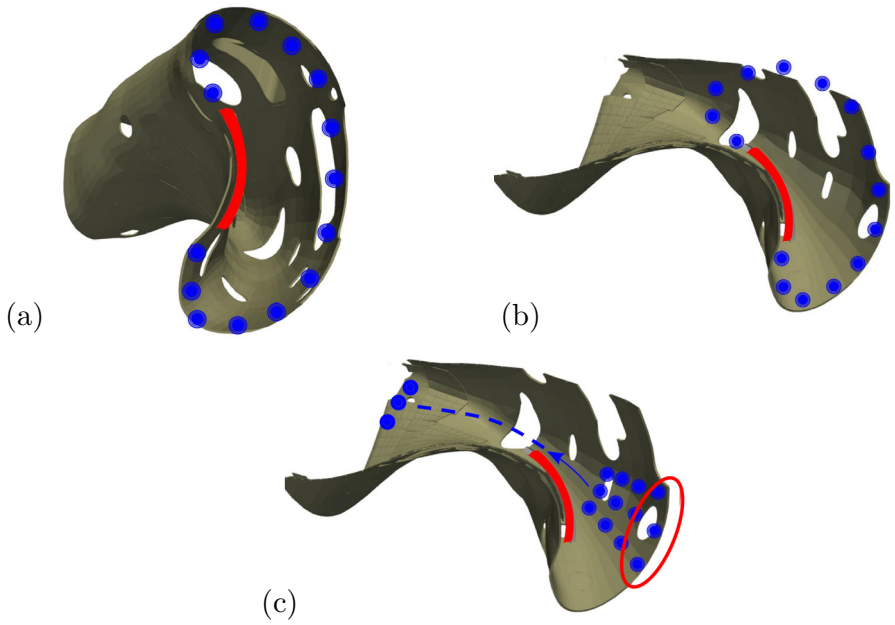

Figure 4.18: Schematic (1/10) of the W7-X covered by the computational domain: (a) shows the first toroidal sector element with additional oxygen point sources uniformly distributed poloidally; (b) shows the same sector from a different angle; and (c) shows the distribution of three exemplary oxygen point sources (marked in red) along each toroidal sector. In all three schematic plots, the impurity source for carbon impurities (originating from the limiter tiles) are indicated by red tiles.

plasma scenario Λ^O use the input parameters in Figure 4.1. Simulation results shown for the variation

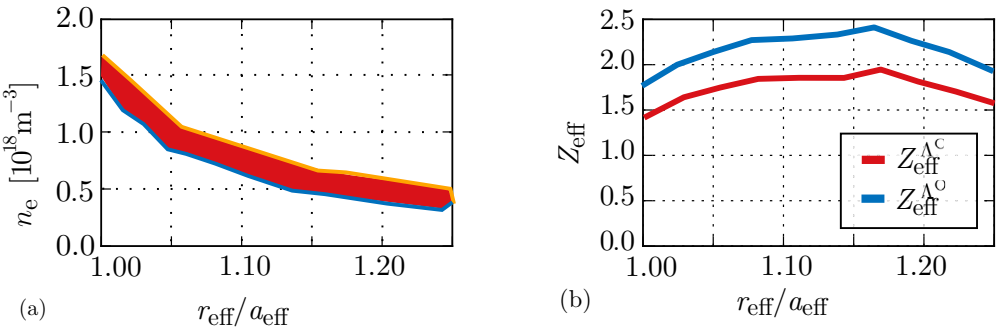

Figure 4.19: All seven resulting n_e profiles from the scan of $P^O_{rad}/P^{total}_{rad} \in \{0.1,...,0.9\}$ plotted in the red-shaded region shown in (a). Carbon dominant case Λ^C (orange) and oxygen dominant case Λ^O (blue) frame the set of n_e data sets. Subfigure (b) shows the Z_{eff} profiles of Λ^C and Λ^O.

of P^C_{rad}/P^O_{rad} (see Figure 4.19 (a) and (b)) are framed by the simulation using Λ^C (mainly C impurities) on the bottom and by the simulation using Λ^O (mainly O impurities) on the top. The influence of

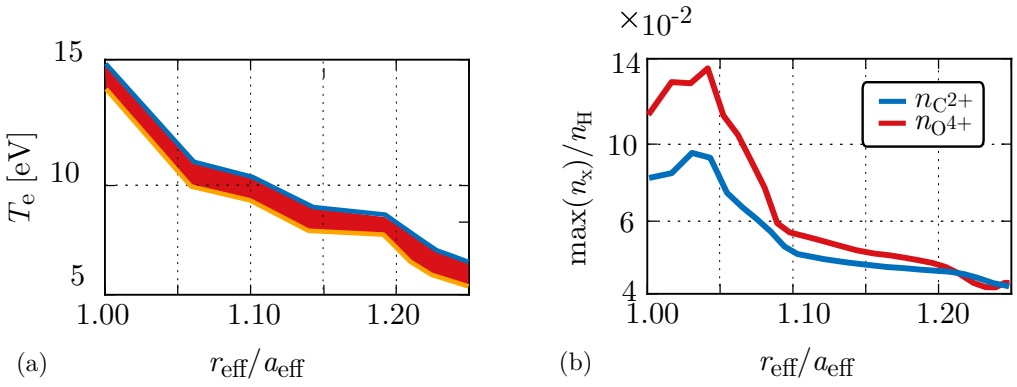

Figure 4.20: The same Figure as 4.19, but T_e and the highest carbon and oxygen impurity charge state are shown.

the variation of P^{C}_{rad}/P^{O}_{rad} is notable in Figure 4.19, but remains quite small on n_e (see Figure 4.19(a)). Becauseof the approach chosen for postprocessing, the electron density in the oxygen-dominant plasma $n^{\Lambda^C}_{e,EMC3}$ exceeds the electron density $n^{\Lambda^O}_{e,EMC3}$, because the number of ionization states of oxygen in the computational domain exceeds that of carbon. Then, the complete radiated power is lost over fewer oxygen impurities than carbon impurities. The major contribution to the overall electron density from a single impurity charge state density must differ between carbon and oxygen. This is observable in Figure 4.20(b), where the major contribution of carbon is the second charge state as well as that of oxygen is the fourth charge state. This difference occurs in a direct comparison of the effective charge state profiles (see Figure 4.19(b)). Here, $Z^{\Lambda^C}_{eff}$ values lie below values of $Z^{\Lambda^O}_{eff}$. The EMC3 impurity model does not treat the attenuation effect of n_e. An a posteriori approach is chosen to consider the contribution of each ionization state to the electron density of the main plasma during postprocessing.

In Figure 4.20(a), the effect of the change in P^{C}_{rad}/P^{O}_{rad} is not highly pronounced for T_e either (compared with the effect of n_e). However, it is crucial to note that the $T_e^{\Lambda^C}$ profile lies above the $T_e^{\Lambda^O}$ profile (see Figure 4.20). The plasma is slightly cooled because heavier impurities reach the plasma in case of higher oxygen fractions. The influences of the assessed Z_{eff} and m_{eff} become demanding. In section 4.0.2, only carbon impurities were included in the refinement of Langmuir porbe measurements. Here, the question arises of whether the results of the iterative processes (shown in Figure 4.11) undergo a significant change when oxygen is introduced to the plasma. Thus, the aforementioned iterative process $\Xi_{c_s}^{single*}$ is conducted for the carbon dominant Λ^C and oxygen dominant Λ^O plasma. Only final results are compared because the scheme of process $\Xi_{c_s}^{single*}$ is unchanged. A direct comparison of $n^{\Lambda^C}_{e,EMC}$ and $n^{\Lambda^O}_{e,EMC}$ with the refined MPM measurement results of Figure 4.11(a) shows only a marginal difference between the carbon- and oxygen-dominant plasmas (see Figure 4.21). Figure 4.21 indicates that consistency is maintained for the full range of studied C/O ratios, between

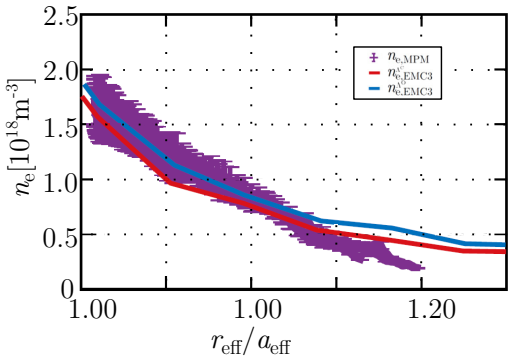

Figure 4.21: Comparison of the rederived $n_{\mathrm{e,MPM}}$ (with $n_{\mathrm{e,EMC3}}^{\Lambda^{\mathrm{C}}}$ and $n_{\mathrm{e,EMC3}}^{\Lambda^{\mathrm{O}}}$) and density profiles from simulations Λ^{C} and Λ^{O}, which were both obtained after the iterative process described in section 2.4 and 4.8.

reinterpreted Langmuir probe datasets and the EMC3-EIRENE n_{e} profiles after the iterative process is applied. Using this justification, one can infer the corresponding impurity release rates for O and C as the next step. The corresponding release fraction (relative to the incident hydrogen flux) $R_{\mathrm{EMC3}}^{\{\mathrm{H}\rightarrow\mathrm{C,O}\}}$ by EMC3-EIRENE is stored as an output separately for each impurity species. Figure 4.22 shows the

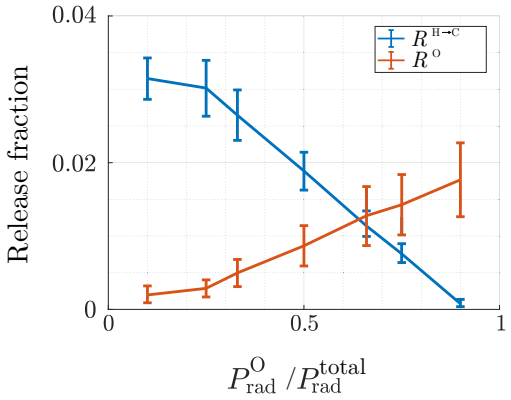

Figure 4.22: Release fraction $R_{\mathrm{EMC3}}^{\{\mathrm{H}\rightarrow\mathrm{C,O}\}}$ using plasma edge modeling plotted against each simulation setup of the scan of $P_{\mathrm{rad}}^{\mathrm{O}}/P_{\mathrm{rad}}^{\mathrm{total}} \in \{0.1,...,0.9\}$ reaching from the carbon-dominant plasma (Λ^{C}, left-hand side) to the oxygen-dominant plasma (Λ^{O}, right-hand side).

resulting release rates for each simulation of the scan over $P_{\mathrm{rad}}^{\mathrm{O}}/P_{\mathrm{rad}}^{\mathrm{total}} \in \{0.1,...,0.9\}$ With increasing oxygen contributions to $P_{\mathrm{rad}}^{\mathrm{total}}$, the release rate of carbon drops linearly. This linearity is also to be expected from the (linear) impurity code model, in which the direct attenuation effects of impurities on electron densities are neglected. The crossover point with a higher release rate for oxygen than for carbon is reached at approximately $P_{\mathrm{rad}}^{\mathrm{O}}/P_{\mathrm{rad}}^{\mathrm{total}} \approx 0.7$, ending at the uppermost level of the scan at Λ^{O}. Plausible and frequently used empirical chemical release rates for carbon can be found in [56] are

often taken to be $R^{H \rightarrow C} = 0.02$. Here, this carbon release rate corresponds to a case where approximately 50% of the power is radiated through carbon and 50%through oxygen. Figure 4.22 depicts the previously discussed influence of these two impurity species on the spatially resolved effective charge state distribution function. This clearly indicates that a significant overall oxygen source may exist in the system in addition to the expected limiter carbon release rate.

CHAPTER 5

PLASMA EDGE MODELING FOR THE DIVERTOR CONFIGURATION OF W7-X

This chapter follows roughly the same structure as Chapter 4. However, some differences from the previous chapter's structure exist because of the difference between limiter and divertor plasmas (see Table (a) and (b) in Section 2.2). Limitations on the discussed EMC3 impurity model are reached by a given combination of plasma heating and radiated power. Thus, the first key question of this chapter is as follows,

- *What are the limits on the applied interpretative studies and hence the limits of the impurity transport code?*

From here, the same structure of the interpretative impurity study shown in Chapter 4 is followed. However, the same amount of plasma edge diagnostics is not available for a single plasma scenario. The resulting key questions are as follows,

- *Which plasma edge diagnostics enable a direct or indirect measurement of the effective charge state density? How do these values compare with numerical results?*

The Thomson scattering system [57] provides a direct insight into a line integrated effective charge state value, which is compared with numerical results from the interpretative study (3D resolution). From there, the next key questions are as follows,

- *What are the results of the re-applied interpretative impurity study (from limiter plasmas; see Chapter 4)? Which predictions can be made?*

The same study is applied to answer this key question. However, the introduced interpretative process is stretched to its limits by the plasma's high impurity content. Nevertheless, predictions are possible and provided at the end of this chapter. Then, numerical results from the interpretative impurity studies for limiter and divertor plasmas are directly compared to answer the last key question of this chapter,

- *What insights are gained from a direct comparison of limiter and divertor plasmas?*

5.1 Study of impurity content and transport in the divertor plasma

The discussed OP1.1 studies, including the iterative process between Langmuir probe measurements and EMC3-EIRENE simulations as well as the assessment of carbon and oxygen release fractions, can be applied to the operational phase of OP1.2. Key facts about operational phase OP1.2, a divertor configuration, were introduced in section 2.1 and subsection 2.1.2. Again, constraints for EMC3-EIRENE input parameters ($P_{\text{heat}}^{\text{SOL}}$, $P_{\text{rad}}^{\text{SOL}}$, n_{e}, and T_{e}) must be found by conducted Langmuir measurements and bolometric power measurements on suitable reference plasmas. However, only a single plasma setup can be used as reference because the number of duplicated—and thus reproduced plasmas recorded by the MPM—is low in contrast to OP1.1. This study selects the construction of a typical plasma scenario as the first step with the following parameters $P_{\text{heat}}^{\text{SOL}} = 0.8$ MW, $P_{\text{rad}}^{\text{SOL}} = 0.5$ MW, an input density of 0.4×10^{18} m^{-3}, and an electron temperature of 50 eV. This typical simulation setup is referred to as Υ. Simulation parameters are orientated on the MPM measuring the plasmas. Measurements on these helium plasmas are not comparable to hydrogen EMC3 simulations because the main plasma is different. However, helium plasmas guide simulations setups, which push the EMC3 impurity model to its limits. The effects that occur are discussed in the following section.

5.1.1 Code artifacts from high radiation losses

$P_{\text{heat}}^{\text{SOL}}/P_{\text{rad}}^{\text{SOL}}$ has a significant percentage difference between OP1.1 to OP1.2 plasmas, and thus Υ is chosen. The considered OP1.1 plasmas (numbers 20160308.22 – 24) have smaller radiation losses than the OP1.2 plasma (20171026.38) with $P_{\text{heat}}^{\text{SOL,OP1.2}}/P_{\text{rad}}^{\text{SOL,OP1.2}} = 1.6 \ll 11 = P_{\text{heat}}^{\text{SOL,OP1.1}}/P_{\text{rad}}^{\text{SOL,OP1.1}}$. Such high radiated powers only occur in plasma with main components of a higher charge number Z . These may be introduced to the plasma by the remaining gases of the previous plasma or in vessel components. The initial guessed free cross-field transport parameters remain the same as for OP1.1, and are set as $D_{\perp} = 3\chi_{\text{e},\perp} = 3\chi_{\text{i},\perp}$. The same initial comparison scheme of LP measurements versus EMC3- EIRENE reference simulations from OP1.1 (see Chapter 4) is applied for OP1.2 and simulation Υ. The typical electron density near the LCFS of $n_{\text{e}} = 0.4 \times 10^{18}$ m^{-3} is set as the core boundary condition; furthermore, an initial electron temperature of $T_{\text{e}} = 40$ eV for the main plasma is assumed at the same position. A more precise mean coordinate $\langle z \rangle_{\text{Pin}i}$ was introduced in subsection 2.3.1 to differentiate between different MPM plasma profiles (where i was the number of used MPM Langmuir probe pins). Characteristics in Langmuir probe profiles change drastically if a magnetic island is passed through by the MPM probe head.

These islands occur through active perturbations of the magnetic field $\boldsymbol{B}$. Then, an island is formed by nested magnetic flux surfaces and is limited by continuous flux surfaces. Furthermore, a flux tube is formed, which runs toroidally alongside the unperturbed flux surfaces. The inner magnetic island topology is separated from the overall SOL magnetic topology. The same periodicity variables defined in Chapter 2.2 can be applied to characterize the shape of two magnetic islands. The poloidal

symmetry is given by m and the toroidal one is given by n,

$$\frac{m}{n} = \frac{1}{\iota} \tag{5.1.1.1}$$

The coordinates of the magnetic field line are given by $\theta_B = n\phi/m$ because $\theta_B = 2\pi\iota$ is at a poloidal angle, $\phi = 2\pi$. A poloidal displacement $\Delta\theta$ is found between two magnetic islands,

$$\Delta\theta_{\text{island}} = \theta_{\text{island}} - \frac{n}{m}\phi = \theta_{\text{island}} - \iota\phi \tag{5.1.1.2}$$

Intentionally, magnetic islands are created by the radial component $\boldsymbol{B}$ with the amplitude b_r and a periodicity in $\Delta\theta_{\text{island}}$,

$$B_r(r, \Delta\theta_{\text{island}}) = b_r(r)\sin(m\theta_{\text{island}} - n\phi) \tag{5.1.1.3}$$

The radial expansion of the island is given by the magnetic shear of $\boldsymbol{B}$, and the island has a width of w [17],

$$w \approx 4 \cdot \sqrt{\frac{r_0^2 b_r}{m B_\theta s(r_0)}} \tag{5.1.1.4}$$

The radial coordinate of the island's center is r_0, which has a magnetic shear of s. From equation 5.1.1.4 follows that the island width is strongly correlated to the amplitude of the toroidal magnetic field B_θ of $\boldsymbol{B}$. Such islands do occur in tokamak plasmas if a distortion occurs in the plasma-driven current, which is followed by an increase in perpendicular transport. Magnetized vessel installations of diagnostics, can produce distortions in the magnetic field to create island structures. However, the W7-X favors island structures because of its island divertor concept.

The W7-X uses an island divertor configuration (discussed in section 2.1.2). Intersected islands are a feature of this heat-diverting concept. The "D-shaped" cross-section shows the intersected island in Figure 2.11. Particles trapped by the internal closed magnetic topology of the island remain in the plasma longer than do particles traveling on an open magnetic flux surface of $\boldsymbol{B}$. The consequence is that n_e and T_e cluster in the island, which may be recorded by the Langmuir probes of the MPM if the probe head intersects such an island structure. A distinct plasma temperature and density peak would be observable in an MPM probe profile. Figure 5.1 shows an exemplary plasma cross-section of the divertor configuration adapted from Figure 2.4. Magnetic islands are a feature of OP1.2's magnetic configuration. In the exemplary Figure 5.1, the SOL electron density is assumed to be equal to 1, whereas the density within the magnetic island ramps up to 2 and 3 (values given in [$a.u.$]). Notably, the abrupt n_e jumps shown in Figure 5.1 are not realistic and rather are a feature of the assumption about n_e for the example. The Langmuir probe of the MPM records a density peak within the magnetic islands, as shown at the bottom of Figure 5.1. Thus, the created computational domain (following the scheme of subsection 3.4) must feature these types of island structure to obtain consistency between simulations and MPM measurements. Similarly, consistent results between OP1.1 EMC3-EIRENE simulations and Langmuir probe measurements should be obtained for OP1.2

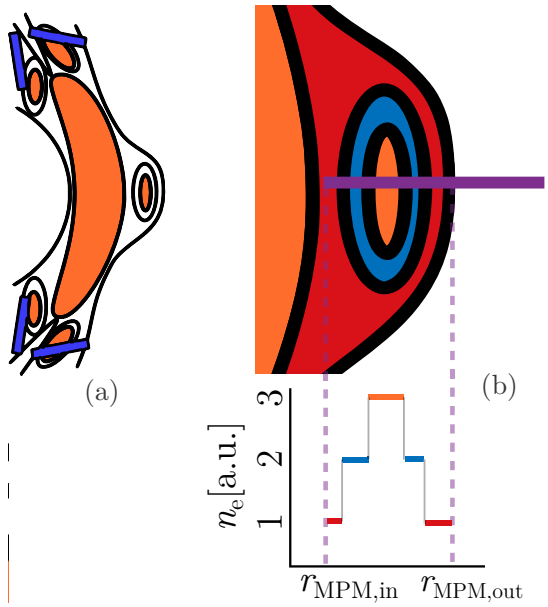

Figure 5.1: (a) Poloidal cross-section adapted from Figure 2.4 shown on the left hand side; (b) magnification of the magnetic island on the right-hand side of the cross section. The magenta line depicts an arbitrary Langmuir probe plunge path. An exemplary plasma consists of different electron densities in [a.u.], red= 1, blue= 2 and orange= 3. The measured electron density profile is shown at the bottom of (b).

setups.

Clusters of n_e and T_e do not have to be uniformly distributed in the cross-section of the island nor along the toroidal expansion of the island. Input parameter studies of simulation Υ are performed to check whether the cluster formation within the island is strongly connected to the chosen input density. The input density changes from 0.4×10^{18} m^{-3} to 1×10^{19} m^{-3}. Only a drop in the plasma temperatures, at first sight, is observable in Figures 5.2 and 5.3. Lower plasma temperatures in a denser plasma are a consequence because the same heating power is applied to more particles in the same plasma volume. However, divertor target plates are observable in the teardrop cross-section in Figure 5.2(c) and 5.3(c), because the open flux surface ends there. But, the anticipated island structure shown in Figure 2.11 is not reproduced, and therefore, changes in the input densities must be excluded as a reason for obtain distinct magnetic island characteristics in the presented cross-section.

This changes whether the chosen heating power is varied through the ECRH system. In the present study, a shared heating power $P_{\text{heat}}^{\text{SOL}}$ is equally distributed over the electrons and ions. This might seem inconsistent with the discussed ECRH heating mechanism [24] where electrons are heated; however, ion heating can result from collisional energy transfer from heated electrons [22]. Thus, a uniform heating distribution is applied to favor this kind of plasma state. Initial ion temperatures are ampli- fied by the higher amount of $P_{\text{heat,i}}^{\text{SOL}}$ than for a plasma setup where the complete heating

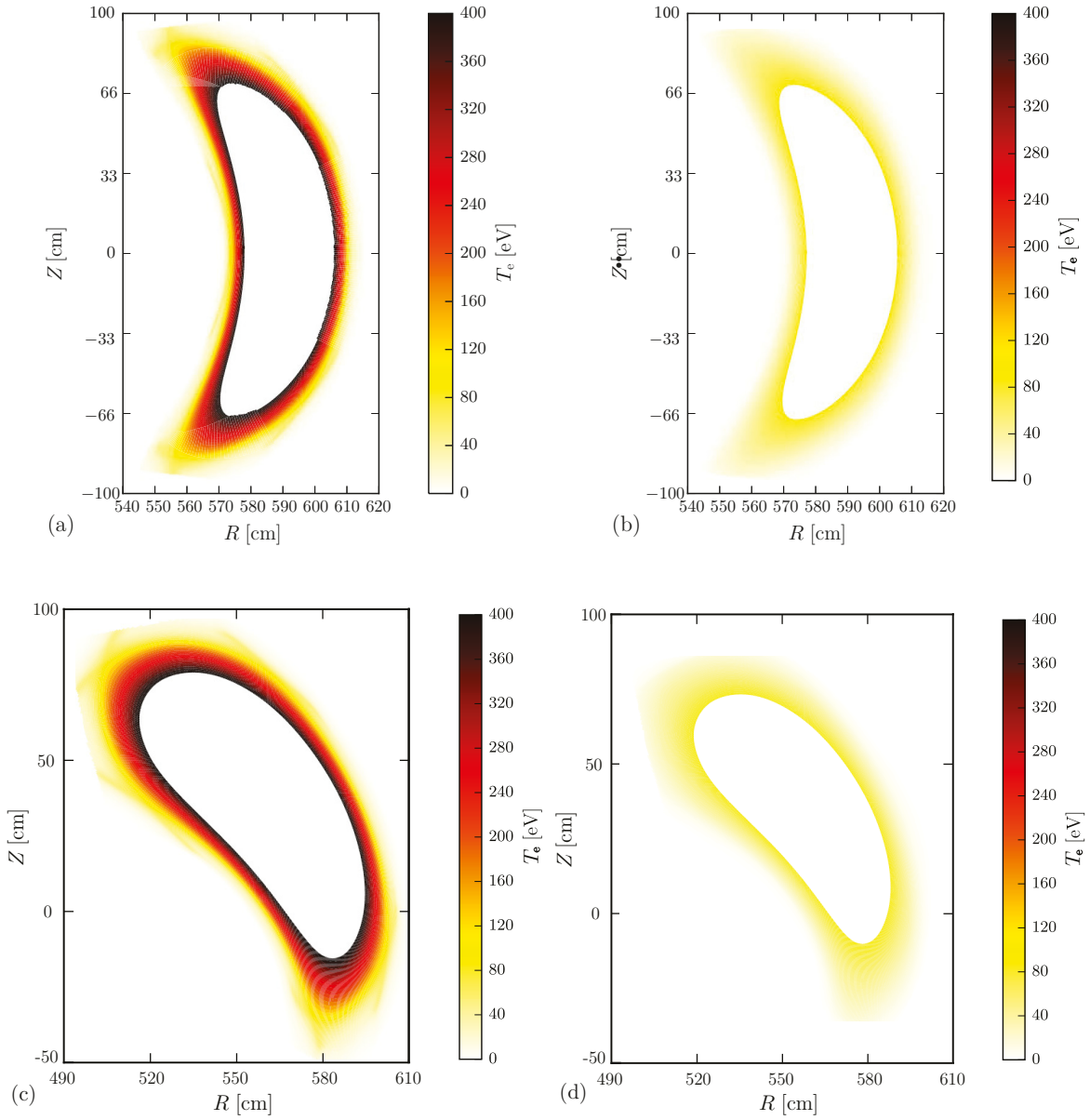

Figure 5.2: Cross-section view of T_e for a low density case ((a) and (c)), taken from simulation Υ, and a high density case ((b) and (d)) based on simulation Υ but with $n_{e,sep} = 1 \times 10^{19}$. A bean shaped cross-section is shown in (a) and (b),and a teardrop cross-section is shown in (c) and (d).

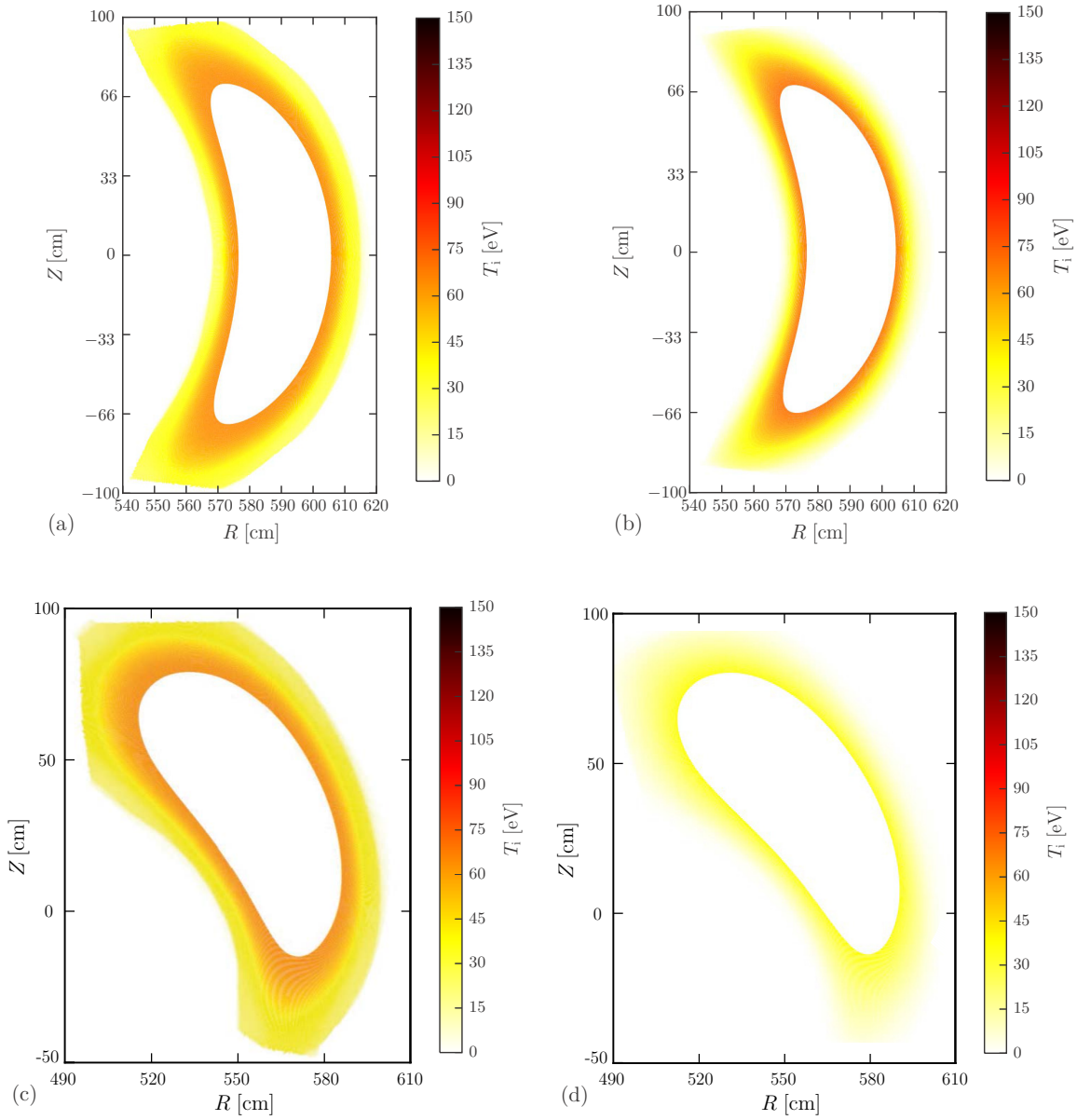

Figure 5.3: The same as 5.2 but T_i is the shown plasma property.

energy is applied to the electrons. Hence, $P^{\mathrm{SOL}}_{\mathrm{heat,e}} = 0.4$ MW and $P^{\mathrm{SOL}}_{\mathrm{heat,i}} = 0.4$ MW are used in Υ for the electrons and ions, respectively. A reduction of $P^{\mathrm{SOL}}_{\mathrm{heat,i}}$ fits as a more realistic setting. In Figure 5.4, the SOL radiation pattern shows a clear dependency on $P^{\mathrm{SOL}}_{\mathrm{heat,i}}/P^{\mathrm{SOL}}_{\mathrm{heat,e}}$, which is changed from 1 to 1/9 . The island characteristics of the radiation pattern are strongly coupled to this fraction because the formation of disjointed P_{rad} peaks is more distinct for $P^{\mathrm{SOL}}_{\mathrm{heat,i}}/P^{\mathrm{SOL}}_{\mathrm{heat,e}} = 1/9$ (see Figure 5.4). All

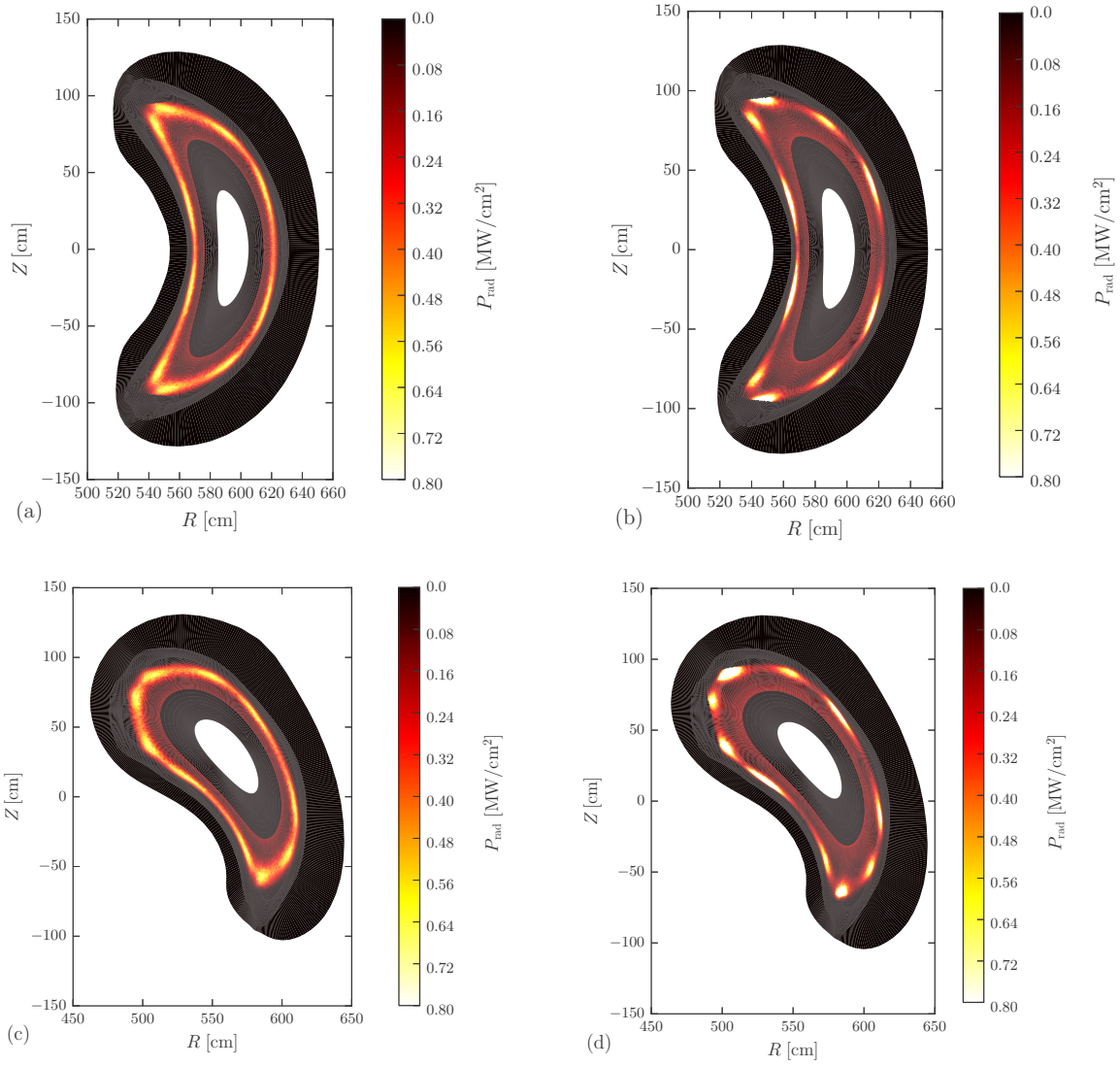

Figure 5.4: Cross-section overview of $P^{\mathrm{SOL}}_{\mathrm{rad}}$ for a high ion heating case ((a) and (c)), simulation parameters taken from Υ with $P^{\mathrm{SOL}}_{\mathrm{heat,i}}/P^{\mathrm{SOL}}_{\mathrm{heat,e}} = 1$, and a high electron heating case ((b) and (d)) based on simulation Υ but with $P^{\mathrm{SOL}}_{\mathrm{heat,i}}/P^{\mathrm{SOL}}_{\mathrm{heat,e}} = 1/9$. A bean-shaped cross-section is shown in (a) and (b), and a teardrop-shaped cross-section is shown in (c) and (d).

subfigures of Figure 5.4 show an island structure that is contradictory to the introduced magnetic configuration of Figure 2.11. Figure 5.5 shows the used magnetic configuration from Figure 2.11 in the overlay, and the divertor target plates clearly do not cause these radiation peak structures. Each

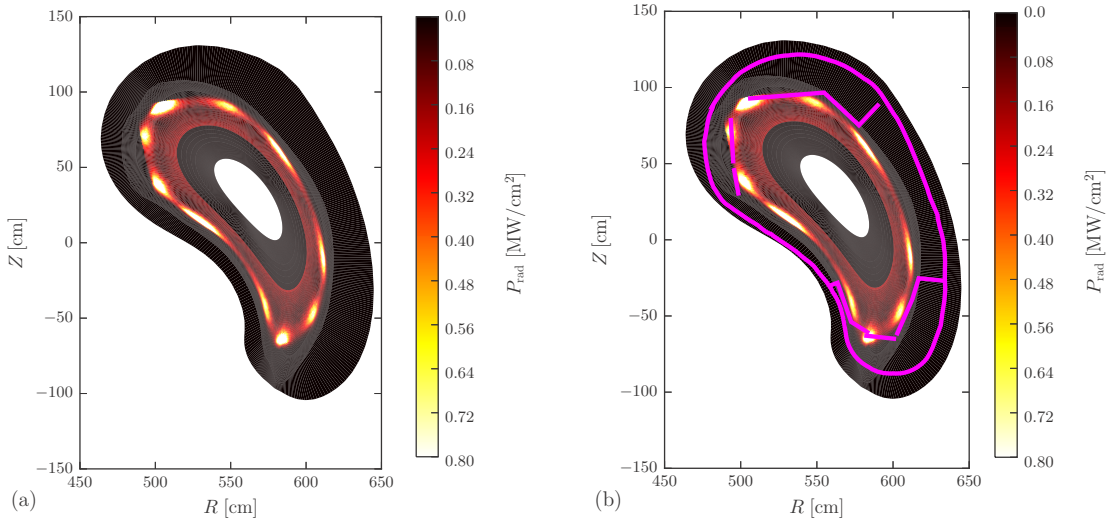

Figure 5.5: The same as 5.4(d), but with magenta bars indicating the plasma-facing wall components of the island divertor.

island has two internal radiation peaks, which are also noticeable in Figures 5.2(c) and 5.3(c) (see $Z = [50:100]$ cm and $R = [490:500]$ cm). These radiation peaks are correlated to the electron density and electron temperature. However, Figures 5.2 and 5.3 do not show the same internal peak structure within the islands. This might be because of the chosen color code of the Figures or because the effects on $T_{e,i}$ remain rather small. For now, these island characteristics are treated as a feature of the EMC3-EIRENE plasma edge code. Impurity temperatures and their radiation benefit from the heating power if a larger portion is assigned to ions. This clarifies why the internal radiation patterns in Figure 5.4(a) and (c) broaden and the maximum peak values of P_{rad} drop in comparison to peak values in Figure 5.4(b) and (d). When the distribution of the applied heating power is switched from a uniform distribution $P^{SOL}_{heat,i}/P^{SOL}_{heat,e} = 1$ to a heavy electron heating distribution $P^{SOL}_{heat,i}/P^{SOL}_{heat,e} = 1/9$, the radiation pattern with two distinct radiation peaks still occurs.

A peaking structure of the plasma temperature pattern and a peaking structure of the density pattern within the island would be challenging for a reapplication of applied processes in OP1.1 between MPM measurements and EMC3-EIRENE simulations. Discussed probe measures such as $\Delta z_{1,4}$ (introduced in subsection 2.3.1 and Figure 2.13) must be considered in this case. Figure 5.6 shows a magnified poloidal cross-section with its radiation pattern. The size of the distinct peaking structure is halved along the island orientation. Introducing s_{peak} as the mean island surface coordinate for one single radiation peak within the island (in the shown poloidal cross-section) leads to a drop in length of roughly 10 cm for the top island (see Figure 5.6(c) and (d)). Radiation pattern peaks within the island to the right decrease by roughly 2 cm, which is a crucial quantification because this island is passed through by the MPM. Hence, a successful comparison of EMC3-EIRENE simulations to MPM measurements depends strongly on the peaking structure within the islands, which may be hidden on first sight. One does not expect such a strong radiation pattern dependence on different

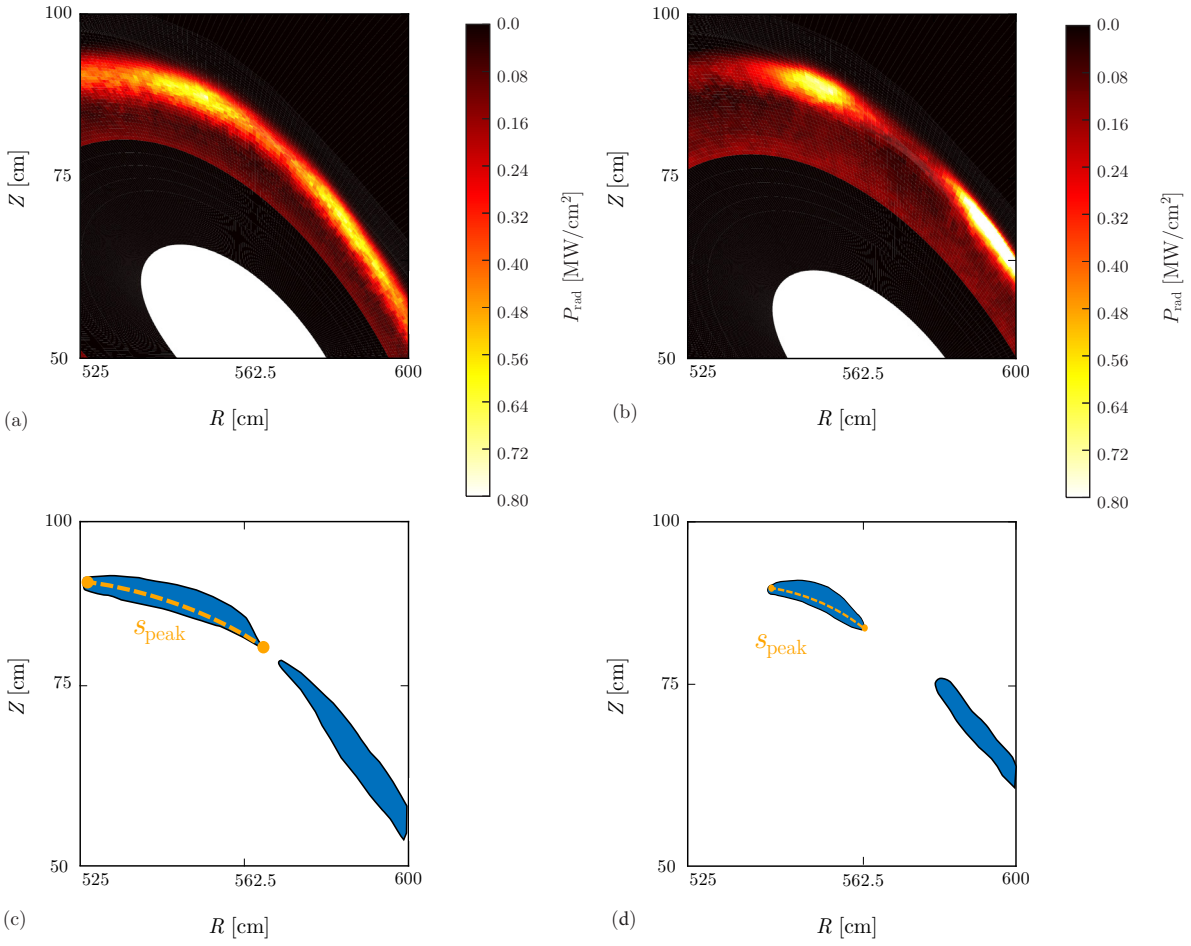

Figure 5.6: (a) and (b) show the same as 5.4(c) and (d) but with enlarged image sections of the island structure region. Estimated island boundaries in (a) and (b) are shown in (c) and (d). The internal island structure is shown in blue.

EMC3-EIRENE input parameters. Relevant changes in island size must be considered regarding the distance between MPM probe heads $\Delta z_{1,4}$.

Although the used input parameters from simulation setup Υ are orientated to MPM Langmuir probe measurements, a rather unrealistic release rate of impurities is obtained. The same point source coverage as in section 4.0.3 and Figure 4.18 in the computational domain is used for the oxygen introduction in simulation Υ. Plasma scenarios with high power losses (via radiation) introduce high impurity densities into the main plasma, because the influx for an impurity species $\Gamma_{\mathrm{in}}^{\mathrm{imp},a}$ is given until the chosen radiated power $P_{\mathrm{rad}}^{\mathrm{SOL}}$ is reached. Thus, simulation setup Υ suffers from large impurity contributions to the main plasma density because $P_{\mathrm{heat}}^{\mathrm{SOL,OP1.2}}/P_{\mathrm{rad}}^{\mathrm{SOL,OP1.2}} = 1.6 \ll 11 = P_{\mathrm{heat}}^{\mathrm{SOL,OP1.1}}/P_{\mathrm{rad}}^{\mathrm{SOL,OP1.1}}$ is given. Figure 5.7 shows that the impurity model of EMC3-EIRENE must treat a plasma containing 60% carbon impurities. The major assumption of the EMC3 impurity model, a

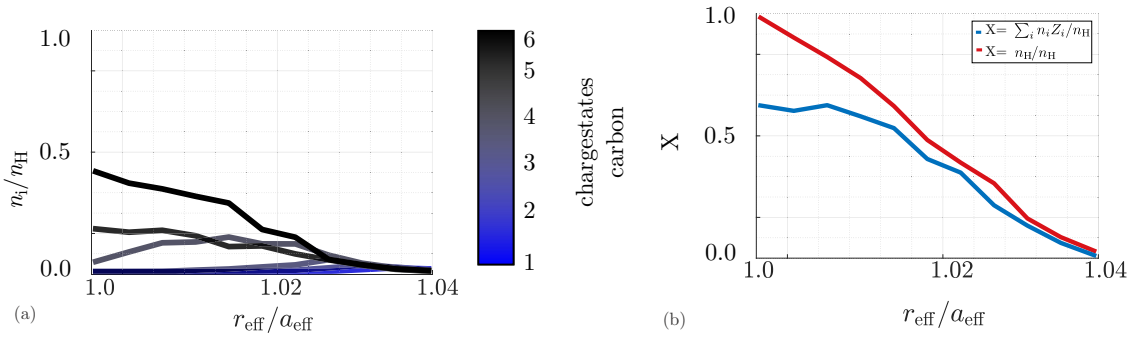

Figure 5.7: Single charge state densities of simulation setup Υ plotted and color coded from blue to black ($Z = 1$ to $Z = 6$) compared with the main plasma density n_H in (a). The sum of all single charge state densities is shown in (b).

quasi-neutral plasma, is strongly violated. Hydrogen plasmas with a high impurity contamination will not be stable over the complete plasma time. Hence, an intermediate conclusion can be drawn that the main plasma is not a clean hydrogen plasma but rather a strong contaminated hydrogen and carbon plasma. Assessed release fractions of carbon impurities into the plasma do not provide reasonable realistic values, because $R^{H\to C} = 0.9$ is necessary to supply the chosen lost power P^{SOL}_{rad}. The reapplied scan over radiation fractions (see section 4.0.3) in Figure 4.22 shows unreasonable and unrealistic values for all simulations. Changing the impurity influx boundary condition to an impurity

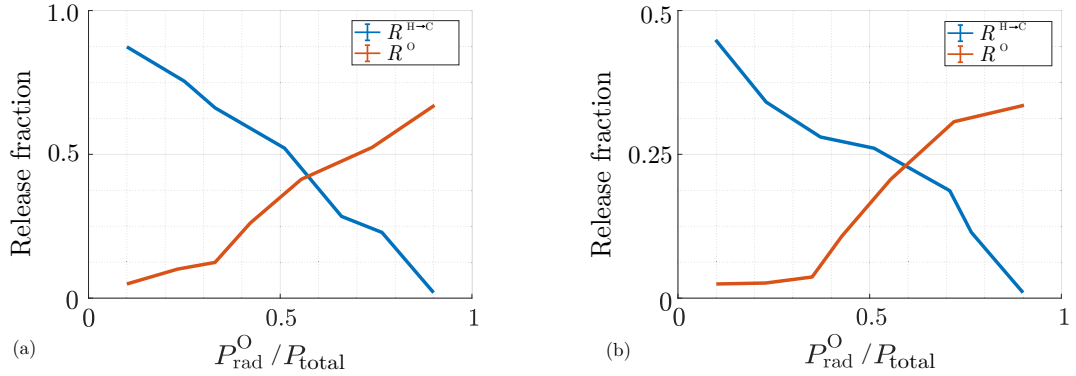

Figure 5.8: Release fraction $R^{\{H\to C,O\}}_{EMC3}$ plotted against each simulation setup of the scan of $P^{O}_{rad}/P^{total}_{rad} \in \{0.1,...,0.9\}$ reaching from the carbon-dominant plasma (Υ^{C}, left hand side) to the oxygen-dominant plasma (Υ^{O}, right hand side). Simulation setup Υ with varied P^{SOL}_{rad}(a); simulation setup Υ^* with varied P^{SOL}_{rad} (b).

con- centration boundary condition is done to study the capability of the impurity model and treat the artificially constructed plasma scenario Υ. Realistic release fractions of impurities into the plasma are only obtained below an impurity concentration of $0.002 n_H$ (this simulation setup is referred to using Υ^*). Corresponding release rates are shown in 5.8(b), where a release fraction of $R^{H\to C} = 0.42$

for a carbon-dominant plasma and $R^{\mathrm{O}} = 0.36$ for an oxygen-dominant plasma are assessed. One

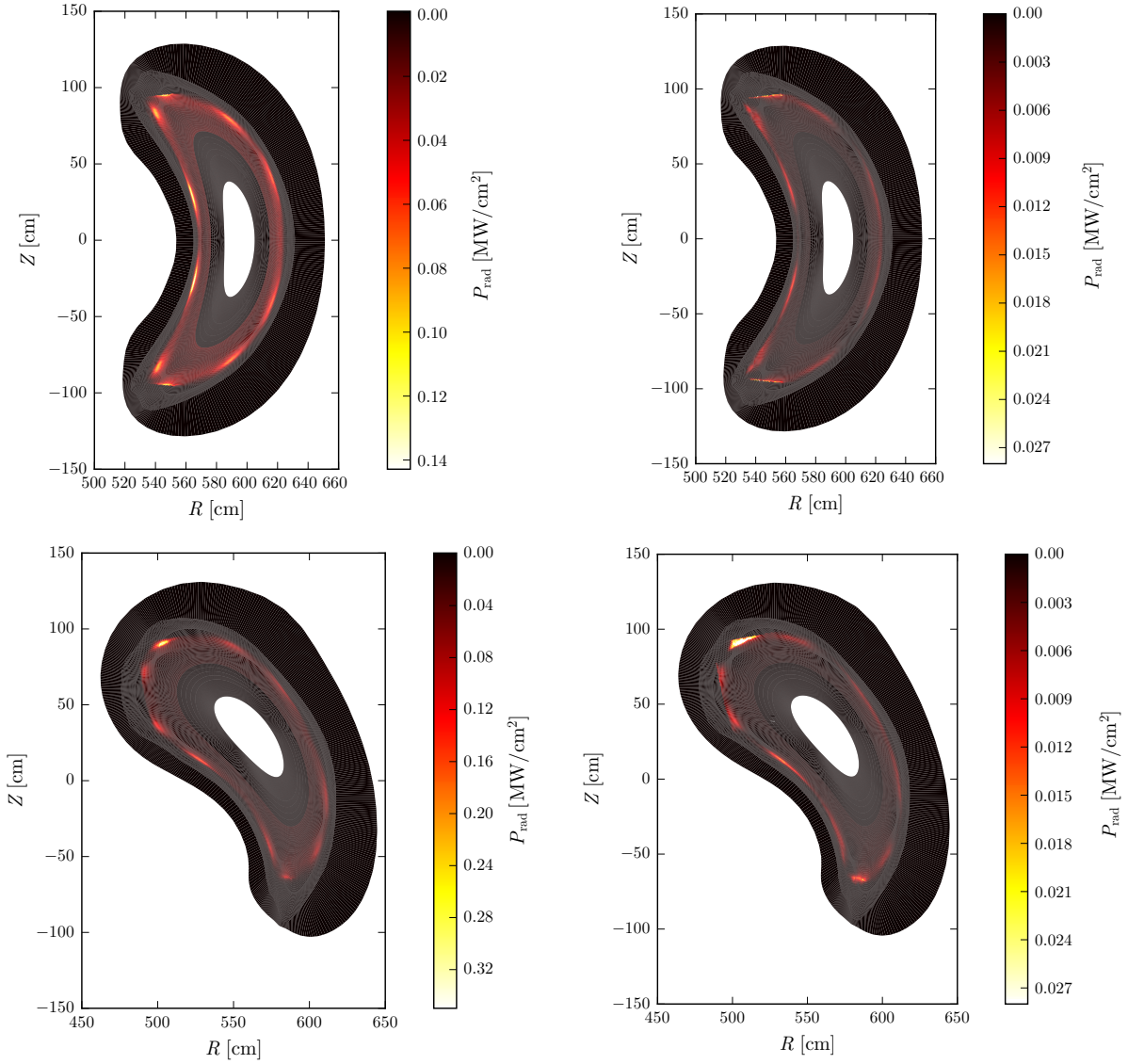

Figure 5.9: The same as 5.2, but with $P_{\mathrm{rad}}^{\mathrm{SOL}}$ from simulation setup Υ and Υ^* shown as the plasma property.

flaw of simulation Υ^* remains: $P_{\mathrm{rad}}^{\mathrm{SOL}}$ values orientated toward bolometric power measurements are not reproduced in the cross-sections of Figure 5.9. Hence, EMC3-EIRENE simulations for plasma scenarios with lower $P_{\mathrm{heat}}^{\mathrm{SOL}}/P_{\mathrm{rad}}^{\mathrm{SOL}}$ fractions must be treated with great caution.

5.1.2 Hot divertor plasmas

Section 5.1.1 showed that EMC3-EIRENE results must be treated with caution if the fraction of $P_{\mathrm{heat}}^{\mathrm{SOL}}/P_{\mathrm{rad}}^{\mathrm{SOL}}$ drops close to 1. Simulation setup Υ is only based on recorded He plasmas. Other plasmas must be considered to study the physics of impurities regarding the effective charge state of the

plasma. Section 4.1 did not cover a comparison of effective charge state measurements because they were not available for OP1.1. Now, for OP1.2, these are available on plasmas recorded by the Thomson scattering system. However, no plasmas are available that were recorded by the combined probe (see subsection 2.3.1) and Thomson scattering system. Thus, a comparison with the Thomson scattering system (plasma number 20171109.45) is conducted followed by a comparison with the MPM measurements (plasma number 20180814.36).
Thomson scattering systems, described in [57], give with plasma 20171109.45 a first reference and input parameter constraint for the plasma density and temperature. Again, bolometric power measurements are used to constrain the lost power $P_{\text{rad}}^{\text{SOL}}$. Plasma 20171109.45 is chosen for EMC3-EIRENE impurity studies, because the fraction $P_{\text{heat}}^{\text{SOL}}/P_{\text{rad}}^{\text{SOL}} = 5.6 > 1$ is given. Thus, the effect discussed in section 5.1.1 can play a significant role here. EMC3-EIRENE does not solve time-dependent model

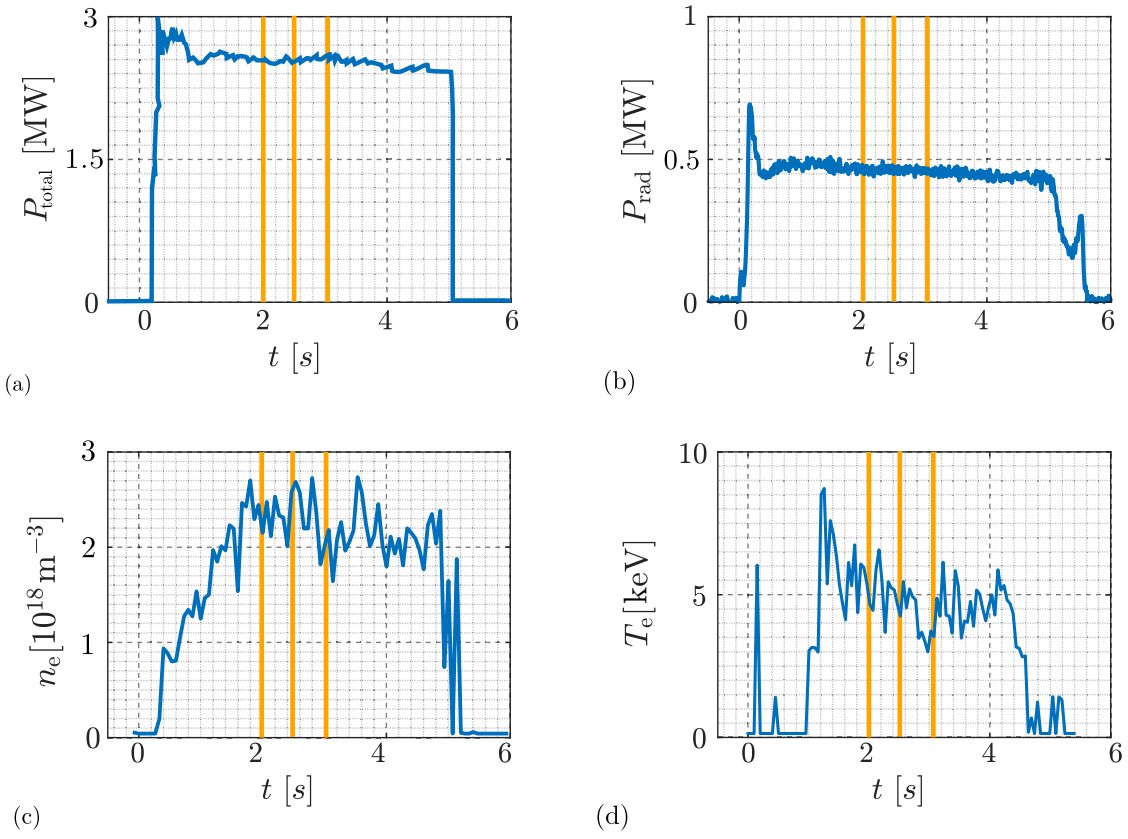

Figure 5.10: Overview of guiding measurements of heating power (a), radiated power (b), and Thomson scatteringn_e (c), T_e (d) of plasma 20171109.45 at $\varphi = 171.2°$. Measurements ((a) to (d)) were conducted using bolometer measurements and Thomson scattering. Different Thomson scattering reference timestamps are indicated by the orange bars.

equations ; thus, a direct comparison with three different Thomson scattering timestamps requires three disjunct simulation setups ($\Upsilon_{\text{Thomson}}^{t=2,2.5,3}$). A set of different input densities and temperatures

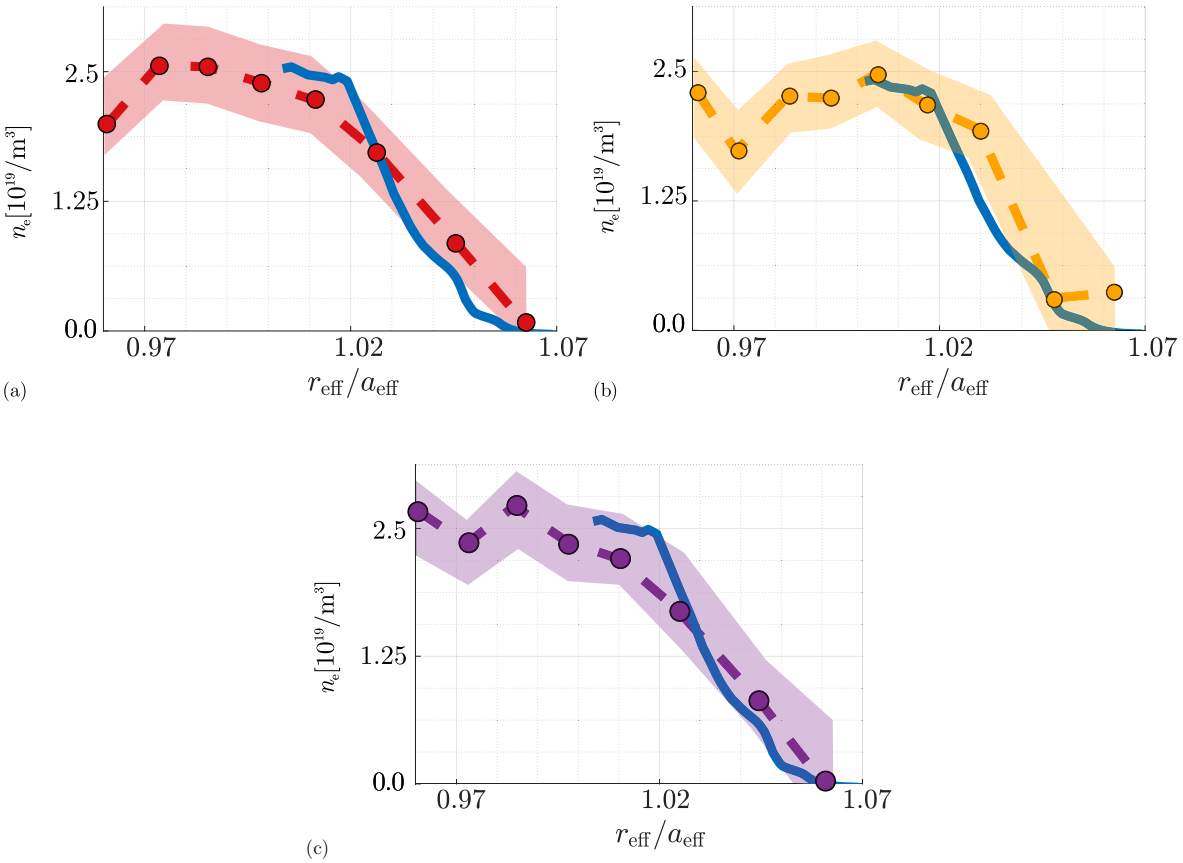

Figure 5.11: Thomson scattering n_e profiles (dashed, with shaded areas as error bars) of three different timestamps $t = 2, 2.5, 3$ s (a)-(c) compared with EMC3-EIRENE simulations using setup $\Upsilon_{\text{Thomson}}$, plotted in a solid line.

(shown in Figure 5.10; orange bars mark three different reference points) are used. Consistency is enforced because these measurements are used as input parameter constraints in Figure 5.11. Small offsets between the shown profiles are neglected because the overall trend of the plasma density is the main reference to compare Z_{eff} values. However, three different EMC3-EIRENE simulations exhibit results consistent with corresponding Thomson scattering measurements. Constraints on the T_e of simulations $\Upsilon^{t=2,2.5,3}_{\text{Thomson}}$ are necessary in addition to n_e constrains. Figure 5.12 shows consistent T_e profiles for the three reference times $t \in \{2, 2.5, 3\}$. Measured profiles exhibit a small constant plateau-like flattening between $2-4$ s to the left-hand side of plots in Figure 5.10. Input parameters in this time interval do not change much. As a consequence, assessed EMC3-EIRENE T_e profiles do not exhibit a significant change in shape and overall trend for each reference point (see Figure 5.12(a)-(c)). Furthermore, characteristic profile maxima for Thomson scattering close to $r_{\text{eff}}/a_{\text{eff}} = 1.02$ are present for the assessed EMC3-EIRENE electron temperature. These maxima occur because of the magnetic island grouping effect discussed in section 5.1, and coincide with the laser beam path shown in Figure 2.2.3 from [57]. A magnetic island is intersected by the laser beam close to the LCFS. Additionally, profiles

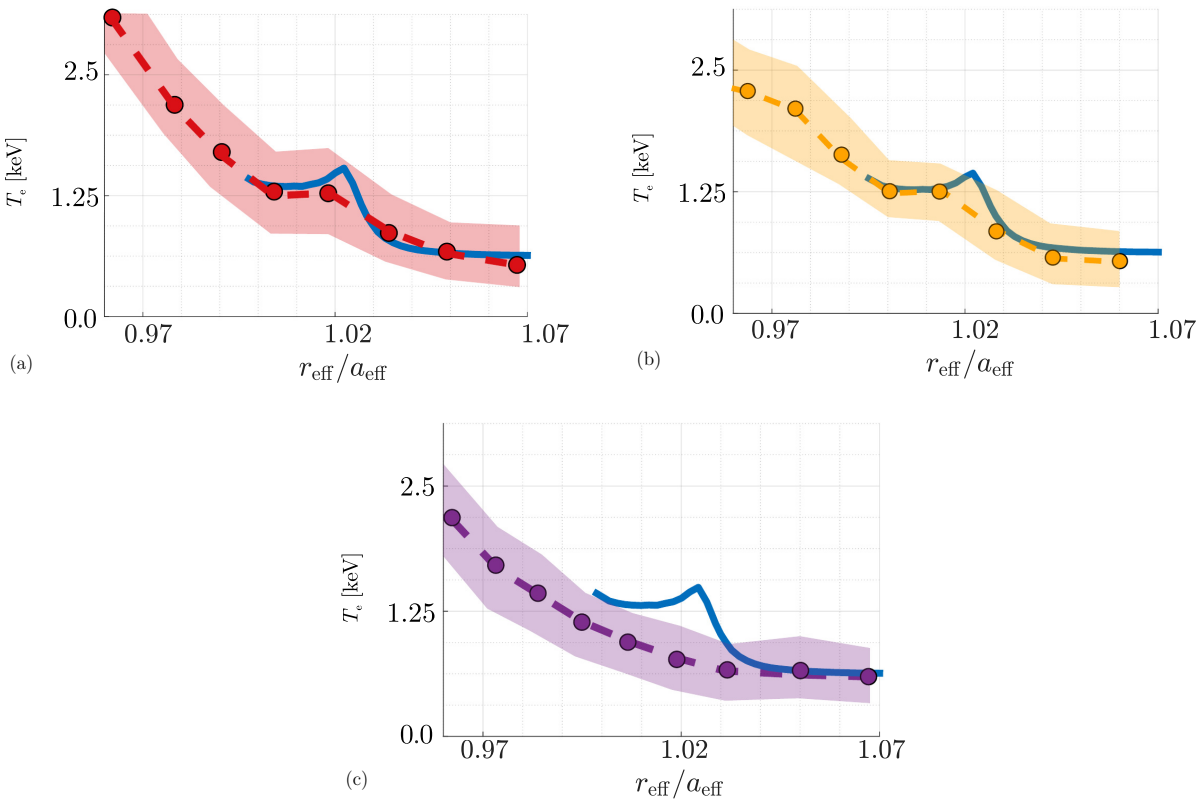

Figure 5.12: The same Figure as 5.11 but T_e is the shown plasma property.

taken from EMC3-EIRENE simulation $\Upsilon^{t=2,2.5,3}_{\mathrm{Thomson}}$ at the same spatial position intersect this magnetic island, as shown in Figure 5.13. Radiation patterns in Figure 5.13 have the same peak separation inside the magnetic island. This fraction $P^{\mathrm{SOL}}_{\mathrm{heat}}/P^{\mathrm{SOL}}_{\mathrm{rad}} = 5.6 > 1$ is not high enough to be free of the discussed separation effects within the magnetic islands. A spatial uncertainty would then result in an offset between the characteristic Thomson scattering T_e peaks of Figure 5.12 because a $P^{\mathrm{SOL}}_{\mathrm{rad}}$ minimum is observable. The same inner island structure is visible for the electron density in Figure 5.13 (second row) but not for the electron temperature in the same Figure 5.13 (third row). Hence, n_e (including the EMC3-EIRENE impurity results) profiles do not exhibit characteristic maxima. Following presented schemes from [58, 59], one obtains an integrated Z_{eff} value along the laser path of the Thomson scattering ($\varphi = 27.2°$, see Figure 2.2.3 from [57]). This value can then be compared with a single radial Z_{eff} profile, which is deduced from EMC3-EIRENE simulations $\Upsilon^{t=2,2.5,3}_{\mathrm{Thomson}}$ along the laser line of sight. Figure 5.14(a)–(c) display Z_{eff} profiles consistent with the integrated values at the three chosen reference times. The Minerva framework integration region is defined by the spatial resolution of the Thomson scattering. Properties in the enclosed region of the plasma are recorded and contribute to the mean $Z^{\mathrm{minerva}}_{\mathrm{eff}}$. However, core plasma dynamics are not accessible using EMC3-EIRENE because the computational domain is constructed on the basis of open magnetic flux tubes. Thus, the overlap between Thomson scattering and EMC3-EIRENE datasets ends at the

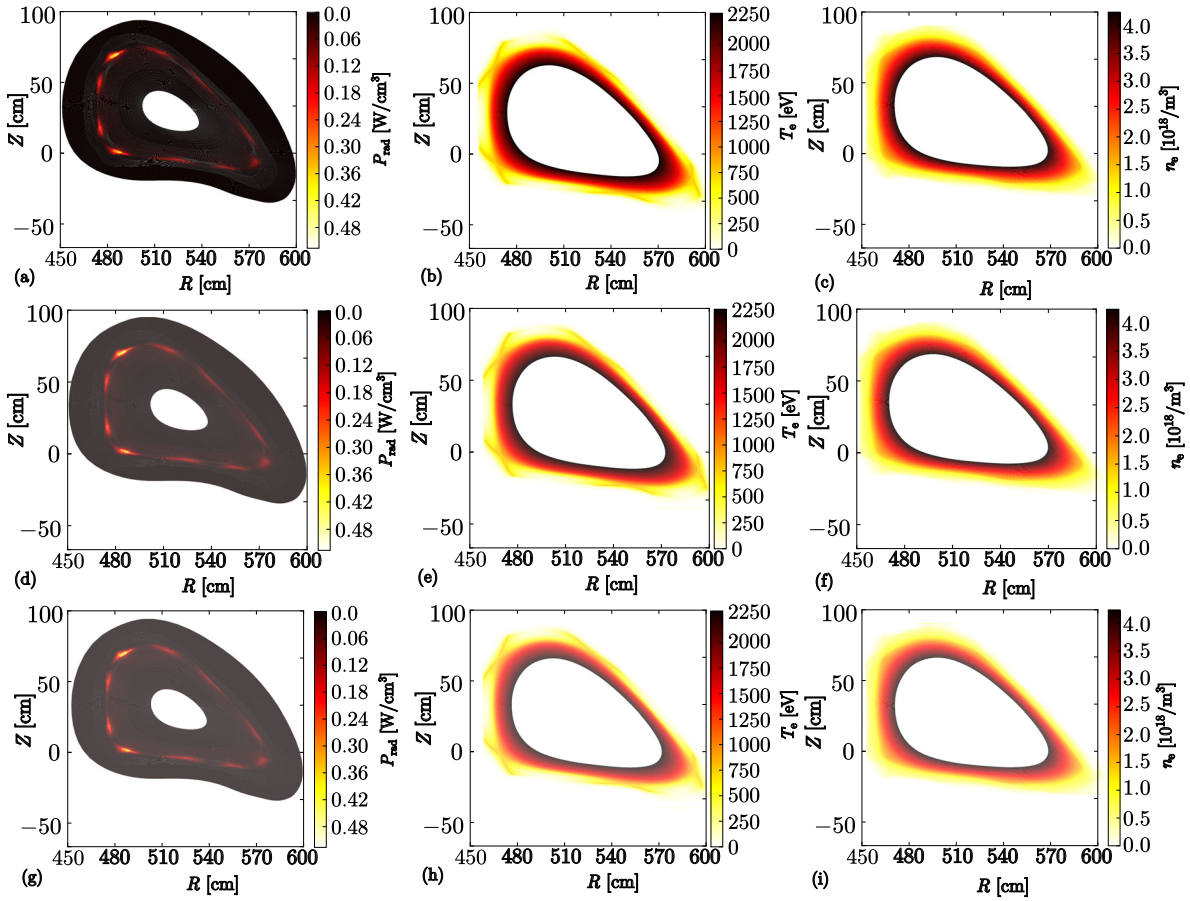

Figure 5.13: Radiation pattern at Thomson scattering position shown for the three chosen time points of Figure 5.10 ((a), (d) and (g)) in comparison to the electron temperature and density cross section.

LCFS. However, $Z_{\text{eff}}^{\text{minerva}}$ values are integrated, including the enclosed region, and compared with assessed EMC3-EIRENE profiles of the SOL region. Then, only a mismatch with the more outer region of the SOL is observable. Constrained n_e input parameters for simulations $\Upsilon_{\text{Thomson}}^{t=2,2.5,3}$ are taken at the LCFS (see Figure 5.13). Furthermore, Thomson scattering profiles change their trend to a plateau after the LCFS, and n_e is roughly constant in the enclosed region. As a result, mismatches between the Z_{eff} and $Z_{\text{eff}}^{\text{minerva}}$ are limited. Direct comparisons of measured and numeric Z_{eff} are successfully conducted for OP1.2. This was not possible for OP1.1 plasmas because no measurements of Z_{eff} were available. Plasmas from OP1.2 show a higher numerical effective charge state than do OP1.1 plasmas because of the applied heating power of the studied plasmas. Higher heating powers lead to higher plasma temperatures, and thus to higher charge states. Hence, the effective charge state's magnitude is strongly correlated to the applied heating powers. OP1.1 plasmas lack comparable heating powers compared with OP1.2, because maximum heating powers of 2 MW were applied.

Plasma 20171109.45 owns a high $P_{\text{heat}}^{\text{SOL}}/P_{\text{rad}}^{\text{SOL}}$ fraction. Thus, the amount of impurities introduced via the influx $\Gamma_{\text{in}}^{\text{imp},a}$ is reduced compared with the artificial plasma discussed in section 5.1.1. Compared

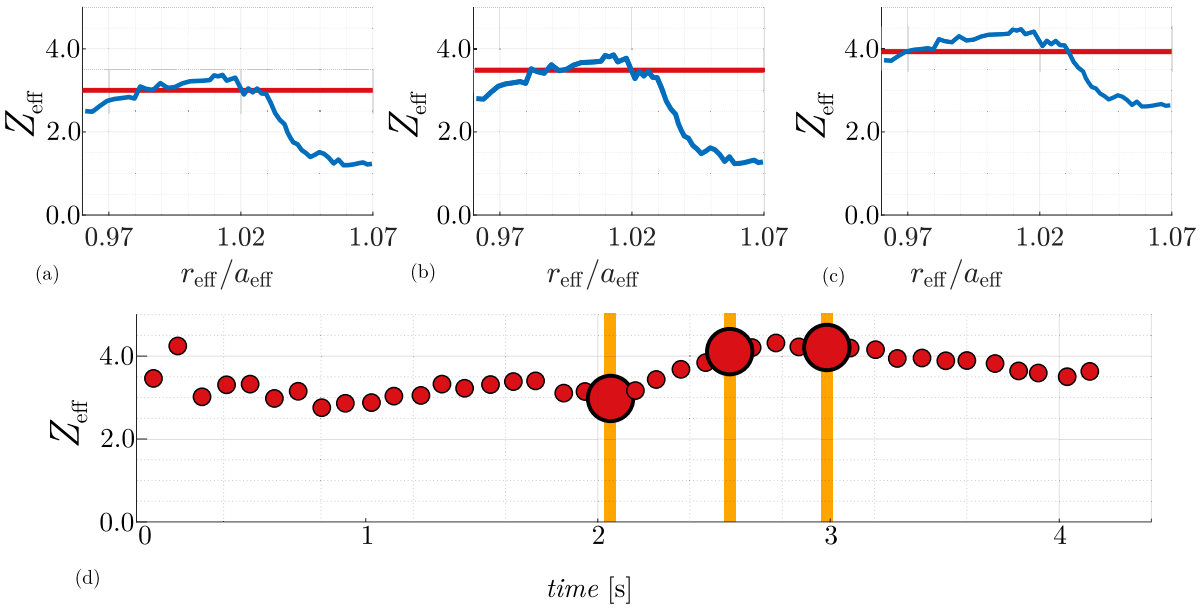

Figure 5.14: Z_{eff} profile (blue, in (a)–(c)) compared with integrated values of the Minerva framework (red, in (a)–(c)). (a) to (c) show the Z_{eff} profile compared with the integrated values for the plasma times $t = 2, 2.5, 3$ s. The time trace of the measured Zeff is shown in (d). Large dots represent the chosen comparison times.

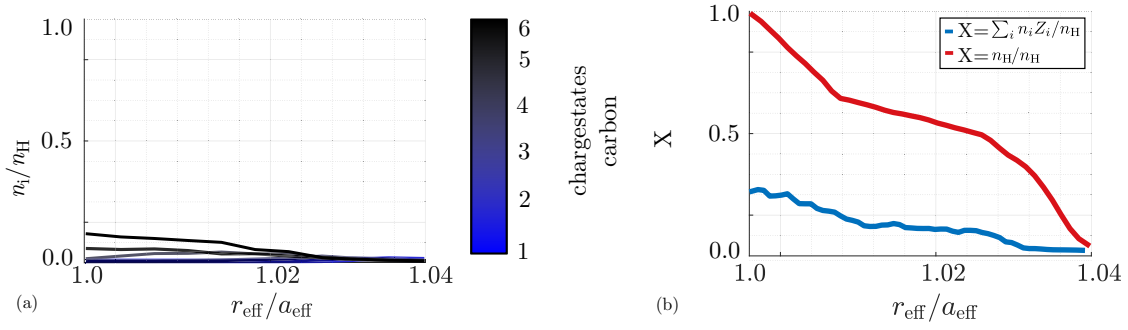

Figure 5.15: Single charge state densities of simulation setup $\Upsilon^{t=2,2.5,3}_{\mathrm{Thomson}}$ plotted and color coded from blue to black ($Z = 1$ to $Z = 6$) compared with the main plasma density n_{H} in (a). The sum of all single charge state densities is shown in (b).

with Figure 5.7, Figure 5.15 shows single charge state densities that reach a maximum contribution of 10% in respect of the main plasma density n_H. Thus, a quasi-neutrality violation is absent for simulations $\Upsilon^{t=2,2.5,3}_{\text{Thomson}}$ because $\sum_i n_i Z_i / n_H = 0.2$ is reached at a maximum.
Repetitively used MPM measurements and the previously used Thomson scattering datasets are not available simultaneously for one plasma. Hence, studies with input parameter constraints from these diagnostics must be conducted separately. Plasma 20180814.36 fulfills the requirement of a W7-X plasma with P $P^{\text{SOL}}_{\text{heat}} / P^{\text{SOL}}_{\text{rad}} \gg 1$, for an EMC3-EIRENE impurity study. The necessity of a plasma with a high fraction of $P^{\text{SOL}}_{\text{heat}} / P^{\text{SOL}}_{\text{rad}} \gg 1$ was introduced in section 5.1.1. Figure 5.16 provides an overview of relevant input parameters and their measurements by the bolometer and MPM. Recorded results are used to constrain the input parameters of simulation setup Υ_{MPM}. An overview about the applied

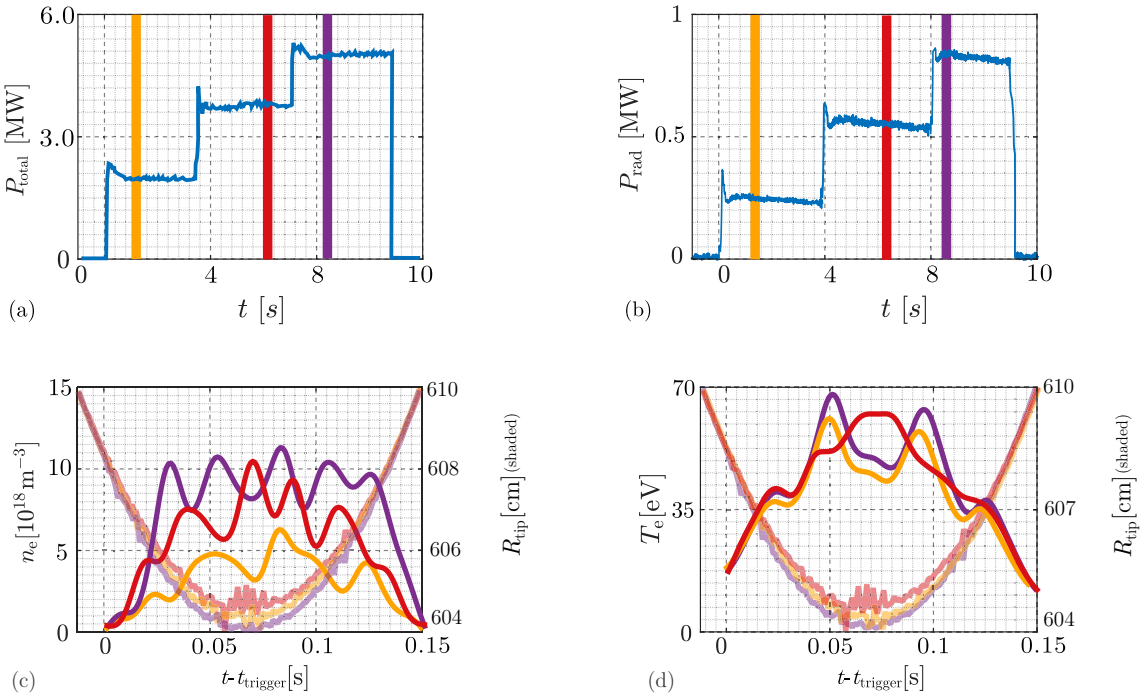

Figure 5.16: Overview of characteristic measurements of heating power (a), radiated power (b), MPM Langmuir probe ne (c), and Te (d) n_e (c), and T_e (d) for plasma 20180814.36. Different MPM plunge intervals are indicated by orange, red, and violet bars, and shaded lines give the radial depth of the MPM within the system. The plunge time interval is $\Delta t_{\text{MPM}} = 0.15$ s for all plunges.

heating power to the plasma over a plasma duration of roughly 9 s is presented in Figure 5.16. Three levels of ECRH heating power are applied at intervals of 3 seconds. The heating power increases from 2.5 MW at stage one, to 3.8 MW at stage two, and finally to a maximum of 5 MW at stage three. MPM plunges into the plasma's SOL are performed for all three stages. In Figure 5.16(a) and (b), linked plunge time intervals of $\Delta t_{\text{MPM}} = 0.15$ s are indicated by orange, red, and magenta bars. The plunge beginnings must be chosen carefully because the MPM's Langmuir probes assume a steady state

plasma is being measured. Figure5.16(b) shows a dependency of P_{rad} on the applied heating power P_{heat} as P_{rad} as well has three different stages of radiation loss. Thus, Figure 5.16(a) and (b) give a set of three different input parameters for all plasma stages.

By contrast, the MPM measurements do not exhibit a distinct change in the recorded plasma properties for the plasma stages one, two, and three. Only the recorded electron density n_{e} of stage one exhibits a slight drop in the overall trend, compared with stages two and three. Hence, an impurity study of stage one is conducted first. A full in-depth discussion of stages two and three, including the introduced iterative process to account for impurity effects, is outside of the scope of this study. Instead, stage one is discussed in detail.

An overall applied heating power of $P_{\mathrm{heat}} = 2.5$ MW, overall radiated power of $P_{\mathrm{rad}} = 0.25$ MW, MPM electron density of $n_{\mathrm{e}} = 6 \times 10^{18}$ m^{-3}, and an MPM electron temperature of $T_{\mathrm{e}} = 60$ eV are found and constrained as input parameters for simulation setup $\Upsilon^{\mathrm{stage1}}_{\mathrm{MPM}}$. The results of simulation setup $\Upsilon^{\mathrm{stage1}}_{\mathrm{MPM}}$ show (in Figure 5.17) profiles consistent with MPM measurements of stage one, because these were used to constrain the EMC3-EIRENE input parameters. Separation effects of plasma properties

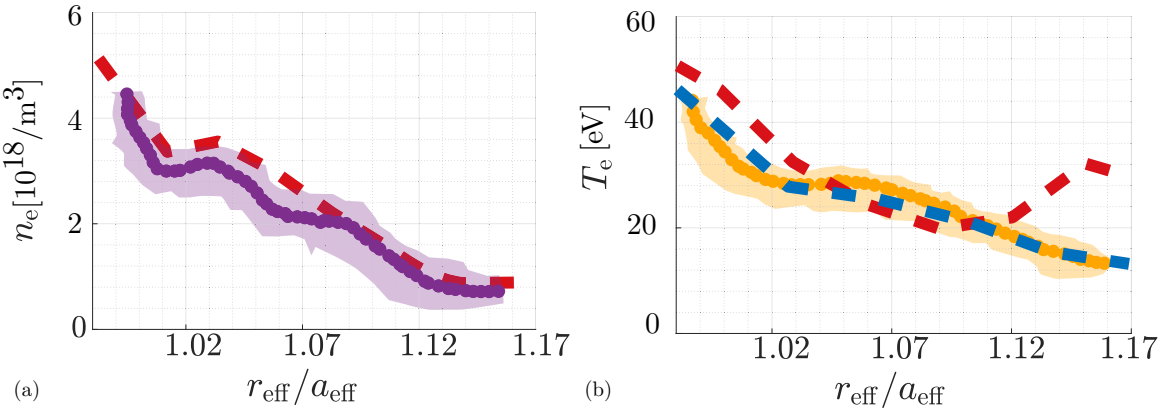

Figure 5.17: MPM Langmuir probe measurement (dots, uncertainties of the measurements shown in the shaded region) of density n_{e} (a) and plasma temperatures T_{e} (blue) and T_{i} (red) (b) shown in comparison with EMC3-EIRENE simulations (dashed); simulation parameters from $\Upsilon^{\mathrm{stage1}}_{\mathrm{MPM}}$.

within the island do not occur for the considered plasma (see Figure 5.18). Thus, discussed offsets to the mean coordinate of the MPM Langmuir probe system (see Figure 2.13) are not of importance in this particular case. Effective charge states Z_{eff} of plasma 20171109.45 were successfully assessed and compared with measured values to perform an impurity study (see Figure 5.11 and 5.12). The same iterative process is reapplied to the MPM electron density profiles shown in Figure 5.17(a). First, an effective speed of sound $c_{\mathrm{s}}^{\mathrm{single}^*}$ from equation (4.0.1.2) is constructed by assessing the Z_{eff} and m_{eff} from simulation$\Upsilon^{\mathrm{stage1}}_{\mathrm{MPM}}$; second, these properties are used to reprocess MPM datasets of the considered plasma in stage one, which are then reused as input parameters constraints for the next simulation setup within the iterative process. Simulation $\Upsilon^{\mathrm{stage1}}_{\mathrm{MPM}}$ is the iterative processes base with $\Upsilon^{\mathrm{stage1}}_{\mathrm{MPM}} = \Upsilon^{\mathrm{stage1},l=1}_{\mathrm{MPM}}$. Iterative process $\Xi_{c_{\mathrm{s}}^{\mathrm{single}^*}}$ is reapplied with steps l. The assessed effective

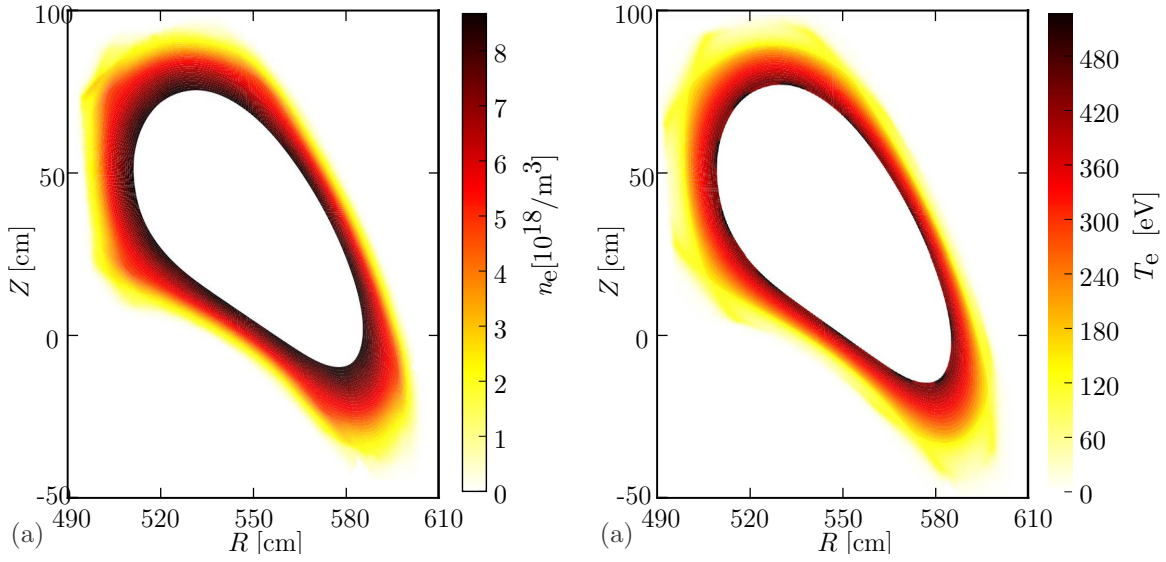

Figure 5.18: Cross-section of n_e (a) and T_e (b) at the toroidal measurement location of the MPM.

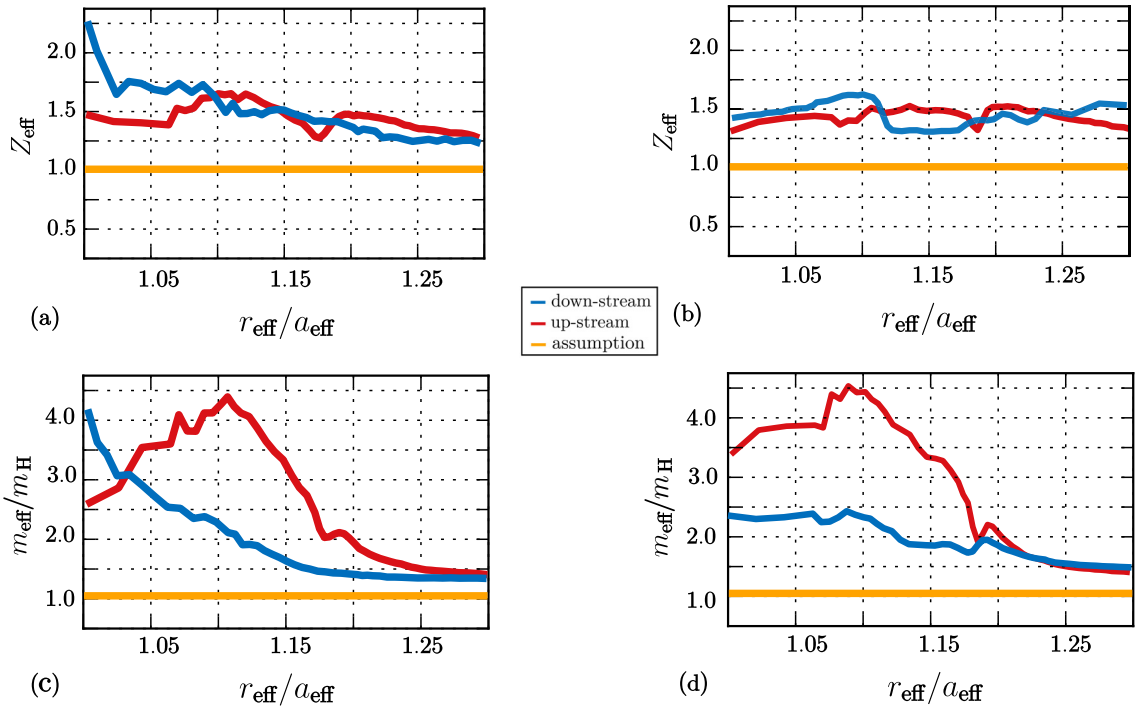

Figure 5.19: Comparison of the simulated Z_{eff} for processes $\Xi_{c_s}^{single*}$ and $\Xi_{c_s}^{multi}$; steps $l = m = 1$ in (a), steps $l = m = 6$ in (b). The same subplots are shown in (c) and (d), but m_{eff} is the shown plasma property. Profiles were taken at the MPM measurement location. The previously assumed $Z_{eff} = 1$ and $m_{eff} = 1$ are shown in yellow bars. All results are plotted against the effective radius r_{eff} normalized to a_{eff}.

charge state and mass show higher values than for OP1.1 (see Figure 2.18 in Chapter 4). This is due to different input parameter constrains; applied heating and lost powers in OP1.2 are higher than those for OP1.1 (see Figure 4.1 versus Figure 5.16). One finds that $P_{\text{heat}}^{\text{SOL,OP1.1}} \ll P_{\text{heat}}^{\text{SOL,OP1.2}}$, and plasma temperatures of OP1.2 are higher than those of OP1.1 as a consequence. Thus, higher impurity ionization levels are reached and the plasma reaches a higher effective charge state and mass level. Profiles shown in Figure 5.19 are then used to construct an effective speed of sound from equation (4.0.1.2). An error Ω_{12} with the percentage change $\delta_{\Omega_{12}}$ is again made in comparison to the exact speed of sound (4.0.1.1). This error is estimated using the maximum density contributions of each impurity charge state in Chapter 4. For plasma scenario $\Upsilon_{\text{MPM}}^{\text{stage1}}$, an error of $\delta_{\Omega_{12}} = 9\%$ is obtained. Thus, the use

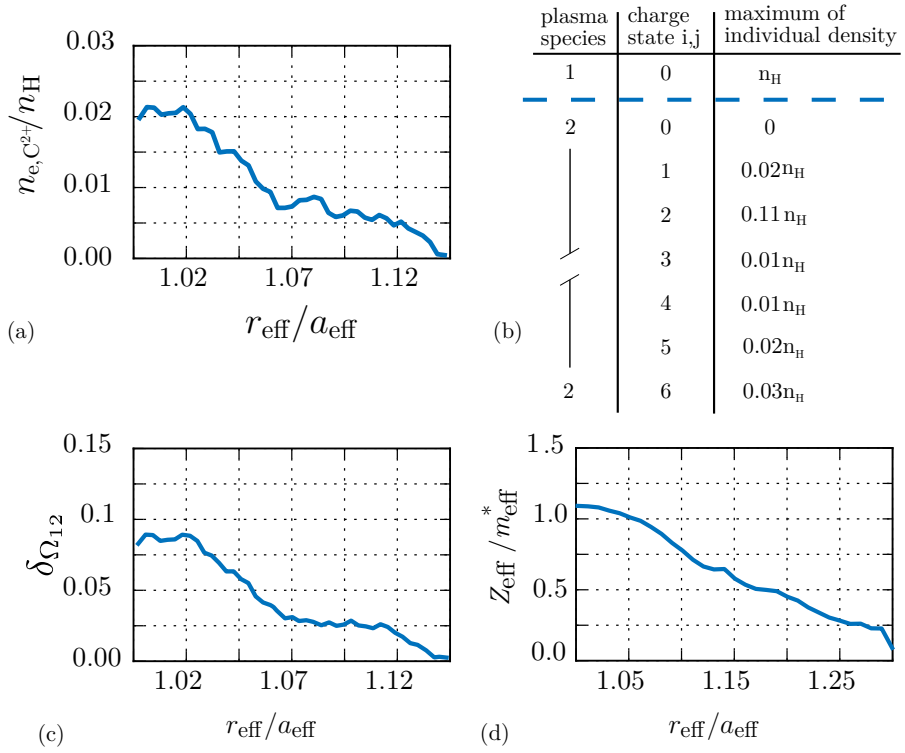

Figure 5.20: Maximum impurity density contribution plotted in (a). Overview of the error made by assumption Ω_{12} for $\delta_{\Omega_{12}}$ for EMC3-EIRENE simulation $\Upsilon_{\text{MPM}}^{\text{stage1,l=1}}$ at the MPM location in (c). The error estimations are calculated with values shown in chart (b). The proportionality $c_s \propto Z_{\text{eff}}/m_{\text{eff}}^*$ is plotted in (d) of process $\Xi_{c_s^{\text{single}^*}}$. The effective mass is normed to the hydrogen mass $m_{\text{eff}}^* = m_{\text{eff}}/m_H$.

of an effective speed of sound is again justified and the effective and exact sound speed profiles are separated by 8% (see Figure 5.20). The reprocessing of MPM Langmuir probe measurements is again performed by applying $c_s^{\text{single}^*}$ to equation 2.3.1.13), and subsequently reprocessed results are taken as the next input parameters constrains for simulation $\Upsilon_{\text{MPM}}^{\text{stage1},l=2}$. Similar to the MPM measurements in OP1.1 plasma, an iteration is conducted that is quantified by the overall $n_{e,\text{MPM}}$ change between iterative steps l, given in ϵ^l by equation 4.0.2.2.

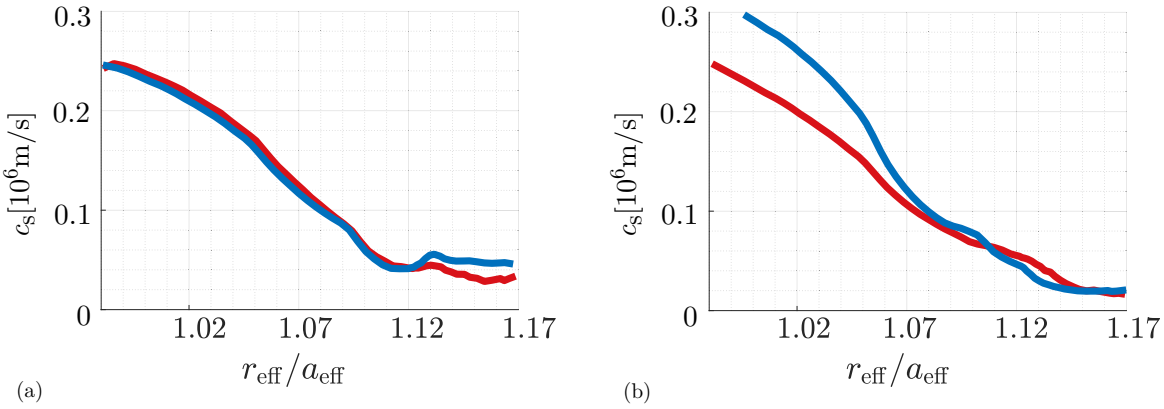

Figure 5.21: Effective speed of sound $c_s^{single^*}$ compared with the multi-species speed of sound c_s^{multi} at the MPM measurement location. Results from step $l = 1$ are shown in (a), and those of step $l = 6$ are shown in (b).

The first iterative step $l = 1$, including all performed sub steps, is shown in Figure 5.22. The application of Z_{eff} and m_{eff} (see Figure 5.22(b)) introduces an offset between $n_{e,MPM}^{l=1}$ and $n_{e,EMC3}^{l=0}$ in Figure 5.22(c). This offset must be matched again with simulation input parameters, as was achieved in Figure 5.22(d). The percentage error between these two substeps drops to a maximum of 5%. Thus, the first iterative step $l = 1$ is completed successfully. Notably, the used grid resolution seems to be insufficient regarding the island structure, because the electron density peak (recorded by the MPM) is only covered by a single grid point. Furthermore, executed iterative steps of process $\Xi_{c_s^{single*}}$ show a convergence in ϵ^l , of which Figure 5.23 provides an overview. Changes of Z_{eff} and m_{eff} remain quite small for step $l = 1$. However, ϵ^l significantly changes for step l = 2 because a change of 28.6% for the effective mass is observed. The related change of Z_{eff} is rather small. Such a significant effective mass change can only occur if a shift occurs in the ionization levels reached by the plasma. The maximum impurity density contribution changes from charge state two (step $l = 1$) to charge state six (step $l = 6$). The Z_{eff}/m_{eff} fraction was studied in section 2.4 to quantify the suppression effect of higher impurity charge states regarding each iterative step. Figure 4.16 shows OP1.1 fractions Z_{eff}/m_{eff} (MPM and limiter Langmuir probe measurements) that have very similar values and profile shapes. Assessed results of the applied iterative processes show roughly the same result. This type of similarity is not observed between step $l = 1$ and $l = 6$ (see Figure 5.20(d) vs. Figure 5.24(d)). Hence, effects of the higher charge states are no longer suppressed, which is observable in Figure 5.21 , where $c_s^{single^*}$ and c_s^{multi} show a clear offset at the last iterative step $l = 6$. Thus, a direct comparison of 5.20(d) versus Figure 5.24(d) shows a higher Z_{eff}/m_{eff} fraction in step $l = 6$. However, ionization levels are affected by the plasma temperatures, but the plasma temperature $T_{e,EMC3}$ does not change significantly, and thus cannot affect the amount of ionization levels significantly. One can easily conclude that single ionization states may be assessed in a false magnitude. Step $l = 2$ must be treated with caution, but $\epsilon^{l=2} = 28.6\%$ is accepted for the moment. Iterative process $\Xi_{c_s^{single*}}$ proves to

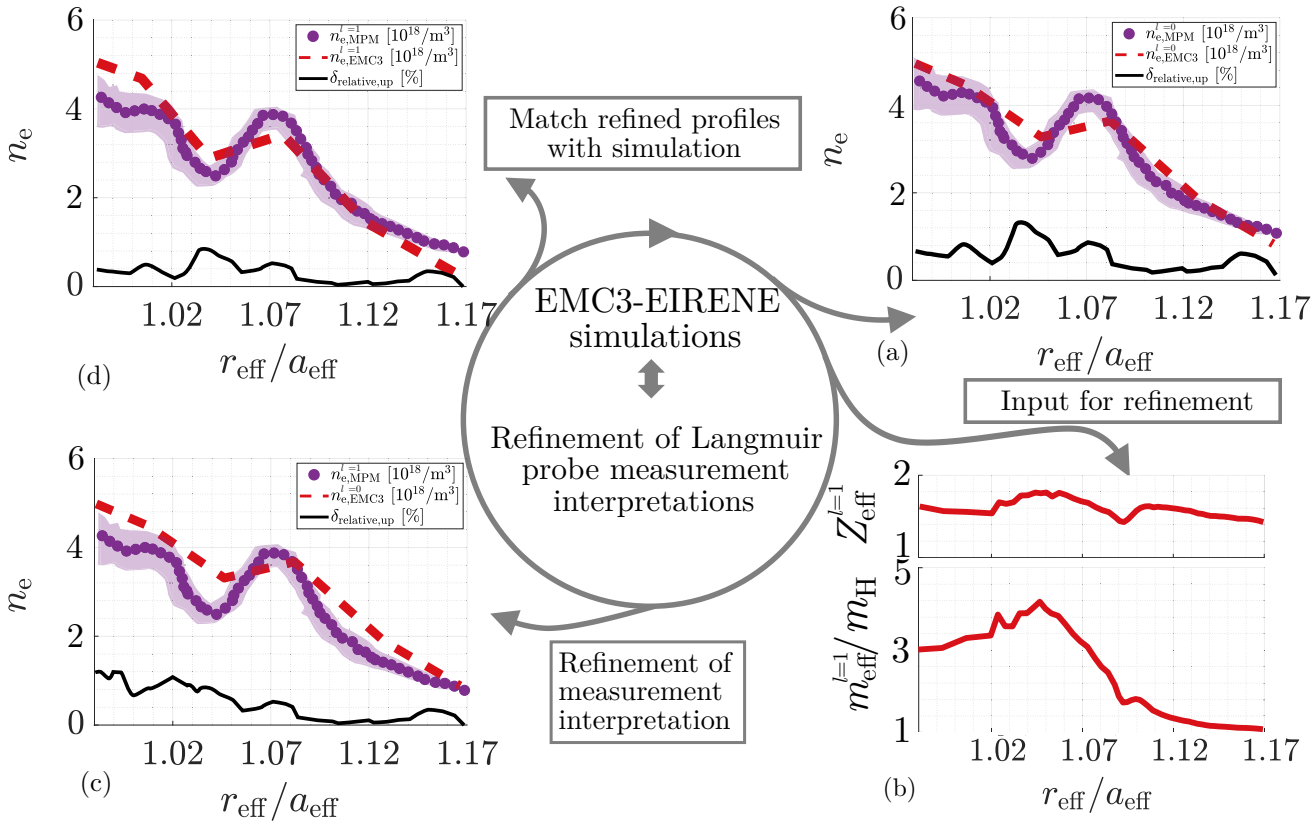

Figure 5.22: Schematic overview of the first step $l = 1$ of the iterative process for MPM measurements. The electron densities from Υ_{MPM}^{stage1} (a), $Z_{eff} = 1$, and $m_{eff} = 1$ were assumed for $n_{e,MPM}$. Deduced Z_{eff}^{l} and m_{eff}^{l} profiles are shown in (b). Relative deviation $\delta_{relative,up}^{l}$ (see equation (4.0.2.1)) plotted in the comparison plot of the numeric and measured density dataset (c) and (d). A reworking of plot 5.22(a) is shown in (d).

be robust enough to withstand such features of an EMC3-ERIENE simulation, because the process continues to converge to final plasma profiles in step $l = 6$. An input density of 3.28×10^{18} m^{-3} was used to obtain $\epsilon^{l} = 0.998$ and a relative change of Z_{eff}, m_{eff}, and $n_{e,MPM}$ close to 1%. Thus, the relative changes in the last step are comparable to the relative and final changes of profiles in OP1.1 plasmas (see Figure 4.10 vs. Figure 5.23). This study drew the conclusion that iterative reprocessing of Langmuir probe measurements is unnecessary at first glance for relatively clean OP1.1 plasmas. This intermediate conclusion must be revised for OP1.2 plasmas (Υ_{MPM}^{stage1}) because they have high heating and radiation powers. Thus, process $\Xi_{c_s^{single*}}$ has a higher impact on OP1.2 plasmas than on OP1.1 plasmas. Figure 5.25 presents the final simulation results and adjusted MPM Langmuir probe measurements. The electron density profiles shown are refined by 33%, and thus drop out of the uncertainty area of the unrefined MPM measurement (see Figure 5.25(a)). This was not found for OP1.1 plasmas in section 2.4, because refined electron density profiles dropped to the lower edge of the unrefined MPM measurement (see Figure 4.11). This led this study to draw the conclusion that

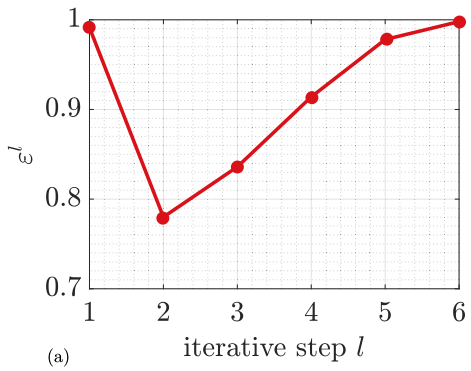

(a)

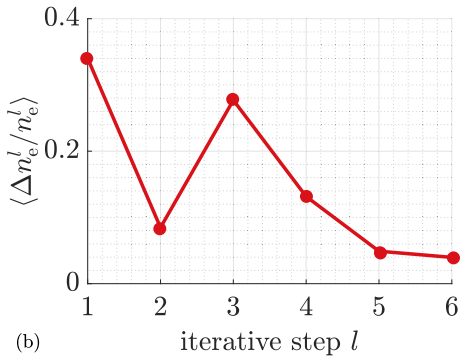

(b)

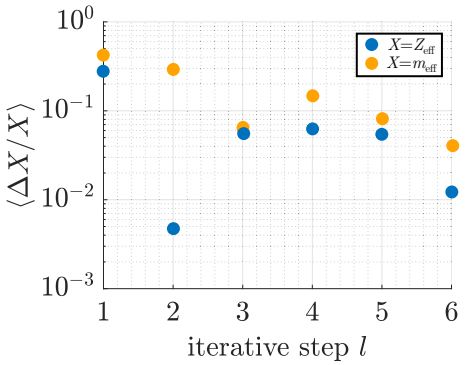

(c)

step l	input density [m^3/10^{18}]	ε^l	$\langle \Delta\ Z_{\text{eff}} / Z_{\text{eff}} \rangle$	$\langle \Delta\ m_{\text{eff}} / m_{\text{eff}} \rangle$	$\langle \Delta\ n^l_{\text{e,MPM}} / n^l_{\text{e,MPM}} \rangle$
1	6.0	0.9913	0.2752	0.41	0.397
2	5.978	0.78	0.0047	0.286	0.0847
3	4.67	0.836	0.06022	0.067	0.277
4	3.85	0.914	0.062	0.152	0.1316
5	3.51	0.978	0.054	0.0836	0.049
6	3.28	0.998	0.01211	0.040	0.032

(d)

Figure 5.23: (a) Factor ε^l plotted against each iteration step; (b) the relative change of the refined Langmuir probe measurement of n_e^l (MPM - red) plotted against each iteration step; and (c) the relative change in the upstream Z_{eff} and m_{eff} profiles plotted against each iteration step. Simulation parameters are taken from plasma scenario $\Upsilon^{\text{stage1}}_{\text{MPM}}$, but n_e was iterated from 6×10^{18} m^{-3} down to 3.28×10^{18} m^{-3}. Chart (d) shows the exact values of each iterative step for the upstream location.

the impact of process $\Xi_{c_s^{\text{single*}}}$ for OP1.2 exceeds the impact of OP1.1.

Next, MPM profiles are reprocessed with the use of c_s^{multi}, the exact speed of sound, with no effective charge state or effective mass required. Instead, ion fluxes are used to calculate the exact multi-species ion speed of sound. The second iterative process is referred to by $\Xi_{c_s^{\text{multi}}}$, and iterative steps are named m. The profiles shown in Figure 5.17 are again the basis of process $\Xi_{c_s^{\text{multi}}}$ and used for the first calculation of c_s^{multi}. Nevertheless, Z_{eff} and m_{eff} are studied to obtain a quantification of the impurity content in the plasma. The applied multi-species sound speed c_s^{multi} is shown in Figure 5.21, where c_s^{multi} and $c_s^{\text{single}^*}$ are quite consistent. Hence, Figure 5.26(a) shows roughly the same effective charge state and mass in the first iterative step as for process $\Xi_{c_s^{\text{single*}}}$. Figure 5.26(a)-(d) further illustrate all applied substeps of iterative step $m = 1$. An overview of all applied steps m is given in 5.27. Reprocessed profiles are matched by refined simulation parameters, mainly n_e. Here, MPM profiles are corrected to higher density values in direct comparison to the results of process $\Xi_{c_s^{\text{single*}}}$ (see Figure 5.23).

The relation of $\varepsilon^l = 0.9913 < \varepsilon^m = 1.0211$ is found. Furthermore, a percentage difference of 3% is

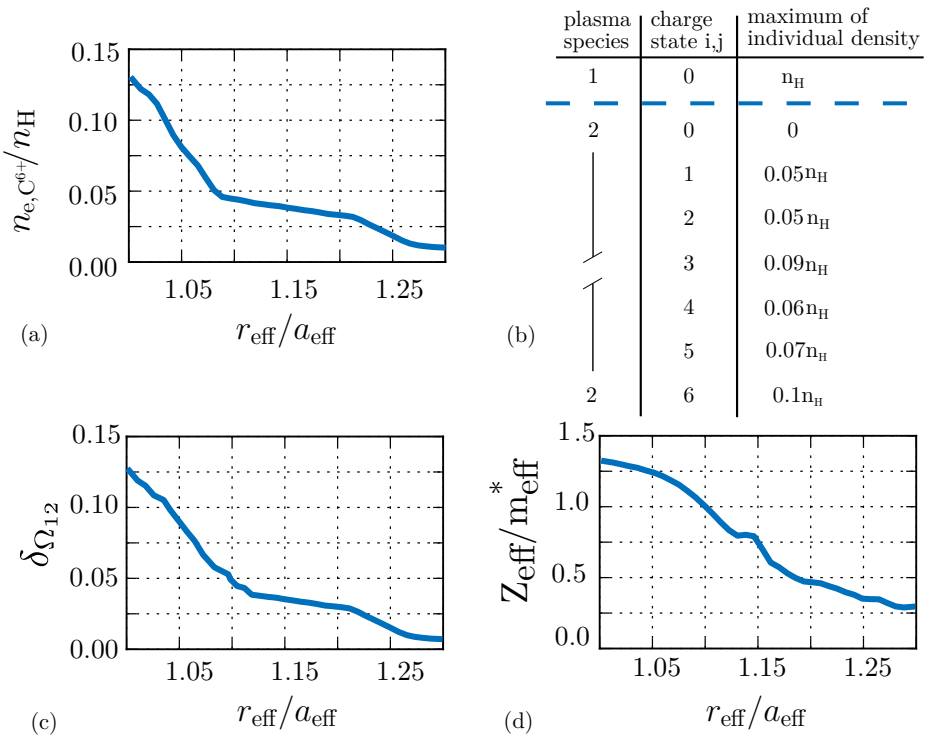

Figure 5.24: Maximum impurity density contribution plotted in (a). Overview of the error made by assumption Ω for δ_{Omega} for EMC3-EIRENE simulation $\Upsilon^{\mathrm{stage1,l_{end}}}_{\mathrm{MPM}}$ at the MPM location in (c). The error estimations are calculated with values shown in chart (b). The proportionality $c_s \propto Z_{\mathrm{eff}}/m^*_{\mathrm{eff}}$ plotted in (d) of process $\Xi_{c_s^{\mathrm{single*}}}$. The effective mass is normed to the hydrogen mass $m^*_{\mathrm{eff}} = m_{\mathrm{eff}}/m_{\mathrm{H}}$.

given between these values, which equals the overall profile's difference of $c_s^{\mathrm{single*}}$ and c_s^{multi} in Figure 5.21. Thus, a relatively difference between applied sound speed profiles can strongly affect the "refinement orientation" of processes $\Xi_{c_s^{\mathrm{single*}}}$ and $\Xi_{c_s^{\mathrm{multi}}}$. Regardless of the refinement orientation, the same number of iterative steps for converged profiles is required for processes $\Xi_{c_s^{\mathrm{single*}}}$ and $\Xi_{c_s^{\mathrm{multi}}}$. However, a large difference exists between final Z_{eff} and m_{eff} profiles, as shown in Figure 5.19(c) and (d). The amount of impurities in both final plasma scenarios $\Upsilon^{\mathrm{stage1,l_{end}}}_{\mathrm{MPM}}$ and $\Upsilon^{\mathrm{stage1,m_{end}}}_{\mathrm{MPM}}$ remains roughly the same (see Figure 5.19(a) vs. (c) and (b) versus (d)). However, the amount of higher charge states in the plasma differs largely over simulation $\Upsilon^{\mathrm{stage1,l_{end}}}_{\mathrm{MPM}}$ to $\Upsilon^{\mathrm{stage1,m_{end}}}_{\mathrm{MPM}}$ (given in all iterative steps, see A.7 versus A.8). This is a logical consequence because only the input density n_e is adjusted to meet refined measurement profiles. Constrained input powers $P^{\mathrm{SOL}}_{\mathrm{heat}}$ and $P^{\mathrm{SOL}}_{\mathrm{rad}}$ are held constant. Thus, the impurity influx $\Gamma^{\mathrm{imp},a}_{\mathrm{in}}$ is also held constant and plasma radiation losses are distributed over a lower input n_e. Higher impurity charge states are reached in case of process $\Xi_{c_s^{\mathrm{single*}}}$, thereby changing the effective mass. The sound speed profiles of processes $\Xi_{c_s^{\mathrm{single*}}}$ and $\Xi_{c_s^{\mathrm{multi}}}$ start to differ strongly, as shown in Figure 5.21(b). The effective sound speed $c_s^{\mathrm{single^*}}$ elevates to higher values than c_s^{multi}. Nevertheless, a convergence is again obtained for all studied plasma properties, as there are relative

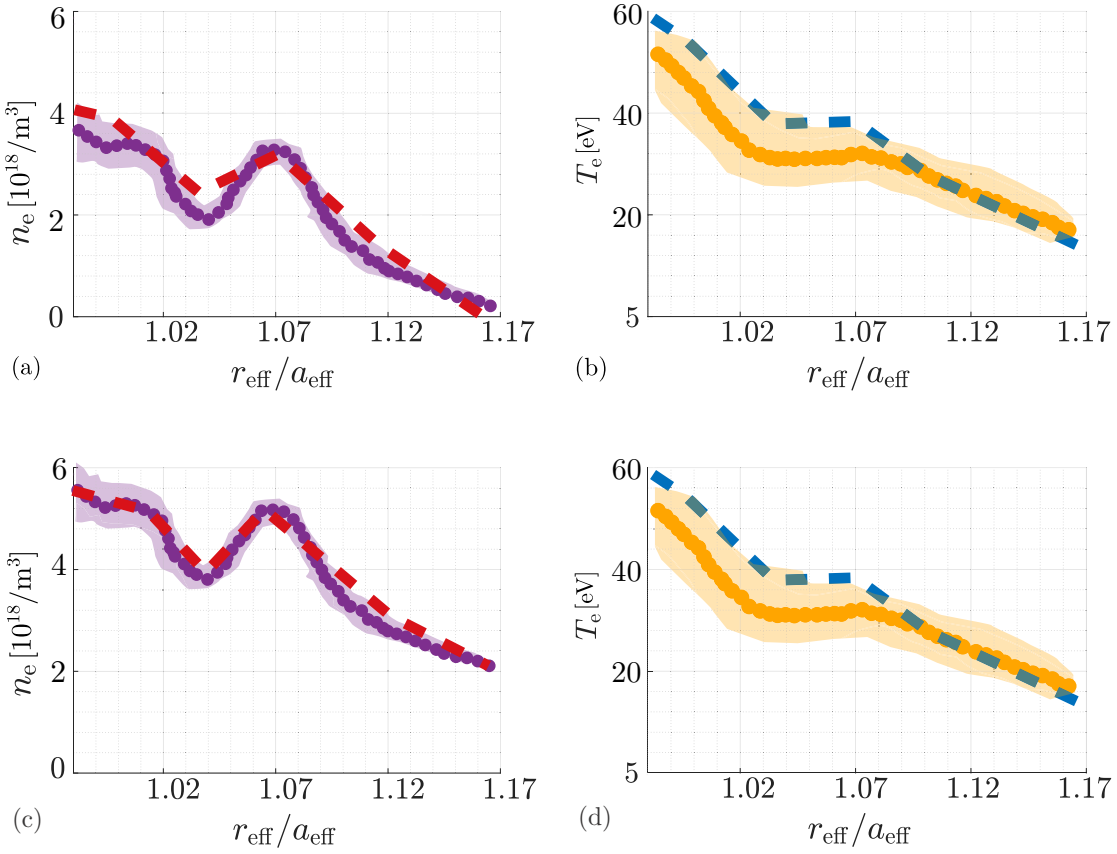

Figure 5.25: Final comparison between EMC3-EIRENE simulation (dashed) and $Z_{\text{eff}}^{l_{\text{end}}}$ adjusted MPM Langmuir probe measurements (dots). Plot (a) n_e, (b) shows T_e. Simulation parameters used from plasma scenario $\Upsilon_{\text{MPM}}^{\text{stage1}}$ of iterative process $\Xi_{c_s^{\text{single}*}}$. Subfigures (c) and (d) are the same plots as (a) and (b) but the results of process $\Xi_{c_s^{\text{multi}}}$.

(in the last step $m = 6$) changes for Z_{eff} of 3%, for m_{eff} of 1% and $n_{\text{e,MPM}}$ of 2%. An final input density of 6.83×10^{18} m^{-3} is applied. Thus, $n_{\text{e,MPM}}^{m_{\text{end}}}$ profiles are not as strong refined as $n_{\text{e,MPM}}^{l_{\text{end}}}$ profiles. A direct comparison is shown in Figure 5.25, where $n_{\text{e,MPM}}^{m_{\text{end}}}$ peaks at 4×10^{18} m^{-3} and $n_{\text{e,MPM}}^{m_{\text{end}}}$ at 5.8×10^{18} m^{-3}. This results in refinement of 12% for $n_{\text{e,MPM}}^{m_{\text{end}}}$ in an direct comparison to $n_{\text{e,MPM}}^{l_{\text{end}}}$ of 33%. Roughly same percentage refinement values were assessed for limiter Langmuir probe measurements in OP1.1 (see chapter 2.4). It was conclusively found that limiter results of this comparison process have to be treated with caution, since the plasma impurity content is quite high. The same goes for simulation $\Upsilon_{\text{MPM}}^{\text{stage1,m}_{\text{end}}}$. Hence wise, results of process $\Xi_{c_s^{\text{single}*}}$ have also be treated with caution.

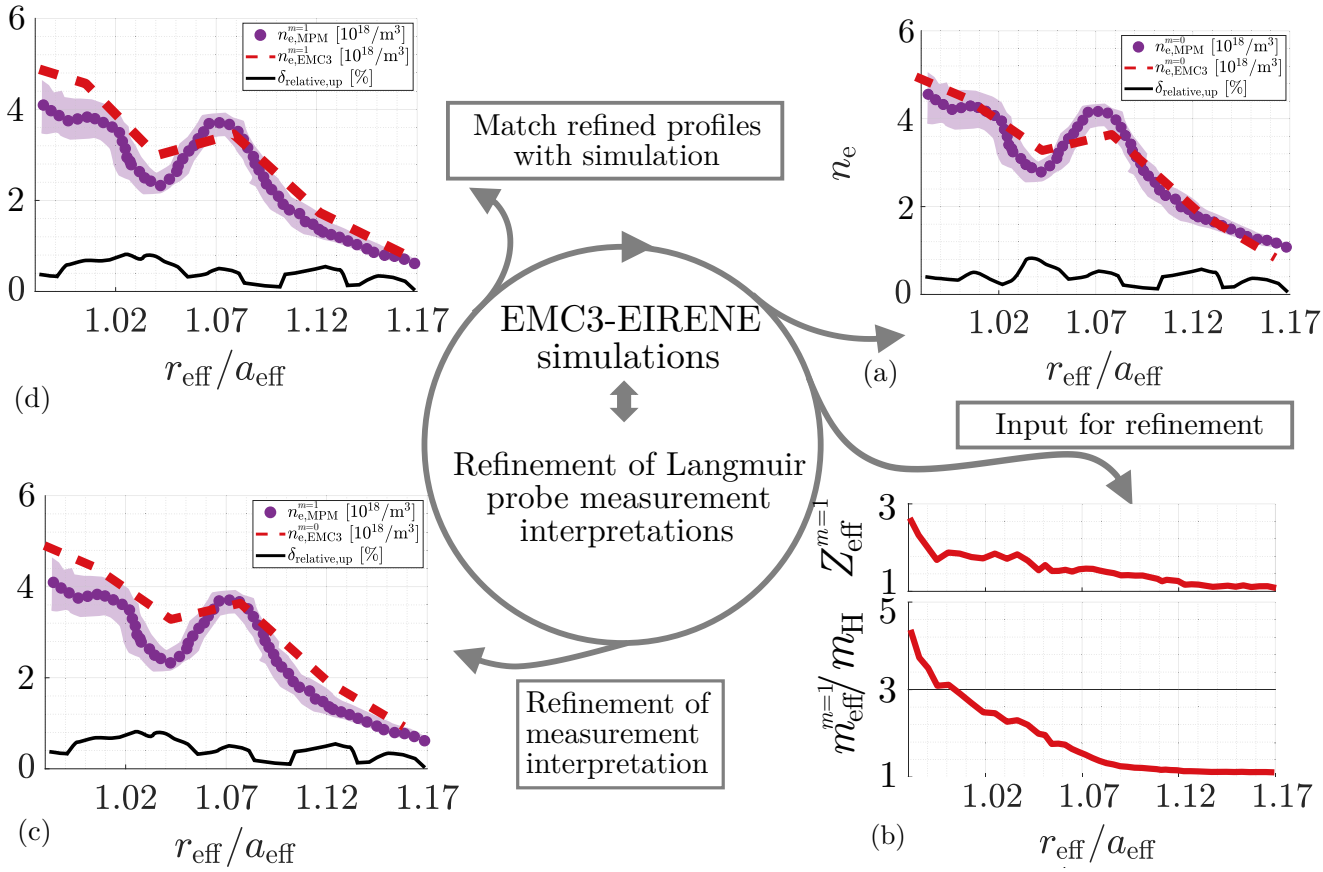

Figure 5.26: Schematic overview of the first step $m = 1$ of the iterative process $\Xi_{c_s^{\mathrm{multi}}}$ for MPM measurements. Electron density from $\Upsilon_{\mathrm{MPM}}^{\mathrm{stage1}}$ (a), $Z_{\mathrm{eff}} = 1$ and $m_{\mathrm{eff}} = 1$ was assumed for $n_{\mathrm{e,MPM}}$. Deduced Z_{eff}^{m} and m_{eff}^{m} profiles (b). Relative deviation $\delta_{\mathrm{relative,up}}^{l}$ (see equation (4.0.2.1)) plotted in the comparison plot of the numeric and measured density data-set(c) and (d). The rework of plot 5.26(a) is shown in (d).

5.1.3 Influence of main impurities and their quantification on divertor plasmas

Subsequently, the scheme for assessing the impurity release fraction in OP1.1 plasmas is applied to plasma 20180814.36. Simulation setup $\Upsilon_{\mathrm{MPM}}^{\mathrm{stage1,m_{end}}}$ is extended to a second impurity species: oxygen. Similar to section 2.4, oxygen point sources are distributed along first-wall elements. The same distribution scheme as in Figure 3.11 is followed. Again, plasma radiation losses are split over carbon and oxygen. The fraction $P_{\mathrm{rad}}^{\mathrm{C}}/P_{\mathrm{rad}}^{\mathrm{O}}$ is guessed to be the free input parameter; however, previously chosen fractions of $P_{\mathrm{rad}}^{\mathrm{C}}/P_{\mathrm{rad}}^{\mathrm{O}}$ for OP1.1 (see Figure 4.22) are also applied for simulation $\Upsilon_{\mathrm{MPM}}^{\mathrm{stage1,m_{end}}}$. A carbon-dominant plasma (named $\Upsilon_{\mathrm{MPM}}^{\mathrm{stage1,C}}$) is passed from $P_{\mathrm{rad}}^{\mathrm{C}}/P_{\mathrm{rad}}^{\mathrm{O}} > 1$ over a uniformly distributed plasma $P_{\mathrm{rad}}^{\mathrm{C}}/P_{\mathrm{rad}}^{\mathrm{O}} = 1$ to an oxygen-dominant plasma case $P_{\mathrm{rad}}^{\mathrm{C}}/P_{\mathrm{rad}}^{\mathrm{O}} < 1$ (named $\Upsilon_{\mathrm{MPM}}^{\mathrm{stage1,O}}$). The span between these chosen rations is covered by an iterative process, and $P_{\mathrm{rad}}^{\mathrm{total}} = (P_{\mathrm{rad}}^{\mathrm{C}} + P_{\mathrm{rad}}^{\mathrm{O}})$ is enforced. Results for OP1.1 showed that n_{e} and T_{e} profiles are not significantly affected by the chosen ration $P_{\mathrm{rad}}^{\mathrm{total}} = (P_{\mathrm{rad}}^{\mathrm{C}} + P_{\mathrm{rad}}^{\mathrm{O}})$. The same goes for the results of OP1.2. Figure 5.28(a) shows only a small effect

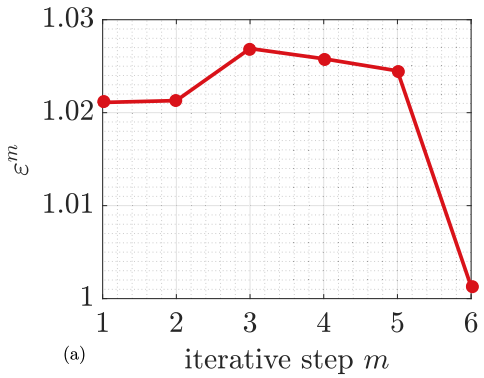

(a)

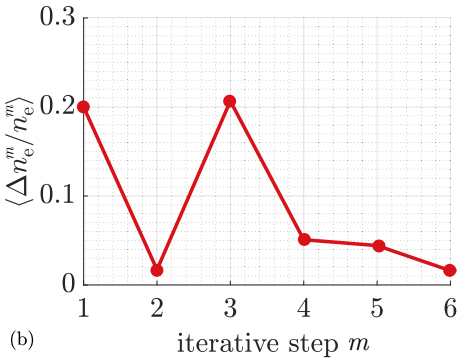

(b)

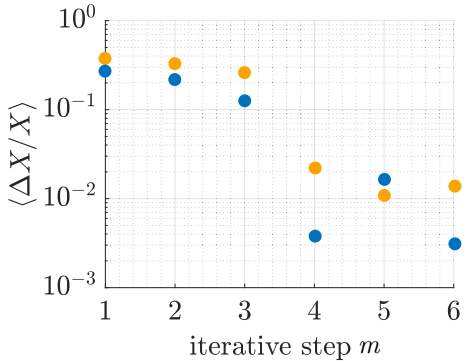

(c)

step m	input density [m^3/10^{18}]	ε^m	$\langle \Delta\ Z_{\text{eff}} / Z_{\text{eff}} \rangle$	$\langle \Delta\ m_{\text{eff}} / m_{\text{eff}} \rangle$	$\langle \Delta\ n^m_{\text{e,MPM}} / n^m_{\text{e,MPM}} \rangle$
1	6.0	1.0211	0.27	0.375	0.0397
2	6.126	1.0213	0.22	0.33	0.0847
3	6.322	1.0269	0.125	0.264	0.277
4	6.50	1.0258	0.0038	0.022	0.1316
5	6.67	1.0245	0.0165	0.0108	0.049
6	6.83	1.0013	0.0031	0.0137	0.024

(d)

Figure 5.27: (a) Factor ε^m plotted against each iteration step; (b) the relative change of the refined Langmuir probe measurement of n_e^m (MPM - red) plotted against each iteration step; and (c) the relative change of the upstream Z_{eff} and m_{eff} profiles plotted against each iteration step. Simulation parameters are taken from plasma scenario $\Upsilon^{\text{stage1}}_{\text{MPM}}$, but n_e was iterated from 6×10^{18} m^{-3} up to 6.83×10^{18} m^{-3}. Chart (d) shows the exact values of each iterative step for the upstream location.

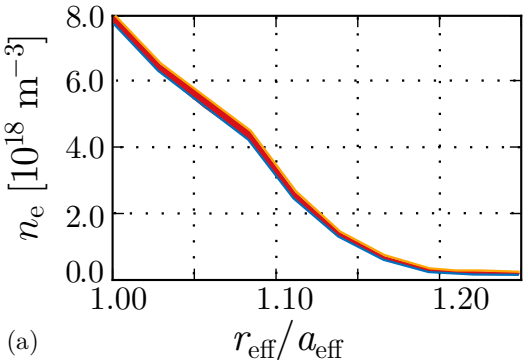

(a)

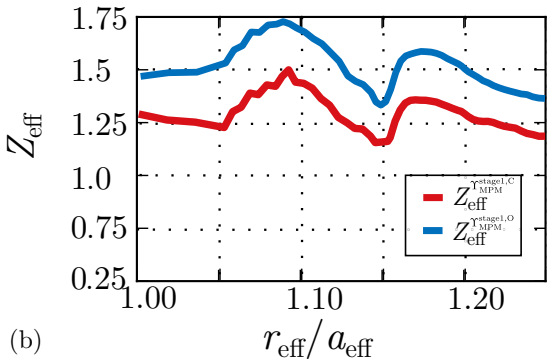

(b)

Figure 5.28: All seven resulting n_e profiles from the scan of $P^{\text{O}}_{\text{rad}} / P^{\text{total}}_{\text{rad}} \in \{0.1, ..., 0.9\}$ plotted in the red-shaded region, are shown in (a). Carbon-dominant case $\Upsilon^{\text{stage1,C}}_{\text{MPM}}$ (orange) and oxygen-dominant case $\Upsilon^{\text{stage1,O}}_{\text{MPM}}$ (blue) frame the set of n_e datasets. Subfigure (b) shows Z_{eff} profiles of $\Upsilon^{\text{stage1,C}}_{\text{MPM}}$ and $\Upsilon^{\text{stage1,O}}_{\text{MPM}}$.

of scanned radiated powers on n_e. Additionally, effects on T_e remain small (see Figure 5.29(a)). The consistency between EMC3-EIRENE simulation $\Upsilon_{\mathrm{MPM}}^{\mathrm{stage1},m_{\mathrm{end}}}$ and refined MPM measurements exist throughout all radiation fraction scans. Computational n_e and T_e results are framed by plasma profiles of the carbon and dominant simulations. More pronounced effects of the scanned fraction

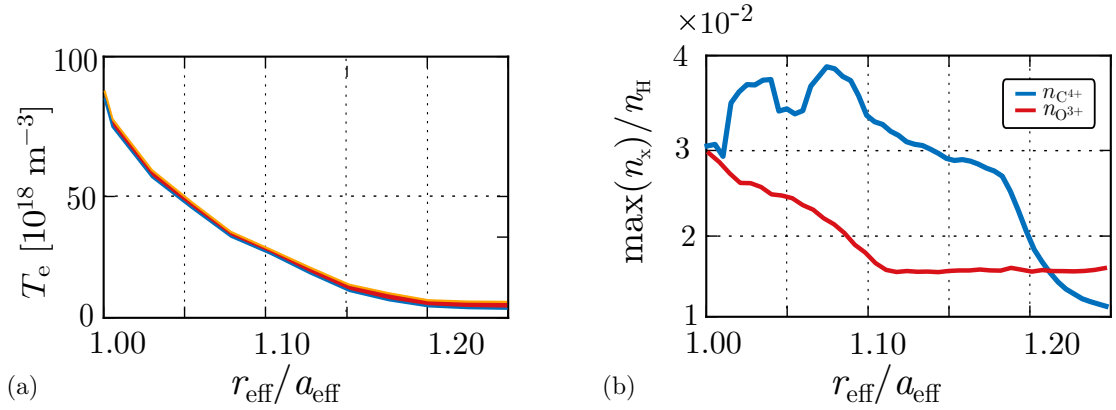

Figure 5.29: All seven resulting T_e profiles from the scan of $P_{\mathrm{rad}}^{\mathrm{O}}/P_{\mathrm{rad}}^{\mathrm{total}} \in \{0.1,...,0.9\}$ plotted in the red-shaded region, are shown in (a). Carbon-dominant case $\Upsilon_{\mathrm{MPM}}^{\mathrm{stage1,C}}$ (orange) and oxygen-dominant case $\Upsilon_{\mathrm{MPM}}^{\mathrm{stage1,O}}$ (blue) frame the set of n_e datasets. Subfigure (b) shows the maximum impurity charge state density profiles of $\Upsilon_{\mathrm{MPM}}^{\mathrm{stage1,C}}$ and $\Upsilon_{\mathrm{MPM}}^{\mathrm{stage1,O}}$.

$P_{\mathrm{rad}}^{\mathrm{C}}/P_{\mathrm{rad}}^{\mathrm{O}}$ are observable in Figures 5.28(b) and 5.29(b), where the effective charge state Z_{eff} and maximum impurity density contribution are shown. The effective charge state for a carbon dominant plasma shows lower values compared with an oxygen dominant plasma. Because, simulation $\Upsilon_{\mathrm{MPM}}^{\mathrm{stage1,O}}$ has $n_{O^{3+}}$ as the maximum impurity density contribution. No considerable carbon charge states are reached for $\Upsilon_{\mathrm{MPM}}^{\mathrm{stage1,O}}$. However, this changes for simulation $\Upsilon_{\mathrm{MPM}}^{\mathrm{stage1,C}}$, where the maximum impurity density contribution comes from the fourth charge state of carbon. Figure 5.29(b) shows that $n_{C^{4+}}$ has a higher density than $n_{C^{3+}}$.

As the next step, corresponding impurity release fractions can be deduced. Particular release fractions are again taken from the code output and normed to the recycling flux onto the divertor targets. Thus, oxygen release fractions (coming from point sources) are also normed to the hydrogen influx. Assessed release fractions are shown in Figure 5.30. The same linearity, as shown in Figure 4.22 for OP1.1 plasmas, is again obtained and shown in Figure 5.30. Assessed release fractions pass from a carbon-dominant plasma with $R_{\mathrm{EMC3}}^{\mathrm{H}\rightarrow\mathrm{C}} = 5.6\%$ to an oxygen-dominant plasma with $R_{\mathrm{EMC3}}^{\mathrm{O}} = 2.8\%$. Thus, the assessed OP1.2 released fractions do have the same order of magnitude as those of OP1.1. However, the crossover point changes from case $P_{\mathrm{rad}}^{\mathrm{O}}/P_{\mathrm{rad}}^{\mathrm{total}} = 0.5$ to 0.66. A higher carbon portion remains within the oxygen-dominant cases, which matches the results in Figure 5.29. A direct comparison shows that the carbon release rates of OP1.2 drop more slowly than those for

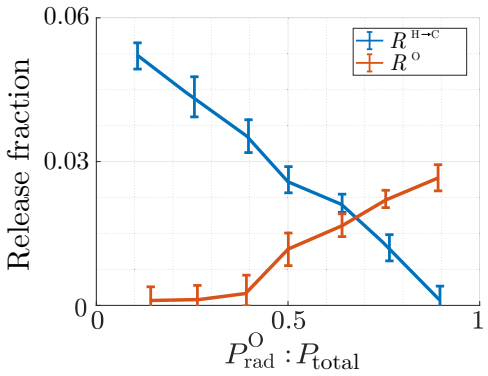

Figure 5.30: Release fraction $R^{\{H\to C,O\}}_{EMC3}$ plotted against each simulation setup of the scan of $P^{O}_{rad}/P^{total}_{rad} \in \{0.1,...,0.9\}$ reaching from the carbon-dominant plasma ($\Upsilon^{stage1,C}_{MPM}$, left-hand side) to the oxygen-dominant plasma ($\Upsilon^{stage1,O}_{MPM}$, right-hand side).

OP1.1. This might be because of to different measured radiation losses or higher recorded electron densities. However, the empirical chemical release rate of carbon can be found at the same fraction of $P^{O}_{rad}/P^{total}_{rad} = 0.5$ as for OP1.1 plasmas (see Figure 4.22).

5.1.4 Comparison of assessed limiter and divertor impurity plasma characteristics

Divertor and limiter plasma do not share the same magnetic configuration nor the same key parameters which are used to constrain EMC3-EIRENE input parameters. Thus, a direct comparison of these plasmas seems not obvious. However, key plasma properties, assessed by discussed EMC3-EIRENE plasma simulations, like the ions sounds speeds, effective charge state and mass plus impurity release fractions of both operational phases are directly compared in the following.
Only OP1.1 and OP1.2 plasmas which have approximately the same key parameters are compared in the scope of this chapter, to assure that studied plasmas differ not much. Simulation $\Lambda^{l_{end}}$ is chosen as OP1.1 plasma, while simulation $\Upsilon^{stage1,m_{end}}_{MPM}$ is chosen for OP1.2. They have approximately the same fraction of $P^{SOL,OP1.2}_{heat}/P^{SOL,OP1.2}_{rad} \approx P^{SOL,OP1.1}_{heat}/P^{SOL,OP1.1}_{rad}$. Iterative processes were applied in chapter 2.4 and 5.1.2 to account for the plasmas impurity content and thereby refine MPM Langmuir probe measurements. Only end results of these processes are shown and compared in this chapter.
The effective charge state and mass were combined to an effective speed of sound $c^{single^*}_s$ and compared to an exact speed of sound c^{multi}_s. These speed of sounds do not show a significant difference in between them. But, for OP1.2 plasmas they do, which is shown in Figure 5.31. Profiles shown in Figure 5.31(a) and (b) do not share the same spatial resolution (here r_{eff}), which is due to the different magnetic configuration of OP1.1 and OP1.2. Ions in the OP1.2 plasma reach higher sound speed, primarily because an higher ECRH heating power was applied to the considered plasma. However, other causes like the change of the magnetic configuration of the closer distance to target plates

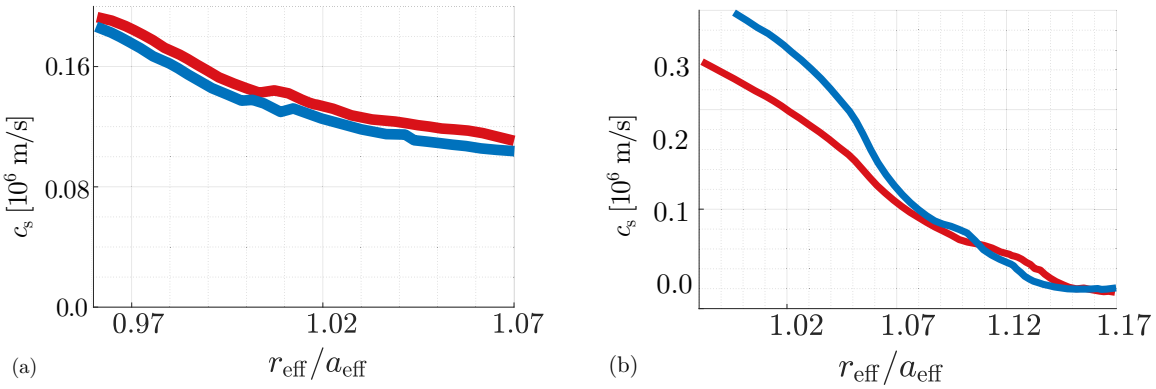

Figure 5.31: Effective speed of sound $c_s^{\mathrm{single}^*}$ comparison to the multi-species speed of sound c_s^{multi} at the MPM measurement location. OP1.1 plasma in (a) OP1.2 plasma in (b).

might be relevant. In any case, higher temperatures are reached and as a consequence equation (4.0.1.2) and (4.0.1.1) change to higher velocities. Corresponding effective charge state density and effective mass profiles are shown in Figure 5.32. Roughly the same impurity contamination (quanti-

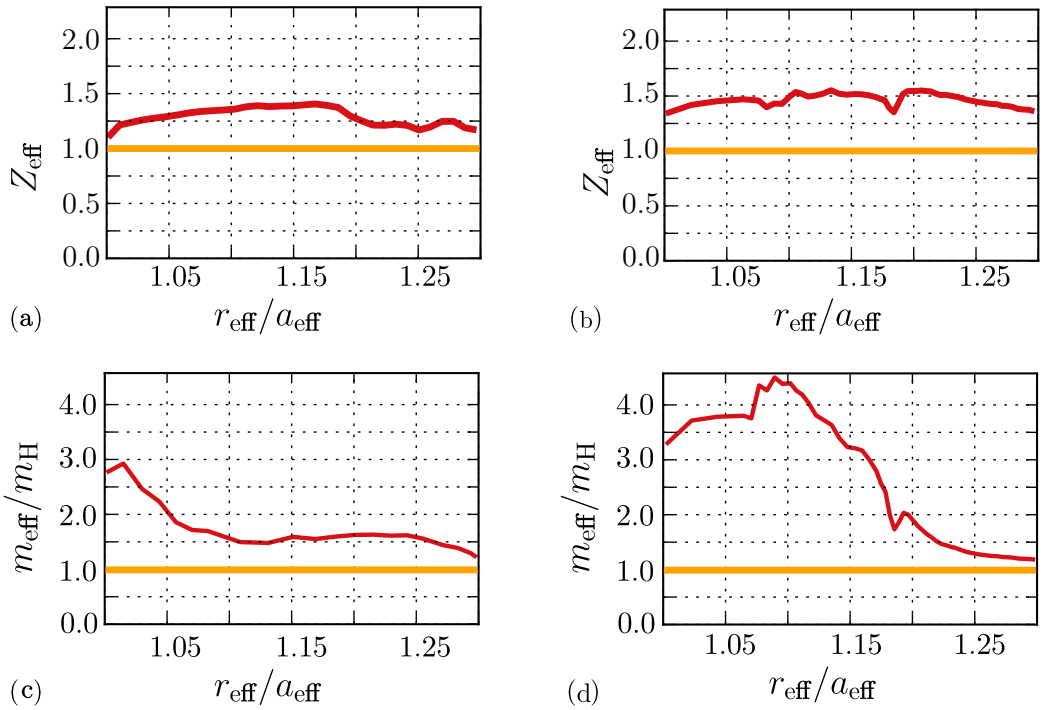

Figure 5.32: Effective charge and mass profiles of OP1.1 ((a) and (c)) and OP1.2 ((b) and (d)) plotted over the effective radius at the MPM measurement location.

fied by Z_{eff}) is given for simulation $\Lambda^{l_{\mathrm{end}}}$ (see Figure 5.32(a)) and $\Upsilon_{\mathrm{MPM}}^{\mathrm{stage1},m_{\mathrm{end}}}$. But, different effective masses are the result of higher OP1.2 temperatures. Then, higher temperatures (see Figure 4.4 (OP1.1)

versus 5.25 (OP1.2)) provide energy on which higher impurity charge states are reached. Only a maximum temperature, measured by the MPM at an toroidal angel of $\varphi = 200°$, of $T_e^{OP1.1} \approx 15$ eV was reached in OP1.1 in comparison to $T_e^{OP1.2} \approx 40$ eV for OP1.2. Again, the change of the plasma set-up or the change in the magnetic configuration might play a role here. However, the overall profile trend remains the same for OP1.1 and OP1.2 plasmas.

The introduction of oxygen as second impurity species into OP1.1 and OP1.2 plasmas was used to study the impurity release fractions. Pure carbon simulations $\Upsilon_{MPM}^{stage1,m_{end}}$ and $\Lambda^{l_{end}}$, from OP1.1 and OP1.2 (see chapter 4 and 5), were modified form carbon dominant simulations (small oxygen contamination, Λ^C and $\Upsilon_{MPM}^{stage1,C}$) up to oxygen dominant simulations (small carbon contamination, Λ^O and $\Upsilon_{MPM}^{stage1,O}$). OP1.1 simulations Λ^C (solid blue line in Figure 5.33(a)) and Λ^O (solid red line in

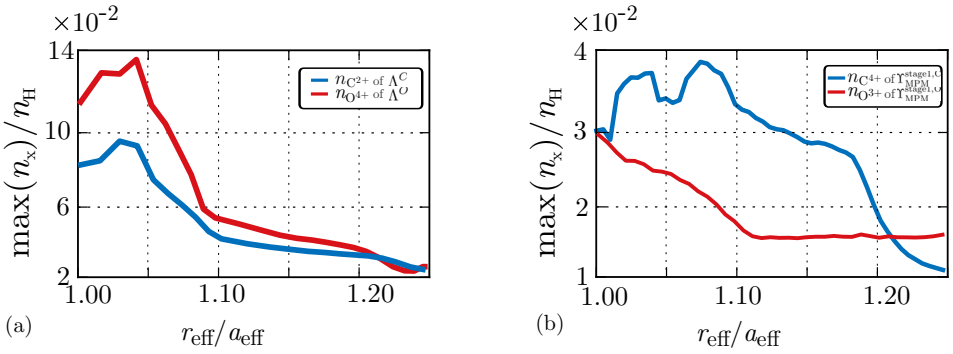

Figure 5.33: Maximum impurity densities of OP1.1 (a) and OP1.2 (b) plotted over the effective radius at the MPM measurement location.

Figure 5.33(a)) show profiles where the fourth charge state of oxygen has a higher contribution to the main electron density than second charge state of carbon. The exact opposite is obtained from OP1.2 simulations $\Upsilon_{MPM}^{stage1,C}$ (solid blue line in Figure 5.33(b)) and $\Upsilon_{MPM}^{stage1,O}$ (solid blue line in Figure 5.33(b)), where the fourth charge state density of carbon transcends the third charge state density of oxygen. Then, a direct comparison of the profile magnitudes shows, that considered OP1.1 plasmas have a higher impurity contamination than considered OP1.2 plasmas. This effect occurs due to higher applied input densities for simulation $\Upsilon_{MPM}^{stage1,C}$ while the radiated power remains in the same order of magnitude as for simulation Λ^C. Thus, the impurity contamination is reduced. Assessed impurity release fractions are shown in Figure 5.34(a) and (b). The same fractions of $P_{rad}^C : P_{rad}^O$ were scanned for OP1.1 and OP1.2 plasmas. Carbon dominant plasmas, for the limiter Λ^C and divertor $\Upsilon_{MPM}^{stage1,C}$, do have roughly the same release fractions for carbon and oxygen impurities (see Figure 5.34 (a) and (b)). The same goes for oxygen dominant plasmas, Λ^O and $\Upsilon_{MPM}^{stage1,O}$ (see Figure 5.34 (a) and (b)). Additionally, carbon release fractions drop, while oxygen ones rise, linear for both operational phases in respect to the chosen radiated power $P_{rad}^O : P_{rad}^{total} \in \{0.1, ..., 0.9\}$. This is expected since a nearly linear impurity core model is implemented. The often used empirical carbon release fraction $R^{H\to C} = 2\%$[56] is found in the results of both operational phases for a mixture of carbon and oxygen. Pure carbon or carbon dominant plasmas (simulation setups for OP1.1 and OP1.2 Λ^C and $\Upsilon_{MPM}^{stage1,C}$)

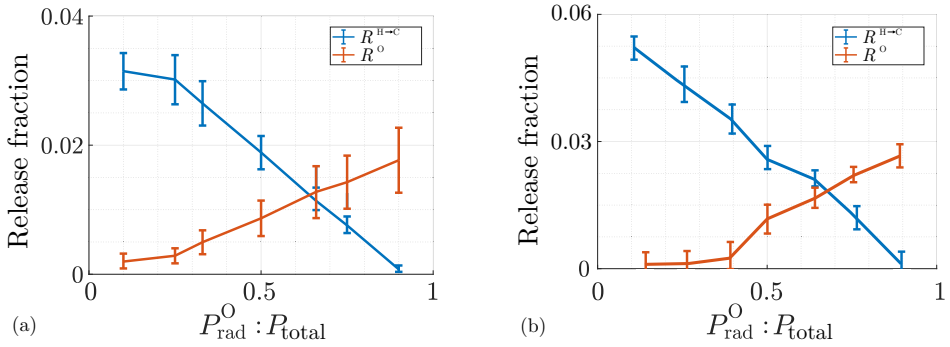

Figure 5.34: Assessed release fractions ($R^{\mathrm{H}\to\mathrm{C}}$ shown in blue, R^{O} shown in orange) of OP1.1 (a) and OP1.2 (b) plotted over scanned fractions of $P^{\mathrm{C}}_{\mathrm{rad}} : P^{\mathrm{O}}_{\mathrm{rad}}$. Carbon-dominant results on the left-hand side (simulation Λ^{C} and $\Upsilon^{\mathrm{stage1},C}_{\mathrm{MPM}}$, in (a) and (b)), oxygen- dominant results on the right-hand side (simulation Λ^{O} and $\Upsilon^{\mathrm{stage1},O}_{\mathrm{MPM}}$, in (a) and (b)).

show higher release fractions, with $R^{\mathrm{H}\to\mathrm{C}} = 0.03$ and 0.055 than the empirical one $R^{\mathrm{H}\to\mathrm{C}} = 0.02$. Thus, both considered plasma scenarios may have remaining water atoms in the machine or an external oxygen lack might exist. However, release fractions of simulations $\Upsilon^{\mathrm{stage1},C}_{\mathrm{MPM}}$ and $\Upsilon^{\mathrm{stage1},O}_{\mathrm{MPM}}$ have to be treated with caution, because only one reference measurement (MPM Langmuir probes) was available. In contrast to that, simulations Λ^{C} and Λ^{O} were compared to three different reference points.

Iterative processes $\Xi_{c_{\mathrm{s}}^{\mathrm{single}*}}$ and $\Xi_{c_{\mathrm{s}}^{\mathrm{multi}}}$ were applied to OP1.1 and OP1.2 plasmas. The convergence trend in between these four different applied processes shows several varieties. Figure 5.35 shows all four applied iterative processes for OP1.1 and OP1.2 plasmas. Convergence trends are respectively observable for the refinement factor $\varepsilon^{\{l,m\}}$ and for the relative electron density change $\langle \Delta n_{\mathrm{e}}^{\{l,m\}} / n_{\mathrm{e}}^{\{l,m\}} \rangle$. All processes show a convergence of $\varepsilon^{\{l,m\}}$ to one and a convergence of $\langle \Delta n_{\mathrm{e}}^{\{l,m\}} / n_{\mathrm{e}}^{\{l,m\}} \rangle$ to values below two percent. However, the convergence trend of $\varepsilon^{\{l,m\}}$ changes throughout the different iterative processes. $\Xi_{c_{\mathrm{s}}^{\mathrm{single}*}}$ applied on OP1.1 plasmas (see Figure 5.35(a)) shows a continual increase of ε^{l} to $\varepsilon^{l} \simeq 1$. Whereas, process $\Xi_{c_{\mathrm{s}}^{\mathrm{single}*}}$ shows first a refinement of n_{e} to higher values ($\varepsilon^{m} > 1$ for $m = 1$), followed by a drop to a refinement of n_{e} to lower values. From this drop on ε^{m} continual increases to $\varepsilon^{m} \simeq 1$. The same kind of convergence trend is obtained for process $\Xi_{c_{\mathrm{s}}^{\mathrm{single}*}}$ applied to OP1.2 plasmas. The second iterative step $l = 2$ shows the same kind of drop to $\varepsilon^{l} = 0.78$, which is also followed by a increase to $\varepsilon^{l} \simeq 1$. A complete different trend results from the application of $\Xi_{c_{\mathrm{s}}^{\mathrm{multi}}}$ to OP1.2 plasmas. Electron densities are refined successively to higher density values, starting at $\varepsilon^{m} = 1.21$ which is then followed by a continual decrease to $\varepsilon^{l} \simeq 1$. In conclusion the "convergence orientation" may change in between different processes or even internally of a single iterative process, but the successful convergence to final results is not affected.

Results for $\varepsilon^{l,m}$ are accompanied by the relative change $\langle \Delta n_{\mathrm{e}}^{\{l,m\}} / n_{\mathrm{e}}^{\{l,m\}} \rangle$ in Figure 5.35 on the right hand side ((b),(d),(f) and (h)). Since all applied processes do show a continual convergence, this convergence is also present for $\langle \Delta n_{\mathrm{e}}^{\{l,m\}} / n_{\mathrm{e}}^{\{l,m\}} \rangle$. However, the convergence trend of these profiles differ

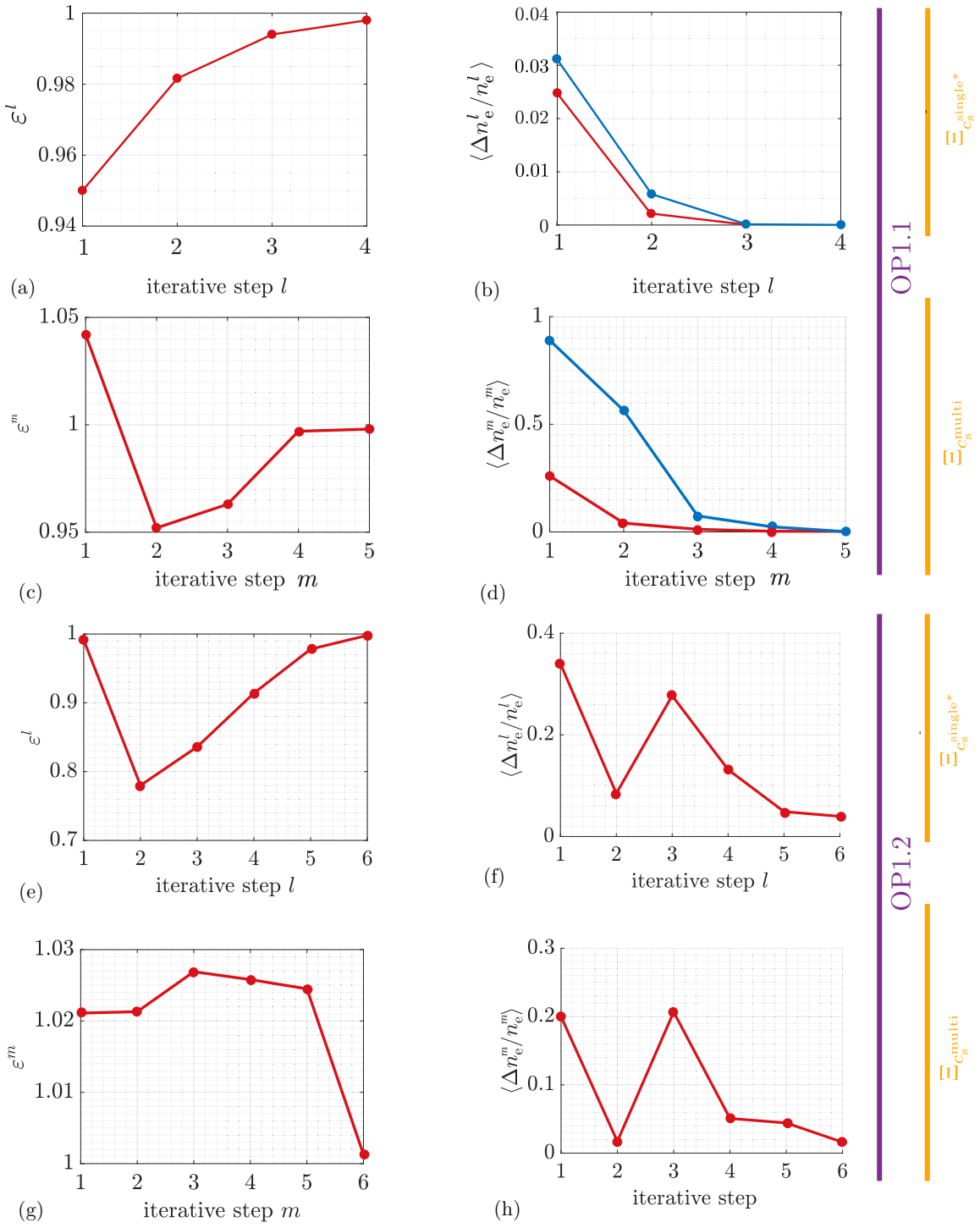

Figure 5.35: Factor $\varepsilon^{\{l,m\}}$ (left-hand side ((a),(c),(e), and (g))) and relative change of $\langle \Delta n_e^{\{l,m\}} / n_e^{\{l,m\}} \rangle$ (right-hand side ((b),(d),(f), and (h))) shown for all iterative processes. Process $\Xi_{c_s^{\text{single*}}}$ is applied for OP1.1 and OP1.2 plasma in (a) to (b) and (e) to (f). Process $\Xi_{c_s^{\text{multi}}}$ is applied for OP1.1 and OP1.2 plasmas in (c) to (d) and (g) to (h). Results for the MPM measurement location are shown in red, whereas results for the limiter location are shown in blue.

in between applied processes as well. Smaller and bigger steps in the refinement factor $\varepsilon^{\{l,m\}}$ result in a smaller and bigger steps of $\langle \Delta n_e^{\{l,m\}} / n_e^{\{l,m\}} \rangle$ respectively. Thus, Figure 5.35(f) shows a characteristic high change of the electron density with 35%. Nevertheless, all $\langle \Delta n_e^{\{l,m\}} / n_e^{\{l,m\}} \rangle$ converge to relative changes below 2%.

CHAPTER 6

SUMMARY AND CONCLUSION

6.1 Summary

In this study, EMC3-EIRENE was applied as a 3D interpretative tool to perform impurity studies on different experimental fusion plasma scenarios of the stellarator W7-X. The operation of the W7-X was split into two heat exhaust concepts. In the first operational phase, a limiter served as the main heat and particle exhaust option to protect first-wall elements from damage. This was changed to an island divertor for the second operational phase. A clear difference between the two operational phases was their magnetic configuration, and thus also their individual key plasma parameters. These parameters were introduced and compared. Major differences were the maximum allowed heating power and duration. EMC3-EIRENE calculated plasma properties of magnetic field lines of the given magnetic configuration. Thus, different sets of computational domains were introduced, including different sets of boundary conditions and their spatial grid resolution. EMC3-model equations were applied on these domains with different simulation parameters. An overview of the applied simulation parameters was given for each considered limiter or divertor plasma. Simulation parameters remain unknown if they are not constrained via diagnostic input on the W7-X. Therefore, each applied W7-X diagnostic for these constraints was introduced, including their basics. The discussion of Langmuir probes was extended to an iterative process that accounted for the plasmas' impurity contamination, because Langmuir probe measurements were the most diagnostically conclusive for the present study.

The purpose of protecting first-wall elements from damage remained the same. High applied heating powers up to several MW resulted in relatively high heat loads, which plasma-limiting components must withstand. Hence, the high heat-withstanding materials graphite and carbon were chosen as the primary materials for the limiting components. Experimental hydrogen or helium plasmas were then

accompanied by carbon impurities that contaminate plasma. The EMC3 impurity model consists of a particular “trace fluid model.” It neglects the electron density contribution from ionized impurities, but it does account for the associated impurity radiation electron power losses. An upgrade to this was introduced using an a posteriori approach to neglected impurity density contributions. The electron density of each impurity charge state was assessable with EMC3-EIRENE as a code output and taken as a contribution to the main plasma density. Furthermore, often neglected properties such as the effective charge state, mass, and speed of sound were calculated. Diagnostic assumptions, mainly Langmuir probe-type diagnostics, were replaced with assessed plasma edge profiles. Resulting Langmuir probe refinements were reapplied as constraints for consecutive EMC3-EIRENE simulations in an iterative manner. Convergence criteria were introduced to derive precise plasma edge profiles as end results of these iterative processes. Diagnostics that directly measure the effective charge state were absent for the limiter configuration and unavailable simultaneously with Langmuir probe measurements for the divertor configuration. Thus, iterative end results were not compared with effective charge state measurements. Rather, simulation results from Thomson scattering constraints were compared with direct effective charge state measurements. In this case, consistent results were obtained for three different reference times from the considered discharge.

Oxygen was introduced for EMC3-EIRENE simulations via uniformly distributed point source along first wall elements. Then, carbon and oxygen impurity outputs were processed to release fractions of impurities into the plasma, followed by a direct comparison with empirical release fractions of carbon. The fraction $P^{\mathrm{C}}_{\mathrm{rad}}/P^{\mathrm{O}}_{\mathrm{rad}}$ was varied to find plasma scenarios in which an empirical carbon release rate of 2% was reproduced. Both, limter and divertor plasmas reproduced this rate with $P^{\mathrm{C}}_{\mathrm{rad}}/P^{\mathrm{O}}_{\mathrm{rad}} = 1$. Furthermore, relatively high oxygen contamination was obtained for plasmas of both operational phases. This might have been caused by a lack of oxygen in system wall elements or water remaining in a preceding plasma. In these hydrogen atoms, oxygen impurities in and on the plasma facing components react to water retention. However, an expected linearity from the quasi-linear EMC3 impurity model was also reproduced.

Different diagnostic concepts, other than Langmuir probes were successfully compared with plasma edge modeling. Heat-flux measurements, Thomson scattering, and effective charge state measurements showed consistent results. Furthermore, Thomson scattering profiles were used to constrain EMC3-EIRENE simulations with discharges on which Langmuir probe measurements were not available. Simulation results were then directly compared with consistent effective charge state measurements of post processed Thomson scattering results. Additionally, this was given at three different points in time, and therefore for three different EMC3-EIRENE simulations.

Overall, EMC3-EIRENE was applied as a 3D plasma edge interpretative tool. Modifications to basic comparison schemes between plasma edge modeling and diagnostics were introduced and successfully applied to the W7-X limiter and divertor plasmas. Consistent results between modeling and measurements enabled impurity studies, in which impurity effects were theoretically quantified. Langmuir probe measurements benefited from this quantification, where the effective charge state

Z_{eff} and effective mass m_{eff} had to be considered. It was shown that general assumptions that Z_{eff} and m_{eff} equal 1 must be replaced with the exact values from EMC3-EIRENE simulations. Introduced iterative processes were used to constrain these values to plasma edge profiles with a spatial resolution. Furthermore, these were (for OP1.2 plasmas) confirmed by Z_{eff} diagnostics. However, the overall refinement seemed to be limited to values below 20%. This limitation might have occurred because of the given impurity contamination of the considered plasmas, which was not that high. A remaining free and guessed parameter was the impurity species choice for the plasma edge simulation. Carbon and oxygen were selected as the two main impurity species, but other species might have to be considered in future studies. Iron would be the next species to considered, and might have a stronger effect on the effective charge and mass because the charge number and mass of iron is higher than those of carbon and oxygen.

Applied iterative processes for multi-species plasmas were split into processes using an effective speed of sound and an exact speed of sound. The robustness of these regarding the convergence behavior was discussed and had to be treated as vague for the first iterative steps, although a convergence to exact plasma edge profiles was always given.

In addition, applied release rate studies for carbon and oxygen were conducted to assess the exact impurity species mixture in the considered plasmas. Results showed that the same amount of carbon and oxygen impurities were required to reach established empirical ones. Additional studies that include iron as a second or third impurity species would also confirm the existence of a second major impurity species to main carbon impurities. Several plasma edge and core diagnostics were applied for input parameter constraints and further used to check simulation results for consistency with these diagnostics. All numerical plasma edge profiles were consistent with multiple diagnostics. Thus, this study could treat the assessed mixture of carbon and oxygen impurities as justifiable. Moreover, EMC3-EIRENE supplied an insight into the exact distribution of charge states reached by the plasma, which was not given by any diagnostic. An additional error source was the point source distribution being chosen by hand. The most feasible option was chosen for this study because the system wall was approximated with 540 oxygen sources. Using the same point source mesh for an iron species would not be meaningful, because such point sources should only be placed in the region of iron installations. In future studies, the point source mesh can be adjusted to extrapolate a first precise estimate of places where oxygen is possibly lacking in the machine.

Difficulties regarding the applied basic EMC3 impurity model were revealed as separation effects within a magnetic island occurring for the electron temperature and density. Mean MPM coordinates were treated with caution because a shift in these coordinates equals an additional uncertainty for the achieved consistency. However, this uncertainty became nonsignificant because a consistency with multiple diagnostics was given. Nevertheless, a case study could be conducted in the future to provide greater insights into the introduced mean coordinate of MPM Langmuir probes.

6.2 Conclusion

Based on the summary of the thesis contents provided in the previous section, the most important key questions of each chapter can be answered as a conclusion to this thesis. Highlights and direct answers to the research questions postulated in Section 1.4 have an italic font in the following paragraphs.

- What are the characteristic plasma edge measurements in respect to the magnetic topology of W7-X? In which way can they profit from the impurity studies of this thesis?

Calculations of the electron density from measured Langmuir probe signals strongly depend on the plasma impurity content, which can be quantified in the effective charge state distribution function Z_{eff}. An iterative coupling – for limiter and divertor plasma – between diagnostic and numerical results was conducted for the effective and exact values. One can conclude that the use of effective values over exact values leads to a comparable refinement of Langmuir probe results.

- What input can plasma edge diagnostics provide to impurity studies?

A strong dependence between diagnostics and simulations was shown to demand bidirectional input. Free simulation parameters must be constrained with diagnostic findings and can be refined with diagnostic results. The amount of different diagnostics must not be too low to strengthen the consistency between experimental and numerical results.

- Why is the impurity transport and its quantification a key problem for long-pulse steady-state plasma operation in W7-X?

W7-X is an optimized stellarator for mitigating cross-field transport, the neoclassical and anomalous transport. *Neutral particles, of which a great deal are ionized to impurities, are not confined by the magnetic field; these particles may reach first wall elements or installations and disrupt the plasma.* Figure 2.17 provided Z_{eff} estimates, which were confirmed by results of the first impurity simulations of this thesis. Thus, impurity transport was studied in detail for this thesis and must be studied.

- What are the important model parameters in respect of interpretative impurity studies?

The EMC3 model parameters, which are relevant to impurity studies, are free simulation input parameters. *The most important are the radiated power in the SOL and the input density. These were constrained with bolometric power measurements and Langmuir probe measurements, the latter being the point of bidirectional coupling between measurements and simulations.* However, some deficiencies remained because the diagnostic's uncertainties directly affected the numerical results. Bolometric power measurement must be treated with great caution. However, the accuracy of the recorded radiated powers was confirmed by the consistency between EMC3 simulations and LP measurements (for limiter and divertor plasmas).

- What are the quantifications of the assessed impurity effects and what role do they play in respect of characteristic plasma edge measurements of W7-X in limiter configuration?

Chapters 4 and 5 showed that the quantifications of the impurity effects of a limiter and divertor plasma are the effective charge state density, mass, and speed of sound. Nevertheless, the plasmas' impurity content can be explicitly assessed using the EMC3-EIRENE code package. The effective charge state, however, enables a quick overview of the plasma's impurity content; thus, it was the preferred plot throughout this thesis.

- What are the results for a direct comparison of plasma edge modeling and measurement?

The value of the interpretative study was initially proven by the fact that EMC3-EIRENE simulations indicated a constructional offset for the MPM of four cm. *From there, consistency between several diagnostics to a single EMC3-EIRENE simulation was used to perform different impurity studies – using the exact speed of sound and effective speed of sound – as well as to refine Langmuir probe measurements and further constrain numerical results.* The converged results showed a refinement of a maximum of 12 and 19% using the exact and effective speed of sound, respectively. One can conclude that this is an unnecessary step because the results are quite low measured against the effort made. However, this changes for plasmas that reach a higher radiated power.
Impurity release rates assessed through studying the impurity content in the plasma. However, the EMC3 model reached its limits as no option exists to implement an impurity release from sputtering processes into the plasma. Artificial impurity sources had to be implemented in a periodic order along the first wall to replicate oxygen being released into the plasma. Comparing the assessed carbon and oxygen release rates with the literature – where only carbon release rates were found – let to the prediction of a significant oxygen source within the machine. *The somewhat aged assumption regarding the postprocessing of Langmuir probe findings of a pure hydrogen plasma can be replaced by assessed EMC3-EIRENE profiles. Some drawbacks remain because the demonstrated iterative processes require several independent measurements for one single plasma to guarantee the accuracy of the profiles. In the future, this accuracy can be improved by including more independent measurements of a single W7-X plasma.*

- Can predictions for future W7-X plasmas be made (based on the applied interpretive study)?

Chapter 4 showed that a significant oxygen source existed in the studied plasma. Empirical carbon release rates into the plasma can only be obtained with this significant oxygen source. However, the direct measurement of oxygen release rates has not been possible until now. Hence, the applicability and necessity of the applied interpretative impurity study were further proven. This prediction tool can be expanded to study the exact location of the oxygen source (or any other impurity; input from diagnostics is necessary here). The impurity source "blanket" (see Fig. 3.4.0.2) can be altered until given reference measurements are consistent with the impurity study, to identify the exact location of the impurity source. However, a uniform distribution of artificial oxygen sources along the first

experiment wall are fitting for the study of limiter plasmas. Thus, remaining water or evaporation of oxygen atoms from the first wall did play a role in these discharges.

The same questions that were studied for Chapter 4 were studied in Chapter 5 but for divertor plasma. However, some main differences occurred initially because divertor plasma has a higher fraction of plasma heating power to power, which is lost in the SOL. Thus, more heat power remains in the plasma.

- What are the limits on the applied interpretative studies and hence wise the limits of the impurity transport code?

Code artifacts from high radiation losses diminished the applicability of the successfully applied iterative process from Chapter 4. Separation effects of magnetic islands, shown in Figure 5.6 and as follows, are a hurdle for direct comparisons with MPM findings. Here, the plunge path of the MPM can lie within the valley of a separated magnetic island. In this case, consistency between simulation and diagnostics is prevented. Additionally, the assumption of a quasi-neutral plasma is violated by a plasma with such high radiation losses (see Figure 5.7). Thus, one can conclude that the "simple" EMC3 impurity model reaches its limits when applied to plasmas with high radiation losses. The reason for this is the choice of boundary conditions, because the impurity amount is directly coupled to the set radiated power. Limitations of the EMC3 model's applicability to plasma with high power losses over radiation were discovered; however, an exact quantification of the limitation's origin was not evaluated. Rather, a determination of the responsible simulation parameters is provided to aid future studies that use these types of plasma.
The same key questions as for Chapter 4 were answered by the impurity study of Chapter 5.

- What are the results for a direct comparison of plasma edge modeling and measurement?

Thomson scattering measurements were available for the divertor configuration of W7-X, which are processed into line-integrated effective charge state values. A direct comparison of assessed Z_{eff} profiles with line-integrated values was possible, and the results are shown in Figure 5.14. *The line-integrated values were confirmed by the simulation results for three different timepoints.*
This shows that the EMC3 code cannot resolve plasma dynamics in time. It can only resolve different points of time from a W7-X plasma – or any other fusion plasma – if for each timepoint an independent simulation is performed. However, this is outside the scope of this thesis. Nevertheless, another study applied the EMC3 code in a sequence of time-dependent simulations [60]. Input parameters are then connected in a sort of "daisy-chain" because results of simulation η are then input parameters for simulation $\eta + 1$. *One can conclude from this conformation of Z_{eff} values that the results of the interpretative impurity study from Chapter 4 can be trusted. Furthermore, advantages of an iterative impurity study (coupling of diagnostics to the EMC3 code) become clear. The main advantage is the 3D resolution of the full experiment compared with a line-integrated value deduced from the Thomson scattering system. Additionally, the coupling effect becomes profitable if the input parameter*

constraining diagnostics is affected by the simulation results.
Langmuir probes are effected by the results an EMC3-EIRENE simulation, as was shown in subsection 2.3.1. However, the amount of available diagnostics for a divertor plasma dropped. Neither divertor Langmuir probes nor the Thomson scattering system are available—along the MPM—for a single discharge. Thus, the comparison in Chapter 5 was split into a comparison of the Thomson scattering and MPM findings. The divertor plasma considered for a direct comparison with the MPM featured three different heating stages. Applying the iterative impurity study to each of these stages was outside the scope of this work. However, the first stage of the considered plasma was studied in detail following the process applied in Chapter 4 (see Figure 4.8). *Here, the diagnostic results at the end of the iterative process, including the exact and effective speed of sound, were refined by 12% and 33%, respectively.* The next step from here would be to include stages two and three of the considered discharge in the comparison process. The increase in heating power is accompanied with an increase in radiated power. Thus, the EMC3 impurity model might quickly reach its described limits. Hence, another option for continuing this work is upgrading to the impurity model.

- Can any predictions to future fusion plasma been given?

The same predictions can be given for divertor plasma as can be given for limiter plasma. *A significant oxygen source is also possible for divertor plasma because the assessed oxygen release fractions were in the same order of magnitude as for limiter plasma.* Again, the exact location of such an oxygen source could be identified by adjusting the oxygen source "blanket" in an iterative manner. A plasma's exact impurity composition can be used to provide decisive insights into the design of plasma-facing wall components. Here, the material should be selected based on the knowledge of particles that will hit these components. Thus, the assessed accurate plasma composition of OP1.1 and OP1.2, with carbon and oxygen, can play a key role here. This analysis can be widened to the next most common impurities, such as iron.

- What can one learn from a direct comparison between limiter and divertor plasma?

Direct comparisons of limiter and divertor plasmas' diagnostics findings are difficult—if not impossible. However, this changes if the diagnostics findings are supplemented with numerical impurity studies. Then, any results must be weighted with the vast amount of key parameters of W7-X plasmas. These differ considerably, as Table (a) and (b) showed in Section 2.2. *The impurity quantifications of limiter and divertor plasmas, as assessed in this thesis, can be compared with caution to the used code input parameters. Figure 5.24 showed that the effective charge state for different radiated powers—limiter versus divertor plasmas—had approximately the same magnitude. However, a significant difference existed in the effective mass, an effect that was only observable because of the impurity insights assessed in this thesis.* The observed difference was caused by the maximum impurity density contribution, which is the fourth charge state of oxygen for the considered limiter plasma and the fourth of carbon for the considered divertor plasma.

APPENDIX

ADDITIONAL FIGURES - ITERATIVE PROCESS

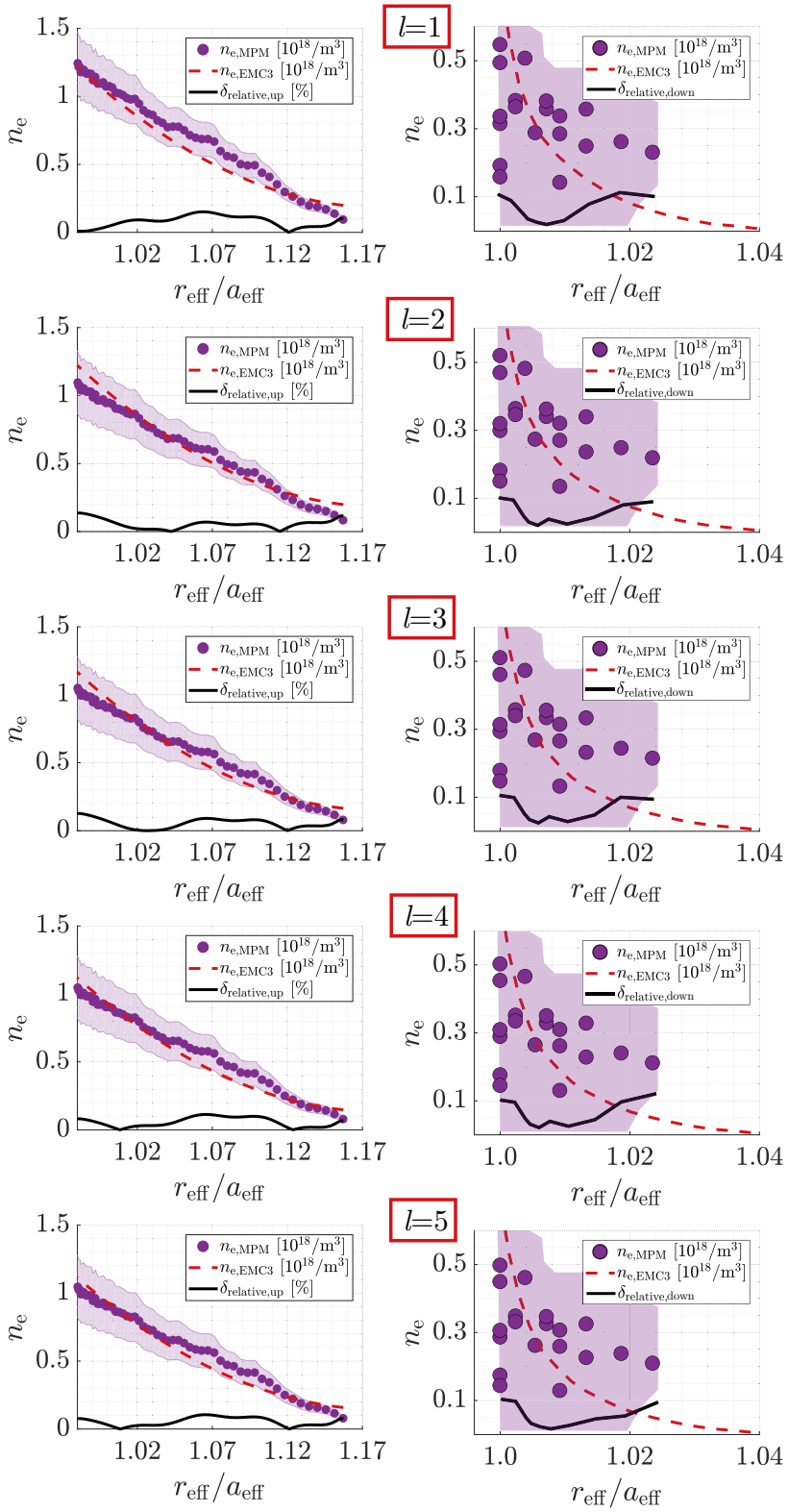

Figure A.1: All n_e profiles of the iterative process from $l = 1$ to $l = 5$.

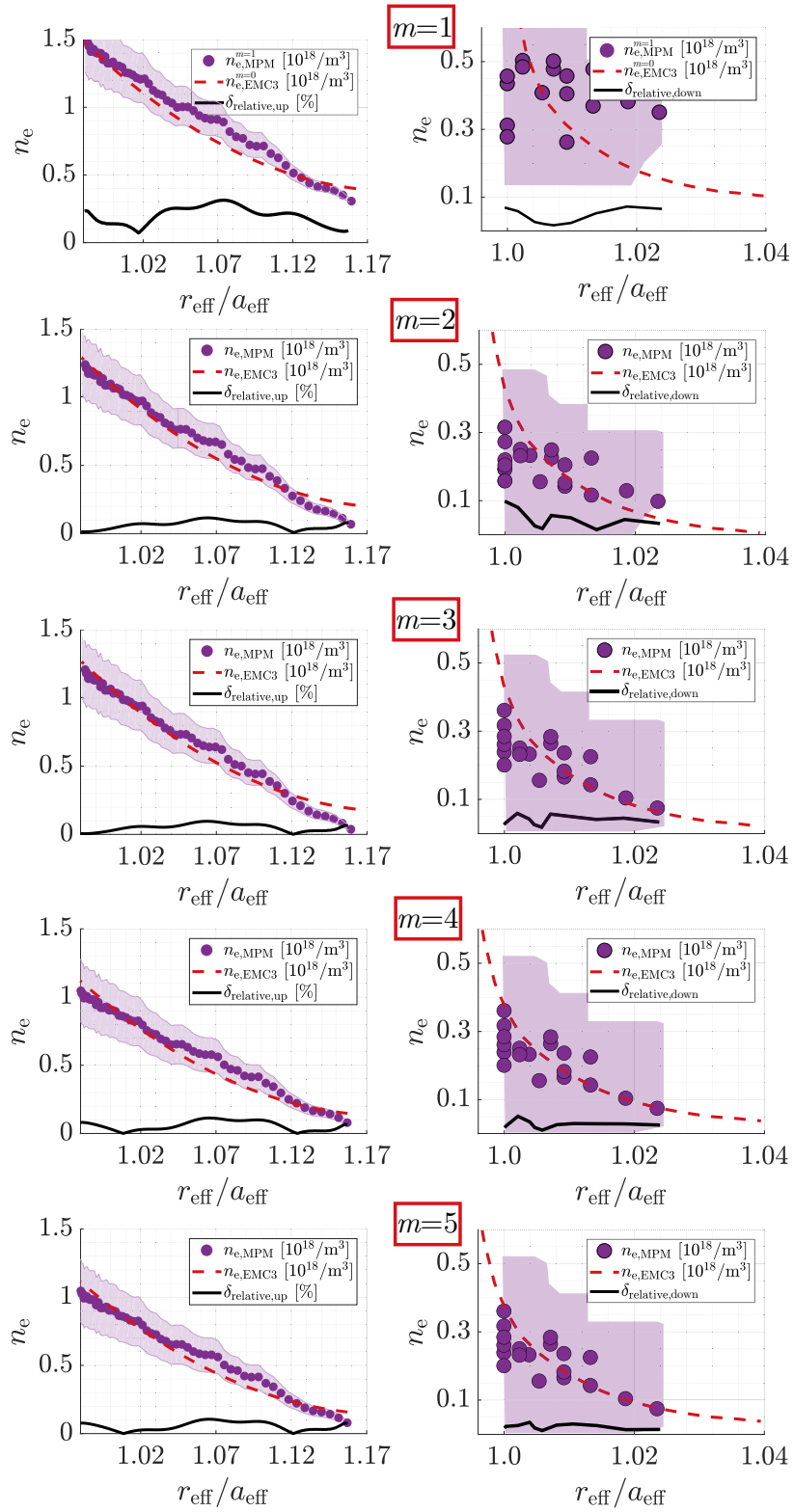

Figure A.2: All n_e profiles of the iterative process from $m = 1$ to $m = 5$.

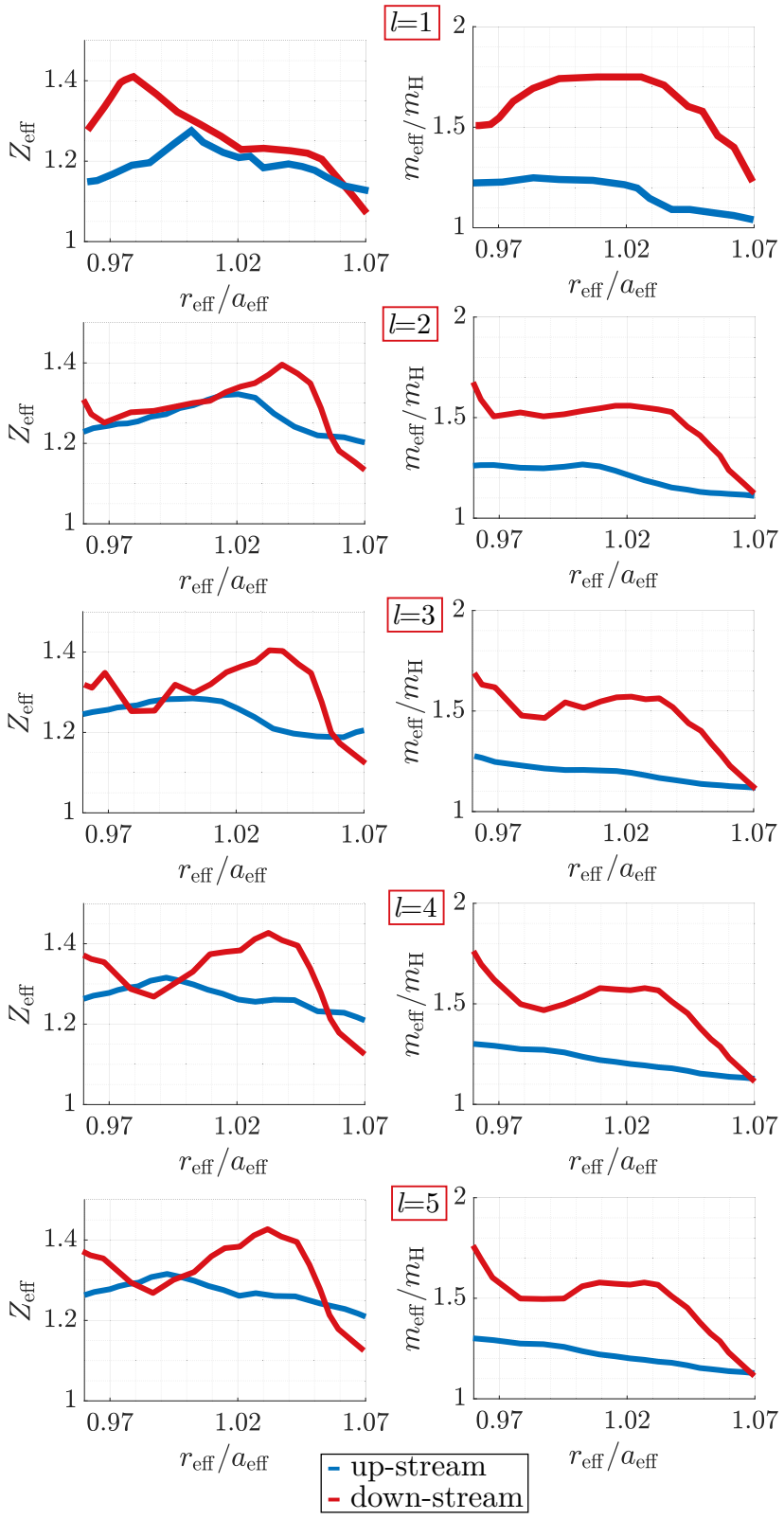

Figure A.3: All Z_{eff} and m_{eff} profiles of the iterative process from $l = 1$ to $l = 5$.

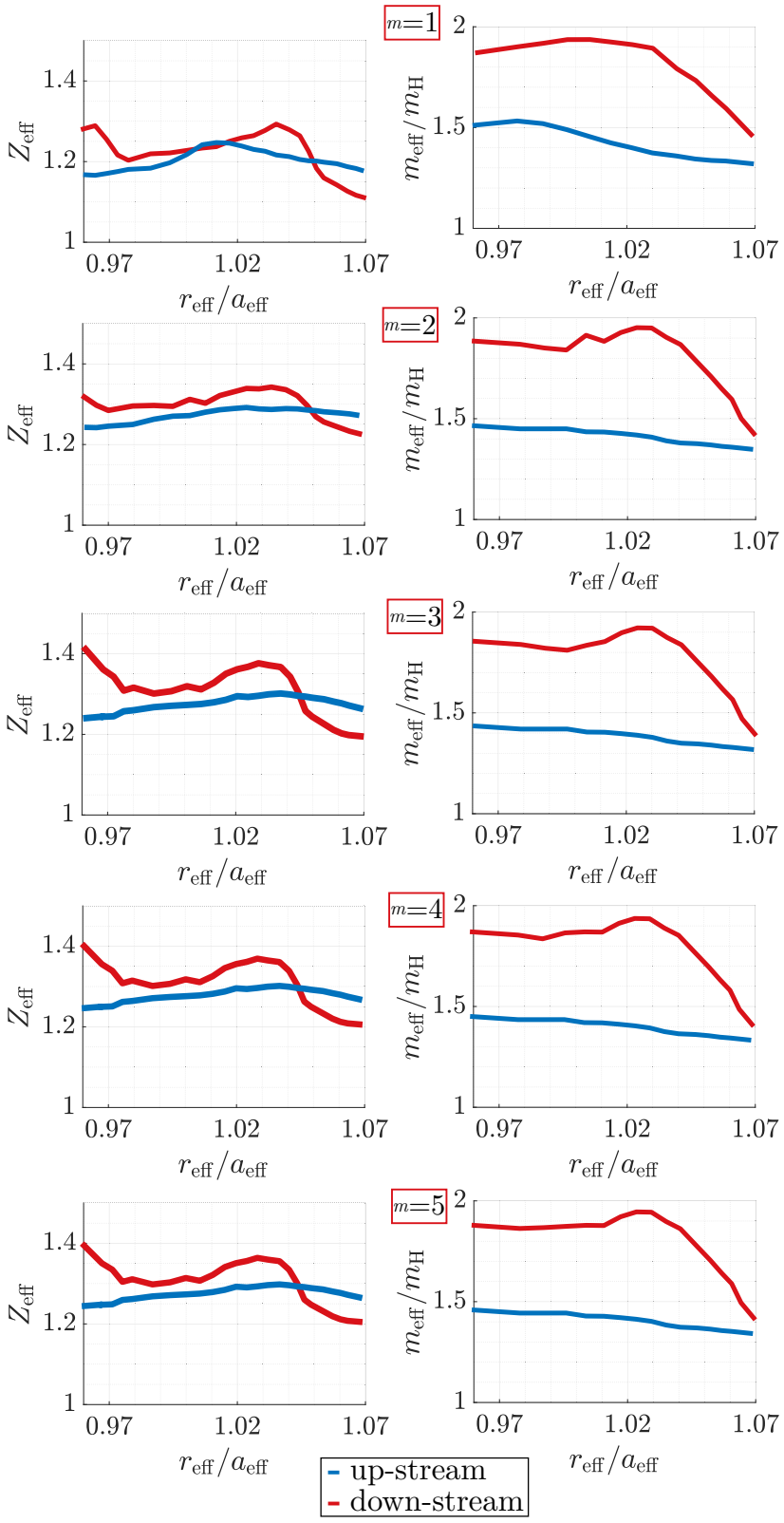

Figure A.4: All Z_{eff} and m_{eff} profiles of the iterative process from $m = 1$ to $m = 5$.

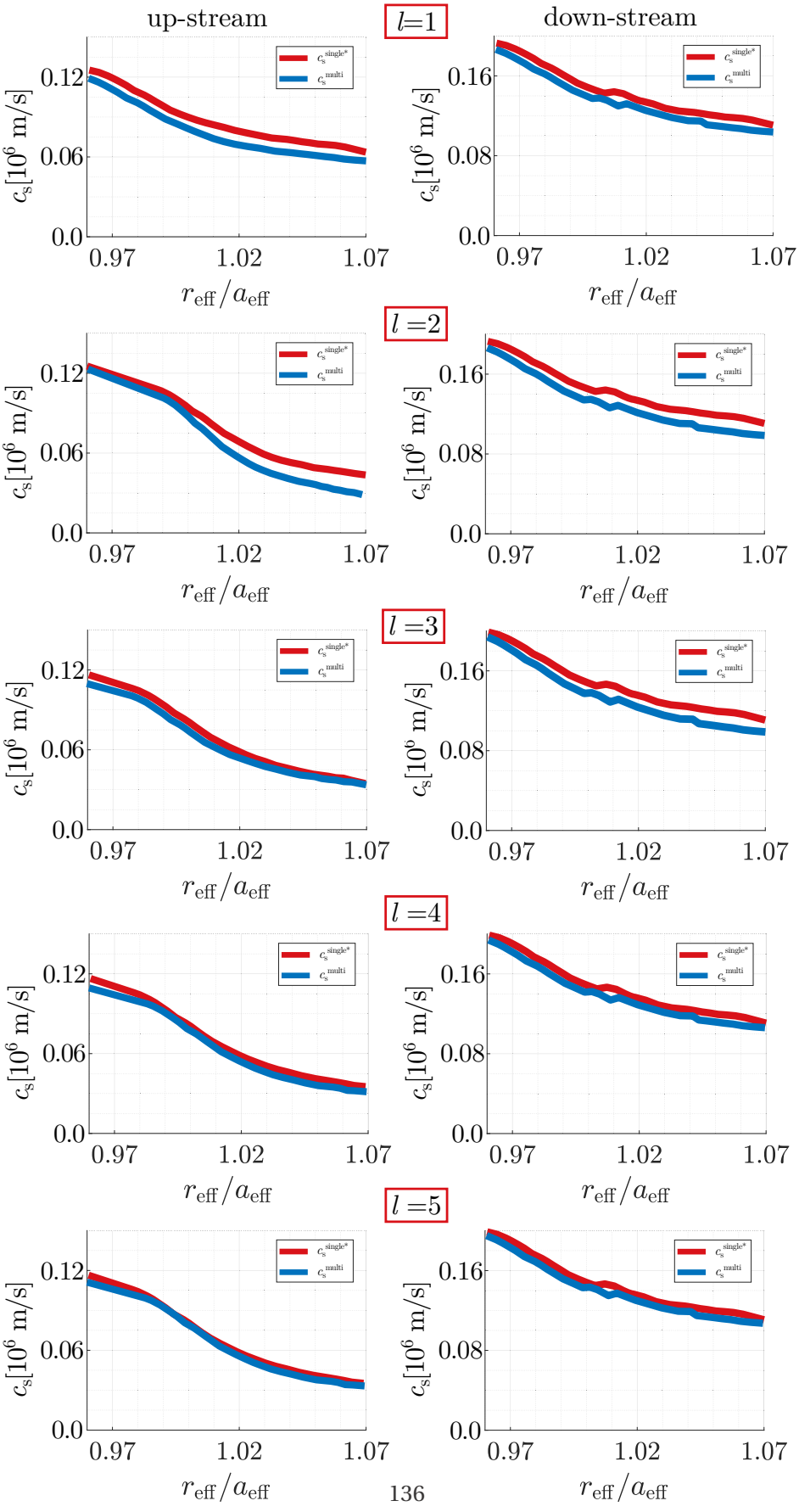

Figure A.5: All c_s profiles of the iterative process from $l = 1$ to $l = 5$.

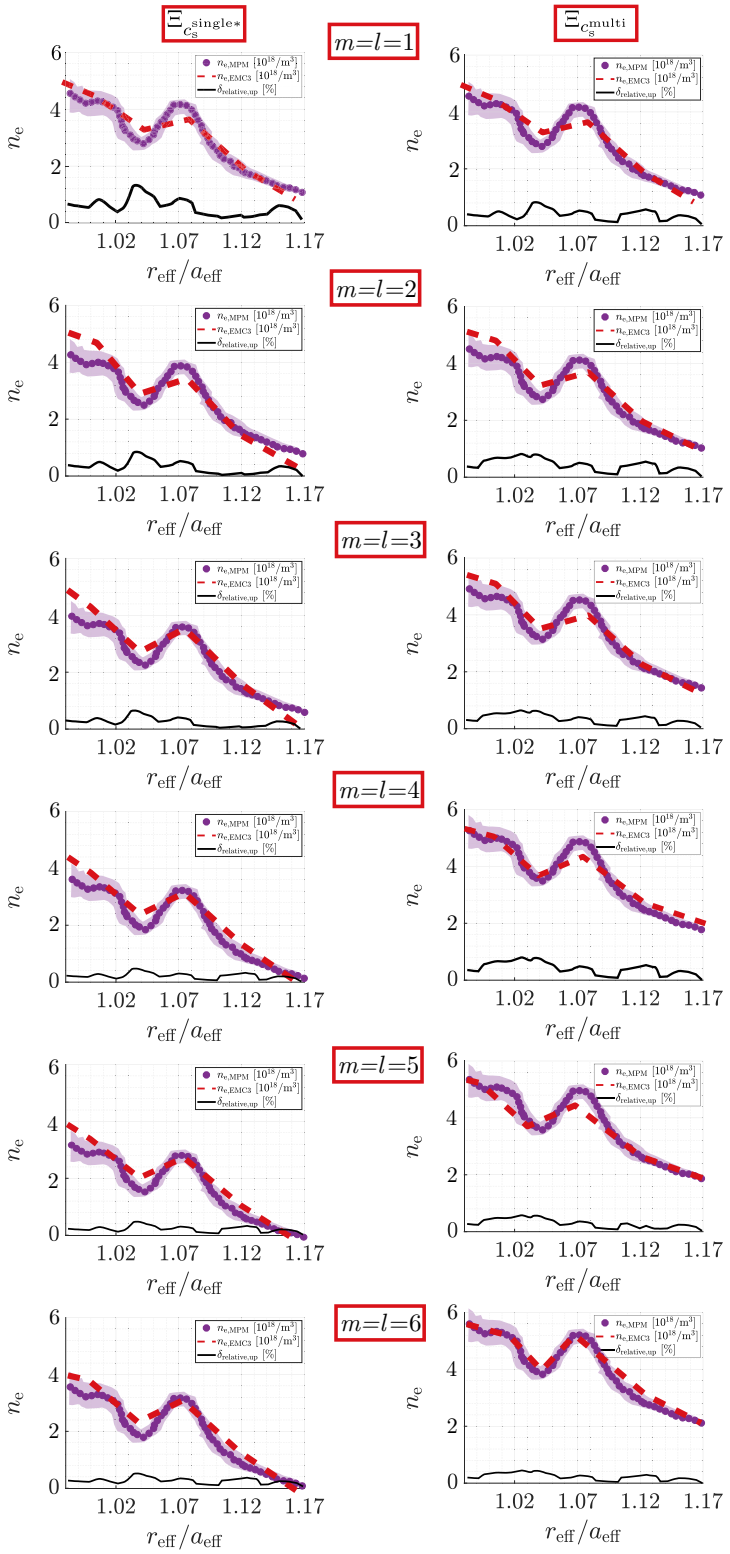

Figure A.6: All n_e profiles of the iterative process from $l = m = 1$ to $l = m = 6$.

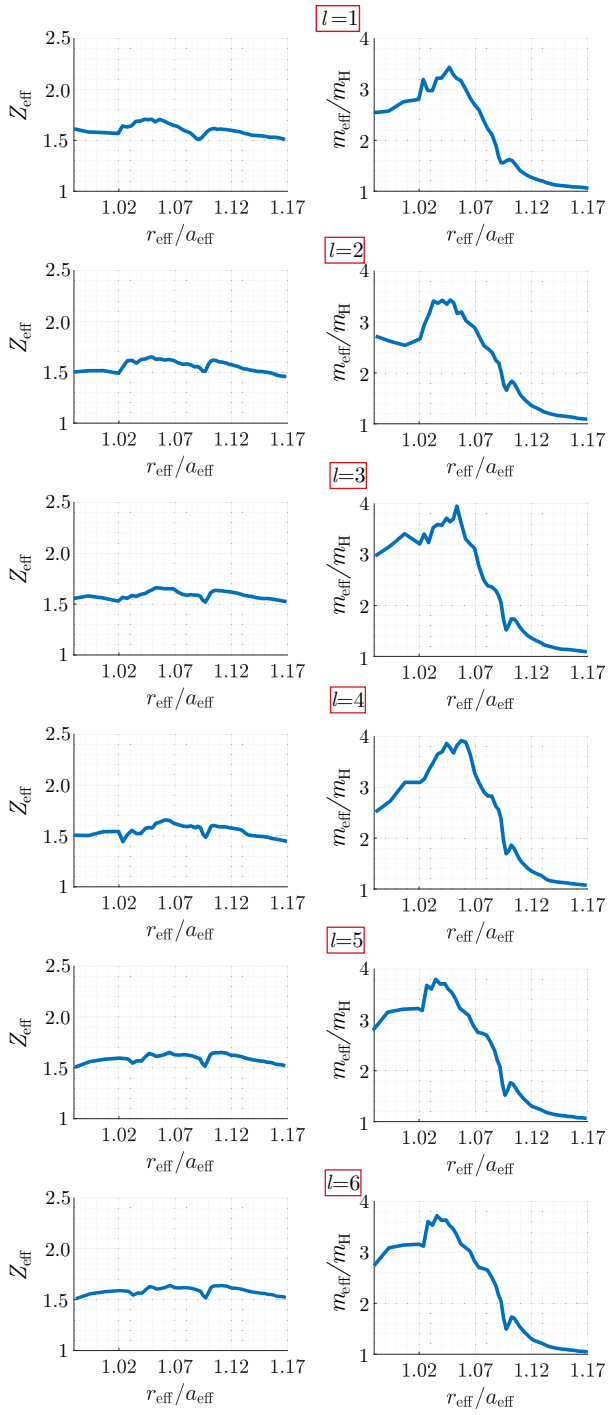

Figure A.7: All Z_{eff} and m_{eff} profiles of the iterative process from $l = 1$ to $l = 6$.

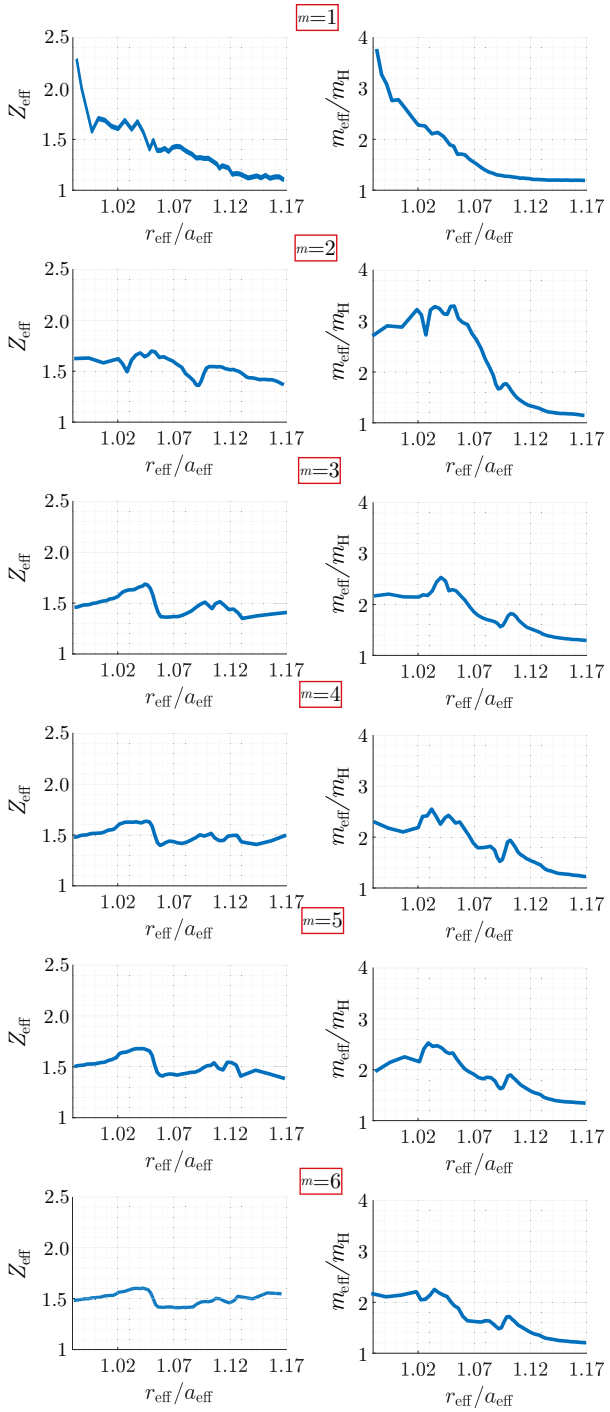

Figure A.8: All Z_{eff} and m_{eff} profiles of the iterative process from $m = 1$ to $m = 6$.

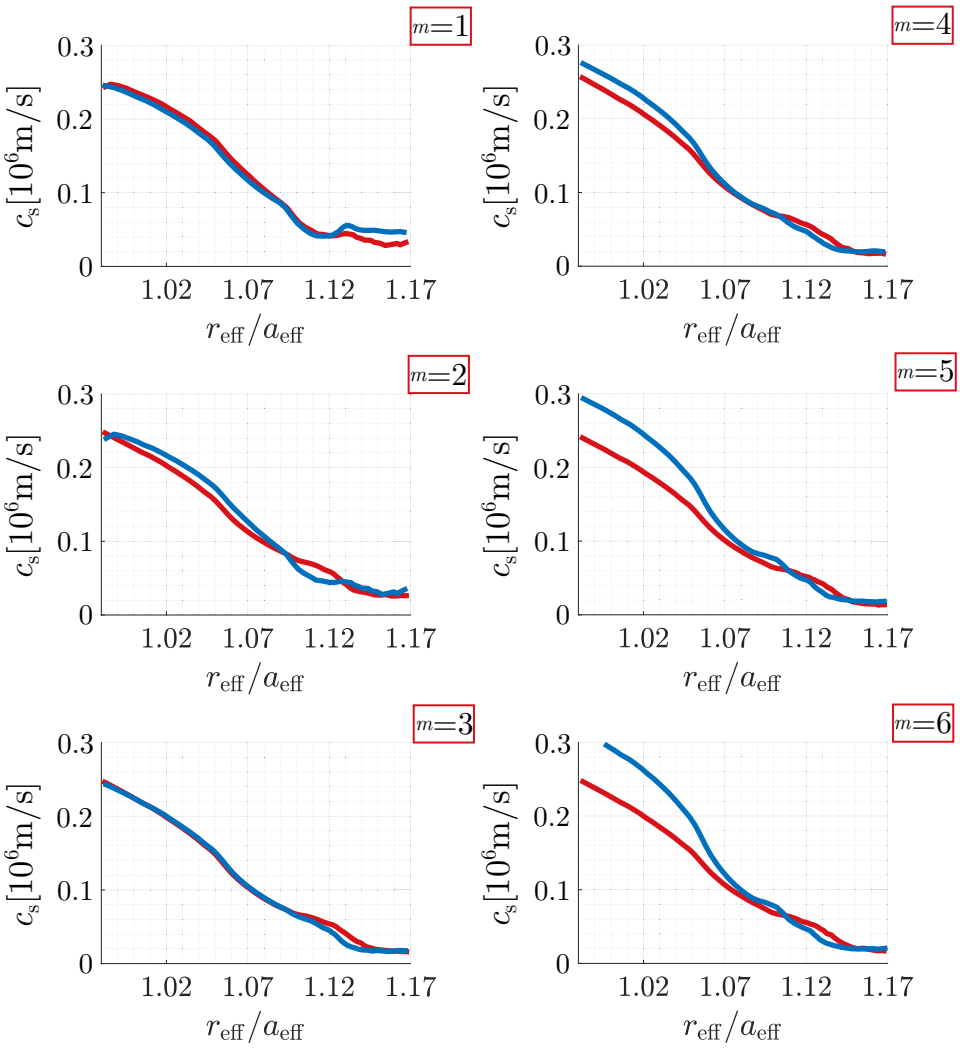

Figure A.9: All c_s profiles of iterative process $\Xi_{c_s^{\mathrm{single}*}}$ (red) and of $\Xi_{c_s^{\mathrm{multi}}}$ (blue) from $m = 1$ to $m = 6$.

Dedication and Acknowledgements

An dieser Stelle möchte ich meinen besonderen Dank nachstehenden Personen entgegen bringen, ohne deren Mithilfe die Anfertigung dieser Dissertation nicht zustande gekommen wäre: Mein Dank gilt zunächst Herrn Prof. Dr. Liang, meinem Doktorvater, für die Betreuung dieser Arbeit, der freundlichen Hilfe und der konstruktiven Ideengebung, die mir einen kritischen Zugang zu dieser Thematik eröffnete. Die zahlreichen Gespräche auf intellektueller und persönlicher Ebene werden mir immer als bereichernder und konstruktiver Austausch in Erinnerung bleiben.

Ich danke Herrn Prof. Dr. Egger für die hilfsbereite und wissenschaftliche Betreuung als Zweitgutachter.

Außerdem möchte ich Dr. Rack meinen Dank aussprechen, für die stetige und unermüdliche Hilfsbereitschaft auf wissenschaftlicher und kollegialer Ebene. Zahlreiche zusammen geführte kritische und konstruktive Diskussionen, sowie die mehrfache Durchsicht meiner Schriften wird mir in Erninnerung bleiben.

Tief verbunden und dankbar bin ich meiner Frau, Beate, für ihre Fähigkeit in aussichstlosen Situation stehts einen Weg zu sehen. Viele Situationen wären ohne Dich nicht lösbar gewesen.

Meinen Freunden, René, Jens, Helena und Jana möchte ich für ihren Beistand und ihre Hilfe bedanken.

Mein ganz besonderer Dank aber gilt meinen Eltern, Iris und Jürgen, die mir meinen bisherigen Lebensweg ermöglichten und denen ich diese Arbeit widme.

AUTHOR'S DECLARATION

I declare that the work in this dissertation was conducted in accordance with the requirements of the University's Regulations and Code of Practice for Research Degree Programmes and that it has not been submitted for any other academic award. Except where indicated by specific references in the text, the work is the candidate's own work. Work done in collaboration with, or with the assistance of, others, is indicated as such. Any views expressed in the dissertation are those of the author.

SIGNED: ..... DATE: .....

BIBLIOGRAPHY

[1] P. Stangeby, "The Plasma Boundary of Magnetic Fusion Devices", Taylor and Francis, 2000.

[2] T. Klinger *et al.*, "Towards assembly completion and preparation of experimental campaigns of Wendelstein 7-X in the perspective of a path to a stellarator fusion power plant", *Fusion Engineering and Design*, vol. 88, no. 6, pp. 461 – 465, 2013.

[3] D. Reiter, *et al.*, "The EIRENE and B2-EIRENE codes", *Fusion Science and Technology*, vol. 47, no. 2, pp. 172–186, 2005.

[4] R. Simonini, *et al.*, "Models and Numerics in the Multi-Fluid 2-D Edge Plasma Code EDGE2D/U", *Contributions to Plasma Physics*, vol. 34, no. 2-3, pp. 368–373, 1994.

[5] S. Wiesen, *et al.*, "The new SOLPS-ITER code package", *Journal of Nuclear Materials*, vol. 463, pp. 480 – 484, 2015.

[6] Y. Feng, *et al.*, "Transport in island divertors: physics, 3D modelling and comparison to first experiments on W7-AS", *Plasma physics and controlled fusion*, vol. 44, no. 5, p. 611, 2002.

[7] M. Kobayashi, *et al.*, "Divertor transport study in the large helical device", *Journal of Nuclear Materials*, vol. 363-365, pp. 294 – 300, 2007.

[8] S. I. Braginskii, "Transport Processes in a Plasma", *Reviews of Plasma Physics*, vol. 1, p. 205, 1965.

[9] F. F. Chen, "Introduction to Plasma Physics and Controlled Fusion", vol. 1. *Springer*, 1984.

[10] L. Spitzer Jr, "The Stellarator Concept", *The Physics of Fluids*, vol. 1, no. 4, pp. 253–264, 1958.

[11] R. Bickerton *et al.*, "Diffusion Driven Plasma Currents and Bootstrap Tokamak", *Nature Physical Science*, vol. 229, no. 4, p. 110, 1971.

[12] G. Jackson *et al.*, "Effects of impurity seeding in DIII-D radiating mantle discharges", *Nuclear fusion*, vol. 42, no. 1, p. 28, 2002.

[13] Y. Feng *et al.*, "3D Edge Modeling and Island Divertor Physics", *Contributions to Plasma Physics*, vol. 44 , no. 1-3, pp. 57–69, 2004.

[14] Y. Feng *et al.*, "3D fluid modelling of the edge plasma by means of a Monte Carlo technique", *Journal of Nuclear Materials*, vol. 266-269, pp. 812–818, 1999.

[15] D. Reiter *et al.*, "The EIRENE and B2-EIRENE Codes", *Fusion Science and Technology*, vol. 47, pp. 172–186, 2005.

[16] T. Klinger *et al.*, "Performance and properties of the first plasmas of Wendelstein 7-X", *Plasma Physics and Controlled Fusion*, vol. 59, no. 1, p. 014018, 2017.

[17] U. Stroth, "Plasmaphysik: Phänomene, Grundlagen, Anwendungen´´, *Vieweg-Teubner*, 2011.

[18] H. H. Bosch *et al.*, "Wendelstein 7-X, Overview and Status of Construction ", *21st IEEE/NPS Symposium on Fusion Engineering SOFE*, 2005.

[19] R. Wolf *et al.*, "Major results from the first plasma campaign of the Wendelstein 7-X stellarator", vol. 57, 2017.

[20] G. A. Wurden, "Limiter observations during W7-X first plasmas", *Nuclear Fusion*, vol. 57, no. 5, p. 056036, 2017.

[21] J. H. Malmberg *et al.*, "Dispersion of Electron Plasma Waves ", *Phys. Rev. Lett.*, vol. 17, pp. 175–178, 1966.

[22] W. M. Stacy, "Fusion Plasma Physics", *Wiley*, 2000.

[23] D. E. Post *et al.*, "Physics of Plasma-Wall Interactions in Controlled Fusion", *Springer Science & Business Media*, 2013.

[24] V. Erckmann *et al.*, "Electron Cyclotron Heating for W7-X: Physics and Technology", *Fusion Science and Technology*, vol. 52, no. 2, pp. 291–312, 2007.

[25] H. Hölbe, "Control of the magnetic topology and plasma exhaust in the edge region of Wendelstein 7-X : a numerical study", *Thesis, Universität Greifswald*, 2016.

[26] H. Renner, *et al.*, "Physical Aspects and Design of the Wendelstein 7-X Divertor", *Fusion science and technology*, vol. 46, no. 2, pp. 318–326, 2004.

[27] P. Drews *et al.*, "Measurement of the plasma edge profiles using the combined probe on W7-X", *Nuclear Fusion*, vol. 57, no. 12, p. 126020, 2017.

[28] T. S. Pedersen *et al.*, "Confirmation of the topology of the Wendelstein 7-X magnetic field to better than 1:100,000", *Nature communications*, vol. 7, no. 1, pp. 1–10, 2016.

[29] J. Nührenberg *et al.*, "Overview on wendelstein 7-x theory", *Fusion Technology*, vol. 27, no. 3T, pp. 71–78, 1995.

[30] Y. Suzuki *et al.*, "Impact of nonlinear 3D equilibrium response on edge topology and divertor heat load in Wendelstein 7-X", *Plasma Physics and Controlled Fusion*, vol. 58, no. 6, p. 064004, 2016.

[31] J. Hopwood *et al.*, "Langmuir probe measurements of a radio frequency induction plasma", *Journal of Vacuum Science & Technology A: Vacuum, Surfaces, and Films*, vol. 11, no. 1, pp. 152–156, 1993.

[32] J. G. Watkins *et al.*, "High heat flux Langmuir probe array for the DIII-D divertor plates", *Review of Scientific Instruments*, vol. 79, no. 10, p. 10F125, 2008.

[33] D. Nicolai *et al.*, "A multi-purpose manipulator system for W7-X as user facility for plasma edge investigation", *Fusion Eng. Des.*, 2017.

[34] G. Satheeswaran *et al.*, "A PCS7-based control and safety system for operation of the W7-X Multi-Purpose Manipulator facility", *Fusion Engineering and Design*, vol. 123, no. Supplement C, pp. 699 – 702, 2017.

[35] O. Neubauer *et al.*, *et al.*, "Diagnostic setup for investigation of plasma wall interactions at Wendelstein 7-X", *Fusion engineering and design*, vol. 96, pp. 891–894, 2015.

[36] D. Zhang *et al.*, "Design criteria of the bolometer diagnostic for steady-state operation of the W7-X stellarator", *Review of Scientific Instruments*, vol. 81, no. 10, p. 10E134, 2010.

[37] R. König *et al.*, "The Set of Diagnostics for the First Operation Campaign of the Wendelstein 7-X Stellarator", *Journal of Instrumentation*, vol. 10, no. 10, p. P10002, 2015.

[38] R. Burhenn *et al.*, "Impurity Transport Studies in the Wendelstein 7-AS Stellarator", *Fusion science and technology*, vol. 46, no. 1, pp. 115–128, 2004.

[39] Y. Nakamura *et al.*, "Plasma performance and impurity behavior in long pulse discharges on LHD", *Nuclear fusion*, vol. 43, no. 4, p. 219, 2003.

[40] Andreeva *et al.*, "Vacuum Magnetic Configurations of Wendelstein 7-X", *IPP-Report*, vol.IPP III/270, 2002.

[41] T. S. Pedersen *et al.*, "Plans for the first plasma operation of Wendelstein 7-X", *Nuclear Fusion*, vol. 55, no. 12, p. 126001, 2015.

[42] A. Dinklage *et al.*, "Magnetic configuration effects on the Wendelstein 7-X stellarator", *Nat. Phys.*, 2018.

[43] S. I. Krasheninnikov, "On scrape off layer plasma transport", *Physics Letters A*, vol. 283, no. 5-6, pp. 368–370, 2001.

[44] S. Chapman, "Thermal Diffusion in Ionized Gases", *Proceedings of the Physical Society*, vol. 72, no. 3, p. 353, 1958.

[45] J. Neuhauser *et al.*, "Modelling of impurity flow in the tokamak scrape-off layer", *Nuclear Fusion*, vol. 24, p. 39, 1984.

[46] Y. Feng *et al.*, "3D fluid modelling of the edge plasma by means of a Monte Carlo technique", *Journal of Nuclear Materials*, vol. 266-269, pp. 812–818, 1999.

[47] Y. Feng *et al.*, "Formulation of a Monte Carlo model for edge plasma transport", *27th EPS Conference on Contr. Fusion and Plasma Phys*, vol. 24, pp. 1188–1191, 2000.

[48] Y. Feng *et al.*, "3D Edge Modeling and Island Divertor Physics", *Contributions to Plasma Physics*, vol. 44 , no. 1-3, pp. 57–69, 2004.

[49] Y. Feng *et al.*, "A simple highly accurate field-line mapping technique for three-dimensional Monte Carlo modeling of plasma edge transport", *Physics of plasmas*, vol. 12, no. 5, p. 052505, 2005.

[50] M. Krychowiak *et al.*, "Overview of diagnostic performance and results for the first operation phase in Wendelstein 7-X", *Review of Scientific Instruments*, vol. 87, no. 11, p. 11D304, 2016.

[51] H. Niemann *et al.*, "Power loads in the limiter phase of Wendelstein 7-X", *43rd EPS Conf. on Plasma Physics P*, vol. 4, p. 5, 2016.

[52] M. Z. Tokar, "Fluid Approximation of the Bohm Criterium for Plasmas of Several Ion Species", *Contributions to Plasma Physics*, vol. 34, no. 2-3, 1994.

[53] Y. Igitkhanov, "Modelling of Multi-Component Plasma for TOKES", *KIT Scientific Reports*, vol. 7564, pp. ISSN 1869–9669.

[54] V. H.B. *et al.*, "Boundary value problems for multi-component plasmas and a generalized Bohm criterion", *Journal of Physics D: Applied Physics*, vol. 29, no. 5, p. 1175, 1996.

[55] J. Cosfeld *et al.*, "Effective charge state modelling for Wendelstein 7-X edge plasmas", *Manuscript submitted for publication to Nuclear Fusion* 2018 and
Report JUEL-4414, ISSN 0944-2952, 2018.

[56] J. Roth, "Status of knowledge of chemical erosion of carbon and critical issues for extrapolation to ITER", *Physica Scripta*, vol. 2006, no. T124, pp. 37, 2006.

[57] H. Damm, "Upgrade of the Wendelstein 7-X Thomson Scattering Diagnostic to Study Short Transient Plasma Effects – A Demonstration on Pellet Injection for Stellarator Fuelling", *Thesis, University of Greifswald*, 2018.

[58] A. Pavone *et al.*, "Minerva neural network based surrogate model for real time inference of ion temperature profiles at Wendelstein 7-X", in *APS Meeting Abstracts*, 2017.

[59] S. Kwak *et al.*, "Bayesian modelling of multiple diagnostics at wendelstein 7-x using the minerva framework", in *APS Meeting Abstracts*, 2017.

[60] T. Lunt, Y. Feng, M. Bernert, A. Herrmann, P. de Marne, R. McDermott, H. Müller, S. Potzel, T. Pütterich, S. Rathgeber, *et al.*, "First emc3-eirene simulations of the impact of the edge magnetic perturbations at asdex upgrade compared with the experiment", *Nuclear Fusion*, vol. 52, no. 5, p. 054013, 2012.